UNIVERSITÀ
DEL SALENTO

Department of Mathematics and Physics "E. De Giorgi"
PhD in Physics and Nanoscience

Thesis for the degree of Doctor of Philosophy

The PADME
Active Diamond Target
and Positron Bremsstrahlung Analysis

Supervisors:
Dr. Gabriele Chiodini
Prof. Stefania Spagnolo

Candidate:
Federica Oliva

Academic year 2019-2020 (XXXIII cycle)

Contents

"That you are here-that life exists and identity,
That the powerful play goes on, and you may contribute a verse."
W. Whitman

Abstract

The lack of direct experimental observation of dark matter candidates at the electroweak scale so far could be justified with the introduction of a dark sector that can only feebly interact with the known word. The corresponding gauge boson of the dark sector is the dark photon. Several experiments around the world are searching for a dark photon in the visible or invisible decays. PADME is the first experiment using the annihilation of a bunched positron beam against a thin target, as a production channel for the dark photon, and the missing mass technique to discover the dark photon as a peak above a smooth background.
PADME exploits a large size thin diamond detector with laser-made graphite strips on both sides as a "full carbon" active target. This is a new kind of detector, entirely developed in my thesis work and operated successfully in PADME. In addition, the first analysis of Bremsstrahlung process is developed, which represents an important achievement for the experiment being the main background to the dark photon search.

Introduction

A puzzling topic nowadays is the nature of the dark matter. Its evidence was indirectly inferred from astrophysical and cosmological observations, starting from Zwicky's work, who called dark matter the missing mass he found applying the virial theorem to the velocity dispersion of galaxy belonging to the Coma Cluster. This thesis work addresses the experimental search with PADME (Positron Annihilation Into Dark Matter Experiment) of a dark photon, which is expected to exist if dark matter constituents are low mass particles not charged with respect to Standard Model gauge symmetries. The lack of hints of new particles at LHC energy scale is a strong motivation to search for light dark matter. In this case, if dark matter is a thermal relic of the Big-Bang, a new sub-GeV mediator is required to exist, to avoid light dark matter over-production, such as a dark photon.
Several experiments around the world are searching for a dark photon in the visible or invisible decays.
PADME is the first experiment using the annihilation of a bunched positron beam against a thin target, as a production channel for the dark photon, and the missing mass technique to discover the dark photon as a peak above a smooth background. In addition, PADME exploits a large size thin diamond detector with laser-made graphite strips on both sides as a "full carbon" active target. This is a new kind of detector, entirely developed in my thesis work and operated successfully in PADME.
In Chapter 1 the various phenomena interpreted as indications of a gravitationally interacting new kind of matter are presented and inserted in the historical context. These are the Coma cluster velocity dispersion, the Galaxy rotation curve, the hot gas in clusters, the Bullet Cluster, and the fluctuations of the cosmic microwave background radiation. This is followed by the presentation of a dark sector as a solution for the lack of direct experimental observation of dark matter candidates at the electroweak scale. The dark sector can only faintly interact with the Standard Model particles through a neutral portal. The simplest model of neutral portal consists of an additional abelian gauge symmetry $U'(1)$ and the corresponding mediator is named dark photon. This particle can determine weak couplings between the Standard Model particles and the dark sector by mixing with the Standard Model photon. Hereafter, the dark photon production mechanisms and decays are presented. Finally, Chapter 1 provides a brief review of the various experiments around the world searching for the dark photon, in the hypothesis of visible or invisible decays, and exploiting different experimental techniques to separate the signal from the background. The regions in the parameter space of mass and mixing coefficient excluded so far and those in the reach of forthcoming experiments are presented.
The fixed target experiment PADME is extensively described in Chapter 2, starting from a description of the Beam Test Facility (BTF) at the Laboratori Nazionali di Frascati (LNF), where it is located. A comprehensive review of each PADME sub-detector is provided together with a description of its trigger-data acquisition system. In Chapter 2 the analysis strategy and the sensitivity of PADME in the search of the dark photon is elucidated, underlying the use of the missing mass technique, which is model independent. The main background process, the

positron Bremsstrahlung, is introduced. Additional searches, that can be pursued in PADME alongside with the search for the dark photon, are finally presented. They aim at observing Axion Like Particles (ALPs) and dark Higgs, or with a thick Tungsten target, the protophobic X boson which is claimed to explain the anomaly seen in ^{8}Be nuclear decay.
In Chapter 3 the details of the active diamond target of PADME, which I designed, built, commissioned and fully characterised, are discussed in depth. Indeed, I was actively involved as forefront person, from the first diamond detector prototype up to the detector maintenance in the PADME experiment. A brief introduction of diamond as material used to detect ionizing radiation is given, together with the state of the art of diamond detectors. This is followed by an extensive discussion of the novelty involved in the design of the PADME active diamond target, which is the first full carbon double-sided strip detector ever used in a high energy physics experiment.
Chapter 3 describes all the steps leading to the construction of the diamond target, starting from a large size (2×2 cm^2) polycrystalline diamond film 100 μm thick and ending with graphitic strips, produced by means of an excimer ArF laser. The front-end electronics chosen, to readout the diamond signal, and the interconnection technique, between sensor and electronics, are illustrated, followed by the the installation in the PADME experiment in September 2018. Finally, the first experience with the target operation and the calibration of the front-end electronics by charge injection are described. Chapter 4 presents the PADME data taking periods, where I have actively participated in all the aspects since the beginning. The tools useful to guarantee an efficient data taking, such as a reliable Detector Control System (DCS) and an online monitor system are described. The first is oriented to solve hardware and data acquisition problems and the second one to provide in real time a check of the data quality for an efficient data taking based on local (from PADME control room in Frascati) and remote shifts.
While I contributed to the general monitor system, I was fully responsible for the development of the DCS of the diamond target, both in the version for experts and users. Chapter 5 is entirely devoted to the active diamond target performance and its task of providing a reliable measurement of the bunch multiplicity during data taking. The target response calibrated in-situ will be reported, along with its dependence on beam features, in particular the beam focusing. Since the first days of operation the diamond target showed good performance, that are reported in the same Chapter. In the last section studies of the detector uniformity response, such as charge sharing and border effects, made possible by the availability of a well focused beam, are described.
Chapter 6 is entirely devoted to the description of the first analysis made in PADME of Bremsstrahlung process. The Bremsstrahlung analysis which I developed for this thesis work represents an important achievement for the experiment being the main background to the dark photon search.
As a necessary introduction to this topic, the software tools used to reconstruct the PADME data and to simulate the experiment are introduced. They consist in the simulation of the beam line and sub-detectors in a GEANT4 based framework and in the reconstruction program, which builds physical objects, from the signals produced by the various detectors. A successful comparison of data and simulation was possible only after equalization of the single channel gain and time alignment were accomplished. In addition, in simulation the tuning of the hit digitization algorithm to the single channel response in data was necessary to improve the comparison. For these reasons, the data processing of the charged particle veto will be presented, together with the tuning of the simulation to data.
Finally, the Bremsstrahlung signal is obtained with two different procedures: from the study of the cluster profile in the positron detector and from the identification of simultaneous photons in the forward calorimeter and positrons in the veto detector. The comparison between data and

predictions is presented and discussed in detail. The main achievements of this thesis work, their impact on the experiment and on dark photon experimental searches and some considerations on potential improvements in the field are summarised in the conclusions.

Chapter 1

Dark matter and dark photon

According to the Standard Model of Cosmology, the Universe consists of ordinary baryonic matter for 5%, dark matter for 26%, and dark energy for the remaining 69%.
The nature of Dark Matter (DM) is perhaps the longest outstanding problem of all modern physics. Although DM is the dominant matter component in the Universe, its composition is still unknown and its investigation could lead to the discovery of new physics.
The dark matter puzzle will be introduced in Section 1.1. The Standard Model of particle physics (SM) is not sufficient to explain the existence of DM; for this reason, models of Physics Beyond the SM (BSM) incorporating DM candidates are attracting the attention of the whole scientific community nowadays. The introduction of a new hidden sector, where dark matter could be confined, represents one of the possible scenarios to go beyond the SM. In particular, a new dark boson could act as a mediator between the SM and this new dark sector.
The theoretical hypothesis of the existence of a dark photon is one of the topics discussed in this thesis. Its phenomenology is summarized in Section 1.2.2, both in the massless and massive case, along with the cosmological implications. After the theoretical introduction, the search of this elusive boson at the accelerators is presented in Section 1.3. There are many experiments around the world that are currently searching for the dark photon; the features and results of these experiments are summarized in Section 1.3.3.

1.1 The Dark Matter puzzle

The Universe as we know it consists not only of ordinary matter but also of something that is still obscure. Currently the Λ Cold Dark Matter model (ΛCDM) is the widely-accepted cosmological model to explain the Universe evolution. Although it is a simple model, it can account for the formation of galaxies and clusters of galaxies, leading to a good agreement between theory and observations at large scale and allowing for a satisfactory understanding of the Cosmos.
The lack of understandings of the dark matter nature is likely due to the fact that it can easily escape detection. DM is literally non-luminous matter and it could be made of slow particles, which neither emit, absorb nor reflect light by definition; for this reason it cannot be detected by standard instrumentation.
Lord Kelvin was one of the first to attempt to estimate the amount of Dark Matter in 1904, followed by the Estonian astronomer Opik in 1915, the dutch astronomers Kapteyn in 1922 and, later, his pupil Oort in 1932. The one widely cited as the pioneer of the study on dark matter is Fritz Zwicky, a Swiss astronomer that provided the very first reliable dark matter evidence, dated back to 1933. He found out a large disagreement between the theoretical calculation and the measurement of the galaxy dispersion velocity of the famous Coma Cluster. From his article

(translated into English) [1] [2]:
"If this would be confirmed, we would get the surprising result that dark matter is present in much greater amount than luminous matter".
For several years the discovery of this *Dunkle Materie* (dark matter) was not taken seriously; only in the 1970s Zwicky's hypothesis was confirmed by the study of Vera Rubin and dark matter was definitively brought to light. Starting from the Coma Cluster anomaly, over the years, several observations of the indirect effects of gravitational interactions with ordinary matter have confirmed the existence of dark matter. The existence of dark matter, inferred from cosmological and gravitational observations, is described in Section 1.1.2. Before presenting the topic in depth, some essential cosmology parameters and tools will be introduced.

1.1.1 Cosmological parameters

The Hubble constant H_0 is the constant of proportionality between the recession speed $\dot{r}$ and the relative distance r, in the expanding Universe, of two distant galaxies; its value is:

$$H_0 = \frac{\dot{r}}{r} \approx 70 \, \frac{\text{km}}{\text{Mpc s}} \tag{1.1}$$

where the subscript zero refers to the current epoch.
Under the assumption of homogeneity of the Universe, it is possible to write the relative distance r as a function of time in terms of the scale factor of the expansion $a(t)$, $r = a(t)r_0$, where r_0 is the current relative distance. In this way the Hubble law becomes:

$$H(t) = \frac{\dot{a}(t)}{a(t)} \tag{1.2}$$

Sometimes, instead of H_0, the variable h is considered, which is a pure number, defined as follows:

$$h = \frac{H_0}{100 \, \frac{\text{km}}{\text{Mpc s}}} \approx 0.7 \tag{1.3}$$

The critical density ρ_c is defined as the value of the total density ρ_t leading to the asymptotic stop of the expansion of the Universe.
The mass density parameter Ω_m is the ratio of the average density of matter ρ_m in the Universe to the critical density:

$$\Omega_m = \frac{\rho_m}{\rho_c}. \tag{1.4}$$

Analogous adimensional parameters are used for the barionic density ($\Omega_b = \rho_b/\rho_c$), the dark matter density ($\Omega_\chi = \rho_\chi/\rho_c$) and the dark energy density ($\Omega_\Lambda = \rho_\Lambda/\rho_c$).
The overall Universe content can be written as follows:

$$\Omega_t = \Omega_m + \Omega_\Lambda \tag{1.5}$$

where $\Omega_m = \Omega_\chi + \Omega_b$ is the mass contribution, which largely depends on the dark matter content Ω_χ and, to a smaller extent, on the barionic component Ω_b. The remaining term Ω_Λ refers to the dark energy. Currently, it seems that Ω_t is very close to 1: however, in general, deviations from this special value can lead to dramatically different scenarios:

- if $\Omega_t > 1$ the Universe is closed; its expansion eventually stops and the Universe will collapse;
- if $\Omega_t < 1$ the Universe is open and it will continue to expand forever;
- if $\Omega_t = 1$ the Universe is flat and contains enough matter to reduce the acceleration of the expansion but not enough to recollapse.

1.1.2 Cosmological evidence for Dark Matter

The main indirect indications of the existence of dark matter will be chronologically listed below, starting from Zwicky's observations.

Coma cluster anomaly

Zwicky is celebrated as the father of dark matter and a pioneer of its discovery. He was one of the first to postulate the existence of a new kind of matter different from and non-interacting with the ordinary matter, therefore not observable. Zwicky applied the virial theorem to the velocity dispersion of galaxies within the Coma cluster, in order to infer its total mass. The virial theorem is a straightforward application of classical mechanics, relating the velocity of orbiting objects to the amount of gravitational energy that binds them. Basically, a cluster of galaxies can be seen as a system of N objects each of them of mass m and orbital velocity v. The single mass, as well as the single velocity, can not be measured directly. However, under the assumption that the system is spherically symmetric and in equilibrium, the velocity is uniformly distributed over all directions.
The kinetic energy K is equal to:

$$\mathrm{K} = \frac{1}{2}\,\mathrm{M}\,\langle \mathrm{v}^2 \rangle \tag{1.6}$$

where M is the total mass of the system and $\langle v^2 \rangle$ is the mean of the orbital velocity square with respect to the cluster center of mass. Assuming that clusters of galaxies are bound systems, the virial theorem can be applied:

$$\mathrm{K} = -\frac{\mathrm{U}}{2} \tag{1.7}$$

where U is the total gravitational energy. In the simplified assumption of uniform mass density, U is given by:

$$\mathrm{U} = -\frac{3}{5}\,\frac{\mathrm{GM}^2}{\mathrm{R}}. \tag{1.8}$$

where R is the cluster radius and G the gravitational constant.
In such a way Zwicky was able to infer the total mass of the Coma Cluster from the measurements of the galaxies radial velocity ($\langle v^2 \rangle = 3\langle v_r^2 \rangle$). From 1.6, 1.7 and 1.8, the following relation can be obtained:

$$\mathrm{M} = \frac{5}{3}\,\frac{\mathrm{R}\,\langle \mathrm{v}^2 \rangle}{\mathrm{G}} \tag{1.9}$$

From the measurements, presented in the journal of the Swiss Physical Society in 1933, the total mass of the Coma cluster, inferred from 1.9, would have to be 400 times greater than the estimate derived from the luminous matter [1]. In other words, Zwicky's results showed that the orbital velocities of galaxies were much larger than the values predicted by a calculation based on the total visible mass of the Coma cluster. Zwicky overestimated the ratio of mass to luminous mass [1] because he used a non precise value of the Hubble constant, relying on the paper of Hubble and Humason published in 1937. In that work [3] the first estimate of the Hubble constant was reported to be H_0=558 km/Mpc s, with an uncertainty of 10-20%. Today we know that the factor of 400 should rather be $\simeq 50$, as a result of the modern value $H_0 = 67.27 \pm 0.66$ [4].
The result was indeed striking. As Zwicky wrote in the original article [1](translated in English): [..] *the large velocity dispersion in the Coma system (and other dense clusters of nebulae) holds an unsolved problem ("Problem in sich birgt").*
Unfortunately, Zwicky's discovery was not taken seriously by the astronomical community. It took another three decades for the phenomenon to be widely observed. And only after Zwicky's

[1] The total mass needed to produce the measured amount of light.

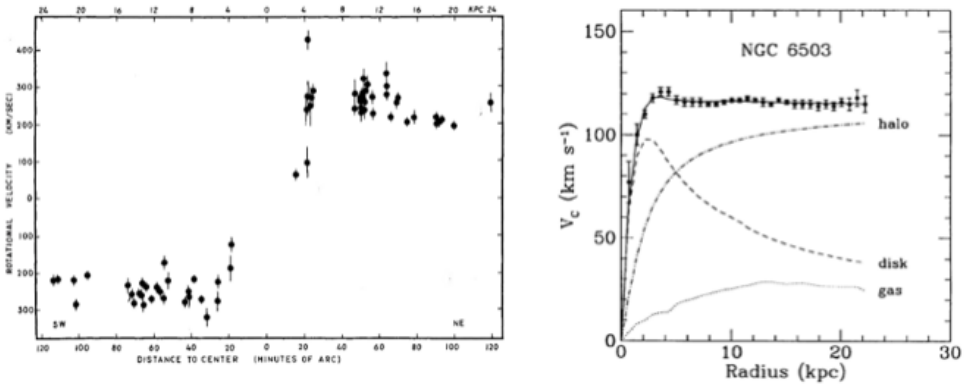

Figure 1.1: Rotational velocity as a function of the radius of the galaxies M31 [5] and NGC 6503 [7].

death, in 1974, dark matter was accepted as part of the cosmological paradigm, thanks to the work of radio astronomers, cosmologists and particle physicists.

Galaxy rotation problem

In 1970s the hypothesis of Zwicky was corroborated by the research of Vera Rubin and her collaborator Kent Ford, who measured the spectra of stars in Andromeda Galaxy (M31) and inferred their velocities [5].
According to the laws of the classical mechanics, applied to the motion of stars into galaxies, the further away an object of mass m is from the centre of the galaxy, the slower it should travel in orbit, because the gravitational pull decreases with the distance r like $1/r^2$. Indeed, if v is the rotational velocity of the object, one can write:

$$m\frac{v^2}{r} = \frac{GM(r)m}{r^2} \tag{1.10}$$

where M is the total mass inside the radius r.
Therefore, an object travelling on a orbit of a radius r around the galaxy centre, moves with velocity $v(r) \sim \sqrt{M(r)/r}$. Outside the visible part of the galaxy, the velocity should scale as $v(r) \sim \sqrt{1/r}$. Rubin and Ford found out that this velocity became approximately constant for large values of r, also outside the visible edge of the galaxy, as shown in Figure 1.1 (left). This flat rotation curve was indeed a proof of the existence of missing and unseen matter. In fact, this discovery suggested the presence of a *dark halo* surrounding the galaxy, whose mass $M(r)$ scales like r, and whose density $\rho(r)$ scales like $1/r^2$.
A more accurate study published in 1978, including a wider sample of galaxies, was performed by Rubin and collaborators, still showing the flatness of the trend of the velocity curve at large distances[6]. In Figure 1.1 (right) the velocity of the NGC 6503 galaxy as a function of the radial distance from the galactic center, taken from a recent article is shown, validating the Rubin's measurements.

Hot gas in clusters

The observations of X-ray emission from the hot Intra-Cluster Medium (ICM) can be classified among the gravitational indications of dark matter [8]. The ICM is made of plasma spread

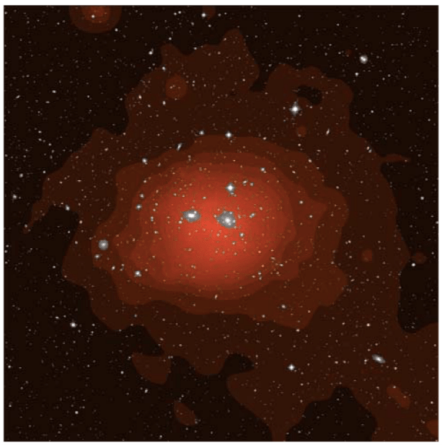

Figure 1.2: Coma Cluster seen with X-rays image from the ROSAT All-Sky Survey in red. Optical image of the Palomar Sky Survey superimposed in grey [10].

out in the space between galaxies in a cluster. The ICM emits X-ray radiation, mostly from Bremsstrahlung processes and X-ray emission from heavy elements, and can be studied through X-ray telescopes. In Figure 1.2 the Coma Cluster is shown as seen in the X-rays image from the ROSAT All-Sky Survey (in red) , superimposed to the optical image from the Palomar Sky Survey (in white). The X-ray view clearly shows that galaxies are not isolated but they are embedded into a wide cluster, which represents a fundamental object of the sky. Isothermal hydrostatic models allow to infer the mass density and temperature of the heated gas from measurements of the X-ray emission within the cluster. Moreover, the presence of such a hot can only be explained by a large dark matter component that provides the potential well to hold it in the cluster [9].

Gravitational lensing and bullet cluster

The existence of matter that does not emit light can be proved gravitationally by exploiting a peculiar effect predicted by the Einstein's general relativity theory. A massive body bends the path of light, so that the light emitted by far-away sources, can be lensed by the presence of a compact, massive object, thus producing distorted or multiple images of the source; the effect is proportional to the quantity of matter on the light way. Gravitational lensing confirmed the abundance of unknown matter in galaxies and cluster of galaxies from the distribution of shapes and alignment of galaxies to measure the foreground mass [11]. In particular, the so called Bullet Cluster [12] (Figure 1.3) (i.e. the cluster merger 1E 0657-56) is considered the strongest evidence for the existence of non baryonic dark matter interacting gravitationally.
The Bullet Cluster, located at a distance of about 3.8 billion light years from the Earth, consists of two colliding clusters of galaxies. This collision is probably the most energetic event happened so far since the Big Bang. It acts as a dark matter particle collider, potentially allowing the discrimination between different particle physics models of DM. The picture in Figure 1.3 is the overlap of different images of the Bullet Cluster coming from different sources and it shows the clusters after the collision. The two pink stacks are detected by Chandra in X-rays and represent the dominant component of the barionic matter, after the collision consisting of hot gas. The gas blobs of the two clusters are slowed down during the collision by electromagnetic interactions. The galaxies in white and orange are taken from an optical image from Magellan and the Hubble Space Telescope. The galaxy component of the two clusters is not slowed down in the collision, due to the large inter-galaxy distances. The most interesting part is the blue one, representing

Figure 1.3: Bullet Cluster (1E 0657-56) picture [13] composed overlapping the X-rays picture from Chandra and an optical image from Hubble Space Telescope and Magellan. (NASA/CXC/CfA/M.Markevitch et al.; Optical: NASA/STScI; Magellan/U.Arizona/D.Clowe et al.[12]; Lensing Map: NASA/STScI; ESO WFI[12]; Magellan/U.Arizona/D.Clowe et al. [14])

matter inferred only by gravitational weak lensing effects, but otherwise unobserved. This is interpreted as dark matter, interacting only gravitationally and therefore remaining unaffected in the collision. As a consequence the dark matter blobs are localized in the same areas where the galaxies are observed, unlike the slowed-down gas clusters that appear delayed, i.e. closer to the collision point.

Fluctuations in the Cosmic Microwave Background radiation

The Cosmic Microwave Background (CMB) radiation provides evidence for the Big Bang. It consists of a isotropic thermal radiation that permeates the entire Universe. The difference in temperature between two random points, the ratio $\delta T/T$, is smaller than 10^{-4} with T=2.275 K. This extreme uniformity today appears surprising. A possible explanation is that all locations of the Universe during the early times were in causal connection. Later, the expansion of the Universe in a short time, due to the inflation mechanism, produced the large separation between originally nearby points, that today appear not causally connected. The temperature dispersion of the CMB is probably one of the most important observable for dark matter studies. Following [15], the temperature variations on a sphere can be written in terms of spherical harmonics, depending on the angular variables (θ, ϕ):

$$\frac{\delta T(\theta,\phi)}{T_0} = \frac{T(\theta,\phi) - T_0}{T_0} = \sum_{\ell=0}^{\infty} \sum_{m=-\ell}^{\ell} a_{\ell m} Y_{\ell m}(\theta,\phi) \tag{1.11}$$

where the $Y_{\ell m}$ functions have the following property:

$$\int d\Omega \; Y_{\ell,m}(\theta,\phi) Y^*_{\ell',m'}(\theta,\phi) = \delta_{\ell\ell'}\delta_{mm'}. \tag{1.12}$$

Therefore the average squared relative fluctuation can be calculated as follows:

$$\begin{aligned} \frac{1}{4\pi}\int d\Omega \; \left(\frac{\delta T(\theta,\phi)}{T_0}\right)^2 = \frac{1}{4\pi}\int d\Omega \; \left[\sum_{\ell m} a_{\ell m} Y_{\ell m}(\theta,\phi)\right]\left[\sum_{\ell' m'} a^*_{\ell' m'} Y^*_{\ell' m'}(\theta,\phi)\right] = \\ = \frac{1}{4\pi}\sum_{\ell m,\ell' m'} a_{\ell m} a^*_{\ell' m'}\delta_{\ell\ell'}\delta_{mm'} = \frac{1}{4\pi}\sum_{\ell m} |a_{\ell m}|^2. \end{aligned} \tag{1.13}$$

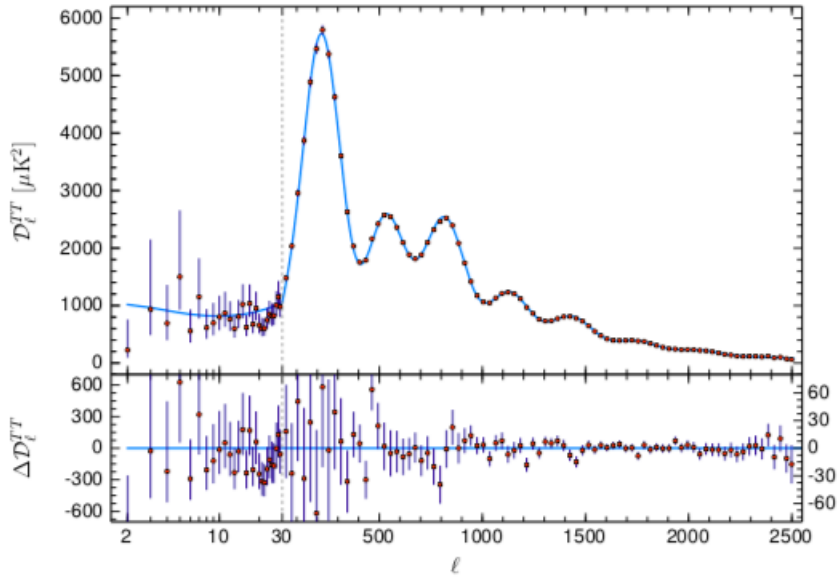

Figure 1.4: Power spectrum as measured by Planck in 2018 in terms of the coefficients $\mathcal{D}_\ell = \frac{\ell(\ell+1)}{2\pi} C_\ell$ as a function of the multiple momentum ℓ. Figure from the Planck collaboration [17].

The *power spectrum* C_ℓ of the CMB temperature is defined as the average of the $|a_{\ell m}|^2$ over m as follows:

$$C_\ell = \frac{1}{2\ell+1} \sum_{m=-\ell}^{\ell} |a_{\ell m}|^2. \tag{1.14}$$

The power spectrum distribution as a function of the multipole momentum ℓ shows several Doppler peaks, that can be interpreted in terms of the cosmological parameters.
In particular, the first peak of the distribution is related to the total matter density $\Omega_m h^2$ while the ratio of the amplitudes of the second to first Doppler peaks depends on the baryonic density parameter Ω_b.
The CMB study was pioneered by the space mission COsmic Background Explorer (COBE), launched in orbit by NASA in 1989, to perform essential cosmology measurements. The first detailed results were provided by its successor, the Wilkinson Microwave Anisotropy Probe (WMAP), a satellite launched in 2001. The most recent result published by the WMAP group is based on the measurements taken in 9 years [16]. The ESA's Planck satellite, launched in 2009, provided the most detailed results so far and the latest are the following [17]:

$$\begin{gathered} \Omega_\chi h^2 = 0.1198 \pm 0.0012, \ \Omega_m h^2 = 0.1428 \pm 0.0011 \\ \Omega_b h^2 = 0.02223 \pm 0.00015, \ H_0 = 67.37 \pm 0.54 \, \frac{\text{km}}{\text{Mpc s}} \end{gathered} \tag{1.15}$$

The Planck collaboration was able to identify up to seven peaks in the spectrum, as shown in Figure 1.4.

Large scale structure

The structure formation models and the present distribution of visible matter in stars, galaxies, and clusters of galaxies, provide further indirect evidence for dark matter. Complex but

reliable simulations are used to test the ability of cosmological models, like CDM, to explain the formation of this structure observed today. Actually, it is impossible to get a match to the observed structure, with voids and clumps, without accounting for Dark Matter. According to the structure formation theories, the structures were born from small perturbations of the distribution of matter in the early Universe, which was overall uniform [18]. The Sloan Digital Sky Survey (SDSS), a sky survey obtained thanks to an optical telescope at the Apache Point Observatory, had a major role in providing maps of the Universe for this kind of studies. The data show features of the Universe that are compatible with galaxy formation models based on the ΛCDM model, describing a Universe almost flat with $\Omega_m \approx 0.3$ [19] , much larger than the luminous matter $\Omega_b \approx 0.05$.

1.2 The dark photon

1.2.1 Dark sector and neutral portals

The strong, weak and electromagnetic interactions are described with high precision by the standard model (SM) of particle physics. Nevertheless the SM is not able to explain the nature of dark matter. An alternative to the dark matter hypothesis, is given by the MOND (Modified Newtonian Dynamics) theory [20], which proposes a modification of Newton's law of gravity. However, MOND is not able to explain the Bullet Cluster phenomenon, presented in Chapter1.1.2. Therefore, the existence of dark matter, demonstrated by cosmological and gravitational observations (see Section 1.1.2), is a compelling motivation to go beyond the SM. The CMB measurements performed with WMAP and PLANCK telescopes helped to have a good estimate of the abundance of dark matter in the Universe. In addition, PAMELA [21] observed an anomalous positron abundance in the energy range 1.5-100 GeV, confirmed by AMS [22] and FERMI [23] measurements. A possible explanation of this abundance can be the annihilation of dark matter particles. However, it is also possible that the flux observed is due to conventional sources like some nearby pulsars. In the first case, the lack of a corresponding anti-proton abundance can be justified assuming that the hypothetical dark matter is light. Another range of dark matter mass hypothesis to be considered is the one suggested first by DAMA and later by DAMA/LIBRA and CoGeNT [24]. In particular, they observed an anomalous signal not compatible with the expected backgrounds and the combination of their results suggests the existence of dark matter with mass ~ 7 GeV [25].
There are several possible scenarios for dark matter which can ideally be probed. Dark matter models with light messenger particles are increasing interest in the scientific community and several DM candidates have been proposed over the years. Non-baryonic matter can be classified as Hot Dark Matter (HDM) and Cold Dark Matter (CDM) depending on their relativistic or non-relativistic status. The cosmological models and the different quantitative indications of dark matter collected tell us that the dark matter cannot entirely consist of relativistic particles, and the non relativistic component must be dominant. Possible well-motivated dark matter candidates are the Weakly Interacting Massive Particles (WIMP), theorized as cold thermal relics in thermal equilibrium with photons since the early Universe. The expected mass range of these particles is 10 GeV-10 TeV, where the lower bound derives from the so-called Lee-Weinberg cosmological limit [26]. A particle with the same properties is also predicted by the super-symmetric extensions of the Standard Model. This very appealing match of predictions, from the cosmological model and from one of the most interesting models beyond the SM of particle physics, is often referred as the WIMP *miracle*. As a consequence, the WIMPs paradigm has always been the driving hypothesis in the experimental efforts aimed at the direct detection of DM. At the present time, the Xenon1T experiment sets the strongest constraint on the mass of WIMP,

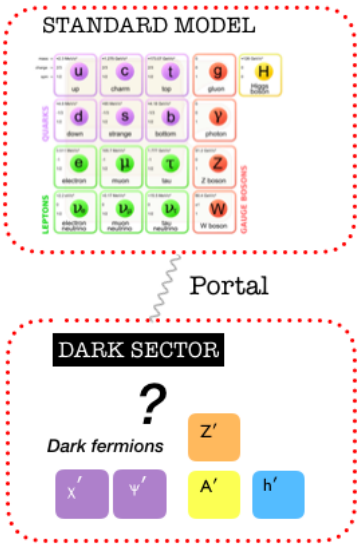

Figure 1.5: A possible beyond standard model scenario involves the existence of a dark sector, feebly interacting with the SM, through a portal.

which can not be higher than 6 GeV, with a minimum cross section value of 4.1×10^{-47} cm^2 [27]. The lack of observation of WIMPs so far has driven the attention of the researchers towards other theories beyond the SM. The introduction of a new hidden sector where the dark particles could interact only among them, constrained by some kind of symmetries, is one of the possible scenarios. A new sector with new interactions could not only explain the dynamics of the galactic structure formation, and so the dark matter abundance, but it could also represent the solution for some of the known unsolved discrepancies between experiments and SM predictions, like the anomalous magnetic moment of the muon or the proton charge radius. The existence of such a hidden sector, with new gauge groups, is well-motivated from a string theory perspective, and on the other hand the interactions of particles of the new sector with the SM could give rise to several interesting phenomenological signatures allowing to test the model. Similarly to the SM, the dark sector can be seen as a collection of (still unknown) particles, that are not charged under the SM strong, weak, or electromagnetic forces. The possible properties of the dark matter can be ideally derived from cosmological observations. The candidate dark particle should be an exotic particle stable, massive and uncharged. The lack of experimental evidence for such kind of particles, so far, tells that if this dark sector exists, it only feebly interacts with the already known world.
The hypothetical interaction between the dark sector and the visible one is established through the coupling of a mediator particle via a portal (Figure 1.5). Although the definition of a dark sector is extremely broad, its physics can be explored effectively and systematically by using portal interactions as a guide.
The four most probable portals considered so far, differing by the spin of the mediator, are [28]:

- Axion portal (pseudo-scalar) where the operator written as:

$$\frac{a}{f_a} F_{\mu\nu} \tilde{F}^{\mu\nu} + \frac{1}{f_a} \partial_\mu a \bar{\Psi} \gamma^\mu \gamma_5 \Psi,$$

  describes both the interaction of the pseudo-scalar, the axion a, with the SM photon $F_{\mu\nu}$ and the interactions with the fermions Ψ;

- Higgs portal (scalar), that foresees the interaction between a scalar Φ and the SM Higgs boson H, written as:
$$(\mu\Phi + \lambda\Phi^2)H^\dagger H;$$
- Neutrino portal (spin 1/2), with the interaction between a heavy fermion N, which is a SM singlet, the SM Higgs boson and the SM fermions L that takes the form:
$$y_N \overline{L} H N;$$
- Vector portal (spin 1), including the dark photon case, that will be discussed in details later on.

1.2.2 The theoretical framework

One of the simplest models of dark sector is the one that introduces an additional gauge symmetry $U(1)$ to describe the interactions among the dark particles. The *dark* photon (or *hidden* photon) known as A' or U boson is the corresponding gauge boson of the dark sector. It was already introduced in the eighties by Holdom [29], whose theories foreseen the introduction of a gauge boson with spin 1 as a mediator of the $U'(1)$ symmetry of the hidden sector. The dark photon in principle has the same properties of the QED photon, in particular, it interacts with fermions proportionally to their electric charges, with an additional suppression factor for the coupling. The so called dark photon can be seen as the mediator between the dark matter particle, assumed to be a Dirac fermion, and the SM fermions.
One of the simplest mechanisms that could determine weak couplings between SM particles and the A' field is the kinetic mixing, between the gauge bosons of the two $U(1)$ symmetries, described by the kinetic term in the Lagrangian:

$$\mathcal{L}_{mix} = -\frac{\epsilon}{2} F^{QED}_{\mu\nu} F^{\mu\nu}_{dark}\,, \tag{1.16}$$

where a low value of the mixing parameter ϵ (below 10^{-3}) could justify the lack of experimental observations of the related phenomenology.
The dark photon can be either massless or massive. The simplest way to generate mass is through the Stueckelberg mechanism [30], which does not involve the spontaneous symmetry breaking. Another way for the dark photon to acquire mass is via a Higgs-like mechanism, through the SM Higgs or a new dark Higgs h' [31]. In this way the symmetry is spontaneously broken, giving mass to the dark boson.
The discussion presented here follows a recent work on the dark photon [32]; both the massless and massive dark photon cases will be treated.
The dark sector (DS) is assumed to communicate with the SM only through the kinetic mixing and the Lagrangian can be written as:

$$\mathcal{L} = \mathcal{L}_{SM} + \mathcal{L}_{DS} + \mathcal{L}_{SM} \otimes \mathcal{L}_{DS}. \tag{1.17}$$

The kinetic part of the Lagrangian of the two Gauge bosons $U(1)_a$ and $U(1)_b$ can be written as follows:

$$\mathcal{L}_0 = -\frac{1}{4} F_{a\mu\nu} F_a{}^{\mu\nu} - \frac{1}{4} F_{b\mu\nu} F_b{}^{\mu\nu} - \frac{\epsilon}{2} F_{a\mu\nu} F_b{}^{\mu\nu}. \tag{1.18}$$

The interaction term $\mathcal{L}'$ should also be taken into account, that describes the interaction of A^μ_b with the SM current J_μ and of A^μ_a with the dark sector current J'_μ. The gauge fields can be expressed in terms of the physical field A and A', as follows:

$$\begin{pmatrix} A^\mu_a \\ A^\mu_b \end{pmatrix} = \begin{pmatrix} \frac{1}{\sqrt{1-\epsilon^2}} & 0 \\ -\frac{\epsilon}{\sqrt{1-\epsilon^2}} & 1 \end{pmatrix} \begin{pmatrix} \cos\theta & -\sin\theta \\ \sin\theta & \cos\theta \end{pmatrix} \begin{pmatrix} A'^\mu \\ A^\mu \end{pmatrix} \tag{1.19}$$

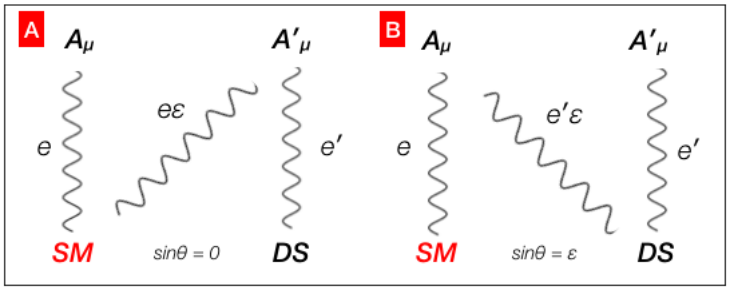

Figure 1.6: The scheme illustrates the two different θ choices. For $\sin = 0$ the dark photon couples with both the SM and DS current (on the left). For $\sin\theta = \epsilon$ the SM photon couples with both the SM and DS current (on the right).

The kinetic term of the Lagrangian $\mathcal{L}_0$ can be diagonalized, as a function of the SM photon field A and the dark photon A', just obtained. The interaction Lagrangian $\mathcal{L}'$ becomes:

$$\begin{aligned}\mathcal{L}' = &\left[\frac{e'\cos\theta}{\sqrt{1-\epsilon^2}}J'_\mu + e\left(\sin\theta - \frac{\epsilon\cos\theta}{\sqrt{1-\epsilon^2}}\right)J_\mu\right]A'^\mu \\ &+\left[-\frac{e'\sin\theta}{\sqrt{1-\epsilon^2}}J'_\mu + e\left(\cos\theta - \frac{\epsilon\sin\theta}{\sqrt{1-\epsilon^2}}\right)J_\mu\right]A^\mu\end{aligned} \tag{1.20}$$

In the massless photon case, the choice of the θ angle is arbitrary, there are no constrains on the parameters. There are in particular two relevant choices: $\sin\theta = 0$ and $\sin\theta = \epsilon$.
The choice of $\sin\theta = 0$ ($\cos\theta = 1$) allows to re-write the interaction Lagrangian $\mathcal{L}'$ as follows:

$$\mathcal{L}' = \left[\frac{e'}{\sqrt{1-\epsilon^2}}J'_\mu - \frac{e\epsilon}{\sqrt{1-\epsilon^2}}J_\mu\right]A'^\mu + eJ_\mu A^\mu \tag{1.21}$$

In this particular case, the coupling of the ordinary photon is permitted only with ordinary current. The dark photon instead couples to both the currents, the ordinary and the dark one, the first suppressed by a factor $e\epsilon/\sqrt{1-\epsilon^2}$.
On the other hand, for $\sin\theta = \epsilon$ ($\cos\theta = \sqrt{1-\epsilon^2}$) the SM photon couples with both the currents, while the dark photon only to the dark current, as follows:

$$\mathcal{L}' = e'J'_\mu A'^\mu + \left[-\frac{e'\epsilon}{\sqrt{1-\epsilon^2}}J'_\mu - \frac{e}{\sqrt{1-\epsilon^2}}J_\mu\right]A^\mu \tag{1.22}$$

The coupling between the SM photon and the dark current, known as *millicharge*, is suppressed by the same factor $e\epsilon/\sqrt{1-\epsilon^2}$. The explicit schemes of the couplings for both the θ values is reported in Figure 1.6.
In case the dark photon is massive, the scenario is different. The Stueckelberg mechanism is responsible for its mass and the term of the Lagrangian can be written as follows [30]:

$$\mathcal{L}_{Stu} = \frac{1}{2}M_a^2 A_{a\mu}A_a^\mu + \frac{1}{2}M_b^2 A_{b\mu}A_b^\mu - M_a M_b A_{a\mu}A_b^\mu \tag{1.23}$$

A different diagonalization is then required to obtain the new Lagrangian $\mathcal{L}''$ that can be expressed, again, in terms of the physical fields A and A'. In this case, there is no freedom on the θ choice; the only way to obtain diagonal terms is by setting:

$$\sin\theta = \frac{\delta\sqrt{1-\epsilon^2}}{1-2\delta\epsilon+\delta^2}\ , \quad cos\theta = \frac{1-\delta\epsilon}{1-2\delta\epsilon+\delta^2} \tag{1.24}$$

where the θ angle value depends on $\delta = M_b/M_a$.
In our case $\delta = 0$, since the SM gauge boson is massless ($M_b = 0$). In this condition the coupling between the dark photon and the electromagnetic current is direct and proportional to $e\epsilon$, since:

$$\mathcal{L} \supset e\epsilon J_\mu A'_\mu. \tag{1.25}$$

1.2.3 Dark matter relic density

Although the evidence for dark matter is compelling, there is still no theoretically favoured production mechanism. Dark matter formation in the early Universe could be due to a thermal or non-thermal production (or both) or it could simply be the result of an initial particle-anti-particle asymmetry.
In this section the possible production mechanisms are presented, supposing the existence of the dark photon, which is an indirect way of probing the dark sector. In addition, some particular scenarios where the dark photon is itself dark matter will be discussed.

Freeze-out

The observed cosmological abundance of DM can be explained by the chemical *freeze out* of a thermal relic; in this regime the dark matter in the early Universe was in thermal equilibrium with the SM particles. A particle species is in equilibrium with the thermal plasma if the interaction rate Γ is higher than the expansion rate of the Universe given by the Hubble constant H (see Section 1.1.1).
The interaction rate of a species is given by:

$$\Gamma = n \langle \sigma v \rangle \tag{1.26}$$

where σ is the cross section, v the averaged thermal velocity and n is the density of particles.
As long as the interaction rate of the dark matter particles is higher than the expansion rate of the Universe, the dark particles self-annihilate into other dark particles. Instead, if the interaction rate drops below the Hubble rate H:

$$\Gamma \ll H, \tag{1.27}$$

the particle species chemically decouples, which means that the number of the dark particles freezes. Hence, only decays into SM particles are accessible. A very long decay time of the dark particles is needed to justify the abundance of dark matter at the present time. Eventually the current abundance might be equal to the one at the time of the decoupling. This production mechanism is called *freeze out*.
The calculation of the freeze-out relic abundance can be estimated in terms of the thermal annihilation cross section. Starting from the Boltzmann equation, that describes the variation with time of the number density $n(t)$, it is possible to write the evolution $\dot{n}_i(t)$ of the number density of a single species, which annihilates with the particles of the thermal bath[15]:

$$\dot{n}(t) + 3H(T)n(t) = -\langle \sigma_{\chi\chi} v \rangle (n^2(t) - n^2_{eq}(t)) \tag{1.28}$$

where the Hubble parameter $H(t)$ is written as a function of the temperature T, which evolves with time t, $\langle \sigma_{\chi\chi} v \rangle$ is the thermal average annihilation cross-section and $n_{eq}(t)$ the number density at the equilibrium. The so called Friedmann equation[2] , for a radiation-dominated Universe with relativistic matter, gives[33]:

$$H(T) = \frac{\pi \sqrt{g_*(T)}}{\sqrt{90}} \frac{T^2}{m_{PL}} \tag{1.29}$$

[2]The general Friedmann equation is $H^2 = \frac{8\pi G\rho}{3} - \frac{kc^2}{a^2}$, where k is supposed equal to 0 in the treatment.

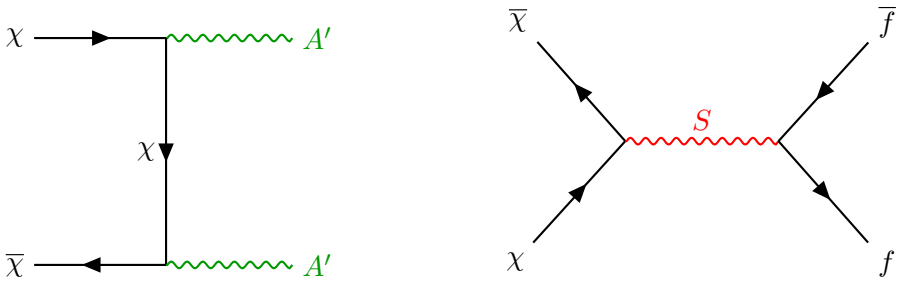

Figure 1.7: Feynman diagrams of two massless DP scenarios.

where m_{PL} is the Planck mass and $g_*(T)$ is the number of the effective degrees of freedom at temperature T, considering the sum over all kinds of particles with negligible mass with respect to the thermal bath temperature:

$$g_* = \sum_b g_b \left(\frac{T_b}{T}\right)^4 + \frac{7}{8}\sum_f g_f \left(\frac{T_f}{T}\right)^4 \tag{1.30}$$

where g_b and g_f are respectively the number of degrees of freedom related to the boson and fermion species.
The balance at the equilibrium requires that the particles produced and destroyed are in equal number.
The form of the Eq.1.28 guarantees that in the particular case of $n = n_{eq}$ the density changes only in such a way to balance the dilution due to the expanding Universe described by the second term on the left in Eq.1.28. This equation together with the initial condition $n(0) \sim n_{eq}$ ($T \to \infty$) allows to determine n(t) for a given thermal averaged annihilation cross section $\langle\sigma_{ann}v\rangle$ at anytime.
The relic density turns out to be [15]:

$$\Omega_\chi h^2 = 0.12 \frac{x_{dec}\ \sqrt{g_*}\ 1.7 \times 10^{-9}\ \text{GeV}^{-2}}{23 \cdot\ 10\ \langle\sigma_{\chi\chi}v\rangle}, \tag{1.31}$$

having defined a new variable $x = m_\chi/T$, where x_{dec} is calculated at temperature T of the decoupling . For example, considering as a benchmark model all SM degrees of freedom (true only for T>175 GeV) and m_χ=100 GeV, the values obtained are $g_* = 106.75$ and $x_{dec} \sim 27.3$. In this case the value of the relic density is equal to:

$$\Omega_\chi h^2 \sim \frac{2.5 \times 10^{-10}\ \text{GeV}^{-2}}{\langle\sigma_{\chi\chi}v\rangle}. \tag{1.32}$$

Let's now consider how this relation is specialized in the case of dark matter models with a dark photon as vector neutral portal.
The massless dark photon case is first considered.
The initial abundance of the dark particles χ could produce a final state made up of only massless dark photons through the diagram shown in Figure 1.7, on the left, corresponding to the process:

$$\chi\overline{\chi} \to A'A'. \tag{1.33}$$

In this case the annihilation rate scales as the square of the coupling of the dark photon to the dark matter and the inverse of the dark particle mass squared:

$$\langle\sigma_{\chi\overline{\chi}\to A'A'}v\rangle \sim \frac{2\pi\alpha_D^2}{m_\chi^2} \tag{1.34}$$

The point now is proving if the relic density value $n_\chi(t_0)$ could sufficiently contribute to the relic abundance of dark matter in the present time. By using Eq.1.34 it is possible to check whether the relic density of χ particles:

$$\Omega_\chi h^2 \sim 2.5 \times 10^{-10}\ \text{GeV}^{-2} \frac{m_\chi^2}{2\pi\alpha_D^2} \tag{1.35}$$

can contribute significantly to the observed abundance of dark matter. Assuming $\alpha_D \simeq 0.01$ and fermions mass ~ 1 TeV, the relic density turns out to be the 1% of the expected relic density for DM ($\Omega_\chi h^2 \simeq 0.11$). This estimation is even lower ($\simeq 10^{-4}$) if a fermion mass of 1 GeV is considered. Hence, in this scenario the dark fermions cannot be considered an important source of dark matter.
Instead, in the annihilation diagram shown in Figure 1.7 (right) the production of two SM fermions occurs, through the exchange of a messenger field S. Under this hypothesis, the thermal cross section could be expressed as follows:

$$\langle \sigma_{\chi\overline{\chi}\to f\overline{f}}\, v \rangle \sim \frac{2\pi\alpha_L^2}{m_S^2}. \tag{1.36}$$

The dark matter density ($\Omega_\chi h^2 \simeq 0.11$) can be obtained combining Eq. 1.35 and 1.36 if it is satisfied the following equation:

$$2\pi\alpha_L^2 \left(\frac{10\ \text{TeV}}{m_S}\right)^2 \simeq 0.23. \tag{1.37}$$

The detection of the dark fermion in this case could occur considering the long range exchange of the massless dark photon and its coupling to the SM magnetic (or electric) dipole moment.
The massive dark photon scenario case leads to different scenarios depending on the relative mass of the DP $m_{A'}$ and the dark fermion m_χ. If $m_{A'} < m_\chi$ the dominant process is the annihilation of the dark fermions into DP, through the same Feynamn diagram of the massless case (Figure 1.8 left). The thermal annihilation cross section of the process can be written as in Eq. 1.34 and the DP on-shell decays into visible states [34].
This is the so called *secluded* case [28]:

$$\chi\overline{\chi} \to A'A', \quad A' \to f\overline{f} \tag{1.38}$$

The thermal cross section of the massless case holds for this case too. Consequently, the considered process is not able to justify the total relic abundance of the dark matter in the early Universe and other processes need to be considered.

When $m_{A'} > m_\chi$, the s-channel annihilation with the A' as mediator is the dominant dark matter scattering process and it can produce as final state a pair of SM particles, through the Feynman diagram shown in Figure 1.8 right. This process is referred to as the *direct annihilation*:

$$\chi\overline{\chi} \to A'^* \to f\overline{f} \tag{1.39}$$

In this case the thermal annihilation cross-section scales as:

$$\langle \sigma_{\chi\overline{\chi}\to f\overline{f}}\, v \rangle \sim \epsilon^2\alpha\alpha_D \frac{16\pi m_\chi^2}{(4m_\chi^2 - m_{A'}^2)^2}. \tag{1.40}$$

This expression can be replaced in the relic density equation 1.32 to find out the mass of an

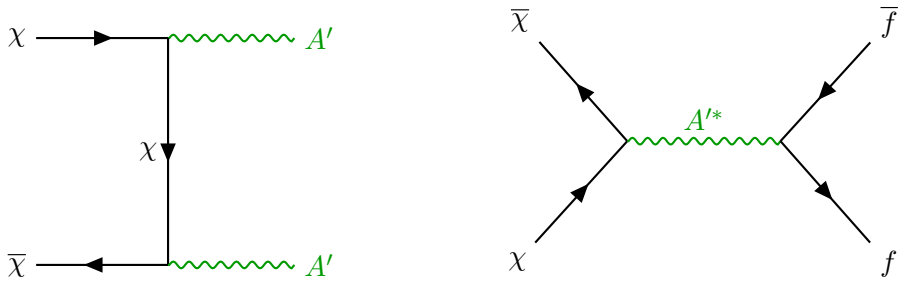

Figure 1.8: Feynman diagrams in the massive DP scenario.

ideal dark particle produced as thermal relic and to probe the model. A new variable is often introduced, called *yield* y [32, 35] and defined as [36].

$$y = \epsilon^2 \alpha_D \left(\frac{m_\chi}{m_{A'}}\right)^4 \tag{1.41}$$

The value of α_D depends on the dark particle type. In the usual assumption $\frac{m_{A'}}{m_\chi} = 3$ and α_D is expressed in terms of a form factor f which is $\leqslant 10$, for a scalar and $\leqslant 1$ for a fermion [37]. The observed dark matter today, $\Omega_\chi h^2 \simeq 0.11$, can be used to set constraints on this combination of model parameters. In particular, the newly defined variable must satisfied the following condition:

$$y\alpha\pi \geq \langle\sigma v\rangle_{relic} m_\chi^2 \tag{1.42}$$

where $\langle\sigma v\rangle_{relic}$ is the averaged thermal annihilation cross section needed to produce the DM abundance observed today. Exclusion limits based on Eq. 1.42 from experiments involved in dark photon searches are reported in Section 1.3.3.

Freeze-in

The freeze-in can be considered as the opposite of the freeze-out production mechanism. Here the idea is that in the early Universe there was a set of particles in equilibrium with the plasma and a X particle named FIMP (Feebly-Interacting-Massive-Particle or alternatively Frozen-In-Massive-Particle), which interacts only feebly with the plasma [38], than requiring very low values of the couplings. Even if this particle does not thermalize with the plasma and the X production considered negligible during inflation, the abundance could have been raised to a maximum when the temperature T dropped below the X mass. This *freezes-in* abundance depends on the coupling strength between the X particle and the thermal bath. In addition to the FIMP, also the Lightest Observable Sector Particle (LOSP) is important. The LOSP is the particle which has a significant interaction with the thermal bath. Depending on the reciprocal mass, the FIMP could be generated by the decay of a LOSP if the LOSP is heavier, or viceversa. The correct relic density could be obtained in terms of the FIMP mass, m_X, and the LOSP mass, m_B, if the coupling ϵ is given by:

$$\epsilon \simeq 1.5 \times 10^{-12} \left(\frac{m_B}{m_X}\right)^{1/2} \left(\frac{g_*(m_B)}{10^2}\right)^{3/4} \tag{1.43}$$

with g_* indicating the number of degrees of freedom in the plasma (see Eq. 1.30) for $\mathrm{m}_B > \mathrm{m}_X$. If $\mathrm{m}_B < \mathrm{m}_X$ Eq. 1.43 is still valid but exchanging the two masses. The application to the dark photon case comes straightforwardly. In a ideal freeze-in scenario the dark photon A' could act

like the LOSP particle, being first produced through out-of-equilibrium scatterings. Hence, it could decay into two dark fermions χ (the FIMPs) for $m_{A'} > 2m_\chi$, contributing to the dark matter abundance if the coupling value satisfies the previous constraint (replacing m_B with $m_{A'}$ and m_X with m_χ):

$$\frac{\epsilon^2 m_\chi}{m_{A'}} \sim 2.25 \cdot 10^{-27} g_*^{3/2} \tag{1.44}$$

Alternatively, a low mass value for A' ($m_{A'} \ll$ eV) could be considered, determining also the production of DM abundance from annihilation of SM particles into DM particles through an off shell A'. In this case the DM relic abundance is independent from $m_{A'}$ and almost also from m_χ and for m_χ=100 MeV the coupling satisfies [28]:

$$\alpha_D \epsilon^2 \sim 3 \times 10^{-24}. \tag{1.45}$$

More scenarios, dark photon as dark matter

A dark photon could be itself dark matter candidate if it was produced via non-thermal mechanism, such as non thermal-misalignment or interaction during the inflation. The first mechanism is the same of the Axion production, which might be occurred during the first early period of the Universe [39]. According to the misalignment mechanism, the DP field should have a constant initial value and then could oscillate around a minimum. This mechanism sets the upper limit for the mixing parameter ϵ which should be below 10^{-9}, and for the mass m'_A, up to 1 MeV[32]. In addition, as mentioned before, there is a theory that foresees the possibility to produce dark matter from couplings between the dark photon field and the inflaton field. In the WIMPs canonical scenario [40], the thermal production mechanism takes place only after the reheat of the Universe by inflation. Instead, some recent studies are trying to address the question of whether inflation, in addition to explain the structure of the Universe, can also be the source of dark matter. The mass of a vector boson can be predicted by saturating the dark matter abundance [41]:

$$m_{A'} \simeq 10^{-5}\,\text{eV} \times (10^{14}\ \text{GeV}/\,\text{H}_\text{I})^4$$

where H_I is the value of the Hubble constant during the inflation [42].
For high value of H_I, in the range $10^{13} < \text{H}_\text{I} < 10^{14}$ GeV, the dark matter abundance is obtained. Consequently, the dark photon mass is in the range $10\ \mu\text{eV} < m_{A'} < 0.1$ eV . A recent study extended the mass of the dark photon down to 10^{-21} eV, obtaining the correct relic abundance [43].

1.2.4 The g-2 anomaly

A puzzling question during these last years is the discrepancy between the measurement of the anomalous magnetic moment of the muon (g-2)$_\mu$ and theoretical value. The $(g-2)_\mu$ anomaly can receive contributions from the dark-sector. The magnetic moment of the muon $\overrightarrow{M}$ can be calculated:

$$\overrightarrow{M} = g_\mu \frac{e}{2m_\mu} \overrightarrow{S}, \tag{1.46}$$

where m_μ and S are respectively the mass and the spin of the muon. The Dirac equation implies that $g_\mu = 2$ but several effects (which takes into account quantum loops) leads to a deviation from this value, which could be parametrised by:

$$a_\mu = \frac{g_\mu - 2}{2}. \tag{1.47}$$

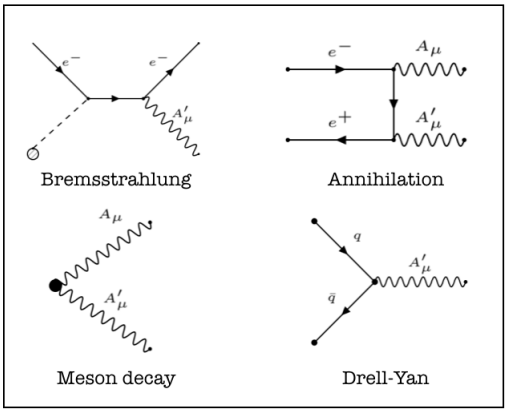

Figure 1.9: Production mechanisms of the massive dark photon at accelerators.

This deviation could be precisely measured and computed in the SM in terms of the contributions that derive from virtual corrections, involving particles with electromagnetic (a_μ^{QED}), hadronic (a_μ^{Had}) and electroweak interactions (a_μ^{EW}):

$$a_\mu^{SM} = a_\mu^{QED} + a_\mu^{Had} + a_\mu^{EW} \tag{1.48}$$

The most recent and precise measurement of a_μ was published by the E821 experiment, obtaining [44]:

$$\Delta a_\mu = a_\mu^{exp} - a_\mu^{SM} = \ (22.4 \pm 10 \ \text{to} \ 26.1 \pm 9.4) \times 10^{-10} \tag{1.49}$$

where a_μ^{exp} is the theoretical prediction. It is possible to calculate the corrections to a_μ due to the interaction between the dark photon and a SM lepton:

$$a_\mu^{DP} = \frac{\alpha}{2\pi} \epsilon F \left(\frac{m_{A'}}{m_\mu} \right) \tag{1.50}$$

with $F(x) = \int \frac{2z(1-z^2)}{(1-z^2)+x^2 z} \, dz$ is a form factor, expressed in terms of $x = \frac{m_{A'}}{m_\mu}$.
For a mass of the dark photon in the range of 10-100 MeV and a coupling constant of the order of 10^{-3}, the dark photon term can account for the discrepancy observed, i.e. $\Delta a_\mu \simeq a_\mu^{DP}$.

1.3 Searches at particle accelerators

Dark photon searches with particle accelerators are possible only for the massive case scenario and $m_{A'} > 1$ MeV. Two possible scenarios can be taken into account: the search for visible decays of the dark photon, that has a clear signature accessible only if $m_{A'} < 2\ m_\chi$, and the search for invisible decays in the regime $m_{A'} > 2\ m_\chi$, where decays into dark matter are dominant with respect to the suppressed decays into SM particles. The secluded scenario, $m_{A'} < m_\chi$, which, as discussed earlier, would not allow to address the thermal dark matter scenario, is not investigated at particle accelerators.

1.3.1 Dark photon production

A variety of dark photon production mechanisms have been exploited in dark-photon searches, which can be categorized as follows:

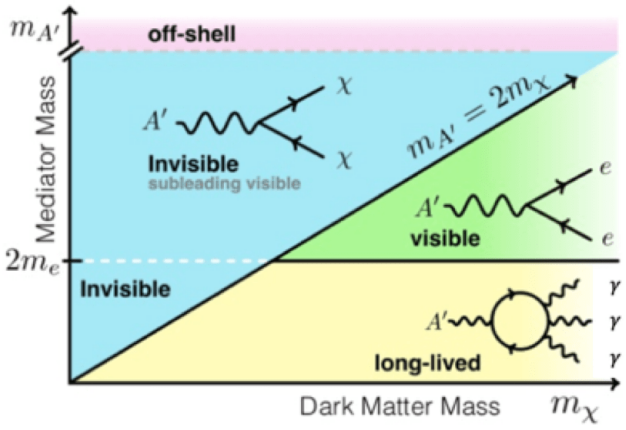

Figure 1.10: Dark photon decay modes for different scenarios of hierarchy between the masses of the Dark Photon, Dark Matter and Standard Model particles.

- Bremsstrahlung, or A'-strahlung on nuclei, $e^{\pm}N \to e^{\pm}NA'$. In a fixed target experiment the dark photon carries almost the entire energy of the beam and it is produced forward, while the slowed down positron or electron is scattered at large angles;
- Annihilation $e^+e^- \to \gamma A'$. Experiments searching for the A' boson by reconstructing its mass with the missing mass method exploits in particular this production mode;
- Neutral meson decays like π°, η, ϕ e Υ. Mesons may be produced in fixed target experiments, e^+e^- colliders or jets in hadron colliders. In this case the mass value depends on the mass of the parent meson;
- Drell-Yan (DY), $q\overline{q} \to A' \to (l^+l^-$ or $h^+h^-)$, at hadron colliders and at proton-beam fixed-target experiments.

The parameter space for the experimental searches consists of the mixing parameter ϵ, the mass of the dark photon $m_{A'}$, with a reach limited by the center of mass energy of the production mechanism, and, depending on the search strategy, the mass of the dark matter particle from the dark photon decay.

1.3.2 Dark Photon decay

The decay modes of the dark photon are determined by its mass and the mass of a hypothetical dark particle χ. The decay modes can be divided into *visible* and *invisible* decays (see Figure 1.10).

- *visible decays*: $A' \to SM + SM$ if $2\, m_e < m_{A'} < 2\, m_\chi$.
  If the mass of A' is lighter than twice the mass of any dark particle, the decays in DM is kinematically forbidden and the dark photon can only decay into SM particles if $m_{A'} > 2\, m_e$. In particular, for a mass of the DP below 0.2 GeV the branching ratio of the decay in e^+e^- is 100%, as shown in Figure 1.11. The width can be calculated as follows:

$$\Gamma_{A' \to f\overline{f}} = \frac{1}{3}\alpha\epsilon^2 m_{A'}\sqrt{1 - \frac{4m_f^2}{m_{A'}^2}}\left(1 + \frac{2m_f^2}{m_{A'}^2}\right). \tag{1.51}$$

  The decay time can be computed with the usual formula $\tau = \hbar/\Gamma$, so it scales as $1/\left(\alpha\epsilon^2 m_{A'}\right)$; for a very low mixing constant ϵ the dark photon would be *long lived*.

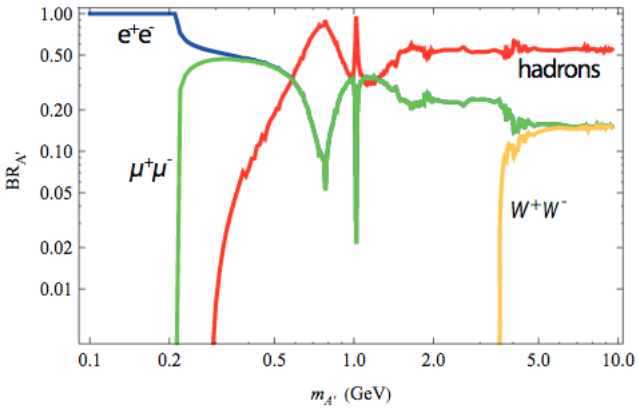

Figure 1.11: Dark photon branching ratio assuming that only visible decays into SM particles are allowed.

In the particular case of $m_{A'} < 2m_\chi$ with $m_{A'} < m_e$, the only accessible process is the production of 3γs in the final state, via electron box diagram. Even in this case the A' is long lived.

- *invisible decays*: $A' \to \chi\,\chi$, if $m_{A'} > 2m_\chi$.
  The decay width is:

$$\Gamma_{A'\to\chi\overline{\chi}} = \frac{1}{3}\alpha_D m_{A'}\sqrt{1-\frac{4m_\chi^2}{m_{A'}^2}}\left(1+\frac{2m_\chi^2}{m_{A'}^2}\right) \tag{1.52}$$

  A reasonable assumption is $\alpha_D >> \alpha\epsilon^2$, implying that the invisible decay dominates. The decay time in this case strictly depends on the α_D value ($\tau \propto 1/(\alpha_D m_{A'})$).

1.3.3 Dark Photon search experiments

Several experiments around the world are taking part to the dark photon hunt, however, just a few of them are designed for this purpose. Here, several experiments will be listed, dividing them according to the decay mode, visible or invisible, and discussing the excluded regions in the parameter space $(m_{A'}, \epsilon)$.
The section concludes with an introduction to the direct search of dark matter at accelerators, which is strongly model dependent, but it tests directly the nature and the existence of thermally produced low mass dark matter.

Visible decay

The experimental methods used to search for dark photon decay in the visible channel are the following:

- beam dump experiments (see Figure 1.12 a);
- fixed target experiments with bump-hunting (See Figure 1.12 b);
- fixed target experiments with detached vertexing (See Figure 1.12 c);
- colliders.

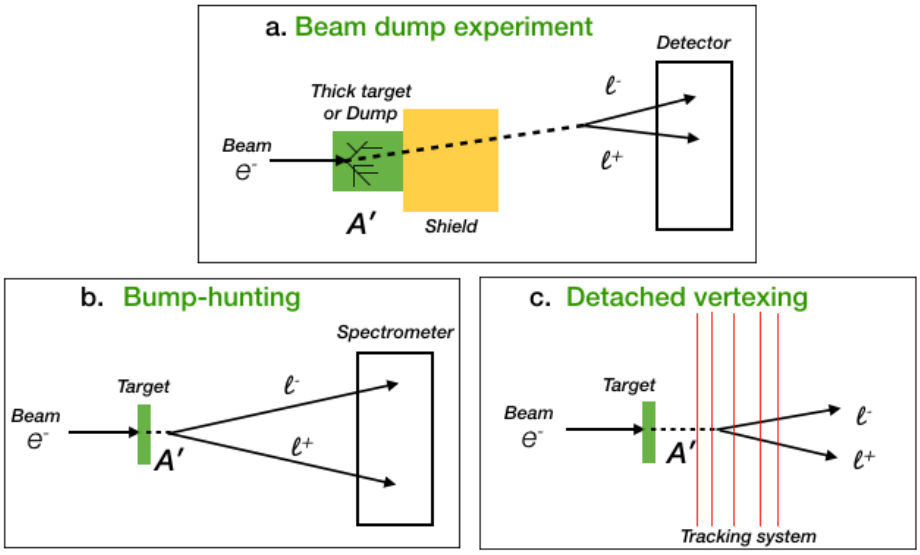

Figure 1.12: The three most common techniques in the search for visible decays of a dark photon. a) Beam dump experiments with thick target (or dump), a shield and a detector placed downstream, b) bump-hunting and c) detached vertexing in fixed target experiments.

A large region of the parameter space $(m_{A'}, \epsilon)$ has already been investigated for this decay channel, as shown in Figure 1.13. The re-analysis of data taken by old beam dump experiments, such as E137, E141, E774, NuCal and CHARM helped to exclude the parameter space for masses below 1 GeV and small ϵ (up to $\sim 10^{-8}$ for E137). Also the measurement of the neutrino flux from the 1987A Supernovae [45] contributes to exclude very low ϵ value (up to 10^{-9}), being equivalent to a huge beam dump experiment. Indeed, the existence of a dark photon provides an alternative cooling mechanism for the Supernova in addition to neutrinos. The top part of the parameter space is mainly excluded by experiments at colliders (large mass), that are essentially limited by the statistics, with the best sensitivity reached by LHCb ($\epsilon \sim 10^{-4}$), and fixed target experiments (small mass).

Beam dump experiments

Beam dump experiments can search for dark photon decays in a pair of visible particles, such as $A' \to \ell^+\ell^-$ or $A' \to h^+h^-$, where the invariant mass can be measured from the reconstruction of the final state. A positron or an electron of a high energy beam hits a thick target or dump, showering and producing at least a dark photon A', mostly from A'-strahlung (see Figure 1.12 a). A visible decay in e^+e^- or $\mu^-\mu^-$ can be detected after a long shield, that allows the survival only of weakly interacting particles. The analysis is based on the search, above a smooth background, of a peak in the distribution of two-leptons invariant mass. A systematic study of the background is needed to achieve a good S/N ratio. In addition, the choice of the beam energy, the length of the shield and the distance from the detector select the range of parameter space to probe, according to the dark photon decay length.
Some constraints have been derived from the reinterpretation of data (recast) from beam dump experiment with fixed target, using electron beams (E141, E137, E774, ORSAY) and proton beam (CHARM, PS191, NOMAD, nu-Cal).

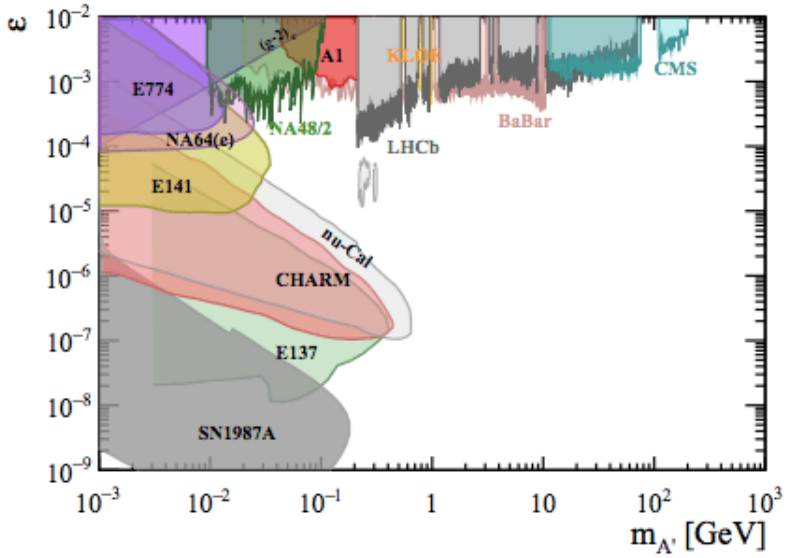

Figure 1.13: Regions of the parameter space $(m_{A'}, \epsilon)$ excluded by different experiments looking for visible decay of the dark photon. From ref. [32].

E141 and E137@SLAC
A search for short lived axion-like particles was performed at SLAC with E141[46]. The experiment used an electron beam of 9 GeV energy dumped onto a 12 cm tungsten target, for a total of 2×10^{15} electrons on target in 1987.
One year later E137[47] took data using a 20 GeV electron beam dumped onto an aluminium target.

E774@FermiLab
The old data allowed to put limits on the $m_{A'}$ mass, using a 275 MeV electron beam hitting a tungsten target [48]. The dark photon might have been produced by Bremsstrahlung in the dump and then detected after decay into e^+e^- pairs downstream of the dump.

ORSAY@CERN
The experiment was designed to search for light Higgs boson using the 1.6 GeV beam provided by the Orsay linac, dumped onto a tungsten target [49]. In 1989 the total number of electrons dumped were 2×10^{16}.

Among the proton beam experiments, that could in the future contribute to the dark photon search, there are multi-purpose experiments such as: SeaQuest at FermiLab, SHIP, NA62 and FASER at CERN. The latter, in particular, will be placed 480 m downstream from the interaction point used by the ATLAS experiment.
The exclusion regions of the parameter space, as seen in Figure 1.14, are very similar for these experiments.

Fixed target experiments

The fixed target experiments (thin target in the dark photon search convention) exploit three techniques: bump-hunting, meson decay in secondary beams and detached vertexing. In the

latter case the reconstruction of the vertex is possible thanks to a tracking system.

A1@Mainz
The A1 [50] experiment searches for the dark photon produced by Bremsstrahlung from a tantalum target using an electron beam of energy in the range $180 < E < 855$ MeV. The mass range investigated is 40 MeV $< m_{A'} <$300 MeV, with a sensitivity on the coupling constant of $\epsilon^2 \sim 8 \times 10^{-6} - 10^{-5}$.

NA48/2@CERN
NA48/2 [51] took data in 2003-2004, collecting 2×10^{11} $K^{\pm}$ decays. The hypothetical dark photon produced in $\pi^0 \to \gamma A'$ is searched in the decay to e^+e^- .
The analysis lead to exclude the mass region of $9 \leqslant m_{A'} < 120\,\text{MeV}$ and $\epsilon^2 > 10^{-6}$.

Future fixed target experiments could also profit of an electron beam and exploit the bump-hunt technique. HPS, in addition, will benefit also from vertexing capability.
In the future there is going to be an upgrade of APEX and HPS, in addition to the new experiments DarkLight@JLAB and MAGIX@MESA.

APEX@JLAB
APEX [52] is an experiment at JLAB which took data in 2011 in a test run. The data allowed to set an upper limit on the coupling constant $\simeq 10^{-6}$ in the range of mass $170 - 250$ MeV.

HPS@JLAB
The Heavy Photon Search (HPS) [53] experiment is located at the JLAB and uses a beam provided by the CEBAF accelerator. The dark photon is produced via electron Bremsstrahlung in a thin W target. It searches for long-lived dark photons through an excess in the e^+e^- invariant mass distribution with displaced vertex. Two engineering runs were performed in 2015 and 2016. The experiment collected data in 2019.

DarkLight@JLAB
DarkLight [54] was proposed to search for the dark photon using an electron beam of 100 MeV and a gas target of molecular hydrogen.

MAGIX@MESA
The new accelerator facility MESA (Mainz Energy-recovering Superconducting Accelerator) [55] with a maximum beam energy of 155 MeV will host the MAGIX experiment, which consists of a gas-jet as a target and a multi-purpose spectrometer as a detector. It will investigate in particular the region for dark photon mass below 50 MeV.

Collider experiments

BaBar@PEPII
BaBar [56] at the collider PEPII of the SLAC laboratory in Stanford searched for the dark photon production in the annihilation e^+e^-, studying the possible A' decay in two leptons. The collected 514 fb^{-1} of data helped to set an upper limit on the mixing strength between the DP and the SM photon at the level of $10^{-4} - 10^{-3}$ with $m_{A'}$ in the range 0.02-10.2 GeV.

KLOE@DAΦNE
The KLOE experiment at the DAΦNE collider of the Laboratori Nazionali di Frascati exploited

several A' [3] production modes, such as annihilation, meson decay and dark-Higgsstrahlung ($e^+e^- \to A'h'$). The collaboration started to search the DP in the 2012 looking for the process $\phi \to \eta A'$ with $A' \to e^+e^-$, tagging the process via the decay $\eta \to \pi^+\pi^-\pi^0$. It found no evidence after collecting 1.5 fb^{-1} of data. The study allows to exclude the region of the parameter space of $5 < m'_A < 470$ MeV and $\epsilon \geqslant 2 \times 10^{-5}$ [57]. The analysis was then improved adding the tagging $\eta \to \pi^0\pi^0\pi^0$, setting other constraint using 1.7 fb^{-1} of data for two regions of the parameter space, $\epsilon < 1.7 \times 10^{-5}$ for $30 < m_{A'} < 400$ MeV and $\epsilon < 8 \times 10^{-6}$ for $50 < m_{A'} < 210$ MeV [58].

LHCb@CERN
The LHCb collaboration searched for $A \to \mu^+\mu^-$decays using a data sample corresponding to an integrated luminosity of 5.5 fb^1 [59]. Even if no sign of anomalies was found, the search contributed to put stringent constraints on dark photon mass excluding $\epsilon^2 > 10^{-7} - 10^{-6}$ in the range $214 < m_{A'} < 740$ MeV and $10.6 < m_{A'} < 30$ GeV.

Future collider experiments searching for the dark photon with mass less than 10 GeV are going to be Belle-II and LHCb.

Belle-II@KEK
The Belle II experiment is placed in the SuperKEKB asymmetric e^+e^-collider, at the KEK laboratory in Japan. The experiment will search for the DP produced in the process $e^+e^+ \to A'\gamma$ using the decays $A' \to e^+e^-$ or $\mu^+\mu^-$ [60]. The data taking started in 2018 and it is scheduled to reach an integrated luminosity up to 50 ab^{-1} in 2025.

LHCb@CERN
The search in the next years will be performed using the di-muon production and the $D^{*0} \to D^0e^+e^-$ decay. The current projections for the future are based on a luminosity per year of 5 fb^{-1}/year, for a total of 15 fb^{-1} in three years. An upgrade of the detector will be needed after the LHC Long Shutdown 2 (2025). Moreover, in the LHC Long Shutdown 4 (2030) the main upgrade II of the detector will be performed, to allow efficient operation with an instantaneous luminosity up to $2 \times 10^{34}\,\mathrm{cm}^{-2}\mathrm{s}^{-1}$ [61].

Invisible decay

Under the assumption of $m_{A'} > 2\ m_\chi$, a large region of the parameter space ($m_{A'},\ \epsilon$) is still unexplored. The major constraints were set by BaBar, E787/E949 and NA64.
The experimental methods for the search of the invisible decay modes are based on anomalies in the distributions of (see Figure 1.16):

- missing mass;
- missing energy;
- missing momentum.

Missing mass technique

Experiments that apply the missing mass technique are either using secondary beams of Kaons, or they are experiments at colliders or at fixed target set-up. The measurement of the dark

[3] In the related articles the DP is called U boson.

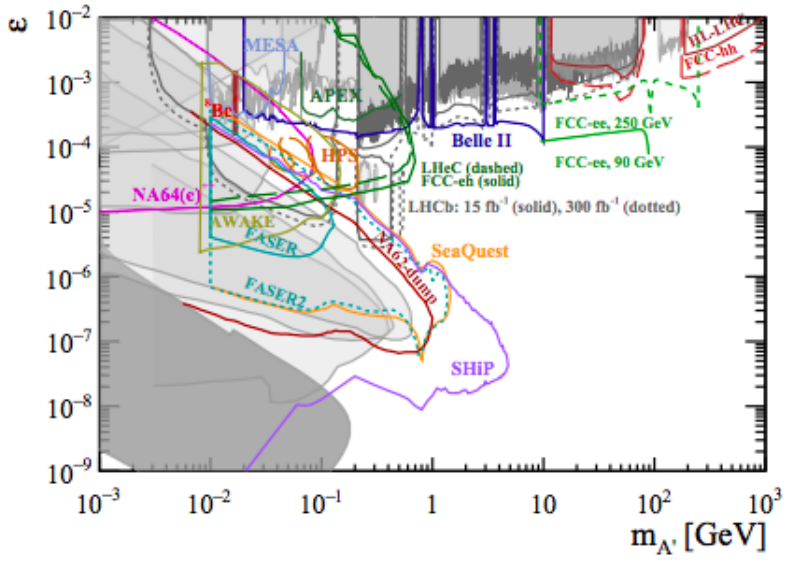

Figure 1.14: Perspectives in terms of exclusion regions of the parameter space $(m_{A'}, \epsilon)$ for visible decay of the dark photon from different future experiments. Plot from ref. [32] and updated from ref. [35].

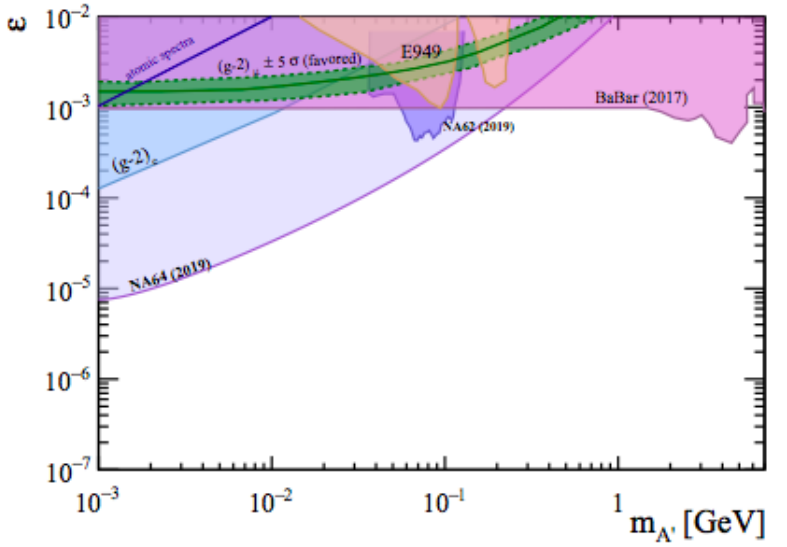

Figure 1.15: Regions of the parameter space $(m_{A'}, \epsilon)$ explored by different experiments for the dark photon invisible decay scenario [32].

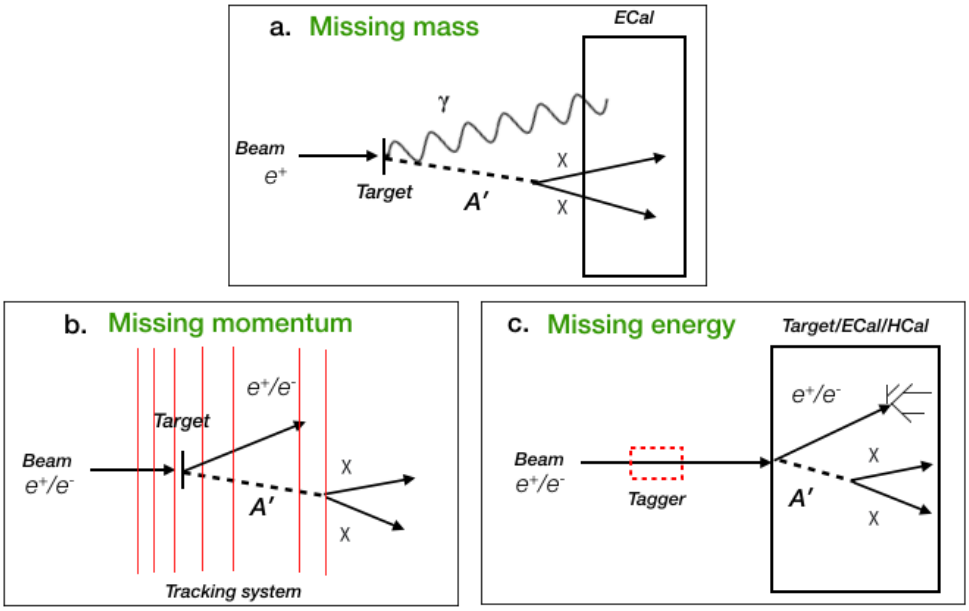

Figure 1.16: The three techniques used for the dark photon search in the invisible channel in fixed target experiments. Missing mass (a), missing momentum (b) and missing energy (c).

photon mass is derived from the position of a bump in the missing mass distribution of a kinematically constraint final state. In these experiments the dark photon A' is produced typically by e^+e^- annihilation or meson decay. The accessible mass range is limited by the center of mass energy of the annihilation or by the meson mass.

E787/E949@CERN
These experiments were designed to search for the very rare decay $K^+ \to \pi^+\nu\overline{\nu}$ [62]. The missing mass, from the neutrinos, in this process may be reinterpreted as due to a dark photon (see the orange exclusion region in the plot of Figure 1.17) thus allowing to set upper limits on the measurement of the branching ratio of the process $K^\pm \to \pi^\pm A'$.

BaBar@PEPII
Constraints on the dark photon production were set by BaBar [63] searching for a single photon with an integrated luminosity of 53 fb^{-1} e^+e^- annihilation. The analysis was done reinterpreting in terms of the dark photon the data set used to search for a light scalar particle from the decay of the $\Upsilon(3S)$ resonance [64]. The searched process is $\Upsilon(3S) \to A'\gamma$, with a single photon in the final state.

The missing momentum and missing energy techniques are based essentially on missing energy detection in Bremsstrahlung processes like $e^-Z \to e^-ZA'$ with $A' \to \chi\bar{\chi}$. Pictures illustrating the techniques are shown in Figure 1.16, where a positron or an electron can interact with a target, and produce a shower in an electromagnetic calorimeter (missing energy), where its energy is measured, or be deflected in a spectrometer (missing momentum), where its momentum is measured.

Na64@CERN
Na64 [37] at CERN SPS used the missing energy techniques with data collected in 2016, 2017

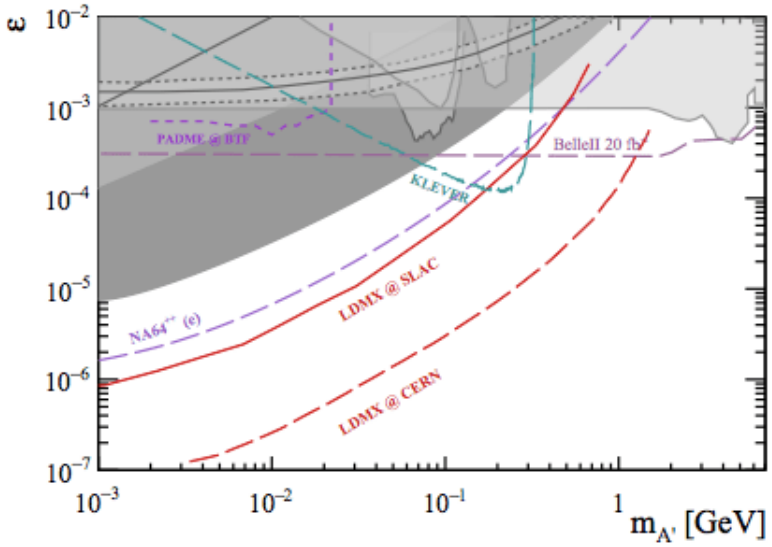

Figure 1.17: Regions of the parameter space $(m_{A'}, \epsilon)$ to be explored by new experiments (coloured lines), supposing a invisible decay scenario for the dark photon. The grey regions have been already investigated. Plot from ref. [32], updated from ref. [35].

and 2018. Using an electron beam of 100 MeV energy, a total number of electrons on target equal to 2.84×10^{11} was collected. Behind the target, the electrons interact with an electromagnetic calorimeter acting as active beam dump. The Na64 data helped to exclude the regions reported in Figure 1.17, for dark photon mass below 200 MeV.

Invisible decay future perspectives

Several experiments are going to set future bounds in the parameter space for the dark photon invisible decay scenario. They are briefly presented in the following. One of them is PADME, treated in details in the next Chapter.

Missing mass experiment

PADME@Frascati
PADME is a fixed target experiment which uses a bunched positron beam of high multiplicity ($\sim 25 - 30$k), directly provided by the Frascati LINAC. It takes advantage of the missing mass technique, searching for the dark photon in the mass region below $23.7\,\mathrm{MeV/c^2}$ and with a target sensitivity on the mixing parameter up to 10^{-3} . The sensitivity region is shown in the plot of Figure 1.17 (PADME@BTF). A possible evolution of PADME is based on the possibility to move the apparatus to Cornell, increasing the mass reach thanks to a positron beam with energy of 5.3 GeV, as shown in the same figure (PADME@CORNELL). Competitors similar to PADME proposed in 2015 are MAPPS [65] and VEPP3 [66], although PADME is currently the only one taking data. The 2020 Update of the European Strategy for Particle Physics [67] credits the experiment hosted at Frascati, searching for low mass dark matter (i.e. PADME), as an essential scientific activity in the roadmap of Particle Physics.

VEPP3@BINP
In 2012 the VEPP3 collaboration proposed to perform the search for the dark photon using

the missing mass technique, covering the DP mass range 5-20 MeV, using a 500 MeV positron beam on a hydrogen target [66]. The scheduled luminosity was 10^{32} cm^{-2}s^{-1}, increased to 10^{33} cm^{-2}s^{-1} in the article which presented the status of the experiment in 2017 [68]. The data taking scheduled for 2019 has not started yet.

MMAPS@Cornell
The layout of this experiment is similar to the one of PADME. It is a fixed target experiment that will be located in Cornell which will use the 5.3 GeV beam extracted from the synchrotron [65]. In the e^+e^- annihilation inside a Beryllium target the isolated photon, emitted in association with the dark photon, can be detected using a CsI calorimeter. It is still a proposal, aiming for an exclusion region as reported in the plot 1.17.

LDMX@SLAC or CERN
Light Dark Matter eXperiment [69] will use a primary electron beam to produce dark matter in fixed-target collisions applying the missing momentum technique. The limits on the dark photon, shown in the plot of Figure 1.17, are referred to a integrated luminosity of 10^{14} electrons-on-target for a beam energy of 4 GeV at SLAC or, alternatively, 10^{16} electrons-on-target and a beam energy of 16 GeV at CERN.

BelleII@KEK
Belle II will look for A' in the process $e^+e^- \to \gamma A'$ at the KEK collider [60]. An estimate of the sensitivity of the experiment is shown in Figure 1.17. A mono-photon trigger, sensitive down to low energies, allows the reconstruction of the isolated photon emitted in association with a dark photon. The value of the missing mass $(E_{CM} - m^2_{A'})/2E_{CM}$ tells the mass of the A'.

Direct dark matter detection

A method to detect directly the dark matter is based on the detection of the rare scattering with nuclei or electrons in matter, as shown in Figure 1.18. This technique is based on the production via A'-strahlung of the dark photon $e^{\pm}N \to e^{\pm}NA'$, the absorption of any secondary product of this reaction in a sufficient long dump, and the consequent decay $A' \to \chi\chi$. The χ is eventually detected by observing the elastic scattering with electrons or nuclei in a large size downstream large mass detector. The entire chain of the process has a total suppression factor given by $\epsilon^4\alpha_D/m_{A'}$. Therefore, these experiments require a high intensity beam and a high Z thick target. The exclusion limits obtained with this kind of technique depend on the four parameters $(m_{A'}, m_\chi, \epsilon, \alpha_D)$. In principle the results obtained using this techniques cannot be compared with the missing mass, energy/momentum experiments, as different parameters are involved. Limits in the parameter space of the hypothetical dark sector particle can be investigated, even considering experiments that do not search for dark matter directly. A simplified model can help to reconvert the parameter space $(m_{A'}, \epsilon)$ in terms of a new variable, $(m_{A'},\ y)$, as described in 1.2.3. The plot in Figure 1.20 is obtained in the assumption of $\alpha_D = 0.1$ and the mass ratio $m_{A'}/m_\chi = 3$. In this plot the target exclusion limits of PADME are reported, that will be treated in Section 2.4.4. Among the experiments contributing here, there are two neutrino experiments, a reinterpretation of an old one, LSND (Liquid Scintillator Neutrino Detector) [70] and the limit foreseen for MiniBoone [71], that is currently taking data. The latest plot collecting the exclusion limits for a thermal relic dark particle is shown in Figure 1.20. An experiment that will be able to probe both the elastic scalar dark matter and the fermion one is BDX [72], at the JLAB. It will try to search for new physics by the interaction between a 10 GeV electron beam and a dump. The experiment is scheduled to take data in 2-3 years.

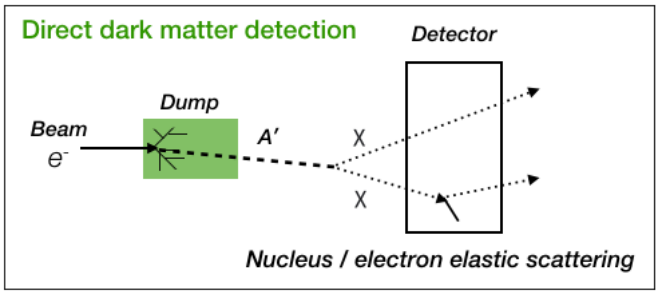

Figure 1.18: A dark photon produced through the A'-strahlung by the interaction of a beam with a target. Later, the dark photon decays into two dark particles, one of them scattering against a nucleus or an electron in a downstream detector.

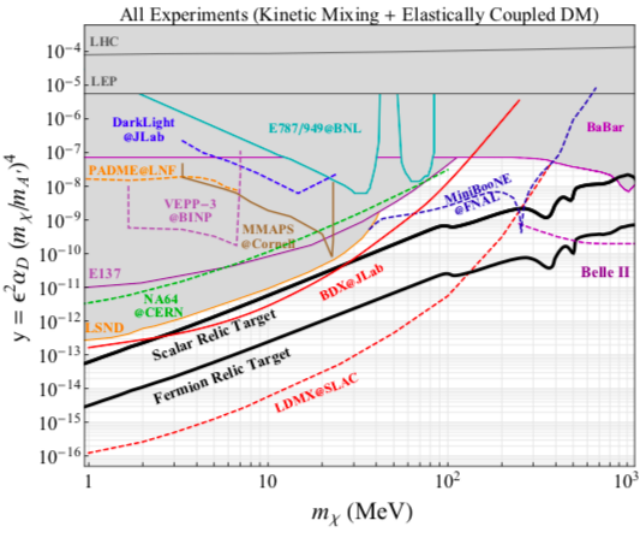

Figure 1.19: Constraints on the model parameters from experiments sensitive to direct detection of dark matter from A' decays, in the assumption of $m_{A'}/m_\chi = 3$ and $\alpha_D = 0.1$. The black thick lines show the correlation of parameters expected, according to astrophysical and cosmological data, in the hypothesis of scalar and fermionic relic dark matter. The region already investigated are reported in grey, the dotted lines correspond to exclusion region projections [28].

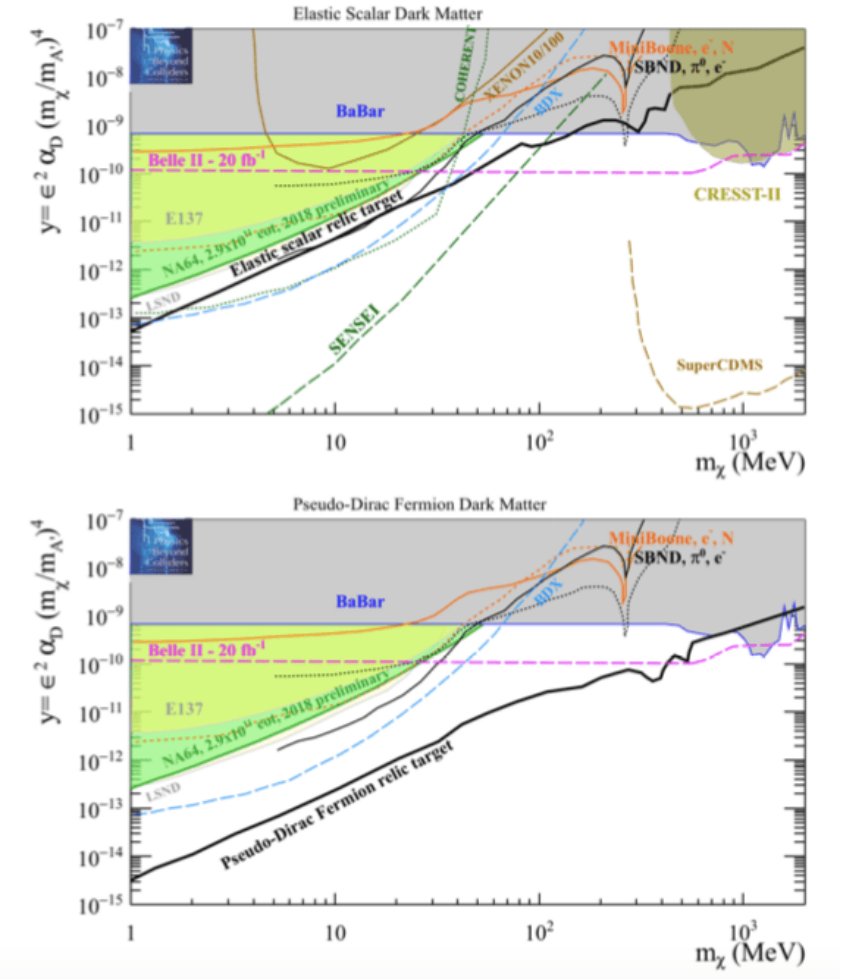

Figure 1.20: Updated excluded region projections of DM search experiment, in the assumption of $m_{A'}/m_{\chi} = 3$ and $\alpha_D = 0.1$ [35].

Chapter 2

The PADME experiment

The LHC at CERN, with the upgrade programs for the accelerator and the experiments foreseen for the coming years, is the focus point of the future of particle physics at the high energy frontier. In addition, several big to medium size experiments will be challenging the SM with precision tests with high intensity accelerated beams.
Beside those efforts, the future search for physics beyond the SM is also entrusted to dedicated and small scale experiments. Among them PADME has a place into the Deliberation document on the 2020 Update of the European Strategy for Particle Physics [67].
PADME (Positron Annihilation into Dark Matter Experiment) [73] is a fixed target experiment located at the Beam Test Facility (BTF) [74] at the Laboratori Nazionali di Frascati (LNF) designed to search for a massive dark photon A' in the process $e^+e^- \to \gamma A'$ (Feynamn diagram of the process shown in Figure 2.1), using a positron beam of energy up to 550 MeV. The experiment exploits the missing mass technique which allows for a search of A' in a manner that does not depend on the decay mode.
Thanks to the closed kinematics of the process, the dark photon mass can be computed as follows:

$$m^2{}_{miss} = (P_{e^+} + P_{e^-} - P_\gamma)^2, \tag{2.1}$$

where P_{e^+}, P_{e^-} and P_γ are the 4-momenta respectively of the positron beam, the target electron and the emitted photon.
The missing mass distribution for signal events has a peak at the dark photon mass, $\mathrm{m}_{A'}$.
For an initial state consisting of a positron from an accelerated beam of energy E_{beam} and an electron at rest in the laboratory frame, the mass of the dark photon can be expressed in terms of the energy E_γ and the angle between the directions of the beam and of the photon θ assumed to be small, as follows:

$$m_{A'} = \sqrt{2m_{e^-}\left[E_{beam} - E_\gamma\left(1 + \frac{E_{beam}}{2m_{e^-}}\theta^2\right)\right]} \tag{2.2}$$

where m_{e^-} is the mass of the electron.
The highest DP mass accessible in PADME depends on the beam energy:

$$m_{A'} = \sqrt{2m_e E_{beam}} \tag{2.3}$$

The maximum energy of the positron bunch delivered in PADME is 550 MeV therefore the maximum dark photon mass probed is equal to 23.7 MeV.
PADME is sensitive to value of the mixing coupling $\epsilon > 10^{-3}$ for the design luminosity of 4×10^{13} Positrons On Target (POT) (see Section 2.4.4). The first PADME proposal is dated back to 2014 [75]. After a design phase guided by the features of a bunched positron beam at the

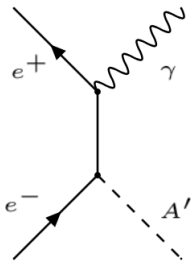

Figure 2.1: Feynman diagram of the process searched at PADME. The annihilation of a positron with an electron of the target producing two photons in the final state, a SM one (γ) and a dark one (A').

Laboratori Nazionali di Frascati and of an experimental hall, the experiment was built and installed in September 2018 and soon after the first data taking started. In this chapter, the beam and the detectors of PADME are described. The preliminary performance of the sub-detectors are also illustrated.

2.1 Experimental hall and beam

The Beam Test Facility (BTF) is part of the DAFNE ϕ-factory complex which includes a high current electron and positron LINAC (LINear ACcelerator), a 510 MeV e^- e^+ accumulator and two 510 MeV storage rings [74]. In Figure 2.2 the scheme of the accelerator complex is shown. The Beam Test Facility is an experimental hall placed in the accelerator complex of the LNF, designed for detector tests, operating since November 2002 [76]. The beam is provided by the LINAC and delivered to the hall thanks to proper magnets. The LINAC with a RF acceleration cavity frequency of 2.856 GHz delivers bunches of electrons with energy and current per bunch up to 800 MeV and 500 mA, or bunches of positrons up to 550 MeV and 100 mA. The bunches have a maximum FWHM duration of 10 ns, with a fixed rate of 50 Hz. From Figure 2.3 the path of the beam is shown: after the production, the beam is sent through a pulsed dipole. Hence, a bunch out of 50 is sent to a hodoscope for energy measurement through the spectrometer line in the scheme. The remaining 49 bunches are sent to the BTF experimental hall where PADME is hosted. Inside the BTF hall the beam is delivered to the PADME target thanks to two dipoles DHSTB001 and DHSTB002 (Figure 2.3, left and right). Between the two bending dipoles, in the straight section, there are two pairs of quadrupoles to focalize the positron beam.
The bunch multiplicity can be adjusted from single positron to hundred thousand positrons. Two pairs of collimators located before the last dipole dictate the energy spread and the angular divergence of the beam, acting one in the x, the second in the y direction.
The design features of the PADME beam are listed below:

- a beam spot of the order of about 1 mm;
- a beam momentum spread below 1%;
- a beam angular divergence not larger than a few mrad:
- a long beam pulse in order to have low pile-up;
- high intensity, of the order of 20k particles on target per bunch.

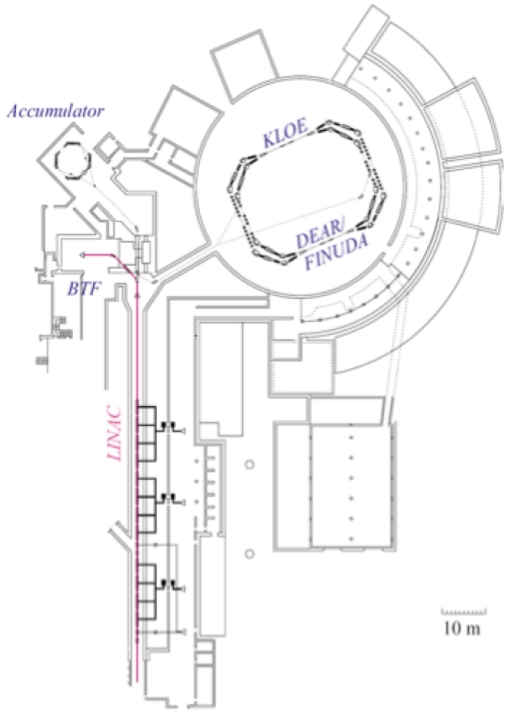

Figure 2.2: The LNF accelerator complex: the beam produced and accelerated by the LINAC is then sent directly to the BTF. The beam can otherwise be injected in the DAΦNE collider. During the PADME data taking, the beam is delivered only to the BTF line.

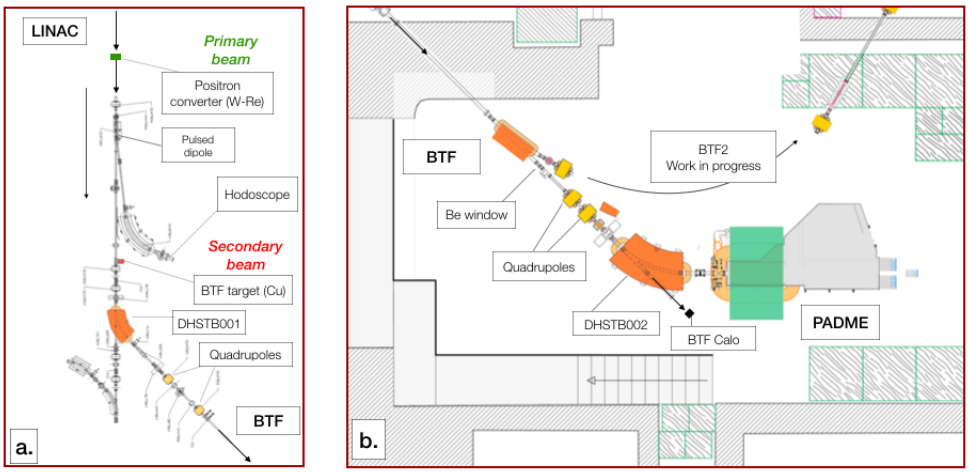

Figure 2.3: On the left the transfer line from the LINAC to the BTF entrance with the location of the production points of the primary and secondary beam. On the right, a drawing of the BTF experimental hall. Both drawings show only the main components.

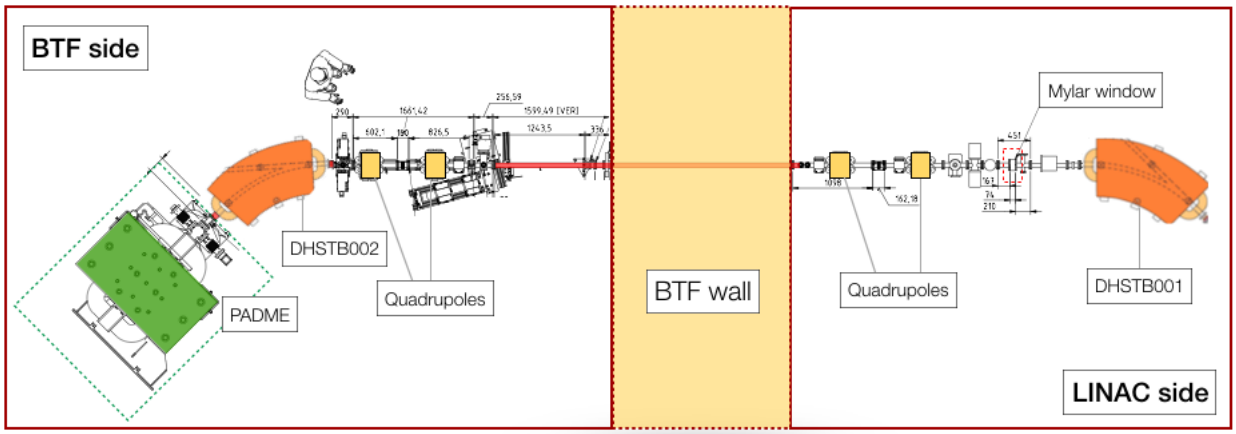

Figure 2.4: The secondary beam line steering the beam to the BTF and to the PADME experiment.

Two kinds of positron beams can be delivered into the BTF, which differ each other for the origin of the positrons (shown in Figure 2.3, left):

- *primary beam*, with positrons directly produced in the LINAC thanks to a W-Re positron converter placed just after the production point of the electrons;
- *secondary beam*, with positrons produced in the interactions of the electron beam in a Cu target placed before the entrance of the BTF hall.

Both positron beam production modes were used during the PADME data taking. The primary positron beam presents a lower background but it can reach a maximum energy of 490 MeV, lower than the maximum energy achievable with the secondary beam, which is about 550 MeV. Since the beginning of the experiment, until July 2019, the LINAC primary vacuum was separated from the BTF beam line vacuum by a 250 μm Beryllium window, located in the BTF, before the last pair of quadripoles (see Figure 2.3, right). The effects of the presence of the Beryllium window were not negligible, due in particular to multiple scattering and Bremsstrahlung. Simulation studies showed that the vacuum separator was an important source of beam induced background. In order to improve the beam quality, the decision was taken to move the BeW in front of the PADME target during the commissioning of the Run 1 (see Section 4) in July 2019. Unfortunately, the risky operation was not successful. During the vacuum operation, the BeW broke up and the experimental hall closed for the recovery operations. After this accident, the beam-line was slightly modified. In particular, the beam pipe was replaced with a new one with a larger cross section, new collimators were introduced, and a 125 μm thick Mylar window was used to separate the PADME and LINAC vacuum. The new vacuum separator was moved back toward the LINAC, compared to the old position of the Be window, just after the last bending dipole on the LINAC side, shown in Figure 2.4.

2.2 The PADME detector

The PADME detector (shown in Figure 2.5) is made of a thin diamond target, a magnet, which bends the beam outside the experimental acceptance, a high resolution electromagnetic calorimeter (ECAL), a fast small angle electromagnetic calorimeter (SAC) and a charged particle veto system (VETO).

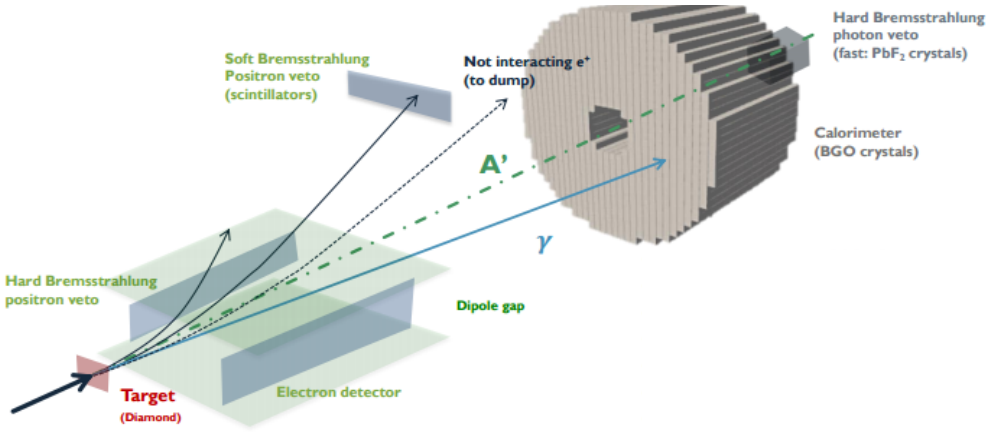

Figure 2.5: Layout of the PADME detector.

In addition, two beam monitors were installed but not yet completely commissioned: a removable monolitic Silicon detector, named MIMOSA, placed in the interaction region, and a hybrid Silicon pixel detector, named TIMEPIX, placed in the beam dump region.
The diamond target and the VETOs are hosted in the vacuum vessel.
Each sub-detector is described in detail below, together with the trigger and the data acquisition system.

2.2.1 Active diamond target

The active diamond target of PADME is a 100 μm thick and 2×2 cm^2 large double sided strip detector. The strips in the two sides are oriented along directions orthogonal to each other and perpendicularly to the beam, with a pitch of 1 mm. The Front-End Electronics provides the readout for a total of 16+16 strips. The diamond target, being one of the main subjects of this thesis work, is described full in detail in Chapter 3.
The target must fulfil three main requirements:

- it must be made of a material with low atomic number (Z=6), to reduce the rate of Bremsstrahlung interactions ($\propto Z^2$), main background of the experiment; the signal cross section, instead, grows linearly with Z;
- it must provide a measurement of the position of the interaction point and beam profiles, in both views: X and Y. The resolution on the missing mass improves with the spatial resolution on the dark photon production point, through the photon polar angle θ, as shown by MC simulation in Figure 2.6, calculated for a dark photon mass of 15 MeV.
- the target should provide bunch per bunch the particle multiplicity allowing to compute the instantaneous luminosity of the experiment.

2.2.2 PADME magnet

The magnet used to bend the positron beam in the experiment is one of the sweeping magnet used for the SPS transfer line at CERN. The dipole is 1 m long and 52 cm wide, with a vertical gap enhanced to 230 mm. The dipole was refurbished in some minor components and the magnetic field remapped in space at Frascati before installation in BTF hall. A calibration of

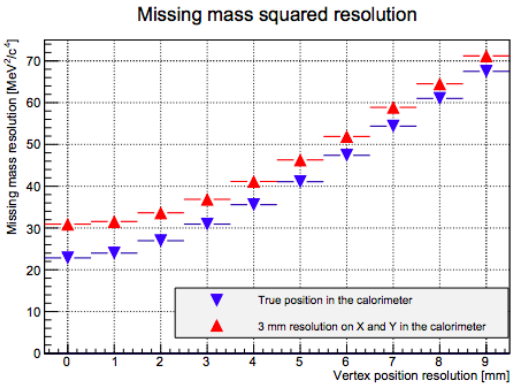

Figure 2.6: The missing mass resolution as a function of the A' production point resolution, for a dark photon mass of 15 MeV.

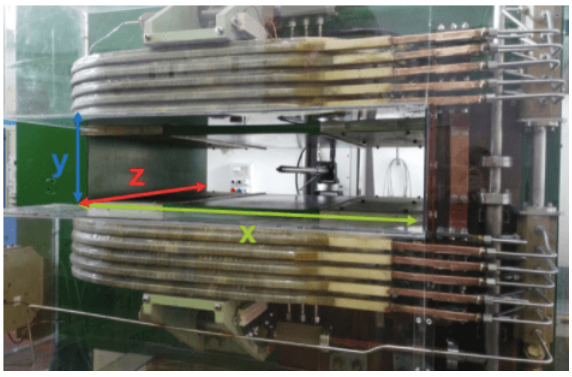

Figure 2.7: Picture of the the PADME magnet before the insertion in the vacuum vessel. The PADME reference system is also reported.

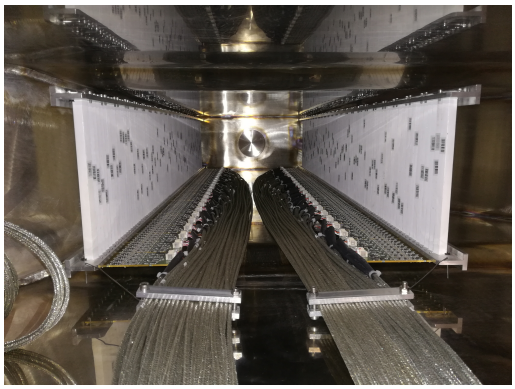

Figure 2.8: Picture of the Positron Veto (right) and Electron Veto (left) assembly inside the vacuum chamber. The beam comes out of the picture.

the magnetic field as a function of the applied current was computed. This measurement lead to the following relation, which connects the supplied current and the magnetic field:

$$\mathrm{B\ (Gauss)} = 19.44\ \mathrm{I(A)} + 32.801 \tag{2.4}$$

The intensity of the magnetic field during data taking is chosen in such a way to ensure that the beam impinges onto the center of timepix and with a minimal energy release in ECAL.

2.2.3 Charged particle veto

The main physics background in PADME is the Bremsstrahlung process that can produce a photon in ECAL, mimicking a signal event, combined with a positron of energy lower than the beam energy by an amount corresponding to the energy of the photon. A system of vetoes was designed to reject these processes, by detecting the positron emitted in coincidence with the photon. It consists of two detectors: the Positron Veto (PVeto), which covers the internal vertical wall of the vacuum chamber, inside the PADME magnet, on the side of the bending for positrons and parallel to the direction of the incoming beam, and a High Energy Positron (HEP) veto, which covers a small angular region between the beam dump and the PVeto. An Electron Veto (EVeto), identical to the PVeto, is placed in front of the PVeto on the opposite side of the vacuum chamber. A good time resolution, below 1 ns, and high efficiency are required for the veto system, to allow Bremsstrahlung events identification also in high pile-up conditions.
A further interesting usage of the veto system, in particular requiring the coincidence between PVeto and EVeto clusters, can be the detection of the hypothetical visible decays of the dark photon or, supposing the existence of a dark Higgs, detecting a final state made up of six leptons (for more details see Section 2.5.2). The charged particle veto system is made of 3 arrays of 90, 96 and 16 scintillating bars for PVeto, EVeto and HEPVeto, respectively, vertically oriented. An aluminium support structure holds these arrays of bars rotated around their longitudinal axis by 0.1 rad to minimize geometrical inefficiencies, together with the Front End Electronics (FEE) boards, each one serving up to four channels. The scintillating bars of size $10\times10\times178$ mm^3 are made of a plastic polystyrene-based material with 1.5% concentration of POPOP and they are produced by UNIPLAST. A longitudinal 1.3×1.3 mm^2 groove houses an optical wavelength shifter (WLS) fiber BCF-92, glued with Eljen EJ500 optical epoxy cement. The BCF-92 fiber has a maximal emission wavelength at 492 nm and maximal absorption wavelength at about 400 nm (matching the POPOP emission spectrum). Silicon photo-multipliers (SiPMs) Hamamatsu 13360, which are able to work in vacuum and sustain a magnetic field of about 0.6 T, allow the conversion of the photons into electric signals. Low cost and low operating voltage are also good

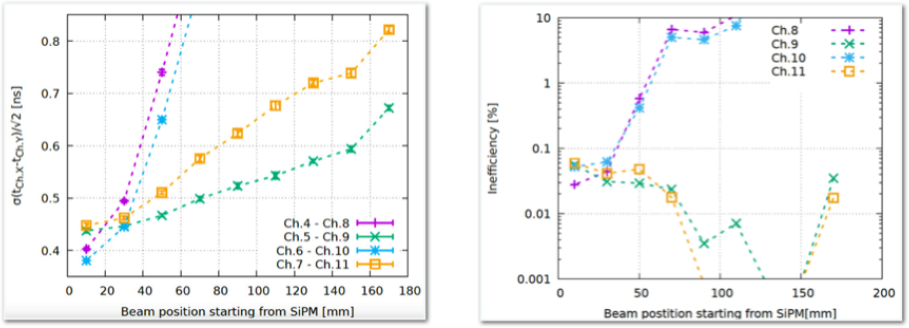

Figure 2.9: On the left the scintillating bar time resolution as a function of the distance between the beam impact point and the readout side is reported. The best performance was observed for scintillators with glued light-guides and readout of both scintillator and fiber (ch. 5-9); the time resolution deteriorated when the fiber was not glued (ch. 7-11) and when the fiber was not readout (ch. 4-8) or was absent (ch. 6-10). On the right the measured inefficiency of the scintillating bars as a function of the distance between the beam impact point and the readout side is shown. The counter is decleared efficient for signals above 10 photo-electrons.

features that motivated this choice of photo-detectors for the experiment.
The scintillating bars of the HEPVeto have SiPM readout at both edges, top and bottom.
In April 2017 a first prototype of the veto system was assembled and tested using a single electron beam at the BTF [77]. It was made of 16 bars with the same geometrical features of the final detector but different Silicon photo-multipliers for the readout (Hamamatsu S12572, more noisy than the final choice S13360). The prototype array of scintillators was aligned with the beam line, so that the beam crossed all bars. An off-line trigger made using the first and the last group of four scintillators was used, to assure the passage of a particle through the two remaining groups of four scintillators placed in the middle. During the beam test, the front-end signals were readout by the same CAEN digitizers using in the experiment V1742 but it was operated at a higher sampling rate, equal to 5 GS/s, instead of 2.5 GS/s. The most important features of the veto system are the time resolution and the efficiency. These parameters were measured varying the distance between the impact point of the beam with respect the photo-detectors, from 10 mm to 170 mm, and using different light collection configurations, as reported in Figure 2.9. The time resolution achieved was lower than 600 ps, with an inefficiency at the per mille level for scintillators with optical fibers either glued or not and collecting light from scintillation bars and fiber edges when the beam was hitting the bars at a distance from the SiPM below 40 mm. These tests lead to the choice of the final veto design for the experiment, i.e. the scintillators are hosting glued fibers in the groove and both scintillators and fibers are readout with SiPM. The time resolution was also measured during the commissioning of the experiment. It was obtained considering the time difference between the hits in PVeto and central crystal of the SAC, assuming a negligible time resolution for the fast calorimeter. The sigma of the Gaussian fit of the distribution core gave a value of about 670 ps (see Figure 2.10), compliant with the PADME design requirement (< 1 ns).

2.2.4 ECAL

The electromagnetic calorimeter (ECAL) is the most important sub-detector of PADME since it must detect the photon produced along with the dark photon and measure its energy with high precision.

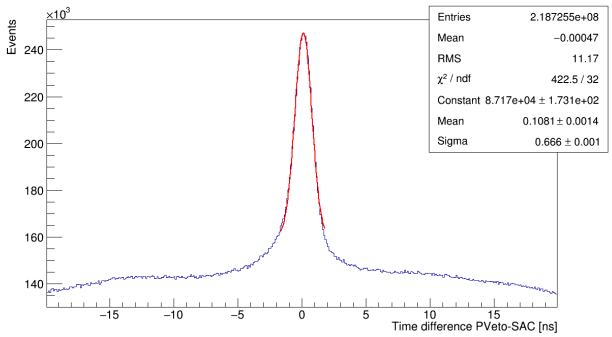

Figure 2.10: Time resolution of the veto measured during the commissioning phase, achieving a value of 670 ps.

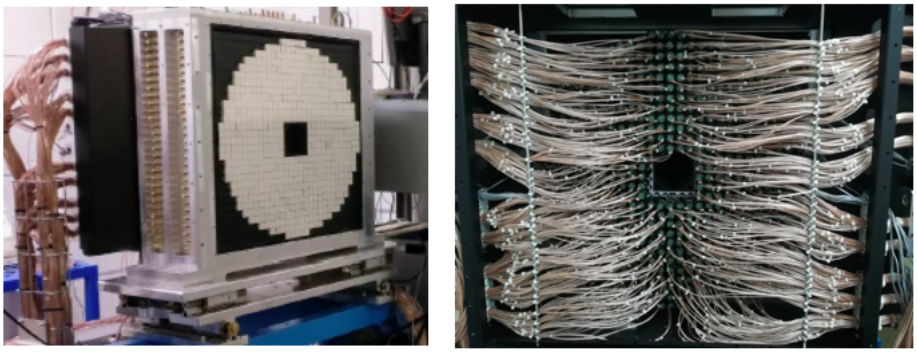

Figure 2.11: Picture of ECAL front side (on the left) and back side (on the right).

This detector is made of 616 BGO crystals of $2.1 \times 2.1 \times 23.0$ cm^3 size each, arranged in a cylindrically shaped array of 29 cm radius with a square hole of 5×5 crystals in the center, reaching a total geometrical acceptance of [15.7, 82.1] mrad, being located at a distance of 3.463 m from the target. The central hole prevents the high rate of forward Bremsstrahlung photons to keep constantly busy the detector. Bremsstrahlung radiation is, indeed, emitted preferentially at very small angles with respect to the direction of the incoming beam, therefore the rate in the forward region implied by the beam intensity would have been unmanageable in ECAL given the slow response of BGO. A picture of ECAL is shown in Figure 2.11. The BGO crystals, reconditioned from the electromagnetic calorimeter of the L3 experiment [78], were assembled inside the metallic cylindrical cage. Tedlar foils of 50 μm thickness were used in order to level the crystal planes without compromising the final resolution. Each BGO crystal was coupled to a photo-multiplier HZC XP1911 type B [79], glued with ELJEN EJ-500 [80] optical cement and covered with three layers of a white painting ELJEN EJ-510 [81]. Before assembly each Scintillating Unit (SU) was calibrated with a ^{22}Na source, in order to obtain the gain curve useful to equalise the response of each crystal to 15.3 pC/MeV (for a detailed discussion of the calibration procedure see [82]). The efficiency of each SU is obtained through an in-situ calibration with cosmic rays, using the cosmic trigger based on external scintillators. The energy resolution obtained during the beam test of a 5×5 prototype is shown in Figure 2.12 and parametrized according to the formula:

$$\frac{\sigma(E)}{E} = \frac{2.0\%}{\sqrt{E[GeV]}} \oplus \frac{0.003\%}{E[GeV]} \oplus 1.1\% \tag{2.5}$$

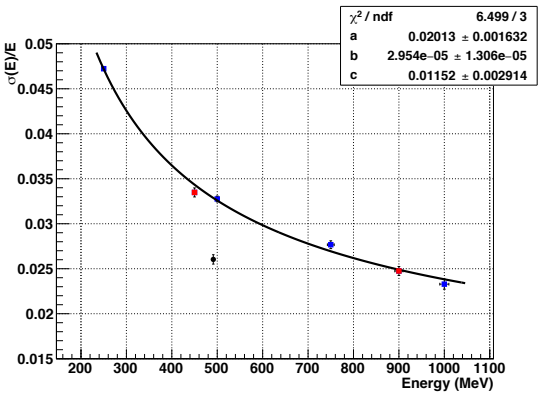

Figure 2.12: ECAL energy resolution as a function of the photon energy obtained with a 5×5 prototype array of crystals (coloured data points). A phenomenological curve is fitted to the data as explained in the text. A much better energy resolution was obtained for a single positron energy of 490 MeV during the commissioning of the experiment.

During the commissioning of the experiment the energy resolution was measured using a single positron beam and compared with the one obtained with the prototype; as expected a better resolution was obtained. ECAL, with respect to the prototype, has a longer crystal length, giving a better containment, the PMTs are glued, and not only optically coupled, and the applied high voltage was adjust to equalize the crystal response.

2.2.5 SAC

The small angle calorimeter is a matrix of 5×5 PbF_2 crystals of size $3 \times 3 \times 14$ cm^3, coupled to R13478UVPMT Hamamatsu photomultipliers [83]. A picture before the final assembly is shown in Figure 2.13. As it produces fast Cherenkov light, it can sustain a high rate of Bremsstrahlung photons.
It is placed behind the ECAL hole, covering the angular region in the range [0, 18.9] mrad and it allows to veto on three photon events, where two of them are produced in the forward direction, hitting the SAC and a third one appears as an isolated photon in ECAL.
A prototype was tested at the BTF using a single positron beam of energy in the range 100-400 MeV. The data showed energy resolution of 10% at 550 MeV with a light yield of 2 photo-electrons per MeV [84]. The main SAC goal is to provide an excellent time resolution; beam test data on a prototype gave a time resolution of about 80 ps.
During the commissioning phase, the SAC crystals were calibrated using both a single positron beam and dedicated cosmic ray trigger runs.

2.2.6 Auxiliary beam diagnostic with pixel detector

The PADME collaboration installed two pixel detector systems to provide powerful auxiliary beam diagnostic: the first in the target region and the second in the dump region. For the PADME beam diagnostic in the target region two MIMOSA-28 placed in parallel to each other, orthogonally to the beam, are used. MIMOSA-28 is a monolithic pixel Silicon detector, consisting of a matrix of 928×960 (rows, columns) pixels ($\sim$ 0.9 Mpixels in total) of 20.7 μm pitch for a size of the chip of 20.22×22.71 mm^2 [85]. The MIMOSA detector is placed inside one of the arms of the vacuum cross, opposite to the target. A remotely controlled motor system (described in details in Section 3.4.1) can move MIMOSA in and out of the beam. This beam monitor can

Figure 2.13: Picture of the back side of SAC during assembly. The crystals coupled to the PMTs are arranged in a matrix 5×5 thanks to a proper structure.

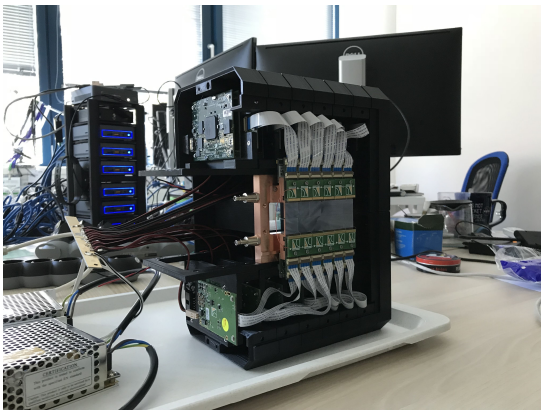

Figure 2.14: TIMEPIX before the installation in the experiment.

measure up to about 500 particles before saturating. It can be used with a low multiplicity beam to measure the beam divergence in the PADME region. It is the first time that the MIMOSA pixel detector is used in vacuum.
The other pixel beam monitor is TIMEPIX, produced by Advacam; it is placed in the region of the beam dump, in order to measure the bunch multiplicity and the spatial and temporal beam profile at single particle level. TIMEPIX is made of an array of 12 TIMEPIX-3 hybrid Silicon pixel detectors for a total area of 8.4 ×2.8 cm^2; each TIMEPIX-3 consists of a 256×256 matrix of pixels, with a pitch of 55 μm. It is the biggest array of TIMEPIX ever used in a high energy physics experiment.
The MIMOSA and TIMEPIX data acquisition are running as stand alone processes, but the collaboration is planning to integrate the two readouts in the PADME DAQ.

2.2.7 Vacuum vessel

The PADME vacuum is composed of three regions:

- *target region*: a vacuum cross is located, hosting the target and MIMOSA. One harm is the beam pipe, the other allows to move the target and MIMOSA in and out of the beam line;

Figure 2.15: The internal (on the left) and external (on the right) part of the vacuum chamber are shown. The flange on the left picture was connected to the cross of the target, while the cylinder on the right picture to the ECAL carbon flange. The two vacuum chamber parts were then screwed together. The beam enters in the page for the left picture and comes out for the right picture.

- *dipole region* the vacuum chamber is housed between the magnet expansions; inside the vacuum chamber the PVeto, the HEPVeto and the EVeto are located;
- the *dump region*: here another section of the vacuum vessel connects the chamber, internal to the magnet, to the carbon flange on the front side of ECAL.

In Figure 2.15 the internal vacuum chamber is shown on the left, before the installation inside the dipole. The visible flange was later connected with the vacuum cross which hosts the target and MIMOSA on opposite sides. The internal chamber hosts both the Positron and Electron veto behind the lateral flanges on the left and on the right of the central flange. On the right it is shown the final part of the external vacuum chamber. The final part of the cyilinder was connected to the front face of the ECAL carbon flange. The HEPVeto was placed just behind the smallest flange visible on the right part of the right picture. The central flange corresponds to the beam dump region, where the TIMEPIX was placed but outside the vacuum, as the calorimeter system. The vacuum in in the PADME experiment ($\sim 10^{-5}$ bar) and beam line was separated from the LINAC vacuum ($\sim 10^{-7}$ bar) by a 250 μm thick Be window, placed in the BTF hall, at the approximated distance of $\sim$ 3-4 m from the target until 2019. Later, in 2020, after unsuccessful attempt to move the Be window closer to the target in July 2019, the line was optimized. A Mylar window was chosen as vacuum separator, and placed just outside the BTF wall, on the LINAC side (see Section 2.1).

2.3 Trigger and Data acquisition

The signals from all sub-detector channels are digitized in 1024 samples and recorded using CAEN V1742 [86]. These boards, based on the DRS4 domino chip, are capable to digitize up to 32 channels, with a maximum selectable sampling rate of 5 GS/s. The PADME data acquisition system reads a total of 891 channels as reported in Table 2.1. The external trigger is provided directly by the LINAC with a rate of 50 Hz (one bunch out of 50 in a second is sent to the hodoscope instead of BTF line, therefore one trigger out of 50 leads to an empty event). In addition, there are other two triggers, a cosmic ray trigger, for calibrations studies, and a delayed trigger, to study pedestals and noise. During the data taking the target and ECAL were digitized at 1 GS/s sampling rate, while the fast detectors, Vetoes and SAC, at 2.5 GS/s.

The DAQ proceeds in two steps: the Level 0 (L0) responsible of recording the data from all channels in five different streams and the Level 1, which merges all the streams, applies zero

Sub-detector	Number of channels
Target	32
PVeto	90
EVeto	96
HepVeto	32
ECAL	616
SAC	25
Total	891

Table 2.1: Number of read-out channels for each detector.

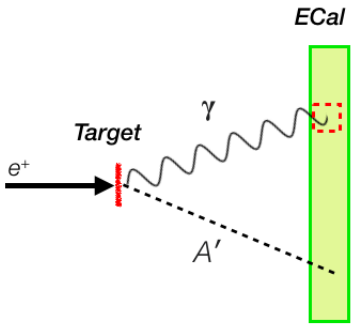

Figure 2.16: A schematic representation of the signature of a dark photon event in PADME. A single SM photon should be detected by ECAL, with nothing else in coincidence.

suppression to the ECAL data to reduce the event size, and produces the final format of the output data.

2.4 Dark photon search with PADME

As already mentioned, the main goal of the PADME experiment is to select events with a single photon in the final state which can be emitted in coincidence with a dark photon, with nothing else in coincidence (see Figure 2.16). The dark photon search is implemented looking for bumps in the missing mass distribution. PADME was designed to reduce to an acceptable level the background without loosing efficiency for the signal, by accomplishing to the following tasks:

- hermeticity in the forward direction;
- good measurements of the photon energy and direction;
- vetoing very forward photons and charged particles.

In this section the dark photon analysis strategy envisaged in the PADME design phase [75] is summarized along with the projected physics reach.

2.4.1 Background rejection strategy

Good background rejection is one of the major requirement of the PADME experiment. The background processes are in particular Bremsstrahlung, annihilation (in two or three photons)

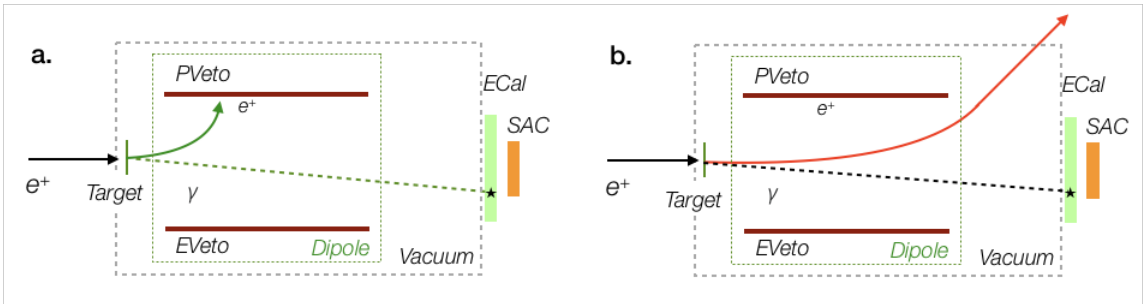

Figure 2.17: Bremsstrahlung process. On the left an example of background suppression, on the right the irreducible background to the dark photon signal.

and Bhabha scattering.
The process with the highest cross section is the Bremsstrahlung, where the positron of the beam interacts with the a nucleus of the target and it is slowed down, emitting a photon, as follows:

$$e^+N \to e^+N\gamma$$

ECAL was designed with a central hole to avoid Bremsstrahlung photons that are mostly emitted forward. A sketch of Bremsstrahlung events in PADME showing the rejection method is shown in Figure 2.17 a. The time coincidence between the photon reconstructed in ECAL and a positron reconstructed in the charged particle veto, in addition to the requirement that the sum of the energies is equal to the beam energy, are the key criteria allowing to veto on Bremsstrahlung interactions.
Unfortunately, in some cases the Bremsstrahlung photon is detected in ECAL but the corresponding positron escapes from the geometrical acceptance of the positron veto, mimicking the signal (Figure 2.17 b). These events represent a source of irreducible background to the dark photon signal.
Another important source of background is represented by the annihilation in 2 or 3γs:

$$e^+e^- \to \gamma\gamma(\gamma).$$

The first could be suppressed rvetoing two ECAL photons in time coincidence, symmetric in the azimuthal angle and with the sum of their energies equal to the energy of the beam. For the rejection of the 3γs final state the role of the SAC is very important, as it allows the detection of any forward photons (Figure 2.18 a, b). The irreducible background in 3γs case is represented by a single photon detected by ECAL, with the second and third escaping not only ECAL, but also SAC (Figure 2.18 c).

2.4.2 Signal selection

Monte Carlo samples where Bremsstrahlung and annihilation in two photons are simulated directly by GEANT4 and dedicated 3γs samples, generated with CalcHEP and later processed by the detector simulation, were used to assess the efficiency of the background rejection strategy in the proposal [87]. Also the Bhabha scattering and pile up of annihilation events were included in the background estimation through the GEANT4 simulation. The distributions shown here are based on a simulated samples with a beam multiplicity of 5000 positrons/bunch of energy 550 MeV, and 40 ns of bunch length. A candidate dark photon event must satisfy the following requirements:

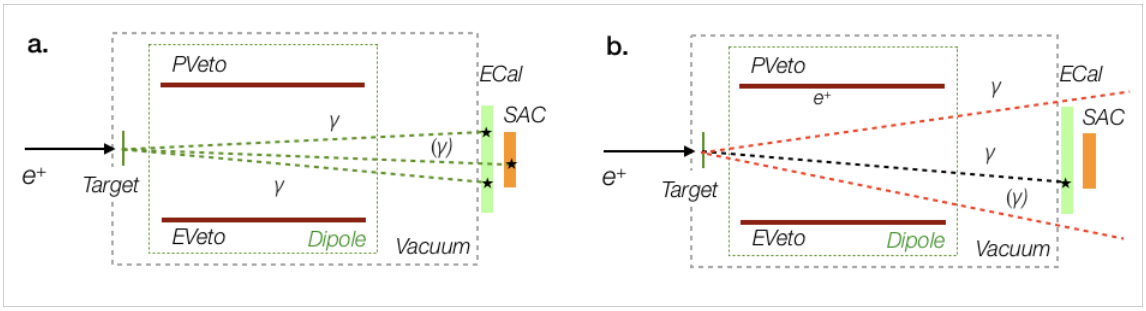

Figure 2.18: Annihilation (in 2 or 3γs) process. On the left an example of background suppression, on the right the irreducible background to the dark photon signal.

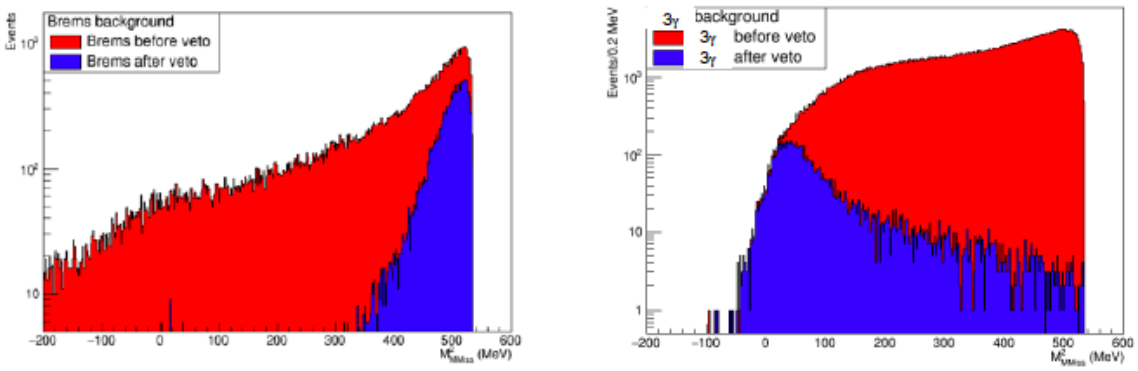

Figure 2.19: On the left it is shown the distribution of the squared missing mass due to Bremsstrahlung events, before (in red) and after (in blue) the positron veto cuts. On the right it is shown the same distribution due to 3γs events, before (in red) and after (in blue) SAC cuts.

- one photon in ECAL inside a radial fiducial region, where the shower is well contained, and no other photons in ECAL and in SAC within ±2 ns, to reject the annihilation final state in two or three photons;
- no positrons in the positron veto within ±2 ns with respect to ECAL photon and with energy summed to the photon energy compatible with the beam energy, to reject events of Bremsstrahlung;

The distribution of the squared missing mass for the events passing the selection outlined above exhibits a peak at the squared mass of the dark photon emerging over the background depending on the strength of the coupling, i.e. on the production cross section. The background rejection capability of the PVeto and HEPVeto and SAC can be appreciated in Figure 2.19.

2.4.3 Analysis strategy

The missing mass square distribution for the background events is shown in Figure 2.20 left, before and after signal selection cuts. Negative values of the squared mass are an effect of the pileup, the peak at zero is related to the annihilation processes, which goes to zero after selection cuts, while at the region of high squared mass is dominated by the Bremsstrahlung interactions. In case signal events produced at PADME, a Gaussian peak with mean equal to $m^2_{A'}$ would appear on top of the distribution of Figure 2.20 left. The width of the signal distribution depends on the mass parameter, which is determined by the energy and angular resolution of the photon reconstructed in ECAL. Figure 2.20 right shows how the signal width depends on the mass hypothesis. The simulated data are obtained by generating a sample of 1000 events, with 5000 positrons/bunch and a single dark photon, of different mass values.
In case of discovery photon-dark photon, the mixing constant ϵ, presented in Section 1.2.2, can be computed [75] as follows:

$$\epsilon^2 \delta(m_{A'}) = \frac{\sigma(e^+e^- \to \gamma A')}{\sigma(e^+e^- \to \gamma\gamma)} = \frac{N(A'\gamma)/\mathcal{A}(A'\gamma)}{N(\gamma\gamma)/\mathcal{A}(\gamma\gamma)} \tag{2.6}$$

where $N(A'\gamma) = N(A'\gamma)_{obs} - N(A'\gamma)_{bkg}$ is the number of observed events in the signal region after background subtraction, $N(\gamma\gamma)$ is the number of annihilation events, corrected by the respectively acceptance $\mathcal{A}(A'\gamma)$ and $\mathcal{A}(\gamma\gamma)$, and δ is the kinematic cross section enhancement factor of the process $e^+e^- \to A'\gamma$ relative to the $e^+e^- \to \gamma\gamma$ process due to mass effects. The acceptance for signal and annihilation is computed by simulations and validated with data. From Eq. 2.6 it is clear that a concurrent selection of SM annihilation events allows a physics driven normalization. On the other hand, the total number of annihilations $N_{\gamma\gamma}/\mathcal{A}(\gamma\gamma)$ can be estimated by measuring the total Number of Positrons On Target (NPOT) and the QED predicted cross section $\sigma_{\gamma\gamma}$.

$$N^{tot}_{\gamma\gamma} = \frac{N_{\gamma\gamma}}{\mathcal{A}(\gamma\gamma)} = NPOT \cdot \sigma_{\gamma\gamma} \cdot \rho_{e^-} \cdot L \tag{2.7}$$

where ρ_{e^-} is the number density of electrons in the target and L the target thickness. The measurements of NPOT with the active diamond target will be explained in depth in Chapter 5.

2.4.4 PADME sensitivity

The lower limit on the mixing constant ϵ in PADME is about 10^{-3} and this is related to the maximum number of positrons per bunch, compatible with a pile-up manageable by the detectors. The limit on the mass is related to the beam energy; for a beam energy of 550 MeV, the

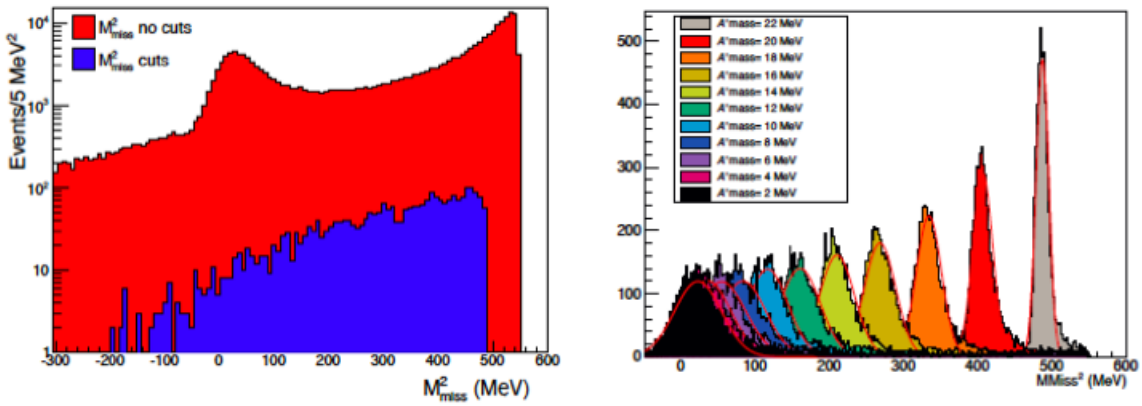

Figure 2.20: On the left the distribution of the squared missing mass for background events, before (red) and after (blue) signal selection cuts. On the right squared missing mass distributions for dark photon events for different masses in pure signal samples are shown to appreciate how the resolution depends on the mass parameter.

maximum energy that can be reached for positrons in the existing LINAC, an upper value of 23.7 MeV for the mass of the dark photon can be obtained. Recent beam-line upgrades allowed to extend the bunch duration up to 300 ns, in such a way the multiplicity of the beam could be raised up to 30000 positron/bunch, keeping the pile-up under control for the detectors. This feature helps to shorten the time to reach the project luminosity: a data sample of 1×10^{13} POT can be collected in 6 month while in 2 years a sample of 4×10^{13} POT can be reached. The excluded region in the parameter space (m'_A, ϵ^2) for invisible decay of the dark photon obtained for these two different values of the integrated luminosity is shown in Figure 2.21.
The parameter space probed by PADME is quite interesting: since it matches the region where the dark photon model might account for the discrepancy between the measured and the theoretical value of the anomalous magnetic moment of the muon, as described in Sec. 1.2.4, and it is relevant in scenarios of thermal production of dark matter. Indeed, the variable y (introduced in Section 1.3.3) connecting m'_A and ϵ to the mass of the dark matter and coupling allows to establish how relevant is the PADME sensitivity for the standard dark matter scenario. For a mixing constant $\epsilon \sim 10^{-6}$ the lower limit on the y value for $\alpha_D = 0.1$ is y$\sim 10^{-9}$, while in case of $\alpha_D = 0.5$ it is y$\sim 10^{-8}$. Therefore, PADME is sensitive to a dark photon hypothesis that is compatible both with scalar and fermion thermal relic dark particles, as shown in Figure 1.20, although the region is probed and mostly excluded today by other experiments.
It is interesting to evaluate the increase of sensitivity if the experiment PADME is migrated to another facility with another beam-line, for example Cornell and Jefferson Lab. In the first case the use of a 6 GeV positron beam would increase the probed range of the dark photon mass [89], up to:

$$m_{A'} = \sqrt{2 m_e E_{BEAM}} \sim 78\,\text{MeV} \tag{2.8}$$

In the second case, using a 11 GeV positron beam would increase the probed mass up to ~ 100 MeV. A first study on the possibility to build a PADME like experiment at the Jefferson Lab has been already carried out recently [90].

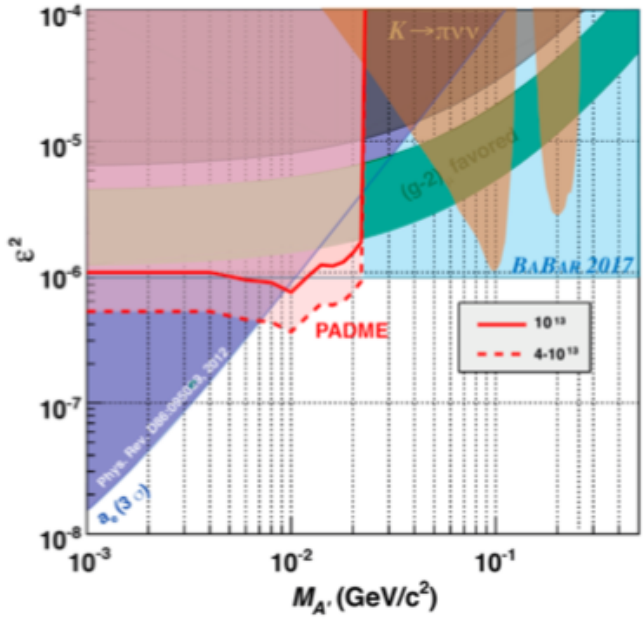

Figure 2.21: PADME exclusion region of the parameter space for a project luminosity of 10^{13} or 4×10^{13} positrons on target, which can be reached in 6 months and 2 years, respectively, with the recent beam-line upgrades [88].

2.5 Additional searches in PADME

Taking advantage of the fact that the missing mass technique used by PADME is model-independent, a light dark particle other than the dark photon can be searched with the PADME detector, considering the same visible final state relevant for the dark photon search:

$$e^+e^- \to \gamma X \tag{2.9}$$

Here the dark photon A' is replaced by the light dark particle X, produced in coincidence with a SM photon. For example, some studies are ongoing to quantify the search sensitivity for the Axion-Like Particle with the PADME experiment.
It is also possible to search for dark particles such as the hypothetical dark Higgs with different final states.
Finally, it is possible to envisage a new search with small changes to the PADME configuration, as in the case of the elusive protophobic[1] X boson, the $X17$ particle, whose existence was proposed by the ATOMKI collaboration after the observation of some anomalies. These scenarios are described below.

2.5.1 Axion-Like Particles

The Axion-Like Particle (ALP) is a possible candidate pseudo-scalar spin-0 mediator between the SM and the DS. A visible decay into e^+e^- pair or 2γ is foreseen if no other dark sector particles lighter than the ALP, $m_{ALP}<m_\chi$, exist. ALPs couple to bosons (like photons with coupling $g_{a\gamma\gamma}$) and fermions (like e^- with coupling g_{aee}) and, in general, no assumptions are made about the relation between mass and coupling (unlike for QCD axions). Starting from a

[1] Literally, *protophobic* stands for *fear of proton*, which means that the particle does not interact with protons.

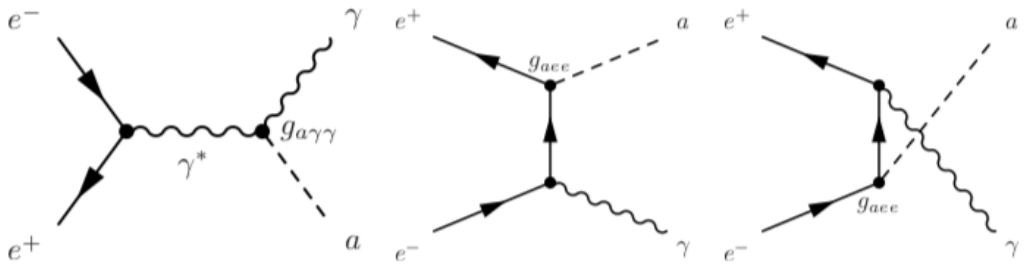

Figure 2.22: ALP production in PADME. On the left the annihilation s-channel is shown, with a virtual photon as mediator. The t-channel and u-channel are shown in the center and on the right, with an electron exchange [91].

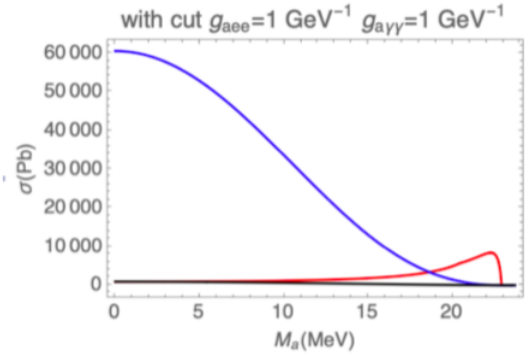

Figure 2.23: Cross-section of ALP production in PADME as a function of the mass with photon mediator (blue line, $g_{a\gamma\gamma}$=1 and g_{aee}=0) and electron exchange (red line, $g_{a\gamma\gamma}$=0 and g_{aee}=1) for center of mass energy of 23.7 MeV.

positron-electron annihilation, the possible Feynman diagrams that give a final state with an ALP and a photon, are reported in Figure 2.22 [91]. Supposing $g_{a\gamma\gamma} = g_{aee}$, the s channel is dominant for ALP masses lower than ∼18.5 MeV, as shown also in Figure 2.23. The cross section calculation assumes a beam energy of 550 MeV and takes into account the ECAL acceptance and an energy threshold of $E_\gamma > 30$ MeV.
The PADME experimental set-up is able to look for the ALP both in visible and invisible decay. The ALP could decay into a couple of e^+e^- or two photons, hence, the signature in PADME would be an e^+e^- pair in time with a photon (Figure 2.24 a) or 3γs in time coincidence (Figure 2.24 b). The invisible decay would have the same signature of the dark photon: a single SM photon in ECAL and a missing mass component (Figure 2.24 c). A special visible case is the one of the long lived ALP: the decay time in such a case is long, so the signature is the same of the invisible case. In literature it is common to refer to the long-lived case as invisible decay. According to several models, in the mass region below 100 MeV the ALP could indeed be long lived, appearing as a missing particle in the PADME set-up.
Preliminary computations of the estimated number of ALPs produced over a 2 years of data taking with 60% of efficiency and 20000 e^+/bunch (assuming about 10^{13} NPOT), report 1000 events for an ALP of mass 22 MeV [91]. A feasibility study for of the ALP search in PADME is currently ongoing.

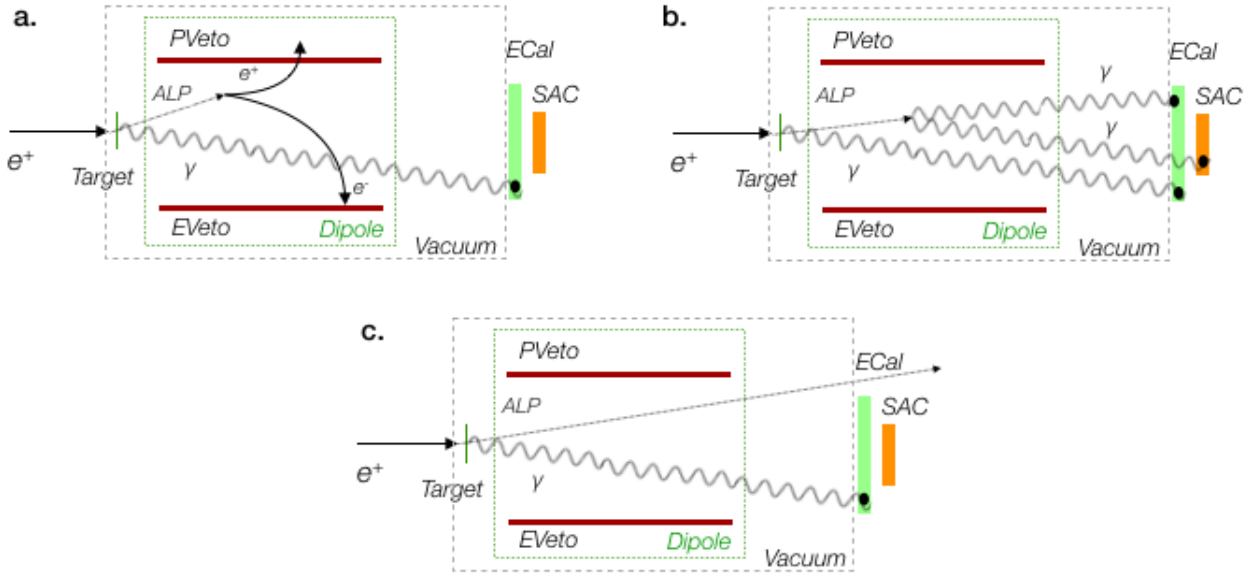

Figure 2.24: Drawing of the accessible final state in PADME, involving the production of a ALP which decays into visible state (a, b) or invisible (c).

2.5.2 Dark Higgs

The dark photon, as mentioned in Chapter 1.2.2, could acquire mass through the interaction with the Standard Model Higgs or through a new Higgs-like mechanism. The latter case foresees the existence of a dark Higgs, whose production, in association with a dark photon $e^+e^- \to A'h'$, might be possible, if the two exotic particles have a similar mass ($m_{A'} \sim m_{h'}$) [92].
The production mechanism involves the mixing of the SM photon to a dark photon, which then emits a dark Higgs, like in a Higgs-strahlung process (see Figure 2.25). Some preliminary studies have been carried out for the scenario where the dark Higgs decays into two dark photons ($m_{h'} > 2\, m_{A'}$) and A' decays in e^+e^-.
The signature consists of 6 leptons in the final state:

$$e^+e^- \to A'h' \to A'A'A' \to 3\,(e^+e^-) \tag{2.10}$$

In the scenario of invisible decays of the dark Higgs and in the case of a long lived dark Higgs, the final state to be searched for becomes e^+e^-X, where the e^+e^- pair comes from a visible decay of the DP.
PADME could search for both the Dark Higgs decay mode scenarios; by means of the coincidence of three charged particles (Figure 2.26 a) in both the PVeto and EVeto for the visible decays mode, or through an e^+e^- pair and missing mass in the invisible or long lived scenario (Figure 2.26 b).
The dark photon interaction with the SM Higgs was already investigated at LHC, in particular by the ATLAS [93] and CMS [94] experiments. The scenario which involves the existence of h' was investigated by KLOE, BABAR and Belle.

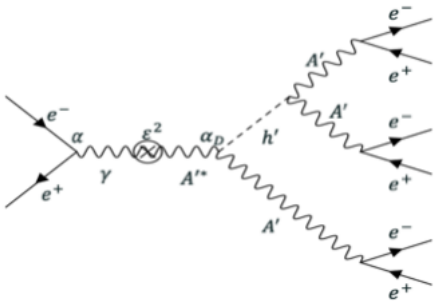

Figure 2.25: The production of the dark Higgs could be studied searching six leptons as final state.

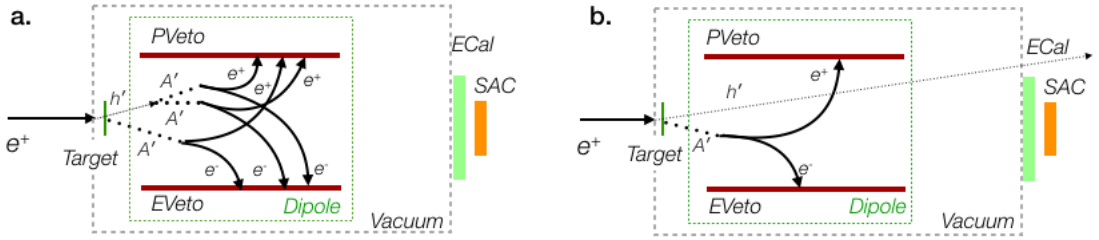

Figure 2.26: Drawing of the accessible final state in PADME, involving the production of a Dark Higgs which decays into visible state (a) or invisible (b).

2.5.3 Protophobic X boson

A recent interesting physics result that could be the smoking gun for new discoveries is an anomaly in nuclear transitions reported by the ATOMKI collaboration. The ATOMKI group built a spectrometer with the aim of performing a simultaneous energy and angular correlation measurement of electron-positron pairs in the decay of excited Be nuclei [95]. The anomaly in excited ^{8}Be transitions was the first to be observed: an excess of pair production with a well defined separation angle was measured, that can explained by the production of a new particle named X17 [96]. The presence of this anomaly was confirmed later by a measurement performed improving the set-up [97]. The most recent measurement of the ATOMKI group reports also an anomaly in ^{4}He nuclear transitions, which can be explained by the same resonance produced in the decay of the exited state [98]. The existence of such new resonance is challenged by several experimental constraints, however a protophobic X boson could be a consistent explanation of these observed anomalies [99]. Possible candidate particles that could give this signature are discussed in [100], along with theoretical and experimental constraints.
The experiment suggests that the new particle is a boson with spin parity $J^P = 1^+$, which would couple to SM particles in a peculiar way and, therefore, it is often referred to as the mediator of a new hypothetical fifth force.

Dark photon as ^{8}Be anomaly explanation

A dark photon with mass $m_{A'}$ ∼17 MeV could justify the anomaly discovered by the ATOMKI collaboration. In order to investigate this interesting mass region ($m_{A'} \sim 17$ MeV), data from several experiments were re-analysed, in particular KEK [101], ORSAY [102] and E141 at SLAC [103], but no firm conclusion has been reached so far. Among the dark photon production modes, the resonant production mechanism $e^+e^- \to A' \to e^+e^-$, reported in Figure 2.27, is favoured [104], being of the order of $\epsilon^2\alpha$. The decay length of the DP does not depend on the boson mass ($\ell_\epsilon \sim 3/2m_e\alpha\epsilon^2$) for a given value of ϵ. This allows to probe the range of the DP mass up to the kinematic limit, with the same sensitivity. In order to investigate the PADME potential for this search, a study of the detector optimizations were carried out and published in [105]. A few set-up changes are needed to allow the search for the dark photon produced in such a way, mainly concerning the target. The beam energy should be reduced to about 282 MeV using Eq. 2.3 in the hypothesis of a dark photon mass of 17 MeV, to investigate the interested resonance region. The probability of resonant production would increase using a thick target of a material with large atomic number, for example Tungsten (W). Such target would allow to overcome the difficulty of producing precisely the center of mass energy corresponding to the narrow resonance. The positrons hitting the thick target would lose energy producing, through a stochastic process, a sample of positrons of almost continuously varying energy. Those with the correct energy would then annihilate with atomic electrons via a resonant s-channel exchange of a dark photon. If the A has a decay length such that it travels through the entire target and it decays next to the exit, the e^+e^- pair of the final state would be detected by the charged particle detectors. The thick target would also act as a hermetic dump for the other positrons of the beam, reducing the background from SM processes. Hence the measurement of the momentum of the positron and electron would allow to identify an excess of events at a value of the invariant mass corresponding to the A mass. The beam intensity could be increased up to about 10^{18} POT/year, close to the maximum value compatible with the possibility to stand the resulting pileup. Figure 2.27 shows the coverage of the parameter space, for different values of the target thickness. In such a way PADME could explore a portion of the parameter space never investigated so far.

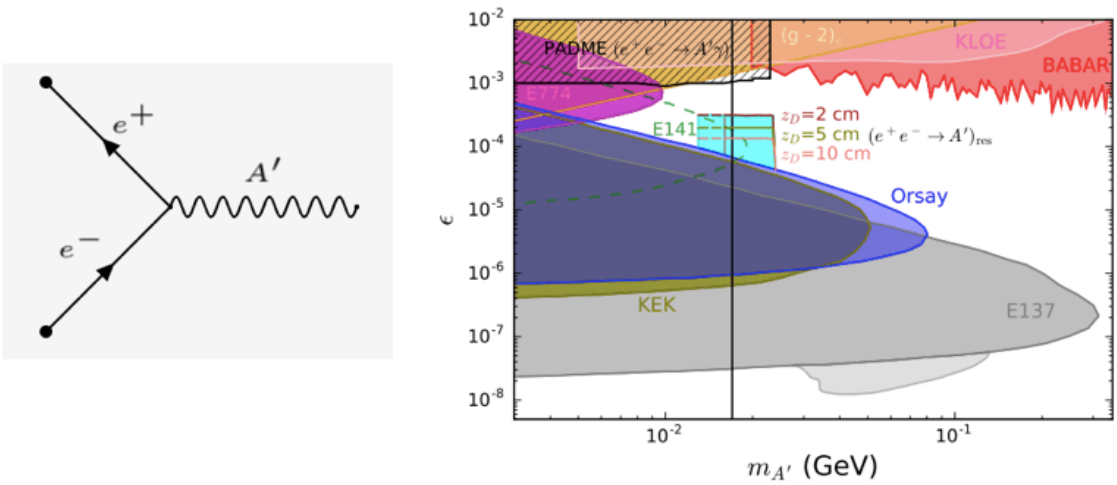

Figure 2.27: On the left the resonant production of the dark photon is shown; on the right, the excluded regions from several experiments and the expected PADME excluded regions for different target thickness.

Chapter 3

The active diamond target

PADME is the only experiment of its kind which uses an active target to determine the beam position for improving the missing mass resolution for the search of the dark photon. A diamond detector is suitable as active target, thanks to its low atomic number (Z=6), allowing to limit the Bremsstrahlung interaction (cross-section proportional to Z^2) with respect to the signal, which scales as the annihilation interaction (cross-section proportional to Z).
The diamond detector plays crucial roles during the data taking such as monitoring the beam, providing the X and Y beam profiles and the number of positrons per bunch. Its peculiarity is to have electrodes made of nano-metric graphite layers, a technology never used so far in a high energy experiment.
The detector was designed and realized in this PhD work together with the PADME Lecce group. In this chapter the properties of diamond as material for particle detector are briefly illustrated, followed by a detailed description of the detector realization work-flow and detector installation in the experiment. At the end, the experience wit the operation of this detector is reported, together with the off-line reconstruction of the signal and the calibration of the front-end electronics.

3.1 Diamond detectors

3.1.1 Diamond properties

Diamond is one of the most exceptional material in nature; the high number of extreme physical properties allows a broad range of applications [106]. Diamond is a metastable allotropic form of carbon, its structure is shown in Figure 3.1: each atom has four covalent bonds directed to the vertices of a regular tetrahedron, forming a very stable structure. The diamond lattice results from bonding between sp^3 hybrid orbitals of neighbouring carbon atoms which form a cubic lattice, with a bond length of 0.1545 nm [107]. The big amount of energy needed to remove a carbon atom from the diamond lattice, due to the strength of the covalent bond (347 kJ mol^{-1}), determines its hardness; it is indeed classified as the hardest material in the Mohs scale. The extreme rigidity of the diamond lattice is the key to many mechanical properties. Thanks to the large band gap of 5.45 eV, the diamond presents also peculiar electrical properties; the very high resistivity, between 10^{13}-10^{16} Ω cm, makes the diamond an insulator in electrical terms, even if it is considered a semiconductor, for its similarity to usual semiconductors, like silicon or germanium. To be precise, diamond can be classified as a large gap semi-conductor, with a few free charges at room temperature, that means low leakage current. The high thermal conductivity of diamond allows also the usage of this incredible material for a lots of technological applications. In fact, it is used in several processes like cutting, grinding, etc. which involves high

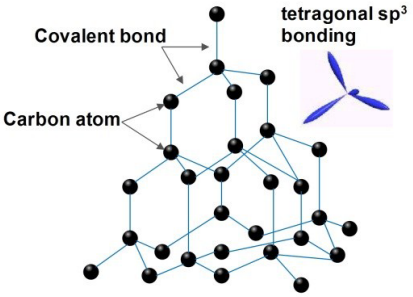

Figure 3.1: Diamond crystal structure.

working temperature [108]. In addition, it is well known that as a gem it is appreciate all over the world for its optical properties. It is optically transparent in the ultraviolet, visible, infrared and far infrared [109]. After all these peculiar properties, it is not surprising that diamond attracts attention even as active material for innovative detectors in high energy physics.

3.1.2 Diamond synthesis

The genesis of the natural diamond occurs at depths of around 200 km, in very high pressure and temperature conditions, such as 70–80 kbar and 1400–1600 °C [110]. The diamond is metastable at room temperature and pressure, for this reason the most stable allotropic form of the carbon is the amorphous graphite. The carbon atoms of the graphite form layers with a hexagonal arrangement and the force between them is weak. Although natural diamond exhibits lots of interesting properties, the low availability did not allow a wide spread of this material in technological applications. From the middle of the 19th century, the development of the synthesis technique allowed to create diamonds artificially for several applications. The first diamond synthesis method used was the High Pressure High Temperature (HPHT) pioneered in the ASEA Laboratory in Sweden, in 1953, although the results were not published. The first commercially available diamond was produced by the General Electric in 1954 and the synthesis procedure was published in 1955 [111]. The HPHT growth is similar to natural diamond formation, but with the addition of some materials that catalyse the crystal growth such as Fe, Co or Ni, that are essential for the success of the process. For many years, the common wisdom was that diamond would form only under the particular conditions of high pressure and high temperature reproduced in the HPHT synthesis. Even today billions of carats of diamonds are manufactured annually by the HPHT process, mostly for industrial applications. The chemical vapour deposition (CVD) growth was first performed in 1952 but only in the 1980s some scientists discovered how to grow diamond using this process in a reproducible way, which allowed the formation of diamond at low pressures [112]. In Figure 3.2 the regions of pressure and temperature, that allow the formation of the natural diamond, are shown, compared with the artificial conditions reached to produce a HPHT and CVD diamond. CVD is a technique that takes advantage of the metastable synthesis of the diamond at low pressure, using mixtures of ionized hydrocarbons (CO or CH4) and hydrogen in presence of plasma. The atomic hydrogen is the most important component in the gas phase mixture while the methane or other hydrocarbon molecules supply carbon atoms [113]. The CVD diamond synthesis development allowed to grow diamonds in the form of thin films or coating on a variety of shapes with controlled grain size. This technique enabled the exploitation of more combinations of the extreme properties of diamond for specific applications. Among the CVD diamonds there are two different types: polycristalline and single crystal. The purest one is the single crystal diamond, which is formed by homoepitaxial growth, starting

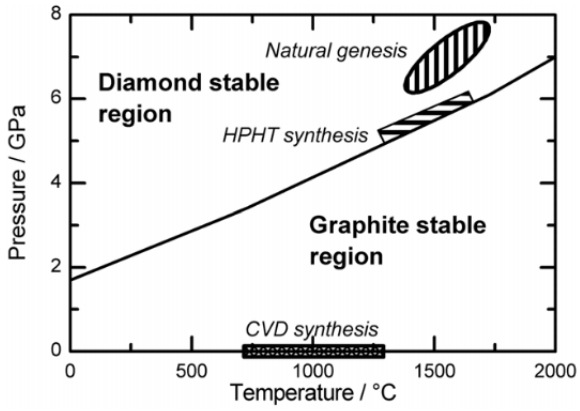

Figure 3.2: Phase space diagram of diamond formation.

from a diamond substrate, which could be either natural or synthetic (HPHT or CVD). If the substrate is made by any other material, such as silicon, tungsten, molybdenum, silicon carbide, silicon nitride, quartz glass, cemented carbide etc., the diamond is labelled as polycrystalline and the growth is called heteroepitaxial.

3.1.3 Working principle

Progress in high energy physics critically depends on the ability to perform experiments at high energy and also high luminosities. Future experiments may require the development and use of detectors able to work in harsh radiation environments, and to sustain a very high particle rate [114]. Thanks to its intrinsic radiation hardness, diamond is a suitable material for the fabrication of high energy physics detectors.
Although the diamond electrical properties were already well known during 1960s, diamond detectors were still utopian, because of their rarity and also very high price. The development of the CVD diamond synthesis allowed to make this idea more achievable. A typical diamond detector is a CVD diamond of about 1 cm^2 of area and a few hundred micrometers thick with the electrical contacts realized on the opposite sides of the diamond film. Before the realization of the electrical contacts, the CVD diamond surface is polished in order to remove the material from the substrate side and smooth out the growth side. Actually, a diamond detector is a solid state detector; the mechanism of detection is based on the generation of an electrical signal in an external circuit due to the passage of a charged particle. When a charged particle passes through the diamond film it generates electron-hole pairs, as schematically shown in Figure 3.3. The electrons and holes, promoted in the conduction bands, are both able to move within the diamond lattice and normally they recombine quickly. Instead, under the influence of an external electric field, the electrons and holes drift towards the electrodes, in particular the holes towards the cathode and the electrons towards the anode.
The instantaneous current $i(t)$ induced on a given electrode by the motion at velocity v of a charge q, under the influence of an electric field E, can be calculated from the Shockley-Ramo theorem [115] [116]:

$$i(t) = -q\vec{v}(t) \cdot \vec{E}_w \tag{3.1}$$

where $\vec{E}_w$ is the so called *weighting* field, which is a fictitious field obtained by applying unit potential to the electrode and grounding all the others. For a uniform constant field between two electrodes the weighting field is E_w=1/d and the flowing current can be written as:

$$\mathrm{i} = \frac{\mathrm{q v_d}}{\mathrm{d}} \tag{3.2}$$

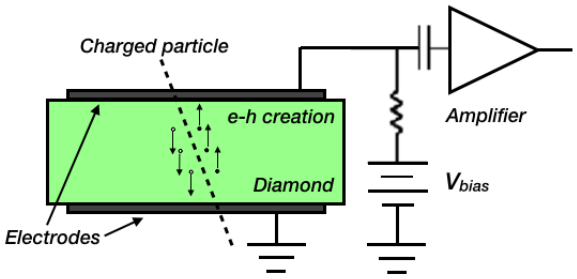

Figure 3.3: Working principle of a diamond detector.

where v_d is the drift velocity and d is the distance between the electrodes. It is important to remark that it is not required that a charge reaches the electrodes to measure an electric signal. In fact, a moving charge induces a current before being trapped in the material.
The drift velocity is proportional to the local electric field E with a coefficient named mobility μ:

$$v_d = \mu E \tag{3.3}$$

Different mobility values for electrons and holes can be found in literature, determined from the types of diamonds, with a mild dependence on the electric field. Typically, the electron mobility in a CVD diamond is 2200 $cm^2V^{-1}s^{-1}$ and for the holes is 1600 cm^2V^{-1} [117] [118]. A minimum ionizing particle (m.i.p) that crosses the diamond material generates about 36 electron–hole pairs per μm of effective path, than the total charge q_g generated in a diamond detector by a perpendicular m.i.p. can be written as [119]:

$$q_g = 36\ e^-h/\mu m \cdot d \cdot q_e \tag{3.4}$$

where d is the diamond thickness and q_e the elementary charge.
If the charges generated in the bulk are for some reasons trapped by the material impurities or defects, their mean free path (λ) can be <<d, i.e. the travelled distance will be much lower than d and the observed charge q_o, defined by the time integral of the induced current, can be written as:

$$q_o = q_g \frac{CCD}{d}. \tag{3.5}$$

where CCD is the so called Charge Collection Distance, an important figure of merit of the diamond material to be used as detector.
In particular, the CCD can be written as follows:

$$CCD\ [\mu m] = d\frac{q_o}{q_g} = \frac{q_o}{q_e\ 36\ e^-h/\mu m}. \tag{3.6}$$

The mean free path and CCD coincide in a pad detector, while they can differ in a segmented one because the mean free path is a local property which depends ultimately by the electric field. The definition of the CCD is more general and preferable to describe the charge collection property of a diamond detector. By definition the CCD is lower than the diamond thickness; the manufacturing process is optimized aiming at CCD values as high as the thickness. However, the grain boundaries in polycristalline diamond reduce the CCD, since they introduce traps, and limit the uniformity of charge collection as a consequence of non-uniform electric fields in the material. A strategy, used by the manufactures, is to growth the material very slowly and up to a thickness much bigger than d. In this way, the material can be lapped to the desired thickness d by removing a large fraction of the substrate side, where the crystal grains are smaller and the bulk quality much worse.

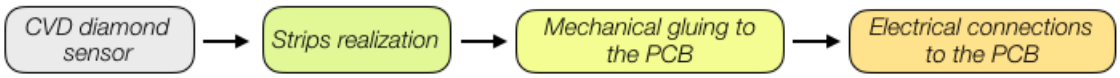

Figure 3.4: The manufacturing chain to build a diamond detector: the realization of the electrodes, the mechanical connections and, at last, the electrical connections.

3.1.4 Application in high energy physics

The diamond detectors used for high energy physics are built with quite simple geometry of the electrodes, like pad, strips and pixels. During the last years they have been used specially as beam monitors and luminometers because the high radiation hardness makes the diamond detectors suitable to be placed near the interaction region. RD42 is a big collaboration that has been working on the development of diamond detectors for high energy physics over the past 20 years [120]. The use of those detectors as beam monitors in the ATLAS experiment is one of the achievement of the RD42 studies [121]. During these years, all the LHC experiments used diamond as sensor material for beam monitors with the aim of background estimation or luminosity measurements [122]. This promising material was used also for the Beam Condition Monitor (BCM) of the Babar experiment at the Stanford Linear Accelerator Center (SLAC)[123] and of the CDF experiment at the Fermilab Tevatron[124].

3.2 PADME diamond detector

At University of Salento and INFN section of Lecce, I realized two diamond detectors to be used as active target of PADME. The two detectors are double-sided strip poly-crystalline diamond sensors 100 μm thick, of area 2×2 cm^2. The first one was realized with innovative laser made graphitic electrodes, never used in high energy physics experiment, and the second one with Cr-Au electrodes. The polycrystalline diamond sensors were produced by Applied Diamond Inc. (USA)[125].
The realization steps of the detectors follow the chain sketched in Figure 3.4. The first step was the fabrication of the ohmic electrodes on the bare CVD diamond film, followed by the mechanical gluing and the electrical connections to a printed circuit board named carrier board. The graphitc strips were realized in the L3 Laser laboratory of Lecce, while the more traditional metal contacts were made by thermal evaporation of Cr and Au layers directly from Applied Diamond. The mechanical connections were realized in Lecce, while the electrical connections were realized half in Lecce, the view interconnected with conductive glue, and half at the INFN section of Perugia, the view interconnected with wire bonding.
The two detectors are named D1Graph100_2017 and D1CrAu100_2017, where D stands for diamond, 1 because they are the first of that type, Graph or CrAu is the technology used for the strips, 100 the thickness in μm and 2017 the year of the fabrication.

3.2.1 Strip electrodes fabrication

Ohmic contacts on the diamond surface play a key role in the overall device performance; the processes followed to realize them are described in the following paragraphs.

Metal contacts

Metal contacts on diamond are traditionally realized through litographic processes. Diamond metallization process usually involves three different metals [126]. The first stage is the deposition of a layer of refractory metal (e.g. Ti, Mo, W, Cr, and T) by evaporation or sputtering. This operation helps to create a ohmic contact on diamond thanks to the formation of a carbide layer, that guarantees also a better adherence for the next metal layers. For this reason, the metal used for the first stage is also called carbide-former. Afterwards, a barrier, mainly composed of palladium or platinum, is applied to minimize the mixing of the chemically active bonding layer with the final metal layer. Finally, an Au or Ag layer is applied, in order to facilitate the electrical connection. The standard metallization of the Applied Diamond is Titanium (1 A), Platinum (1 A), Gold (10 A) but often the carbide-former is Cr because can be thermally evaporated. In fact, as previously mentioned, the Applied Diamond provided a diamond sensor with Cr-Au metal ohmic contacts ready to be interconnected to the carrier board.

Graphitic strips

The metal contacts process requires several steps and sometimes the mechanical adhesion could be poor.
During the last years, laser made graphitic strips, that could act as ohmic contact on diamond, turned out to be a valid alternative to the traditional metal contacts. These contacts are strongly adherent to the surface because chemically bounded with the diamond film. Diamond and graphite are different allotropic forms of carbon, showing very different physical characteristics that arise from the different chemical bonds between the carbon atoms. The graphitization of the sp^3 bonds occurs when the carbon atom received enough energy to overtake the diffusion jump, changing the bounds into sp^2, more stable at atmospheric conditions. The result is the increase of the mean distance between adjacent carbon atoms, with smaller binding energy. It is known from literature that when a laser radiation with proper wavelength and energy density values hits a diamond, the localized heating, induced by electron thermalization, could enable the diamond-graphite transition, overtaking the potential barrier ($T > Tg \approx 700°C$) [127]. The laser graphitization process allows to create in this way ohmic electrodes on the surface of a thin CVD diamond with an electrical conductivity comparable to natural graphite.
During these last years the Lecce group proved that with these electrodes is possible to build efficient and radiation hard detectors [128] [129] [130]. The first diamond detector prototype for PADME with graphitic strips was realized in 2015 and tested, showing good performance [131]. The graphitic strips were realized by means of an excimer laser ArF (λ=193 nm, τ=20 ns) in the L3 Laboratory of Lecce.
The experimental set-up is shown in Figure 3.5 and it is made of:

- an ArF excimer laser with a gas mixture of 50%-50%, from the Lamda Physik Lasertecnik, model LPX305i;
- a square metallic mask, an attenuator, a pin hole and a 15X optical system to focus the beam, choose its size and adjust its energy;
- a target holder connected to a micrometric PI positioning system, remotely controlled by a LabView software, to allow an X and Y displacement in the plane orthogonal to the beam;
- a USB CCD camera to monitor in real time the graphitization process;
- a PC to control and monitor the automatized laser writing, by LabView software.

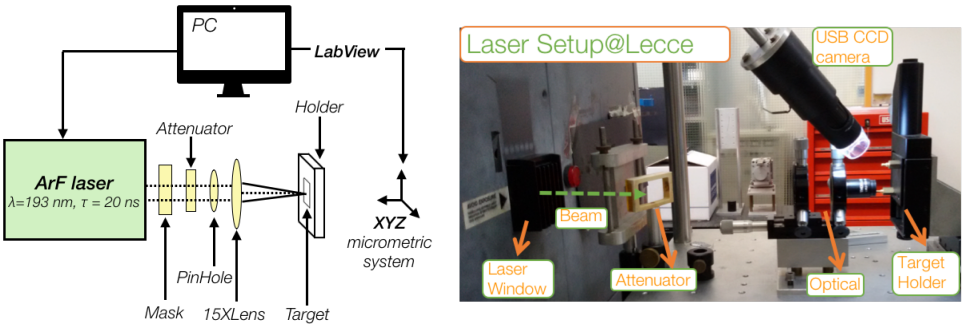

Figure 3.5: Laser graphitisation set-up: the beam comes out from the laser window, meeting first a mask and a attenuator, then a pinhole (not showed in the picture on the right), then the optical made of a 15X lens. The beam laser arrives then to the diamond on the holder.

The CVD diamond was fasten to the holder using a copper tape with the surface perpendicular to the beam direction. On the holder surface a square of 2×2 cm^2 has been engraved to align the CVD diamond sides with the X and Y scanning axis. The holder allowed to keep the target in the required position during laser graphitization and the micrometric system allowed the movement along the X and Y direction. The laser beam crossed firstly a metallic frame, having a square hole of area 1×1 cm^2, and, immediately after, an energy attenuator made of a semi-reflective mirror, which allowed to choose the proper beam energy, adjusting the beam incident angle. Hence, a pinhole of 2 mm was placed to fix the beam size to the wanted value and, at last, 15X lens to reduce the beam spot size to about hundred microns on the focal plane where the holder is placed.
A remote control system displaced the holder during the whole graphitization process. The motors movements were controlled through the LabView software and synchronized with the laser trigger, in order to laser-write the desired strip pattern. The X and Y strip patterns were the same; in order to have orthogonal strips, the sensor, after the conclusion of the first side, was rotated by π, with respect to the Y axis and then rotated by $\pi/2$, around the X axis. Every strip was fabricated by 10 microstrips, displaced by 100 μm, skipping the first one, etching the other 8 and skipping the last one (Figure 3.6).
The diameter of the graphitization spot was 150 μm, so the 8 etched microstrips overlap to each other for about 25 μm. Each strip is 850 μm wide and 1.9 cm long, with a 150 μm gap between strips; the X and Y patterns are shown in Figure 3.6. The maximum energy of the laser beam was 500 mJ, with a 10 Hz repetition rate. The laser beam energy was measured using a Joulemeter Gentec ED-500. The Joulemeter gave a voltage measurement, converted into energy applying the constant conversion factor of 3.05 V/J. The measured voltage just before the process was about 300 mV which corresponds to about 100 mJ energy.
Before turning on the laser, the beam spot position on the diamond was determined by a overlapping red laser pointer. The four diamond corners were taken as reference points in the (X, Y) plane, as shown in Figure 3.7. Using this coordinate frame the diamond area was completely scanned by 200 microstrips. The first five and the last five microstrips were not etched and the etched microstrips were 19 mm long to avoid the borders. The etched microstrips were passed two times, up and down with the laser on. In Figure 3.8 two pictures taken during the realization of the strips are shown.

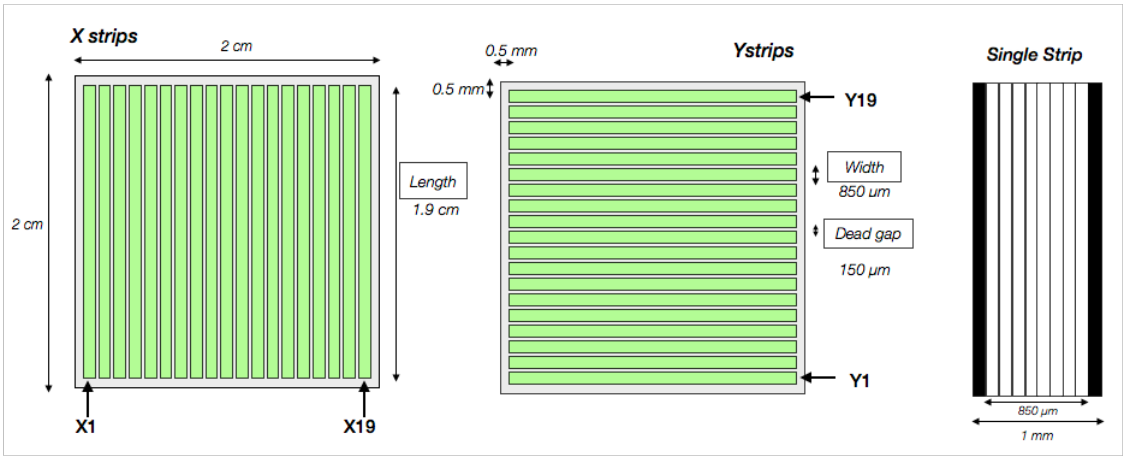

Figure 3.6: The X (left) and Y (center) strip graphitization pattern. On the right is shown a single graphitized strip made of 8 microstrips, with the first and the tenth microstrip skipped, to leave a gap between adjacent strips.

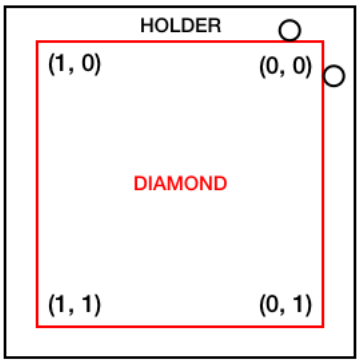

Figure 3.7: The four diamond corners taken as reference points in the graphitization plane.

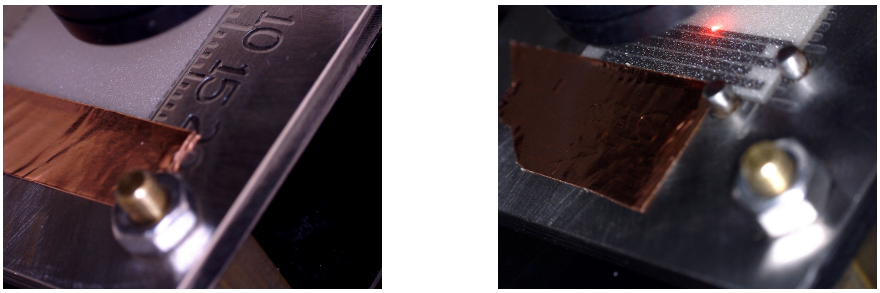

Figure 3.8: On the left the CVD diamond on the holder, before the graphitization, aligned with an engraved square and stopped by a copper tape. On the right the CVD diamond during the graphitization process, with a staggered strip pattern not used for PADME.

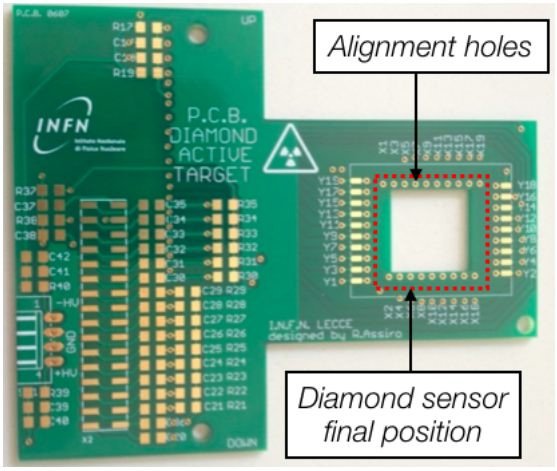

Figure 3.9: Carrier board before gluing the diamond sensor. In the picture the final location of the diamond sensor is shown, together with the metal plated used for the diamond alignment during mechanical connection.

3.2.2 Mechanical connections

The two thin diamonds were precisely fixed on their own printed circuit board (carrier board), above a 1.5 × 1.5 cm^2 hole (Figure 3.9). Several tests with dummy sensors, made of copper or glass, were done, in order to choose the best gluing procedure to apply to the real sensor. In particular, the tests performed using glass slides helped to understand the lateral spread of the glue spots and the final planarity of the sensor. The gluing procedure made use of a thick plexiglass plate, screwed on a micrometric rotational stage, a vacuum pen with a suction cup, connected to a vacuum pump and mechanically attached to a shaft free to move in the vertical direction thanks to a wheel, a USB camera and a Nordon Performus III glue dispenser system. Before gluing, each diamond was cleaned with isopropyl alcohol, followed by an ethanol bath and 15 additional minutes of ultrasonic bath.
The final procedure was composed of several steps, summarised as follows:

- fix the carrier board on the plexiglass plate with screws;
- place by a manual pick-up tool the diamond with the polished side face up on the carrier board, as much as possible in the final position;
- lower the vacuum pen by the manual wheel and pick up the diamond sensor;

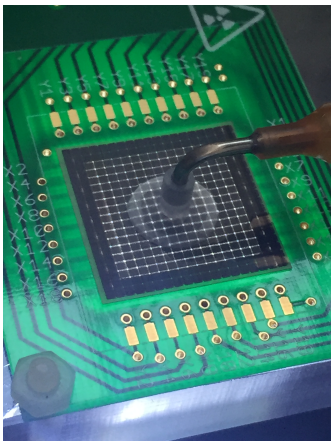

Figure 3.10: Diamond target during the mechanical connection.

- lift the diamond up at a maximum height of 1-2 mm in order to align the carrier board relatively to the diamond strips using the rotational stage and the USB microscope, placed underneath the plexiglass plate. The metal plated holes were used for the alignment of the strips (shown in Figure 3.9);
- remove the plexiglass plate from the rotational stage, keeping the diamond sensor with the suction cup floating in the air;
- deposit eight glue spots on the left and on the right sides of the carrier board hole using the glue dispenser. The type (smoothflow tapered tip) and dimension (0.2 mm diameter) of the syringe was chosen to avoid the spread out of the redundant glue. This step is important because a bad glue deposit could alter the final planarity of the sensor. The bi-component Araldite glue AY 103-1 mixed up with a hardener HY 991(60-40) was chosen for the D1Graf100_2017 sensor and the bi-component Araldite 2011 glue (50-50) was chosen for the D1CrAu100_2017;
- screw back the plexiglass plate on the rotational stage;
- lower the diamond with the vacuum pen, until it reaches the carrier board surface;
- check the alignment of the strips with respect to the carrier board metal plated holes for correct later electrical connections;
- leave the diamond under the suction pressure for at least 24 hours to allow the glue drying.

Each step of the gluing must be done carefully because it is irreversible; in case of errors, the diamond is impossible to remove without breaking it.
In Figure 3.11 two pictures taken during the mechanical connection using the USB camera shows the strips alignment with respect to the carrier board.

3.2.3 Electrical connections

Each diamond sensor was glued on the carrier board with the horizontal strips (Y strips) face up and the vertical strips (X strips) face down in contact with the metal plated holes. Once the mechanical connection of the two detectors was performed, including the curing of the glue, the detectors were ready to be electrically connected. The carrier board provides the high voltage to each strips and the AC coupled input signals to the front-end electronics. Two different

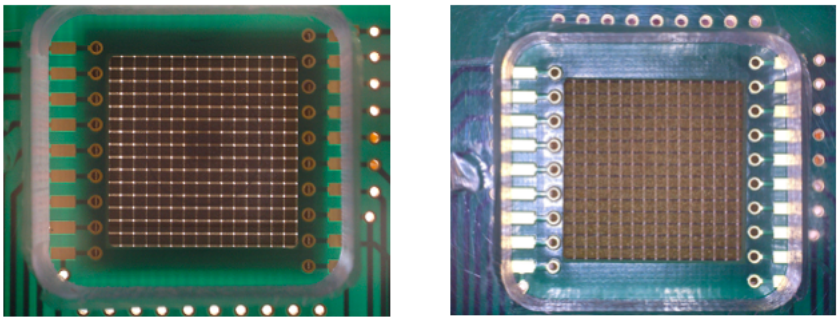

Figure 3.11: The strip alignment during the mechanical connection of the diamond with graphitic strips (left) and metallic strips (right). In the left picture it is also visible the shadow of the suction cup.

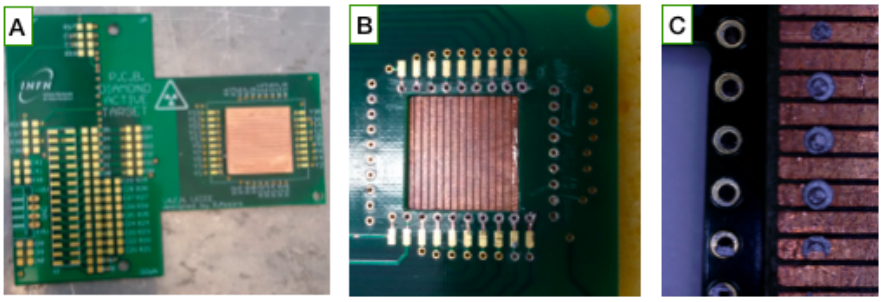

Figure 3.12: A dummy copper sensor with strips glued on the carrier board after the alignment. A) Top view, B) bottom view, C) residual conductive glue spots on the dummy copper sensor strips after the removal.

techniques for the electrical connections were implemented: for the X strips the connections were realized using a conductive glue, for the Y strips the wire bonding technique was exploited.

Electrical connections by conductive glue

The electrical connections were first realized for the X strips, injecting conductive glue from the metal plated holes from the carrier board back. To do that the carrier board with the diamond sensor above was screwed upside down on a metal plate, with a vertical gap of about 2 cm. The gap was filled with a sponge in order to support the diamond sensor during the interconnection of X strips. For this reason, the X strips were the first to be connected: the glue filling after the Y strips wire bonding would have been dangerous for the wires. Several tests were performed using dummy copper sensors with strips realized on both surfaces, to emulate as much as possible the real sensor. In this way during each test was possible to select the better way to fill the holes with the conductive glue, choosing also the ideal volume and the temperature of the glue drops. In Figure 3.12 the steps of the performed tests with the dummy sensor are shown: first the detector was mechanically connected to the carrier board (Figure 3.12 a), then the X strips were electrically connected from the back with the glue drops (Figure 3.12 b). After each hole was filled, the electric contact was checked using a Ohm-meter. The glue drop had to remain inside the strip width, to avoid short circuits of adjacent strips. In Figure 3.12 c the residual conductive glue spots on the dummy sensor are shown, after the removal from the carrier board. The chosen conductive glue was the EPoxy 3025 [132]. It was previously warmed up to reduce

Physical Properties	3025
Color	Silver
Specific Gravity	2.12
Viscosity, 25ºC	Paste
Work life mixed, 20 grams, 25ºC	4-6 hours
Shelf Life, 25ºC	12 months

Technical Properties	3025
Volume Resistivity, ohm-cm	
25ºC cure	0.040
65ºC cure	0.004
Lap Shear Tensile Strength	
ASTM D-1002, 25ºC, psi	
Aluminum to Aluminum	2,000
Butt Tensile Strength, Modified	
ASTM D-429, 25ºC, psi	
Brass to Brass	2,500
Hardness, Shore D	
Operating Temperature	150ºC
Thermal Conductivity	$36x10^{-6}$in/in/ºC

Cure Schedule	3025
25°C	24-36 h
65°C	4 h
100°C	15 min

Figure 3.13: Properties of the Epoxy 3025 used for the electrical connection. In particular, it is interesting to underline that a previous heating of the glue can reduce the curing time scheduled.

the viscosity and also the curing time. The glue properties are reported in Figure 3.13. The metal plated holes of the carrier board were hand-filled with glue drops using a syringe with two different tips of the same diameter: the first one, having a 45 degree angle, was used to put the glue in the hole; the second one having a straight tip, was used to push the glue drop further down inside the hole, in order to touch the strip surface and create the contact. The electric resistance between the carrier board pad and the corresponding strip was monitored during the operation, in order to achieve the desired value of about 2-3 kΩ, for the graphitic strips (dominated by the strip resistance), and a few Ohms, for the metallic strips (dominated by the glue electrical connection). After the correct filling of the hole the electrical isolation between the connected strip and the two adjacent strips was also checked and it turned-out to be 20 MΩ (due to the interstrip electrical isolation). In Table 3.1 the measured electrical resistance values of the strips for the D1Graf100_2017 sensor are reported for measurements taken in two different days, showing a mean electric resistance of about 2.5 kΩ.

Electrical connections by wire bonding

The electrical connections of the Y strips were realized by wire bonding between the golden plated Y pads of the carrier board and the related diamond sensor Y strips. Wire bonding is a standard interconnection technique used for electrically connecting microchips to the terminals of a chip package or directly to a substrate [133]. Among all other techniques, the ultrasonic wire bonding (UWB) is fast, showing good performance, good heat conductivity and good corrosion resistance [134]. In High Energy Physics (HEP) applications, ultrasonic (US) wedge bonding is the predominant method, as it does not require any substrate heating and therefore is very versatile. It is based on the combination of force and ultrasonic power applied during several steps, as shown in Figure 3.14. The bond wire is firstly positioned onto the bond pad of the die, package or board, by the wire bonder tool. Hence, it is pressed on the surface and ultrasonic energy is applied for a set time, to create the first *wedge* [135]. Subsequently, the bonding tool is moved to the target pad site and the second *wedge* is made. As last step, the wire clamp is closed and the wire is break, pulling back the wedge tool. The remaining bond wire forms a small tail ready for the next wire bond. It is important to make the wire loop along a straight

Strip	R1 [kΩ]	R2 [kΩ]
X1	-	-
X2	-	-
X3	3	3.2
X4	1.5	2.5
X5	1.4	2
X6	1.38	2.2
X7	1	3
X8	1.33	2.2
X9	1.5	3
X10	1.5	2.6
X11	1.58	3.3
X12	1.47	2.4
X13	1.64	3.3
X14	1.5	2.5
X15	1.54	3.2
X16	1.6	2.8
X17	2.3	3.2
X18	-	-
X19	-	-

Table 3.1: Electrical resistance values measured in two different days after the electrical connection of the X strips for the detector with graphitics strips. The resistance measurement could not be performed for those strips covered by the carrier board hole borders.

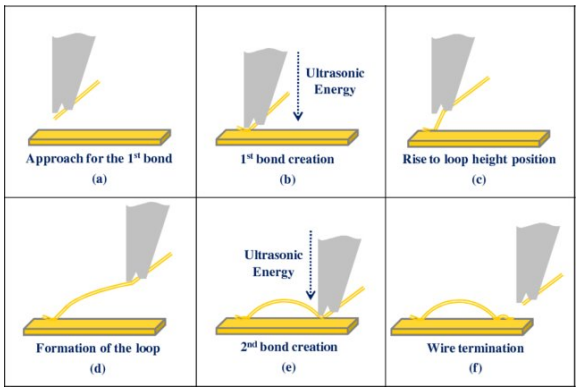

Figure 3.14: Wire bonding steps of the ultrasonic wedge bonding.

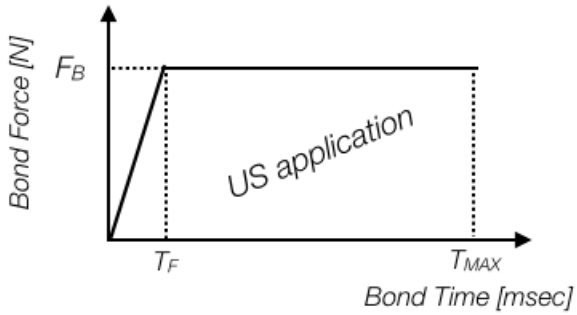

Figure 3.15: Applied force as a function of time for a typical wire bonding machine. The force is applied for a time T_F until the desired force value is reached, followed by the ultrasonic application that lasts until the set time (T_{MAX}).

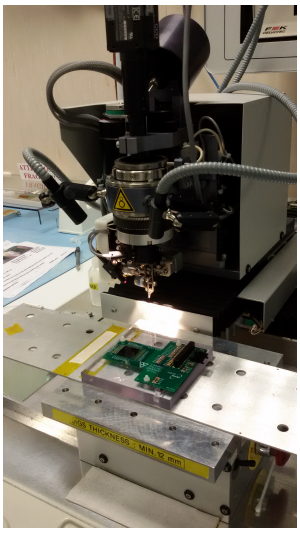

Figure 3.16: Wire bonding machine Delvotec 6320 used to electrically connect the Y strips; the detector is placed on the plexiglass handling plate.

line, to minimise potential weakness and defects. The application of the force to realize the bond usually lasts a few μs, then the ultrasonic energy is applied for a pre-set time, as seen in Figure 3.15. The pre-set time could vary depending on bond conditions and construction. The bond time, the energy and the force are programmable to optimize the results for a given material.
For both detectors the wire bonding was realized at the INFN section of Perugia by means of a ultrasonic wire bonding machine Delvotec 6320 [136](Figure 3.16). The ultrasonic bonding on graphite is not common, and probably never done before. For this reason preliminary tests to tune the wire bonding machine parameters were performed using a spare inner board equal to the real one and a small piece of thermal diamond.
The material chosen for the wires was Aluminium with 1% of Silicon, of medium hardness, with a diameter of 25 μm. The positioning of the wire bonding tool had a minimal step, of 2.5 μm. The wire bonder camera on the machine helped to monitor the operations during the bond. Frequencies between 40 kHz and 160 kHz are usually used for the ultrasonic power, with a clear preponderance of lower frequencies around 60 kHz for thick wires and higher frequencies (100 and 140 kHz) for thin wires. The set bond time was 100 ms and the measured frequency was

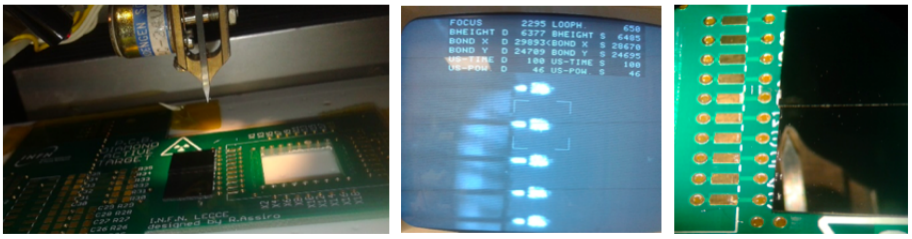

Figure 3.17: First bonding tests performed on a small piece of thermal diamond.

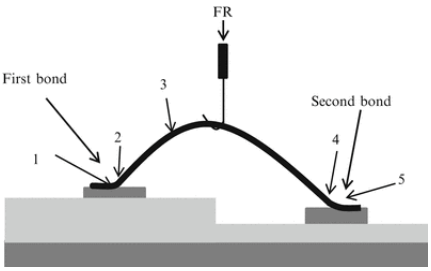

Figure 3.18: Pull test to evaluate the wire bonding strength applying an upward force (FR) under the wire using a hook and pulling the wire away from the die. The ideal breaking point (3) is located in the middle between the first and the second bond.

104.615 Hz. These parameters were set on the wire bonding machine. The first bonding test was performed choosing the diamond for the first bond and the carrier board golden pad for the second bond. The bond was impossible with the ultrasonic power in the range of 35-75 digits, range used for usual printed circuit board golden plated pads. Instead, starting from the golden pad and then moving to the diamond with a ultrasonic power of 46 digits both bonds were successful. The bond strength is in general dependent by many variables, such as ultrasonic power, applied force, welding time, bond pad surface hardness and roughness, and interface temperature. The wire-bond quality can be evaluated either with visual and mechanical testing [137]. The most common test to ensure the strength and the quality of the bond is the wire pull test, where a wire bond is pulled upward (perpendicular to the substrate) by a hook, until there is either a bond failure or a wire break, as shown in Figure 3.18. The pull test provides a value of the pull force that is correlated to the mechanical strength of the bond [138]. The destructive bond pull test defines the minimum force required to break the bond, instead the non-destructive test leaves the wire intact. The first method was used to understand the strength of the wire bonding realized on thermal diamond. The test showed an average destructive force of 4.6 g,[1] with a large standard deviation of 3.88 g, which suggests that the substrate is not uniform. The pull test of a bond between carrier board golden pad and the metallic strip gave a destructive force of 16 g, for the graphitic strip the destructive force value was lower, of about 10 g. These values were bigger than the set force to perform the bond (5-7 g). Similar but different ultrasonic power was set for the two detectors, as shown in Table 3.2. The wire bonding did not succeed always the first time: some bonds needed to be repeated. The number of failed bondings for D1Graph100_2017 is shown in table 3.3. For the strips not mentioned in the list, the bonding succeeded the first time. Four wire bonds per strip were realized for redundancy in case of failure caused by ageing (Figure 3.19).

[1] A gram-force is the most common unit of measure for the pull tests, it corresponds to 9.8 mN.

	Ultrasonic power [digit]	Force [g]	Bond Time [msec]
D1Graf100_2017	48/50	5/7	100
D1CrAu100_2017	48/46-48	5/7	100

Table 3.2: Wire bonding machine parameters set for D1Graph100_2017 and D1CrAu100_2017. The US Power value is written for both the bond on the strip and on the carrier board golden pad.

Strip	Y1	Y2	Y4	Y7	Y11	Y13	Y18
no. failed attempts	1	1	2	1	3	3	1

Table 3.3: The number of failed wire bondings during the wire bonding of the D1Graph100_2017 sensor.

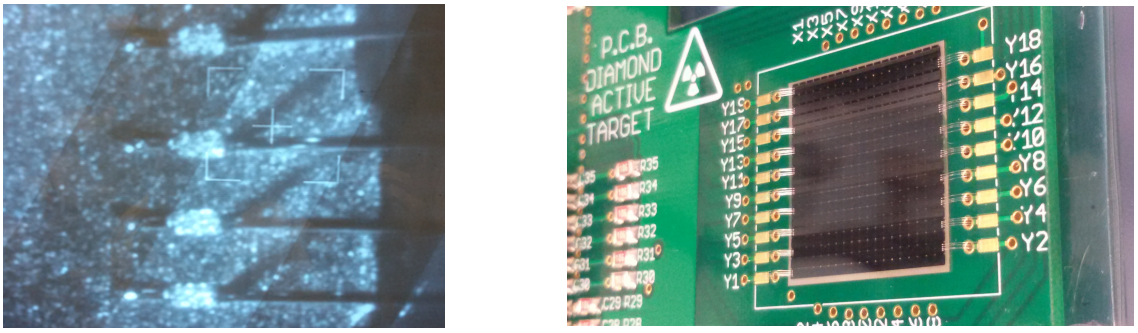

Figure 3.19: On the left the four wire bondings realized for each strip, as seen by the wire bonder camera. On the right the D1Graph100_2017 detector after wire bonding. Each strip was connected electrically using four wire bondings.

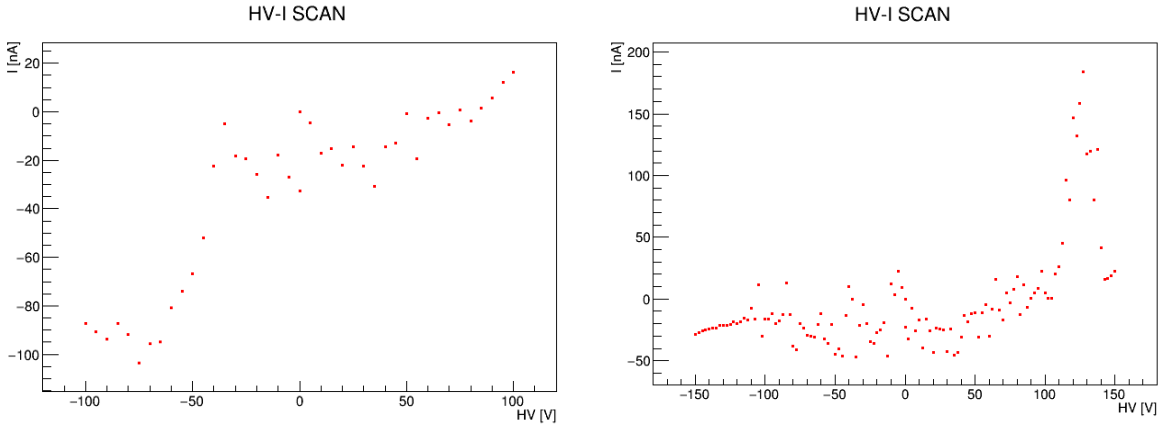

Figure 3.20: HV scan performed to evaluate the current absorption of the diamond detector with metallic CrAu strips after wire bonding.

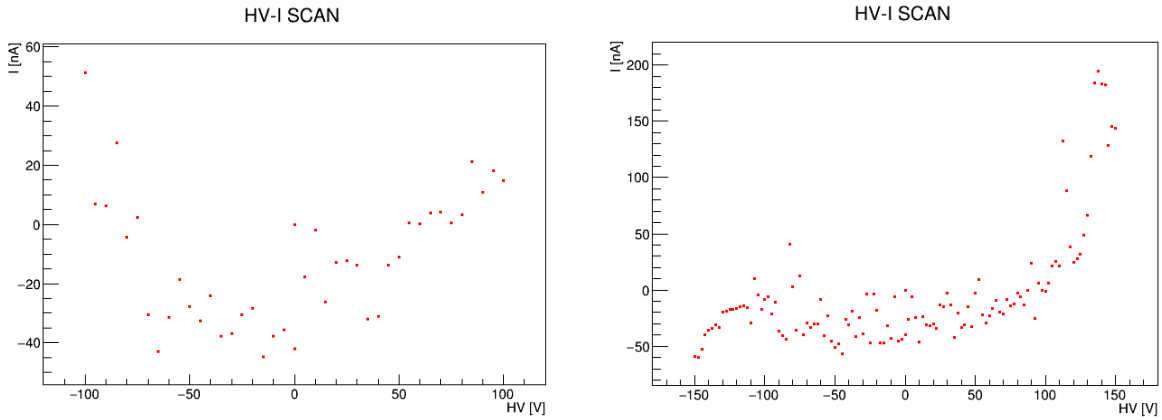

Figure 3.21: HV scan performed to evaluate the current absorption of the diamond detector with graphitic strips after wire bonding.

3.2.4 High voltage test

After the inter-connection of the two detectors a high voltage scan was performed in two different days to measure the leakage current and verify if the sensor could sustain the high voltage. The tests were performed using a high voltage generator Keithley 237 [139]. The first day the scan was performed from -100 to 100 V, the second day from -150 to 150 V. Both the detectors held the high voltage up to 150 V with a measured leakage current less than 200 nA, as shown in Figures 3.20 and 3.21.

3.3 The Front-End electronics

Like every solid state detectors, also for diamond detector, the signal of the charge collected must be amplified with low noise Front-End (FE) electronics. The current signal can be integrated by a charge amplifier, generating a voltage signal proportional to the injected charge.

3.3.1 The AMADEUS chip

The chosen front-end electronics for the PADME diamond detector consisted of two evaluation boards EVAL7048 of the IDE1180 (AMADEUS) chip made by IDEAS (Oslo) [140]. The chip

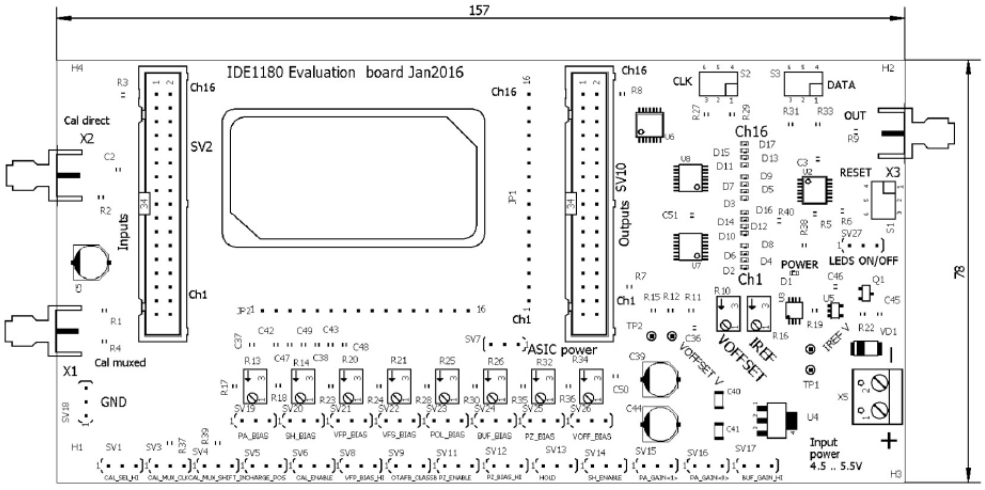

Figure 3.22: Drawing of the Amadeus Chip evaluation board.

IDE1180 contains 16 charge sensitive pre-amplifiers (CSA), of 20-40 ns adjustable shaping time and about 1100 e^-+68 e^-/pF equivalent-input-charge noise, providing 16 analog independent outputs. A drawing of the evaluation board is shown in Figure 3.22. On the left there are the signal input pins and on the right the signal output pins. The line of jumpers on the bottom allows to change some global parameter settings. The allowed charge amplifier gain values are 3-6-12-24 mV/fC; for the data taking it was set at 3 mV/fC. Some hardware changes were performed on the board in order to fit in the vacuum cross. All SMA connectors on the left were replaced by pairs of pins to reduce the encumbrance. Also the Clock, the Data and the Reset buttons were replaced by pins, needed for the calibration of the front-end, as explained in Section 3.5.2. Finally, the input signal connector was removed from the top side and replaced with a row 16 pins long on the bottom side.

3.3.2 Connection with the front-end electronics

The interconnection with the front-end electronics was performed by sandwiching the carrier board between the two front-end boards. In fact, the carrier board has two multi-pin connectors on both sides which match exactly the rows of 16 pins placed on the back of the two front-end boards. The carrier board is secured mechanically by two 3M plastic screws to the front-end board and to the aluminium support.
Sixteen strips (from strip 2 up to strip 17) out of nineteen per view were AC coupled to the charge sensitive amplifiers, with the others (strip 1, 18, and 19) just connected to the high voltage. The X strips were connected to the High Voltage, while the Y to ground. The multi-pin connector on the front side of the inner board corresponds to the X strips, which are face-down, while multi-pin connector on the back side corresponds to the Y strips, which are face up. The pin number does not follow the strip number; each connection was verified by a multimeter (see Figure 3.23).
The diamond target had to be put in the center of a vacuum cross, to intercept the beam just before the magnet, as shown in the layout of the experiment in Section 2.2. The carrier board and the two front-end boards were hold to a precise machined aluminium structure, rigidly connected to a flange by two M6 metallic screws. The electrical services, the control signals and the output signals were routed outside the vacuum through a 50-pins vacuum feed-through

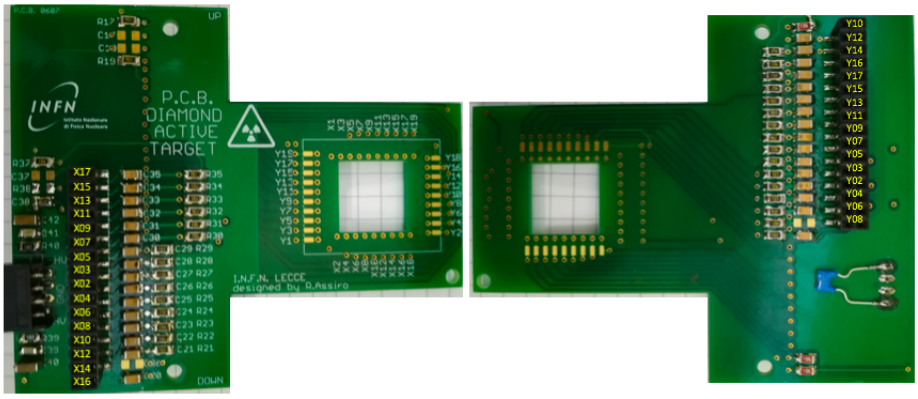

Figure 3.23: Populated inner board front side (left) and back side (right). On the pictures, the strip numbers are written near the corresponding output pins.

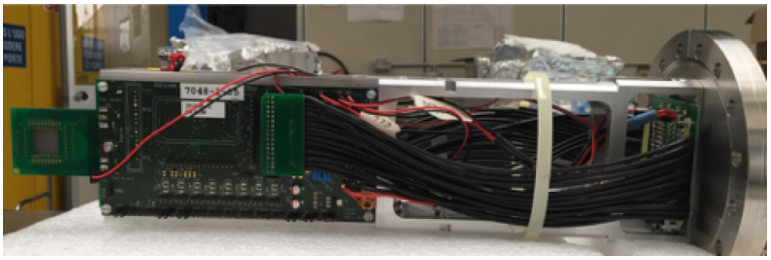

Figure 3.24: Diamond target before installation in PADME. From the left to the right, the carrier board, one of the two the front-end board, the aluminium support and the flange.

connector placed on the flange. A picture of the diamond target with the front-end electronics before the insertion in the experiment is shown in Figure 3.24. The upstream board reads the Y strips, while the downstream board reads the X strips.
Before installation, preliminary tests were performed to measure the final temperature reached by the front-end boards in vacuum. The boards, rigidly connected to the final mechanical structure, was turned-on in vacuum with a pressure of 10^{-6} mbar, to verify that the heat produced by the power dissipation was efficiently removed by the thermal path existing between the inner board and the aluminium structure. An external infra-red thermal camera, through a ZnSe window transparent to thermal radiation, monitored the map of the temperature. The highest temperature was observed at the location of the voltage regulator, which reached 36°C in vacuum (stable over 3 h), with a time constant of about 45 s, with an external temperature of 25°C.

3.4 The installation in PADME

The diamond target with all the instrumentations were moved at the LNF in June 2018 to be prepared for installation. The target was held in position inside a 10 cm diameter vacuum cross by a precisely machined aluminium frame fixed to a vacuum flange. The flange could be moved horizontally by a motorized system and a vacuum bellows. The active diamond target and the pixel detector called MIMOSA were mounted on the two opposite sides of the vacuum cross by two identical linear positioning systems, as can be seen in Figure 3.26. The positioning systems consist of two flanges connected by a bellows and a step motor. One flange is rigidly connected

Figure 3.25: On the left the connectors that allow the connection with the instrumentation. On the right the 50 pins connector matching the 50 pins feed-through connector of the flange. The 32 output signal cables connected to the digitizer are also visible on the right.

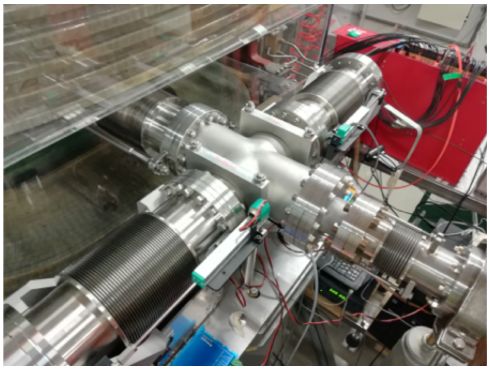

Figure 3.26: The vacuum cross, just before the PADME magnet. The beam comes from the right. The bellows on the right hosts the target, the other one hosts MIMOSA.

to the vacumm cross flange and the other to the detectors. The step motor can adjust the x distance between the two flanges and the position of the two detectors with respect to the center of the vacuum cross. Several tests were performed to measure the maximum horizontal displacement allowed of the two detectors to avoid any mechanical clashes. In Figure 3.27 the target and MIMOSA inside the vacuum cross are shown, together with the mechanical rulers indicating the real position of the corresponding flanges. A mechanical stop was inserted to fix the maximum displacement of the target and to avoid clashes with MIMOSA fully inserted in the vacuum cross. The center of the target and of the MIMOSA sensor were at the center of the vacuum cross when the rulers marked 5.2 mm and 9.5 mm, respectively. In Figure 3.27 the two detectors are shown out of the vacuum cross center when the rulers marked 0 cm. The details of the motor operation are explained in section 3.4.1.
All the diamond target instrumentations were placed nearby the cross. In Figure 3.25 the carrier board adapter, needed to interface the instrumentations and the 50-pin connector of the flange, is shown. In particular, a LEMO connector was used for the low voltage power supply (LV), a SMA connector for the pulse generator, a BNC connector for the high voltage power supply (HV) and a 10 pins two rows connectors to control the charge injection in the front-end.

3.4.1 The linear motion system

The movements of the target and MIMOSA were made possible thanks to two stepper motors ST6018K2008 with the windings connected in series and controlled by two motor drivers SMCI47S-3 from NanoCan (as shown in Figure 3.30). The motors set-up is shown in Figure 3.29. USB-CAN adapters IXAAT, compact V2, were used to connect the motor drivers to the PC.

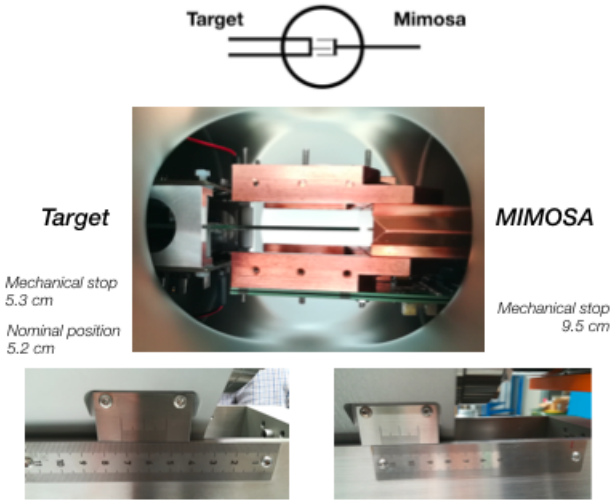

Figure 3.27: Top view of target and MIMOSA in the center of the vacuum cross (the two upper pictures) and the rulers of the corresponding flanges (the two lower pictures).

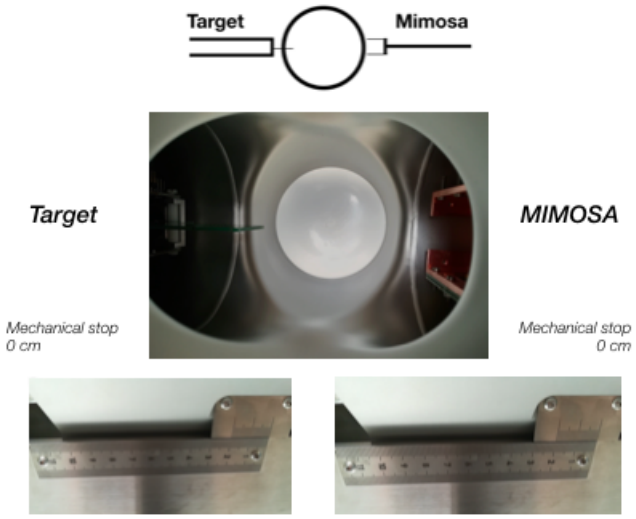

Figure 3.28: The same as Figure 3.27 but with target and MIMOSA out of the vacuum cross.

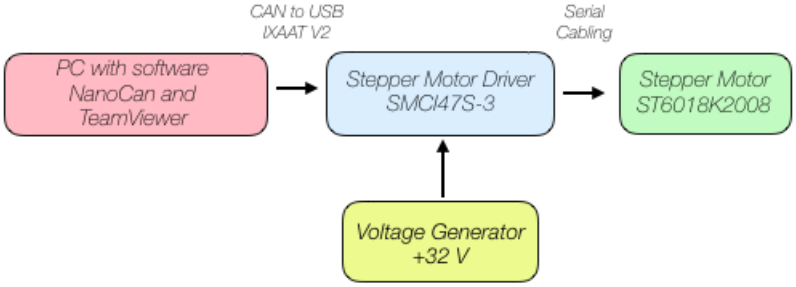

Figure 3.29: Block diagram of the motor control system used for the displacement of the target and MIMOSA.

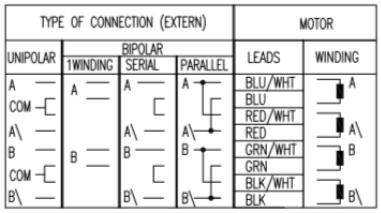

Figure 3.30: The wiring schema of the driver on the right and the corresponding motor winding connections on the left. In PADME the serial motor winding connection was chosen.

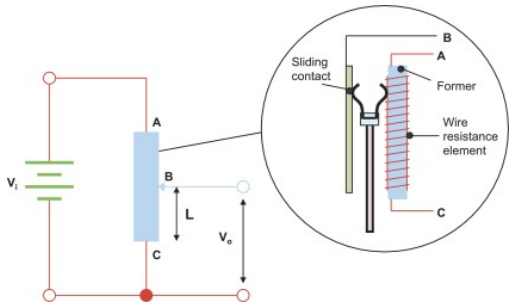

Figure 3.31: Drawing of a linear potentiometric transducer [142].

CANopen standard connectors were used to make cables suitable to connect USB-CAN adapters and motors. Both the drivers were powered with a 32 V voltage generator. Team Viewer on a Windows PC placed in the experimental hall allowed to remotely control the motors by NanoCan software. A minimum movement of 1 μm was allowed. A USB camera connected to a Raspberry monitored constantly the detector position by visualizing the target ruler. In addition, two linear displacement transducers Gefran [141] were fixed on the walls of each bellows to give a more precise feedback of the detectors positions. Linear potentiometers can give a fast position feedback and are also efficient and cheap. A potentiometer is a resistive-type transducer which allows the conversion of a linear displacement in a output voltage by moving a sliding contact along the surface of a resistive element [142] (3.31). Each potentiometer was supplied with a constant current of 3 mA; measuring the output voltage of the potentiometer, it is possible to calculate the X position of the target and MIMOSA, after a proper calibration. In Figure 3.26 it is possible to see the two potentiometers installed in the experiment. The useful electrical stroke of the target potentiometer was 75 mm, as the maximum displacement was 5.3 cm. For MIMOSA a longer potentiometer was chosen, with a 100 mm electrical stroke, to allow a displacement of 9.5 cm. The potentiometers were calibrated moving each detector of known steps and storing voltage and current values. At each step the electrical resistance is measured and associated to the corresponding x displacement. An example of calibration is shown in Figure 3.32, which was done moving the target out of the beam and in the beam. The two curves are fit with linear functions and the fit parameters are used by the target Detector Control System to compute the position and send it to the monitor (see Section 4.3.2).

3.5 Diamond detector operation

In September 2018 the active target, with all the front-end electronics, was placed under vacuum in the positron beam line of the Beam Test Facility (BTF) at INFN Laboratori Nazionali di Frascati (LNF) and commissioned with real beam.
The detector chosen as the final one was the D1Graph100_2017, with graphitic strips. In

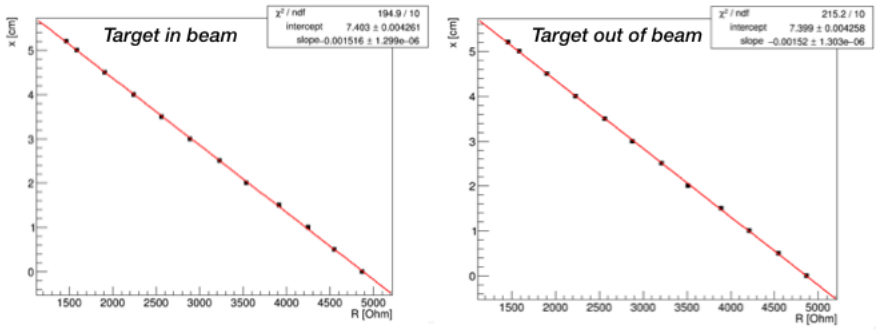

Figure 3.32: X target position marked on the ruler as a function of the measured electrical resistance of the linear transducer. On the left the data correspond to the target entering in the beam; on the right the target was removed from the beam.

Figure 3.33 the mapping of the strips connected to the front-end boards is shown. All 19+19 strips were connected to the high voltage but only 16+16 strips were connected to the front-end, starting from X(Y)2 to X(Y)17. In the same figure the hole of the carrier board is also shown (dashed line). The detector local reference frame (X_{LOC}, Y_{LOC}) follows the strip numbering with the origin (0, 0) corresponding to the diamond down left corner. In this way an integer local coordinate n corresponds to the center of strip n. After installation the local reference frame has the same orientation of PADME reference frame. The central point of the target corresponds to the center of strip X10 and Y10 (X_{LOC}=10 mm and Y_{LOC}=10 mm), or rather (X=0 mm and Y=0 mm) in the PADME frame. The Z position of the target was -1030 mm from the center of the PADME magnet.
After some tests, two strips out of 32 resulted unconnected, probably due to the failure of an electrical contact. The unconnected strips are the X5 and the X17.

3.5.1 Off-line signal reconstruction

An example of the digitized output signal of the target is shown in Figure 3.34. The reconstruction of the target collected charge was performed computing the integral of the signal in a given time window that can be tuned from the target configuration file. For the whole Run 1 the chosen time window was $200 < t < 700$ ns. Thus, the charge collected from a strip can be computed as follows:

$$Q = \frac{1}{G_C}\frac{\int V dt}{R} \tag{3.7}$$

where G_C stands for the adimensional charge gain obtained from the calibration described in section 3.5.2, R=50 Ω is the input termination resistance of the digitizer and dt is equal to 1 ns because the target signal are digitised at 1 GS/s.
The calibration constants are applied to the charge collected thanks to the calibration service of the PADME reconstruction software developed in this thesis. In the experiment a common mode noise was observed on all the output signals. This source of noise was mitigated by subtracting from all signals the first strip not intercepted by the beam. A flag of the software allowed to subtract the common mode noise, improving the resolution on the beam bunch multiplicity.
The target provided the beam profile in both views, X and Y, and an estimate of the number of positrons on target both on-line, during data taking, and off-line, for data analysis. A high voltage scan allowed to choose the working voltage to be applied to the diamond detector. In Figure 3.35 the collected X charge is shown as a function of the applied high voltage. The

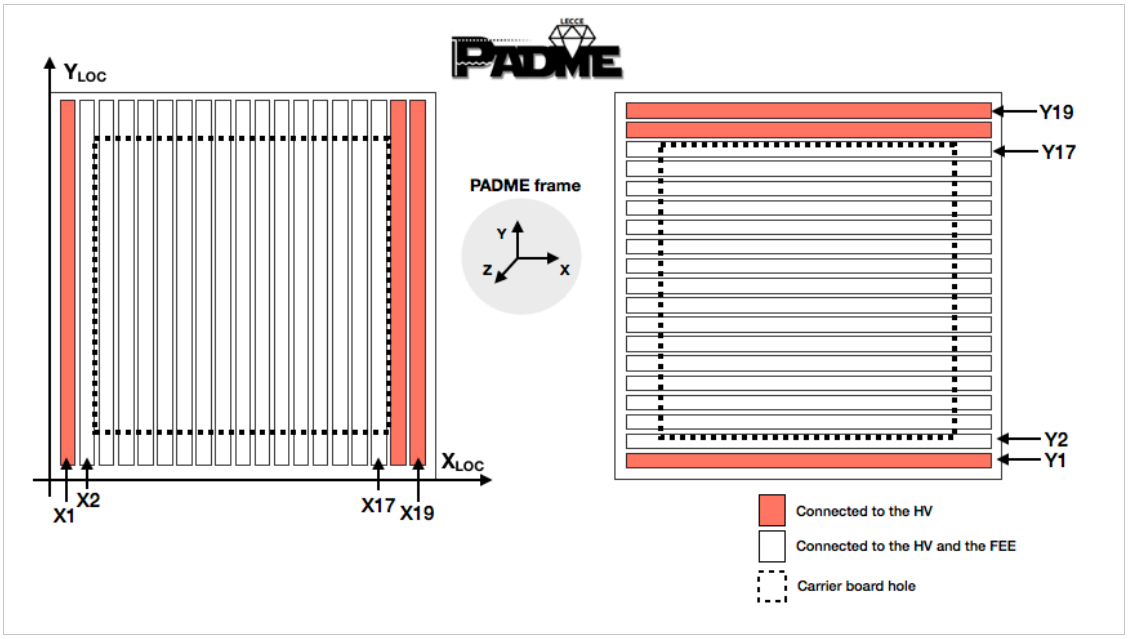

Figure 3.33: Mapping of the X and Y strips. In white the strips connected to the high voltage and readout. In red the strips connected to the high voltage but not to the readout. The dashed squares represent the holes of the carrier board. In the picture the local and the global reference frames are shown.

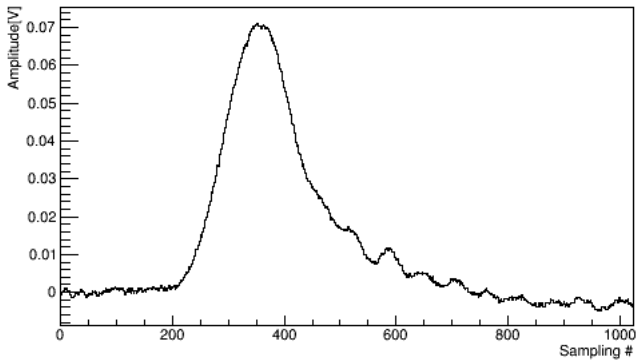

Figure 3.34: An example of the digitized output signal of a central X strip of the target.

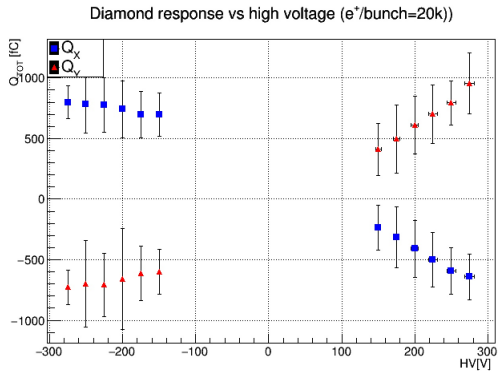

Figure 3.35: Charge collected in the X view, varying the diamond bias voltage.

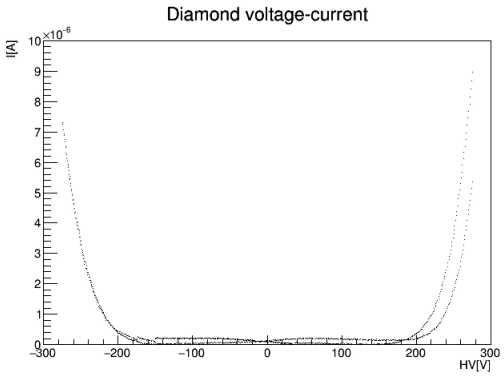

Figure 3.36: The diamond leakage current varying bias voltage.

working voltage was chosen where the output signals reached a plateau, avoiding a very high voltage that could cause discharges. The corresponding current absorption of the high voltage power supply during the scan is reported in Figure 3.36. The bias voltage applied for all the data taking was -250 V (X view collecting hole and Y view collecting electrons), with a current absorption of the order of a few μA.

3.5.2 Front-end electronics calibration

The boards of the front-end are equipped with 16+16 charge amplifiers; the relation between the input charge and the output one can be written as follows:

$$V_{out} = G_V \cdot Q_{in} \tag{3.8}$$

where is the gain of the charge amplifier expressed in mV/pC.
The calibration of all amplifiers had to be performed to equalize the response and compare the charge collected by different strips. Each amplifier of the AMADEUS chip is equipped with an internal charge injection circuit, which allows to test each amplifier and measure the gain.
The charge injection circuit is shown in Figure 3.37 and it is common to all channels. The charge injected is shared between all the channels selected by the internal shift-register. The chip calibration voltage input pin is called CAL_PULSE, shown also in Figure 3.22 . The calibration pulse is given by a voltage step of 20 ns rise time, which was provided by the waveform generator Agilent 33120 [143], using a cable and a LEMO-SMA adapter. The selection of the channel board for the charge injection is done with a input-output (I/O) USB device from National Instrument, as shown in Figure 3.38, which generates the signals Clock, Data and Reset for the

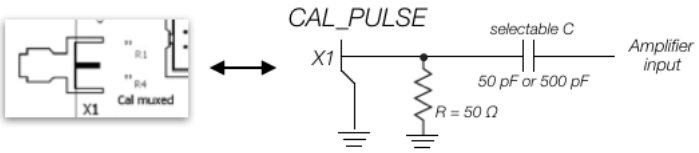

Figure 3.37: AMADEUS chip calibration circuit.

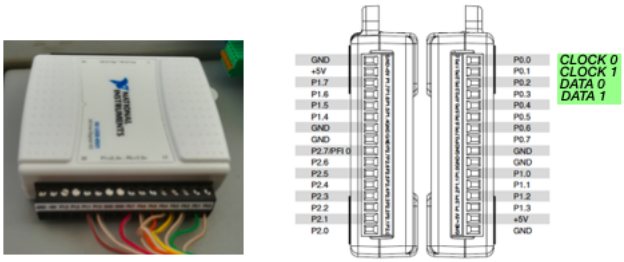

Figure 3.38: Device IO used to select the channel of the AMADEUS chip to inject during the calibration.

chips internal shift-register. In this way a calibration channel by channel was possible. The I/O device was placed outside the vacuum, connected to the front-end boards by the 10 pins 2 rows connector and controlled by a PC Linux placed nearby the target instrumentation. An initial pulse Reset is performed, than the Data is set true, with the Clock and Reset false. While the data is true, a clock pulse is generated to inject the first channel. After the first channel has been selected, it is possible to select another channel n by generating n-1 pulse Clock, keeping the Data false. This is exactly the way a shift register works (Figure 3.39).
The injected charge can be calculated as follows:

$$Q_{CAL} = V_{CAL} \cdot C_{CAL} \tag{3.9}$$

where V_{CAL} was the voltage step and C_{CAL} the injection capacitance value. The front-end electronics allowed to choose between two different injection capacitance values: 50 fF or 500 fF. The chosen one for the calibration was 500 fF.
The voltage step is shared between the two front-end boards and terminated with two 50 Ohms

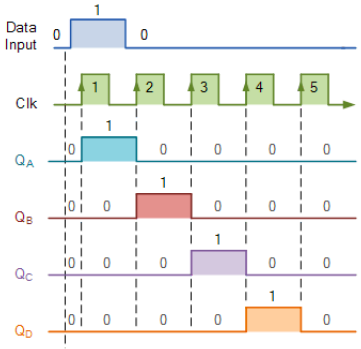

Figure 3.39: Shift register signal sequence to inject the nth-channel of AMADEUS chip for charge injection.

resistors. The effective amplitude of the voltage step was measured with an oscilloscope for different amplitude values displayed by the waveform generator and the injected charge was calculated, from Eq. 3.9 (see Table 3.5.2). The target calibration was performed using the

A [V]	A_{osc}[V]	Q_{CAL}[fC]
2.5	1.6	800
2	1.34	670
1.5	1.02	510
1	0.68	340
0.9	0.616	308
0.8	0.552	276
0.7	0.468	234
0.6	0.4	200
0.55	0.368	184
0.5	0.332	166
0.45	0.304	152
0.4	0.268	134
0.35	0.234	117
0.3	0.204	102
0.25	0.166	83
0.2	0.136	68
0.15	0.1	50
0.1	0.0656	32.8
0.05	0.0304	15.2

Table 3.4: A is the squarewave amplitude of the voltage generator, A_{osc} is the voltage step measured with the oscilloscope and Q_{inj} is the injected charge, for an injection capacitance value of 500 pF.

PADME acquisition system, with a delayed copy of the 50 Hz BTF clock triggering the waveform generator, in order to center the output signal in the digitizer acquisition window. An example of output signal for a ramp amplitude of 200 mV is shown in Figure 3.40. The pulse height values, positive and negative, were stored. The gain as defined in Eq. 3.8 can be obtained correlating the pulse height in output and the injected charge, as shown in Figure 3.41 a. Also the adimensional gain in charge was extracted, integrating the waveform in the corresponding ranges, as shown in Figure 3.40. The adimensional calibration factor for each channel, extracted as explained in Figure 3.41, was inserted in the calibration service of the PADME reconstruction software, in order to estimate the charge collected by the strips.

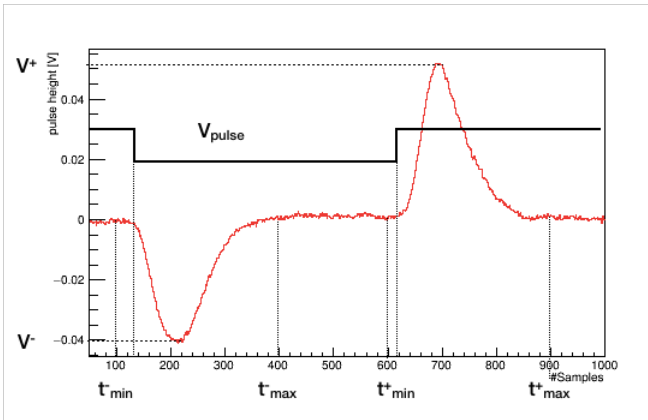

Figure 3.40: Output signal of a channel that corresponds to a pulser amplitude of 200 mV.

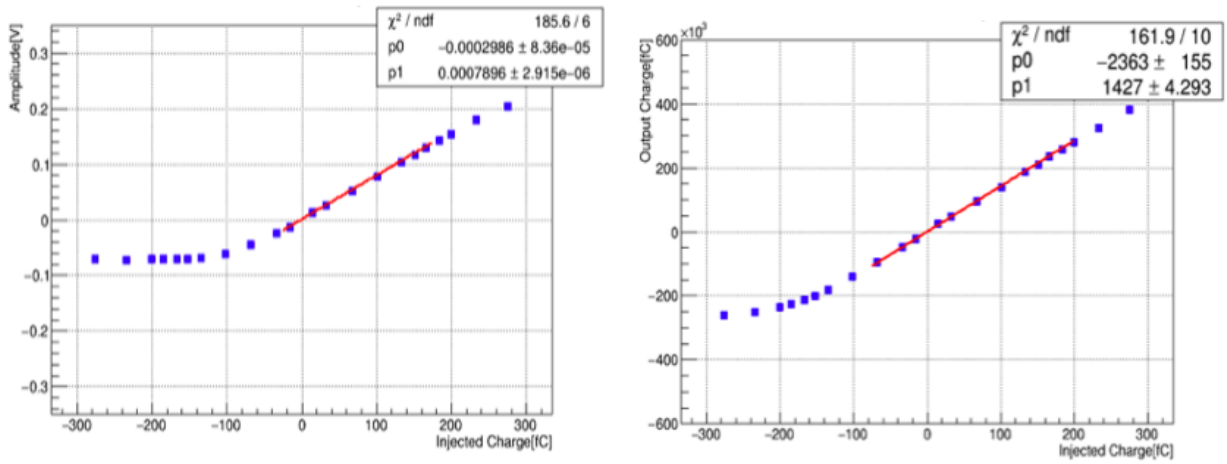

Figure 3.41: Example of calibration curves for one front-end channel in terms of pulse-height (left) and charge (right) as a function of the injected charge. The slopes of the linear fit superimposed on the plots are the amplifier gain in V/fC (left) and the adimensional calibration constants (right).

Chapter 4

PADME data taking

At the beginning of September 2018 the PADME detector was fully installed in the BTF experimental hall and the first positron beam was delivered on 15th September 2018.
The PADME data taking periods spanned more than two years with the last positron beam delivered at the beginning of December 2020. The data taking periods, interleaved by shutdowns of several months, are described in this chapter. A reliable Detector Control System (DCS), together with a detailed on-line monitoring, were essential tools for the data taking. The DCS allows to communicate with all the hardware devices and control all the operating conditions of detectors. The on-line monitoring is important to preserve the stability of data acquisition; a fault of a hardware system can compromise the data taking, reducing the quality of the data. Both systems are briefly described in this Chapter with focus on the functionalities that I have been working on. In fact, in addition to actively participate in all the data taking campaigns, both on-site and remotely, I have developed the DCS of the diamond target and contributed to the improvement of the PADME on-line monitor.

4.1 Data taking periods

The PADME data taking periods can be essentially divided in two groups separated by a very long shutdown of about one year, due to the Be-window accident and Covid-19 emergency.

- **Run 1**, with the old beam line (Figure 2.3), consisting of all the following periods: beam and detector commissioning with secondary beam (see Section 2.1), from 15th September to 30th September, data taking with secondary beam, from 1st October 2018 to 21st February 2019, and data taking with primary beam, from the end of February 2019 to the beginning of March 2019 and in July 2019.

- **Run 2** with the new beam-line upgrade (Figure 2.4), consisting of all the following periods: beam and detector commissioning with primary beam (see Section 2.1) in July 2020 and data taking with primary beam from 15th September to 2nd December 2020.

This sequence of data taking periods was necessary in order to significantly improve the quality of the PADME data. The latter strongly depends on the beam induced background and on the beam features, in addition to detector efficiency, calibration, alignment and software reconstruction. A small beam background is fundamental in order to veto physical objects in time coincidence without reducing significantly the efficiency of the signal. The beam background observed in the detector with the secondary positron beam was found to be prohibitive for the PADME physics program. Therefore, the option of a primary positron beam was chosen from the end of the Run 1, at the cost of a lower beam energy, 490 MeV instead of 545 MeV. The

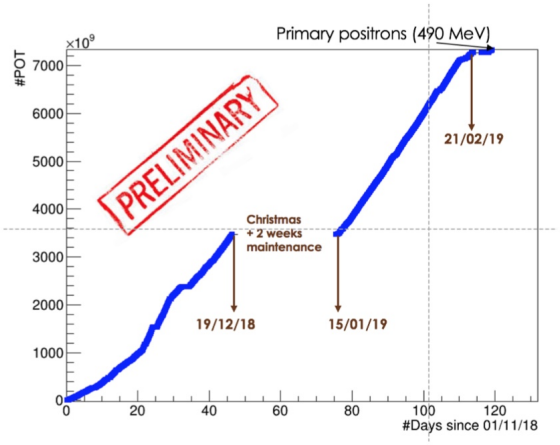

Figure 4.1: Evolution with time of the Run 1 integrated luminosity in terms of number of positrons on target.

beam induced background was further reduced in Run 2 thanks to the new beam-line. A bunch structure as flat as possible and a long bunch length are required to keep the pile-up uniform in time and at a low level for all the detectors, while running with a high multiplicity of particles per bunch. These conditions were achieved only in 2020 using the primary positron beam of energy equal to 430 MeV.
The details of each Run are explained below.

4.1.1 Run 1

The Run 1 integrated luminosity is shown in Figure 4.1, in terms of the number of positron on target (NPOT). Only the first period is shown, where the secondary beam was used for most of the time and the primary beam was used only in the last month.

Secondary beam

The commissioning phase and most of the Run 1 data taking used the secondary positron beam, with an energy up to 545 MeV. The current of the PADME magnet was set at 232.0 A for this value of the beam energy. The commissioning phase was used to finalize the data acquisition, the reconstruction software, the DCS and the on-line-monitor.
Several special runs allowed to calibrate in-situ the detectors, the most relevant calibration runs were:

- out-of-axis single positron runs with PADME magnet off were used to calibrate both ECAL and SAC, scanning several crystals by changing the current of the magnet DHSTB002;
- runs with different number of positrons per bunch (from 2000 up to 30000) were used to perform an absolute calibration of the bunch multiplicity given by the diamond target.

The total visible energy deposited in ECal was of the order of 7 GeV (Figure 4.2, left) for a bunch multiplicity of 20000 positrons/bunch, corresponding to 0.35 MeV/e^+. In this high background conditions, the ECAL was not capable to identify the e^+e^- annihilation events, while the Bremsstrahlung events were clearly visible from the correlations between SAC photons and PVeto positrons. For this reason, at the end of February 2019 the secondary beam was

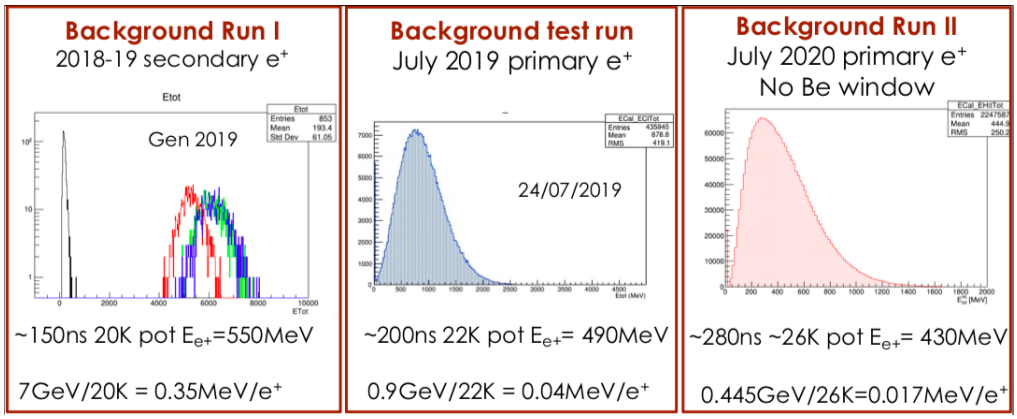

Figure 4.2: ECal total cluster energy during Run 1 with secondary beam with green line (left), Run 1 with primary beam (center) and Run 2 with primary beam and new beam-line (right) [144].

abandoned and the primary beam was used, with the hope to lower significantly the ECal background.

Primary beam

The induced background of the primary beam was lower than the one of the secondary beam. This is because, for the secondary beam, the conversion of the primary electron beam into positrons, happening too near to the first bending magnet, generates a large number of positrons, electrons and photons of all energies, which can propagate through the beam-line, generating secondary particles that eventually reach the PADME detectors. With the primary beam only primary positrons with the desired energy reach the first bending magnet. The total charge released in ECal for a mean multiplicity of 22000 positrons/bunch, was of the order of 0.9 GeV (about 0.04 MeV/e^+), as shown in Figure 4.2 (center), ten times lower than it was with the secondary beam. In these cleaner conditions, the e^+e^- annihilation in two photons was finally visible. The maximum energy achievable with the primary beam is lower with respect to the secondary beam, limiting also the range of dark photon mass accessible. This is because only a fraction of the LINAC can be used to accelerate positrons. The energy of the primary beam in Run 1 was of 490 MeV, and the bunch length was 150 ns, with an intensity not uniform in time within the bunch. The current of the magnet was set at 211.8 A for this positron energy.
The July 2019 runs were mainly devoted to improve the beam quality and disentangle beam induced background from physics signals, such as e^+e^- annihilation and e^+ Bremsstrahlung.

4.1.2 Run 2

After the beam-line intervention (described in Section 2.1), a commissioning phase in July 2020 started and a more focused beam was delivered on the target, with a beam spot of diameter 1 mm, to be compared to the previous, about 2-3 mm. In this condition the target began to saturate for a beam intensity above about 10000 positrons per bunch. The positron beam energy was 450 MeV, even lower than in Run 1, while the bunch length was still of the order of 150 ns. The modulator C of the LINAC could work only at 85% of the nominal power to avoid discharges. At the end of July 2020 the bunch length was increased up to 250-280 ns reducing the pile-up for the same bunch multiplicity.
The acquisition of physics runs started on 15th September 2020 with a quite flat bunch structure.

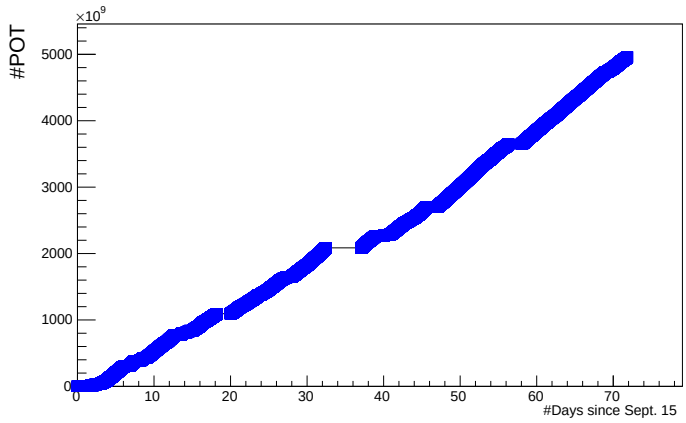

Figure 4.3: Evolution with time of the Run 2 integrated luminosity in terms of number of positrons on target.

The PADME Run 2 ended on the 2nd of December, with a collected integrated luminosity of $\sim 5 \times 10^{12}$, as shown in Figure 4.3.
The beam-line upgrades reduced the beam background. In Figure 4.2 the distribution of the total energy measured in ECAL in a bunch during Run 2 is shown in the right plot. A n average energy of 0.445 GeV is observed for a bunch of 26000 positrons corresponding to 0.017 GeV/e^+. This is one half of the energy observed with the old beam line while the beam energy and intensity are similar. The bunch in Run 2 presented a flat structure in time, with a length of about 280 ns for an energy of 430 MeV. These beam features allowed to run at high multiplicity, from 25000 up to 30000 positrons per bunch. The current of the PADME magnet for this positron energy was set at 183.5 A.

4.2 PADME on-line monitoring

The PADME data taking efficiency was quite high in all periods thanks to versatile data acquisition, on-line monitoring and detector control systems, which were accessible to on-site and remote shifters.
This section is focused on the PADME on-line monitor system where I gave several contributions. The PADME on-line monitor during data taking allowed to probe in real time all the experiment conditions, to assure the quality of the recorded data. The PADME on-line monitoring software is based on a custom Web Application written in JavaScript named PADME MONITOR. It is composed of a Server and a Client. The Server collects information, from beam, detectors, data acquisition, environmental sensors and reconstructed data. This is done by checking periodically JSON files published by the different systems previously listed. The Client reads the data from the Server memory and converts them in web pages as plots, graphs or tables, thanks to a graphical library named PlotlyJS. The on-line monitor web pages are accessible using a simple internet browser from remote locations, using a VPN connection to access the laboratory network. The main web page of the on-line monitor is divided in three sections: Data monitoring (Monitor), DCS monitoring (DCS) and ECAL HV trip alarms (Alarm).

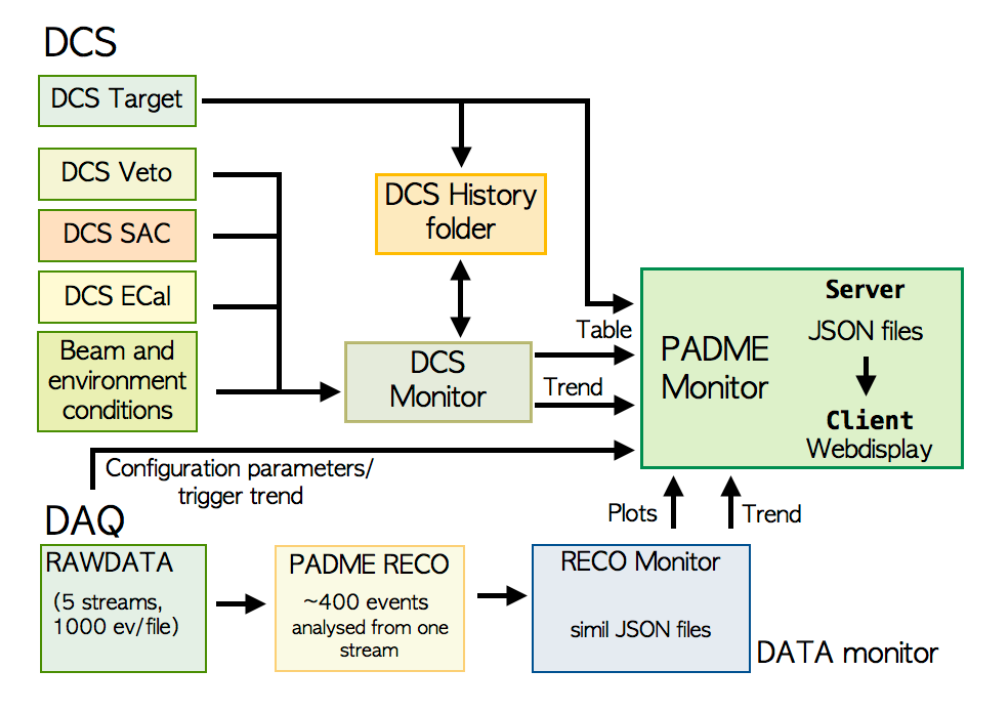

Figure 4.4: The PADME on-line monitor software blocks.

4.2.1 DCS and alarm monitoring

A diagram of the software blocks of the DCS on-line monitoring is shown in Figure 4.4. The parameters controlled give the status of the beam, detectors, DAQ and environment. Each DCS system has its own custom made hardware control and a set of parameters to periodically read-back. The system parameters to monitor are written in text file of JSON format and sent to the DCS MONITOR to be stored. The DCS summary web page shown in Figure 4.5 collects the most relevant information about many sub-systems. The essential parameters, regarding the beam status, environmental conditions of the experimental hall, the vacuum, the target detectors, the data acquisition and the trigger, are displayed in this page.
From the dedicated box *BTF DATA* in the summary, it is possible to check the status of the LINAC electron gun, the current applied to the PADME magnetic dipole and the LINAC charge. The beam energy is related to the currents of two magnets: the DHSTB001 and DHSTB002. As a consequence, the reading of these currents is a good way to have an approximate on-line value of the beam energy.
During the run it is necessary to assure stable environmental conditions because a high temperature could alter the performance of the detectors, such as the ECAL response. Therefore, the temperature of the BTF hall is displayed by the DCS summary page.
In the DCS summary page there is also a box, dedicated to the DAQ, showing many configuration parameters, such as sub-detectors included in the acquisition. In Run 2 new features in the DCS summary page were added, like the trends in time of the rate of all PADME trigger types and the shifter name as stored in the shifter database.
A color code for the display of critical parameters is used to warn the shifter of ant non standard condition. In case of anomaly, the corresponding expert has to intervene.
The alarm web page is dedicated to report the current trips of the ECAL photo-multipliers. In this case an automatic procedure was implemented to recover the faulty channels without the need of an expert intervention.

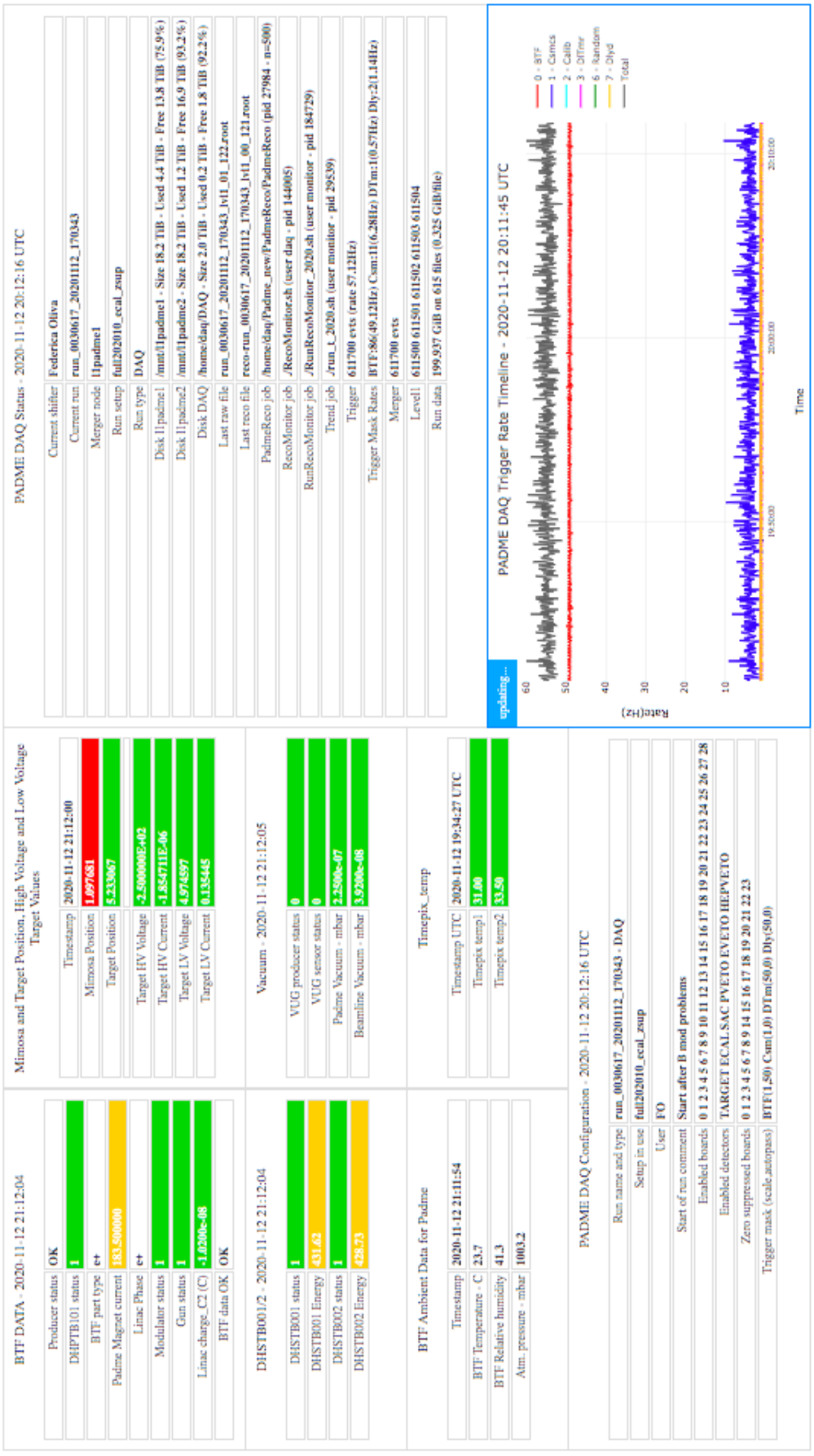

Figure 4.5: PADME on-line DCS summary web page.

4.2.2 Data on-line monitor

The software chain of the PADME on-line monitor is shown in Figure 4.4.
The PadmeDAQ software writes in real-time rawdata files of 1000 events organized in 5 parallel data streams; 400 events of the last closed file, belonging to one stream, are continuously analysed by the PADME reconstruction software (PadmeReco). The reconstruction is executed with the Monitor Flag set to 1 in order to assess the monitoring histograms for each detector, useful to monitor the quality of the data just recorded. The RecoMonitor software based on the ROOT library reads the monitor histograms produced by the PadmeReco. The RecoMonitor dumps the histograms contents in text files of JSON format, which are published graphically on-line by the PadmeMonitor. This implementation acts like a almost real-time on-line monitoring data with reconstruction algorithms identical to the off-line analysis. The data monitor summary web page is shown in Figure 4.6.
The conditions required for a good physics run, in particular in Run 2, were a small spot on target and a high beam intensity (not lower than 20k positrons per bunch but also not exceeding 30000). The trend in time of the bunch multiplicity and the bunch length (not lower than 150 ns) are important figures of merit for the run data quality because they affect the response of the detectors. The time distribution of the hits in the SAC was used to monitor them.
Every shifter has to control that the bunch multiplicity remains constant and flag anomalous runs. The X and Y beam centroids are monitored, to have a beam as much as possible stable for all the data taking period. In addition, the ECal total energy and the ECAL heat map are important quantities to monitor, in order to control the beam induced background. The diamond target provides the only on-line monitoring of the beam profile and of the beam multiplicity per bunch. The determination of these quantities in the PADME reconstruction is explained in Chapter 5. In the monitor summary web page (Figure 4.6) the beam spot and the distribution of the beam multiplicity are displayed. The trend in time of the X and Y beam centroid and of the average beam multiplicity provided by the target are very useful to control the beam stability during a run. For each detector there are dedicated data monitor web pages for experts. In Figure 4.7 it is possible to see X and Y beam profiles from target expert page. In particular, the target expert page displays also all the 32 waveforms of the last processed event from the PadmeReco (i.e. see Figures 5.1 and 5.2).

4.3 Active Diamond Target DCS

In this thesis work the DCS of the target has been entirely designed and implemented. Since the start of the data taking in October 2018, it was successfully integrated with the PADME DCS monitor. The target DCS was supervised by a Graphical User Interface (GUI) interactive based on ROOT software[145], which was able to run several custom made executable written in C-code.
The target instrumentation set-up is shown in Figure 4.8. A GPIB ethernet controller allowed to control remotely the high voltage power supply, to bias the detector, a low voltage power supply which powers the front-end electronics, and a waveform generator for the charge injection.
The GPIB ethernet controller is from PROLOGIX and supports both static and dynamic (DHCP) IP address. The communication between the GUI and the GPIB controller can be easily established by opening a simple socket connection and using the usual client-server protocol. Typically the GUI can both query or send command to any instrument connected to the GPIB hardware bus. Each instrument have assigned a unique GPIB address. Queries are strings that end with a question mark (?), asking informations to the instrument. The commands are strings requiring some actions to the instrument. There are both standard queries

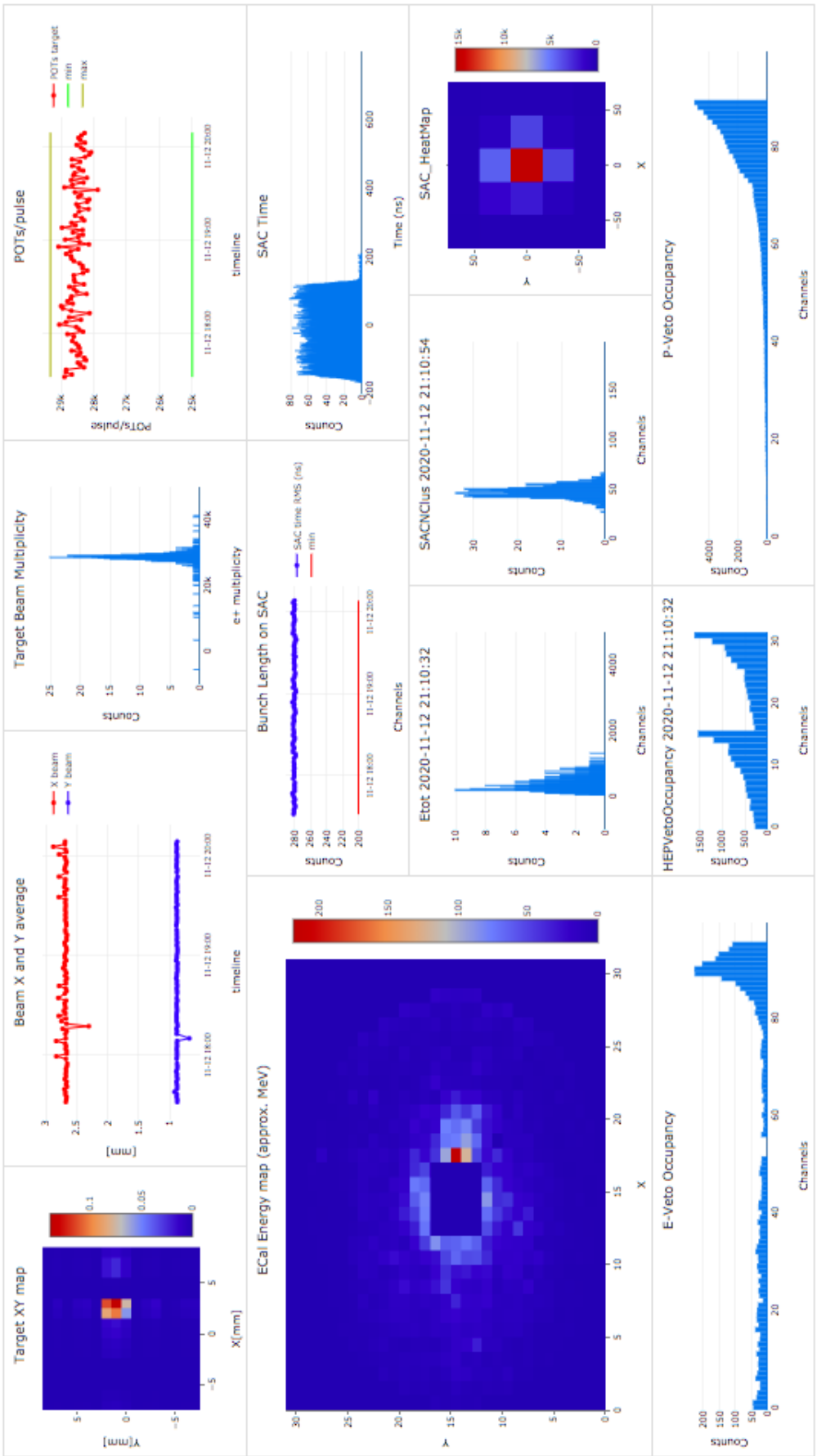

Figure 4.6: PADME monitor summary webpage.

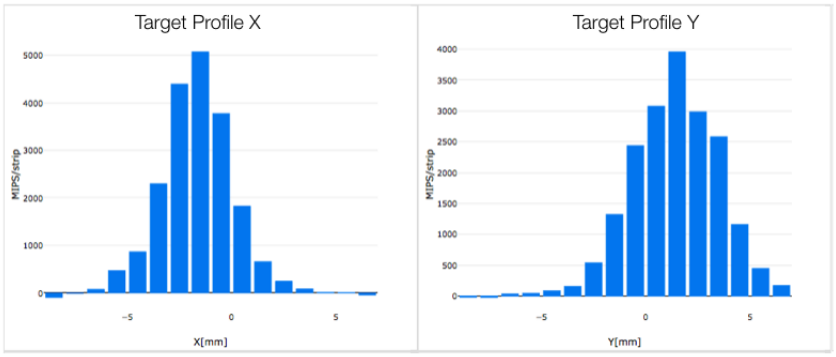

Figure 4.7: Among the plots provided by the target on-line monitor page there are the X and Y profiles (shown here) and the beam spot (shown in Figure 4.6).

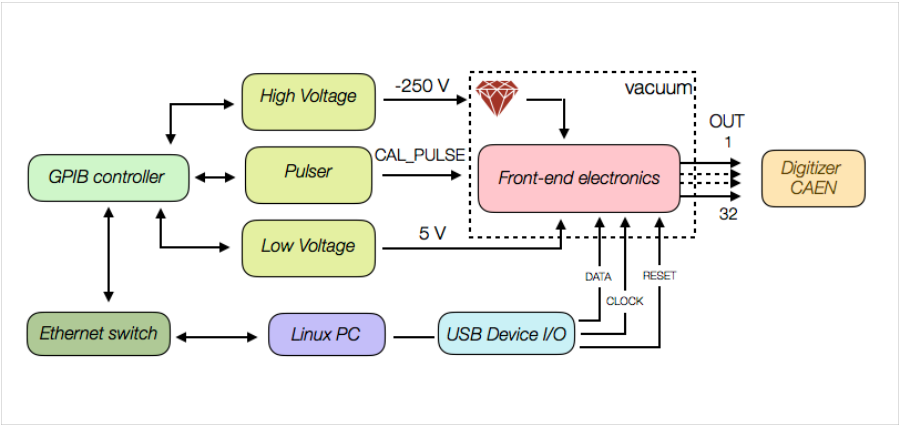

Figure 4.8: Target DCS block diagram.

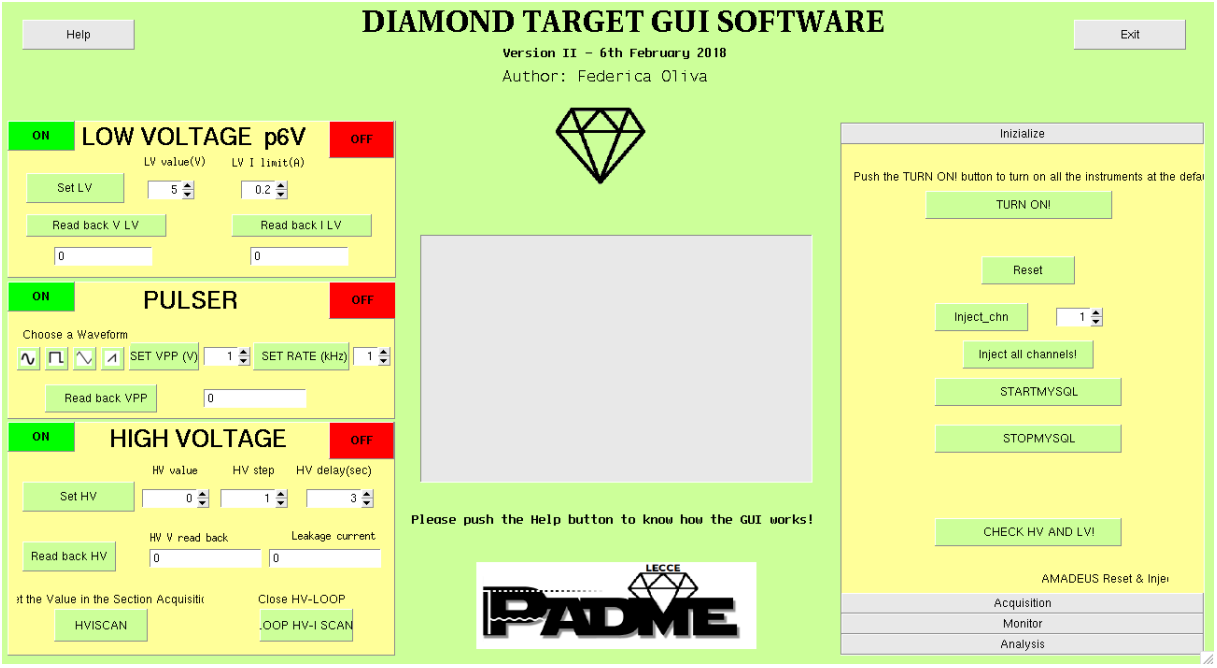

Figure 4.9: Diamond target GUI.

and commands and others that are specific of the instrument. The GPIB controller allows to oversee the following instrumentations:

- a low voltage power supply Agilent E3631A;
- a high voltage power supply Keithley 2410;
- a waveform generator Agilent 33120.

The I/O device needed to enable the charge injection in the front-end was connected to a Linux PC by a USB cable and controlled by a custom C-code which was executed remotely through the ssh protocol.

4.3.1 Diamond Detector GUI

The graphical interface of the diamond detector is shown in Figure 4.9.
The interface is divided in two parts: on the left the communication with the GPIB instrumentation is controlled, while the right section hosts a drop-down lists of operations (Initialize, Acquisition, Monitor and Analysis). These operations were used to test and calibrate the diamond detector in stand-alone acquisition. The first box on left is dedicated to the low voltage. It has to be set at 5 V, with a current limit of 0.25 A.
The second box on the left controls the pulser, useful for the calibration. It is possible to choose the waveform shape (sinusoidal, squared, sawtooth, triangular), and to set the peak to peak amplitude (in V) and the frequency (in MHz). The read-back is implemented only for the amplitude.
The last box on the left allows controlling the high voltage settings: the final value, the steps and the time delay between two consecutive voltage setting. The final high voltage is reached in a safe way by a slow step-wise ramp up or down, depending on the sign of the voltage change.
A high voltage scan (button *Loop HV-I scan*) was implemented to study the detector leakage current performing a loop on the applied high voltage, storing for each step the value of the

acquired voltage and current. The right part of the interface hosts several functionalities useful to record data for specific tasks, such as front-end channels calibration. The Initilize section allows to control the I/O device connected to the interface for digital injection on the FE boards. The *TURN ON* button allows to turn on the FE boards. The FE channel to target for charge injection can be selected using the *Inject chn* button. It is fundamental to inject one channel at the time to perform a reliable calibration. The acquisition was performed using the PadmeDAQ software with two options for the readout hardware: the digitizer of the PADME readout or the desktop version of the CAEN digitizer, named DT5742 used for bench tests. The calibration procedure was explained in chapter 3.
Other functionalities (Acquisition, Monitor and Analysis), used during the diamond detector characterization in Lecce, but not used after installation in PADME, are not explained here. Finally, some buttons control the access to a local MySQL database meant to store test data for the target.

4.3.2 User Target GUI

The Diamond Detector GUI with all the functionalities was used only by experts for tests, debugging and calibrations of the detector. In addition to that, a simpler GUI was designed and realized for the PADME shifter. The User Target GUI must safely turn on and off the target and quickly check the main parameters without expert support. In Figure 4.10 a snapshot of the User Target GUI of the experiment is shown. The target GUI stores continuously the useful operational parameters and sends them to the monitor system of the experiment.
It is basically divided in two sections. On the left side the user can turn on and off the detector, without the possibility to change the low voltage and the high voltage setting, which are hard coded. Detector turns on is done pressing the button *Set LV 5 V and HV at -250 V*. The User Target GUI turns on first the low voltage, setting the voltage value to 5 V, with a current limit of 0.25 A. Once the low voltage power supply is on, the User Target GUI turns on the high voltage power supply. If the low voltage read-back is for some reason off or the read-back has some failures, the High Voltage is not turned on. This assures a safe operation. The Low Voltage and High Voltage values read-back by the power supplies are displayed in the top left part. Detector turn off is done pressing the button *Turn OFF HV and LV*. During this operation the User Target GUI first turn off the high voltage power supply and than turn off the low voltage power supply once the high voltage read-back is 0 V. An additional cross-check during turn on and turn off operation is provided by detailed text strings displayed on the terminal screen. The right side of the GUI displays the positions of the target and MIMOSA as read-back from the linear potentiometers. The currents and voltage of the low voltage supplies connected to the linear trasducer (potentiometer) are monitored, together with their conversions in the X positions of the two detectors, as explained in Chapter 3. The User Target GUI reads back all the displayed parameters and prints them on the screen. Finally, these informations are stored in local log files and sent to the DCS, to be stored in the DCS History Folder, and to the PADME monitor to be displayed on the on-line monitor browser.

Target in the DCS monitor

All the parameters monitored by the User Target GUI are stored in one of the main boxes of the DCS summary page of the on-line monitor, as visible in Figure 4.5. The name reported on the box is *Mimosa and Target Position, High Voltage Low Voltage Target Values*. The box hosts the target and MIMOSA positioning informations and the parameters of the target instrumentations. During the data taking the *Target LV Voltage* must be about 5 V and the *Target LV Current* about 0.125 A, not exceeding 0.25 A. The *Target HV Voltage* is at -250 V,

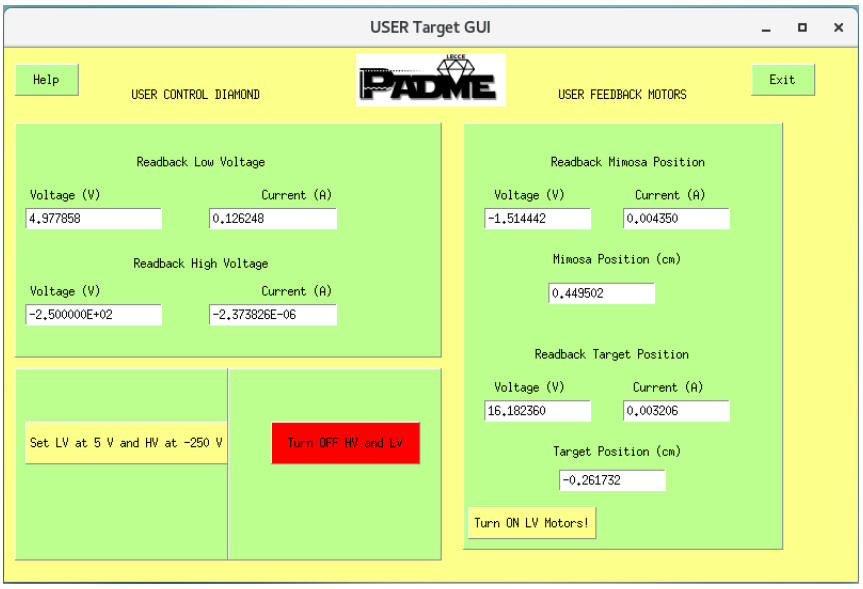

Figure 4.10: The User Target GUI.

and the *Target HV Current* must have a value of a few μA. If for some reasons the values are out of the fixed safety ranges, the color of the box background of the stored parameter value turns red. In normal condition during the data taking the boxes of the target are all green, with no alerts.
In the picture the MIMOSA position value has a red background color, because during nominal runs it is out of beam.

Chapter 5

Active diamond target performance

In this chapter the response of the target in runs with different beam conditions will be presented, focusing on the problem of determining the bunch multiplicity with an appropriate algorithm. The detector performance, measured at the beginning of the Run 1, is presented. Later some new detector specific studies performed in Run 2, thanks to the focused beam, are reported.

5.1 Target response and beam features

The monitoring of the bunch multiplicity exploiting the target is an important and peculiar feature of the PADME experiment which allows to keep the pile-up under control while maximizing the instantaneous luminosity.
The bunch multiplicity is directly related to the total charge measured by the X and Y strips. For this reason, it is essential to characterize the behaviour of the Front-End (FE) according to the beam features. The calibration curve in Figure 3.41 shows that the FE saturation occurs very early for negative injected charges ($\sim$ -100 fC) and later for positive ones ($>$ 300 fC). Once the polarization of the active target is defined, the strips on one side collect a current of incoming electrons ($<$ 0) and the strips of the other side collect a current of incoming holes ($>$ 0). Therefore, the two front-end boards must process signals of different polarity and one of them (receiving a negative input charge) is obviously subject to an earlier saturation. A jumper on the AMADEUS chip board allows to flip the polarity of the signals in input to the amplifiers thus selecting the condition leading to the optimal dynamic range. However, when the target was installed in PADME, the jumpers of both front-end boards were set in the same way, because the high voltage sign to be applied to the sensor was not decided yet. The high voltage working point was defined afterwards based on the response measured with the PADME beam and shown in Figure 3.35. The value of -250 V, applied to the X strips, was finally chosen and this led to the Y view being exposed to saturation much earlier than the X view.
The data taking periods of 2018 and 2019 were done with a relatively large beam spot and not very high bunch multiplicity, therefore no appreciable saturation effects in the charge response were observed. During the commissioning phase of the Run 2, in July 2020, after the beam-line upgrades, PADME moved to a beam set-up leading a reduced spot size and a higher multiplicity of particles in a bunch which caused the saturation of the front-end, especially for the Y strip view.
Therefore, in September 2020 an hardware intervention was done to use the jumper of the Y front-end board in order to change the sign of the signal in input to the amplifiers and delay the saturation to higher values of input charge.
The target response to the defocused and focused beam, before and after the intervention on the front-end board, is described in this chapter in terms of measured total charge, as a function of

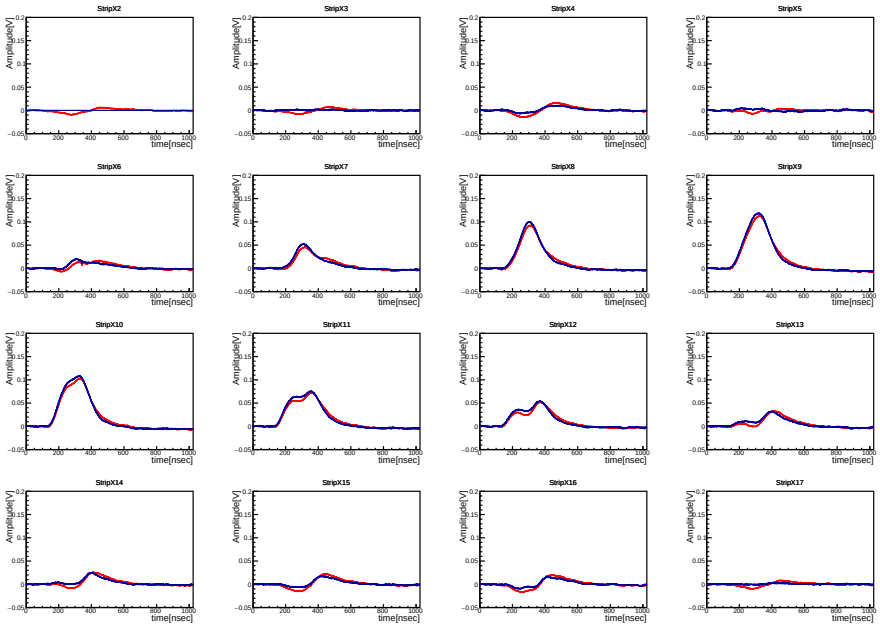

Figure 5.1: X view waveforms after pedestal subtraction (red plot) and after the subtraction of the X2 waveform (blue plot). The bunch multiplicity is of 20000 positrons with 545 MeV energy and the bunch length is of 150 nsec. The data are collected with a secondary positron beam of energy equal to 545 MeV, 20000 particles per bunch, a bunch length of 150 ns and a beam spot size of about 2-3 mm.

the number of positrons per bunch. The impact on the measurement of the number of positrons per bunch is discussed, along with strategies for the analysis of the active target data that can correct the non-linearity of the response.

5.1.1 Defocused beam

The target waveforms, as recorded by the digitizer both for the X and Y views, after pedestal subtraction and converted in Volts, are shown in 5.1 and 5.2. The pedestals are calculated as the mean of the first 100 samples. The same signals after the subtraction of common mode noise are also shown. This suppression of correlated noise can be implemented by subtracting the first readout strip (X2) for the X view and the signal of a strip that is not reached by the beam. In the PADME reconstruction software the common mode subtraction can be activated by a flag and the two front-end channels to be subtracted from the X and Y views can be selected among the 32 available channels. A dedicated study allowed to choose one of the outermost strips for this task; the X2 strip (the first connected to the front-end) was selected since, after subtracting its charge to the charge measured by all X and Y strips, the minimum RMS of the distribution of the total charge in both views was achieved. The waveforms in Figures 5.1 and 5.2 show that the beam hits several strips both in X and Y. The X view channels are far-away from pulse-height saturation while in at least two Y channels the pulse height appears saturated (Y7 and Y10). It is possible to notice how the common mode noise subtraction reduces strongly the amplitude of the bi-polar signal of the strips not hit by the beam (where the integrated charge is zero). The strips hit by the beam tails still have a bi-polar signal with integrated charge different from zero. Finally, the strips hit by the beam core show clear signals of definite sign. Some signals have a two slopes rising edges or two broad peaks, likely sign of front-end strong non-linearity in the pulse-height. Once the charges collected from all strips were computed, the beam profiles was

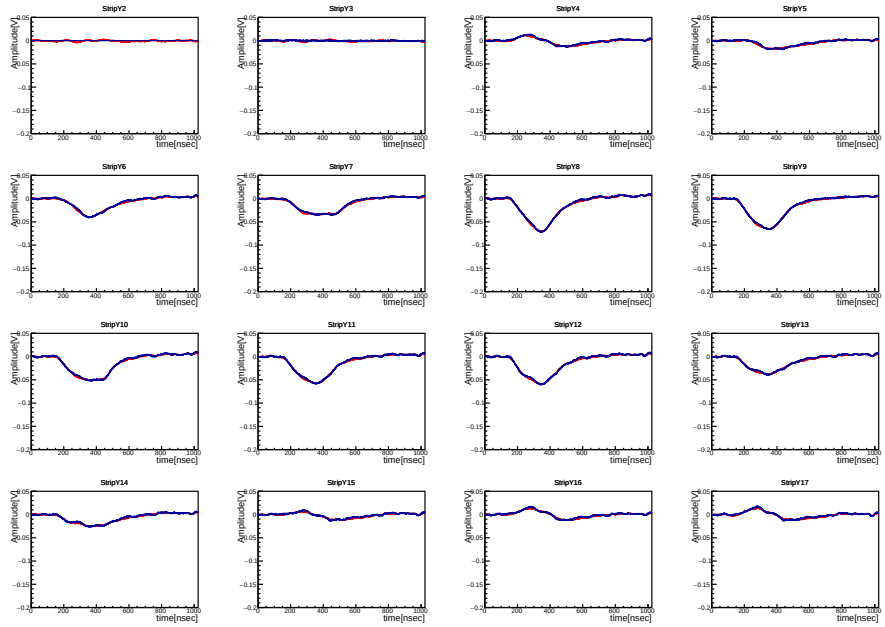

Figure 5.2: Y view waveforms after pedestal subtraction (red plot) and after the subtraction of the Y2 waveform (blue plot). The beam conditions are the same of plot in Figure 5.1

extracted. The X and Y profiles corresponding to the waveforms shown in Figures 5.1 and 5.2 are shown in Figure 5.3. From the beam profiles the spot size was estimated as the Root Mean Square (RMS) of the distribution which is 2.4 mm in the horizontal direction and 2.8 mm in the vertical direction. This is a typical beam size (2-3 mm) for the data taking with secondary beam and primary beam of 2019.
The total charge collected is one of the most important information to extract per bunch, because it is expected to be proportional to the bunch multiplicity.
An absolute calibration with this defocused beam can be performed to extract the bunch multiplicity from the charge collected by the target in both views. The latter was done during dedicated calibration runs as a function of the positron bunch multiplicity measured by a Lead-Glass Cherenkov calorimeter of the BTF. The calorimeter was placed behind the last bending magnet DHSTB002 therefore is reached by the beam if the current of DHSTB002 is turned off (see BTF scheme in Figure 2.3). At each calibration step, the beam was sent to the BTF calorimeter, by turning off DHSTB002, for a reference measurement on the particle multiplicity. After that, the beam was sent again in PADME by turning on the magnet, and the target response was recorded.
Several runs at different bunch multiplicity were taken in order to cross-calibrate the target. In Figure 5.4 the average of the total charge collected by the X and Y views is shown, as a function of the multiplicity measured by the BTF calorimeter. In particular, the slope of the linear fit was used to define the absolute calibration and to evaluate the CCD, a figure of merit of a diamond detector already presented in Chapter 3. This measurement is reported in Section 5.2.1. The absolute calibration factor obtained is used in the software. The multiplicity estimated by the target after the absolute calibration is shown in Figure 5.5 as a function of the bunch multiplicity from the BTF calorimeter for runs taken in two different days.
In addition, in Figure 5.6 the distributions of the charge collected separately by the X and Y views for different bunch multiplicity is shown. When the beam is off or the trigger is cosmics trigger of delayed trigger, the charge distribution for the X and Y views is peaked at zero, with a

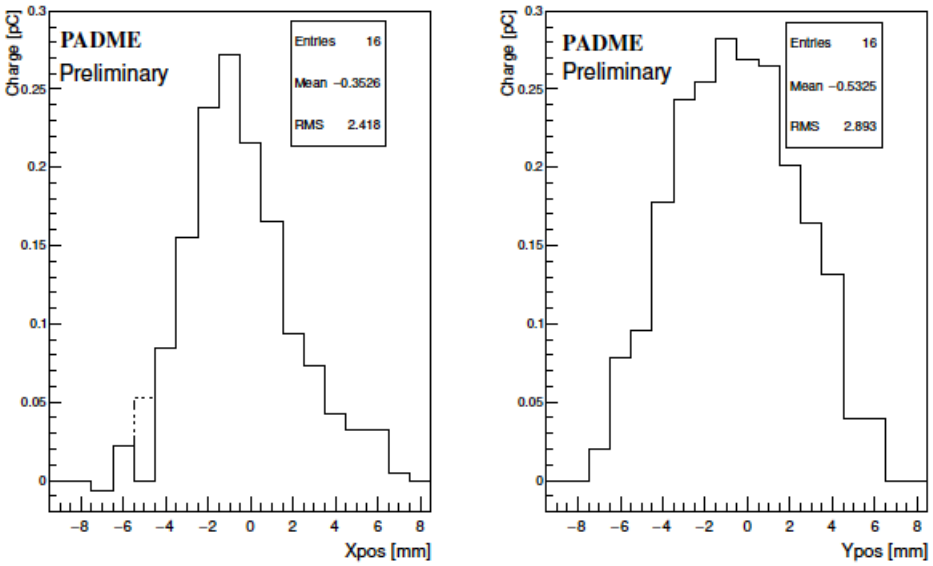

Figure 5.3: X (left) and Y (right) beam profiles of a single bunch. The beam conditions are the same of plot in Figure 5.1.

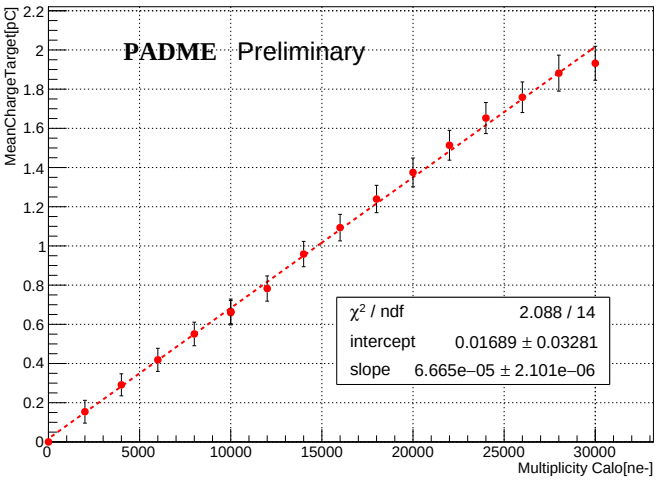

Figure 5.4: Average of the total charge collected by X and Y view as a function of the bunch multiplicity. From the slope of the linear fit superimposed to data, the CCD of the detector. The beam conditions are the same of plot in Figure 5.1, but the bunch multiplicity which is varying. The errors are obtained from the width of the Gaussian fit of the charge distributions.

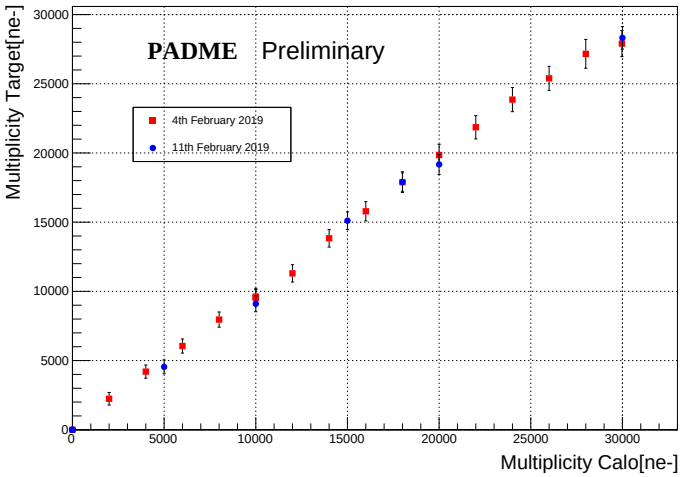

Figure 5.5: Bunch multiplicity measured by the target after absolute calibration for runs acquired in two different days. The errors are obtained from the width of the Gaussian fit of the charge distributions

500 positrons width. A larger noise is observed if the common mode noise is not performed. The measured value of the total charge collected by X and Y views is quite similar but not exactly the same. Likely, this is due to residual systematic errors in front-end calibration, common mode subtraction and graphitic strip electric resistance dispersion.

5.1.2 Focused beam

After the upgrade of the beam-line, in July 2020 it was possible to have a more focused primary beam, keeping the beam background lower than before.
Figures 5.7 and 5.8 show all the waveforms for the X and Y views with and without common mode noise subtraction recorded in a run with a beam of 450 MeV 4500 positrons per bunch and a bunch length of 150 ns. It is visible that the signals corresponding to the FE channels connected to the Y strips saturate both in pulse-height and integrated charge even at this low multiplicity due to the beam focused on only two strips. This is due to the non-optimal choice of the sign of the signals at the input of the front-end board. In this condition, the measured charge is not a reliable measurement of the particle multiplicity in the beam bunch. Instead, the front-end channel of the unique X strip hit by the focused beam does not saturate, both in pulse-height and total charge, thanks to the correct setting of the FE board. For this reason the studies done with these data use only the X view. It is important to notice that the common mode noise appears as a ringing signal correlated to the beam arrival. Also in these data the common mode noise subtraction, using strips outside the beam, is very helpful to reduce the ringing and the noise. However, the procedure was found to be ineffective for some strips. The single event profiles, corresponding to the same beam conditions and bunch multiplicity of Figures 5.7 and 5.8, are shown in Figures 5.9 and 5.10 for two different X target positions: when the beam is centered on one X strip or between two X strips. The profiles are obtained from an average of 4500 positron bunches. The RMS of the distribution of the X and Y profiles are related to the beam spot size in the two views. The RMS of the X profile is ~ 0.6 mm and differs of about 10% for the two positions. The Y profiles in the two positions remain constant as there is no vertical displacement. The RMS of the distribution for both the Y profiles is ~ 1

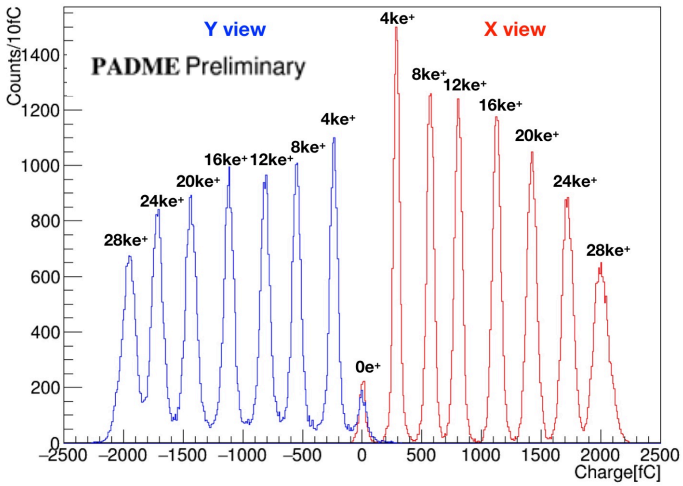

Figure 5.6: Distributions of the charge collected by X and Y views for different bunch multiplicity. The beam conditions are the same of plot in Figure 5.1 with the exception of the bunch multiplicity is varying.

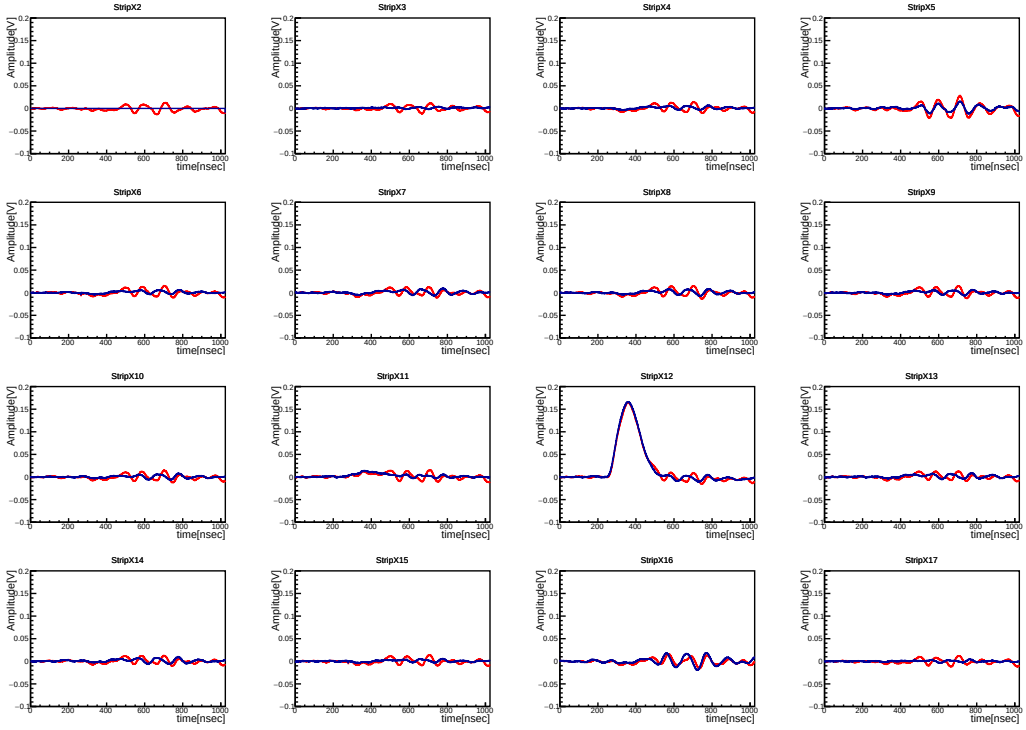

Figure 5.7: X view waveforms after pedestal subtraction calculated with the first 100 samples (red plot) and after X2 waveform subtraction (blue plot). The bunch multiplicity is of 4500 positrons with 446 MeV energy and the bunch lenght is of 150 nsec. The data are taken with primary beam with a beam spot size of about 0.5-1 mm.

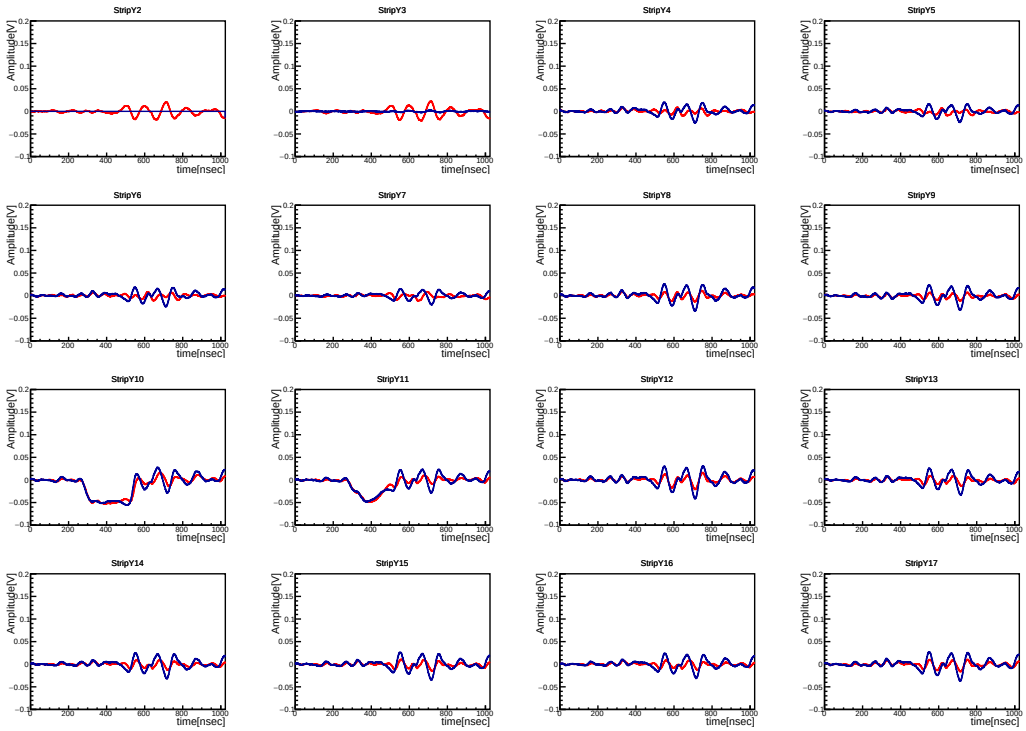

Figure 5.8: Y view waveforms after pedestal subtraction calculated with the first 100 samples (red plot) and after Y2 waveform subtraction (blue plot). The beam conditions are the same of plot in Figure 5.7.

mm, larger than the X profile.
A study of the front-end response for the X strips was performed for different positron bunch multiplicities in two different configurations: with the beam at the center of a strip and with the beam impinging in the gap between two strips. Thanks to the very small beam spot, in the first configuration the charge is collected by just one strip and the linearity of one single front-end channel can be studied. In the second configuration, the charge is shared by to strips. Therefore, the non linear front-end response manifests clearly when total charge, integrated on all strips of the X view is different in the two geometrical configurations. In Figure 5.11 the charge collected by the X view measured assuming a linear response for positron bunch multiplicity from 4500 to 20000 is shown, separately for the two configurations. From the measurements with only one strip hit by the beam, one can observe that non linearity effects in the response start at about 7500 positrons per strip and saturation at about 15000 positrons per strip. It is important to notice that the non-linear and saturation regions depend strongly on the considered channel. This means that also the upper limit of the linear region is channel dependent.
Clearly, collecting the charge using two strips increases the linearity region thanks to the charge sharing. Unfortunately, this feature can be used for multiplicity measurements only if the beam position is stable during data taking. This explains why with unfocused beam the non-linearity in the target response was not an issue. In fact, with unfocused beam the individual strip almost never collected more than 0.6 pC in both views in a single event.
We can conclude that with a focused beam with a spot size smaller than 1 mm the target linear region in terms of Positron On Target is limited to 7500 positrons. The range might be extended by a factor of about two with a non-linear calibration of the front-end which was out of the scope of this thesis, and in any case insufficient to cover the need of the PADME Run 2. Anyway, this

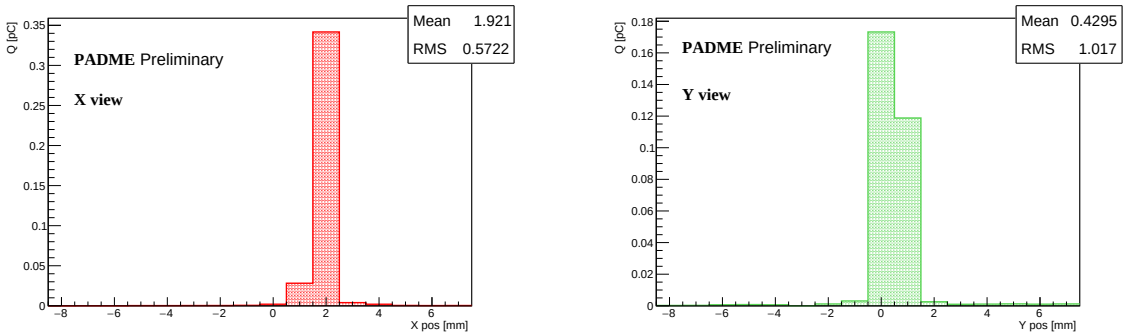

Figure 5.9: X (left) and Y (right) beam profiles of a single bunch with the focused beam hitting only one X view strip.The beam conditions are the same of plot in Figure 5.7.

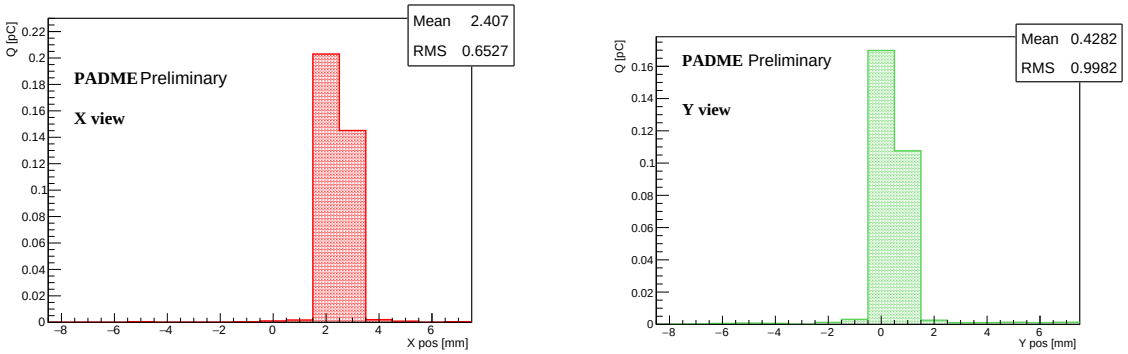

Figure 5.10: X (left) and Y (right) beam profiles of a single bunch with the focused beam centred between two X view strips. The beam conditions are the same of plot in Figure 5.7.

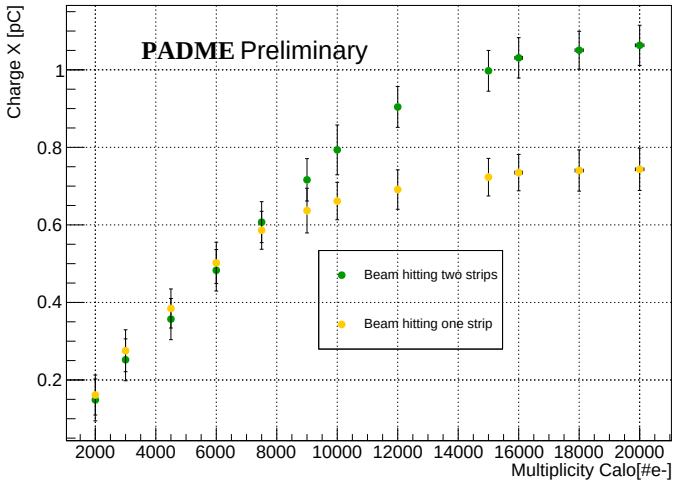

Figure 5.11: Apparent total charge collected by X view for two different X position of the diamond detector. The yellow data points correspond to the focused beam hitting one X view strip, while the green ones correspond to focused beam between two X view strips. The errors are obtained from the width of the Gaussian fit of the charge distributions.

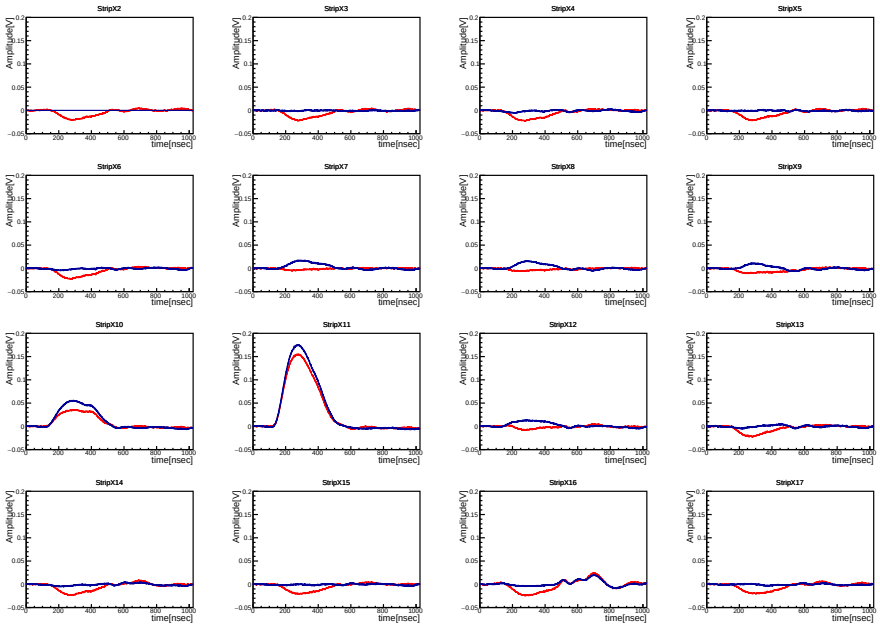

Figure 5.12: X view waveforms after pedestal subtraction calculated with the first 100 samples (red plot) and after X2 waveform subtraction (blue plot). The bunch multiplicity is of 10000 positrons with 430 MeV energy and the bunch length is of 280 nsec. The data are taken with secondary beam with a beam spot size of about 1 mm.

multiplicity range was still too low for the Run 2 beam conditions.

5.1.3 High intensity and focused beam

The hardware intervention in September 2020 allowed to mitigate the saturation of the response of Y strips, thanks to the inversion of the polarity of the signals processed by the front-end. In this way for a negative high voltage on the diamond it is possible to obtain the same output signal polarity and similar responses for all the 32 channels with respect to ionizing radiation. Nevertheless, as discussed in section 5.1.2, the performance achieved was not suitable for the beam configuration that was adopted in Run 2. Indeed, stable and high intensity running conditions were achieved by the LINAC and BTF exerts only with a focused beam, in both X and Y views, and a bunch multiplicity between 25000 and 30000 positrons in Run 2.
This meant that a few strips of the target hit by the beam were almost saturated and a non-linear calibration useless. Anyway, as explained later, a bunch multiplicity measurement is still possible, thanks to the beam features on the Y view and to the extension of the dynamic range of the Y view board. In Figure 5.12 and 5.13 the waveforms of the X and Y views are shown with and without common mode noise subtraction for a focused bunch of 10000 positrons. Already at this moderate intensity it is clear that the strips X11 and Y10 are in saturation regime (V>> 0.1 V). Apparently, the saturation of these strips causes an injection of charge of opposite sign in the neighbouring strips. This behaviour makes the common mode noise subtraction dangerous for both views and for large bunch multiplicities. For this reason common mode correction was disabled in the reconstruction of Run 2 data. In Figure 5.14 the X and Y profiles are shown for a focused bunch of 10000 positrons without common mode noise subtraction. The spot size is larger in the Y direction with respect to the X direction. As expected, the beam position in the Y direction was found to be stable across Run 2, due to the collimators and quadrupoles settings, without any dependence on the bending magnets. The Y strips hit by the beams are

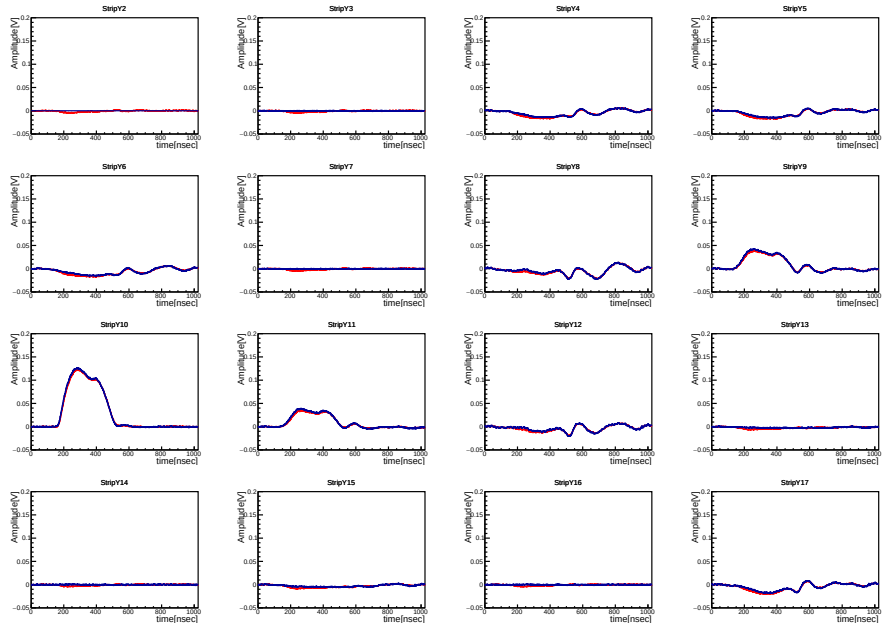

Figure 5.13: Y2 view waveforms after pedestal subtraction calculated with the first 100 samples (red plot) and after Y2 waveform subtraction (blue plot). The beam conditions are the same of plot in Figure 5.12.

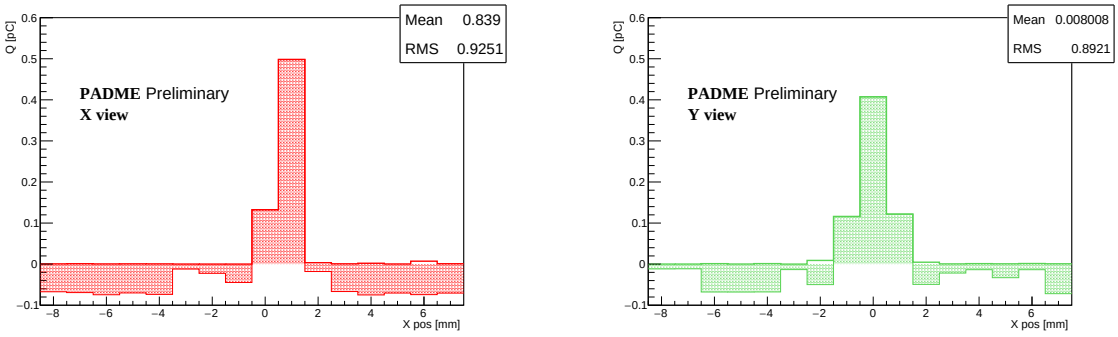

Figure 5.14: X (left) and Y (right) beam profiles of a single bunch in Run 2. The beam conditions are the same of plot in Figure 5.12

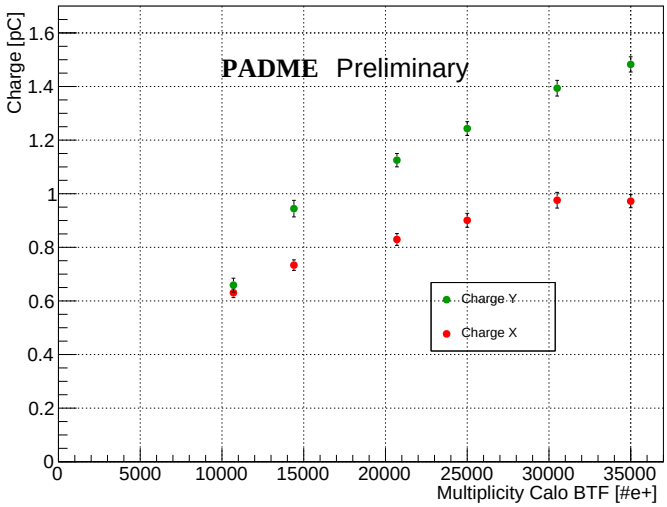

Figure 5.15: Apparent charge collected by the plane of X and Y strips as a function of the bunch multiplicity as provided by the BTF calorimeter with Run 2 data. All beam conditions except the varying bunch multiplicity are equal to those in Figure 5.12. The errors are obtained from the width of the Gaussian fit of the charge distributions.

always one central strip whose amplifier is working in non-linear regime and two lateral strips collecting a charge well below the limit of linear response. All these features allow the extraction of the bunch multiplicity using the beam tails in the Y view. A multiplicity scan during the Run 2 was performed, with the purpose of producing an absolute calibration of the target charge measurement. In Fig 5.15 the total apparent charges collected by the X and Y strips is reported as a function of the bunch multiplicity. As anticipated, this measurement does not allow for an estimate of the bunch multiplicity, due to the saturation of the front-end.
Figure 5.16 shows the apparent charge collected separately by three individual strips in the Y plane, Y10 receiving the core of the beam spot, and the neighbouring strips, Y9 and Y11. The front-end channel of the central strip saturates and the charge is not correlated to the beam multiplicity above 15000 positrons. However, the charge collected by Y9 and Y11 , due to the beam tails, is linearly related to the beam multiplicity. This suggests to extract the bunch multiplicity by the average charge in the lateral strips, thanks to the linear correlation to the beam intensity. The different slopes between charge and multiplicity for the two lateral Y strips is likely due to a small vertical movement of the beam between calibration steps. On the other hand, in the mean of the charges the effects of a small vertical beam motion on the individual strips cancel out and a reliable estimate of the number of particles per bunch can be obtained for the Run 2 beam conditions. In Figure5.16 the black dots represent the mean of the charge collected by Y9 and Y11. A linear fit provides the calibration constant for a bunch multiplicity measurement valid in Run 2. Figure 5.17 shows the distributions of the bunch multiplicity measured by the target calibrated with the beam tails method, for the same multiplicities provided by the BTF calorimeter in Figure5.16.

5.2 Active diamond target performance

The PADME active diamond target designed and realized in Lecce showed good performance[146]; since the first operational day it has provided a reliable measurement of the number

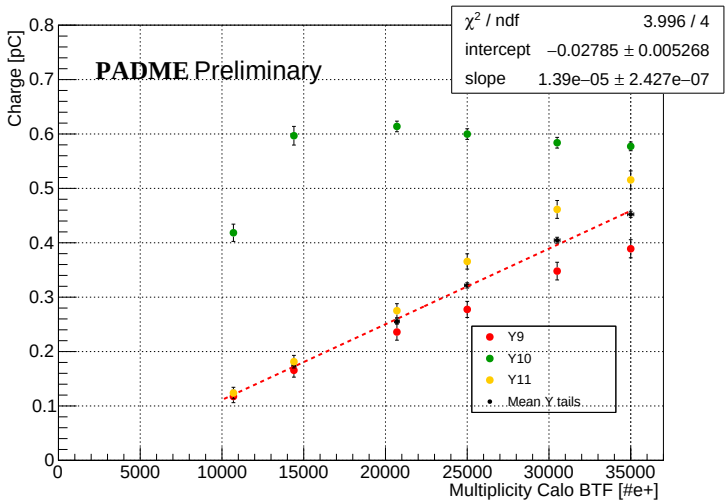

Figure 5.16: Apparent charge collected by the three strips in the Y view hit by the focused beam in Run 2, Y9, Y10 and Y11. The black data points refer to the mean average value of the lateral strips Y9 and Y11, receiving the beam tails. All beam conditions except the varying bunch multiplicity are equal to those in Figure 5.12. The errors are obtained from the width of the Gaussian fit of the charge distributions. In particular, the errors associated to the black data points are calculated with the usual statistical propagation of the error, rescaled to obtain a reduced χ^2 of the order of 1.

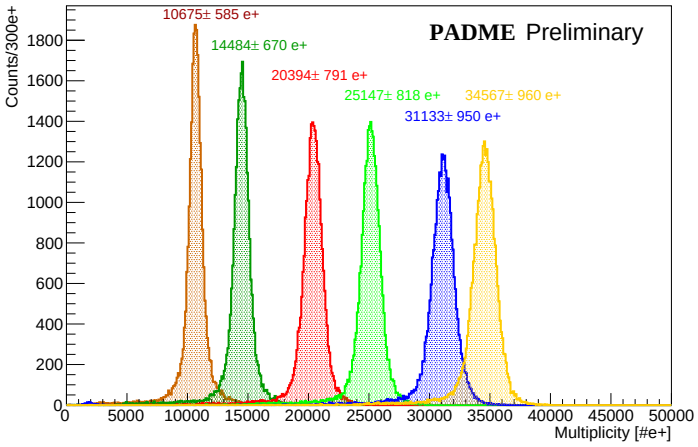

Figure 5.17: Distribution of the bunch multiplicity as obtained by the target after the absolute calibration of Run 2. All beam conditions except the varying bunch multiplicity are equal to those in Figure 5.12.

of positrons, reconstructing bunch per bunch the beam profile in X and Y. The proper detector operation showed the reliability and efficiency of the assembled procedure, even if two strips connections with conductive glue failed. The pioneered choice to assembly the diamond detector with graphitic strips in the final experiment turned out to be robust. In addition to that, the use of aluminium wire bonding to connect graphitic strips with printed circuit board resulted reliable. The good operation so far evidences the efficiency of the manufacturing chain that led to the realization of the diamond target. The detector met the requirement of the PADME experiment, as shown in detail in the rest of this chapter.

5.2.1 Charge Collection Distance

An important figure of merit for detector-grade diamond is the charge collection distance (CCD), already introduced in section 3.1.3.
The CCD can be calculated as follows, assuming, according to literature, that the charge generated by a m.i.p. in diamond is 36 e-h pairs/ μm:

$$CCD = \frac{Q_{X(Y)tot}[e^-]}{N_{e^+} \cdot f_{active} \cdot 36[e^-/\mu m]} \tag{5.1}$$

where $Q_{X(Y)tot}$ is the mean of the total charge collected by each view, N_{e^+} the number of positrons crossing the detector, f_{active} is the fraction of detector active area, a geometrical factor taking into account charge collection inefficiencies.
From the slope of the linear fit in Figure 5.4, a CCD value of $\sim$12 μm is derived.
The fraction of active region is set to f_{active}=1.
Indeed, the active region can be affected by different sources of inefficiencies.
The first source of inefficiency is due to the 150 μm inter-strip gap which must be treated as dead gap, as reported also in the study of the charge sharing (see Section 5.3.1). The total inefficiency in both views reduces the fraction of active area to $f_{active,gap,X,Y} = (1 - 0.15)^2 \sim 0.72$.
The second source of inefficiency is due to unconnected strips and can be measured from beam profiles. Considering the cumulative profiles for 100 events, the computation of the fraction of charge loss can be estimated, as seen in Figure 5.18. The cumulative profile was considered to compensate beam fluctuations. The fraction of beam charge loss is calculated as:

$$\frac{Q_{totxinterp} - Q_{totx}}{Q_{totxinterp}} \tag{5.2}$$

where $Q_{totxinterp}$ is calculated summing up the charge collected by the X view and a fictitious charge assigned to the unconnected strip, calculated as the mean of the charge of the adjacent strips. Hence, if the unconnected strip is the n-strip, its charge is:

$$Q_n = \frac{Q_{n-1} + Q_{n+1}}{2} \tag{5.3}$$

The charge loss is of the order of 3%.
The calculation of the total fraction of active detector has to consider these sources of inefficiencies:

$$f_{active} = f_{active,gap,X,Y} \times f_{active,deadstrip} \sim 0.7 \tag{5.4}$$

Hence, the real CCD value can be computed:

$$CCD_{real} = \frac{CCD}{f_{active}} \sim 17 \ \mu\text{m} \tag{5.5}$$

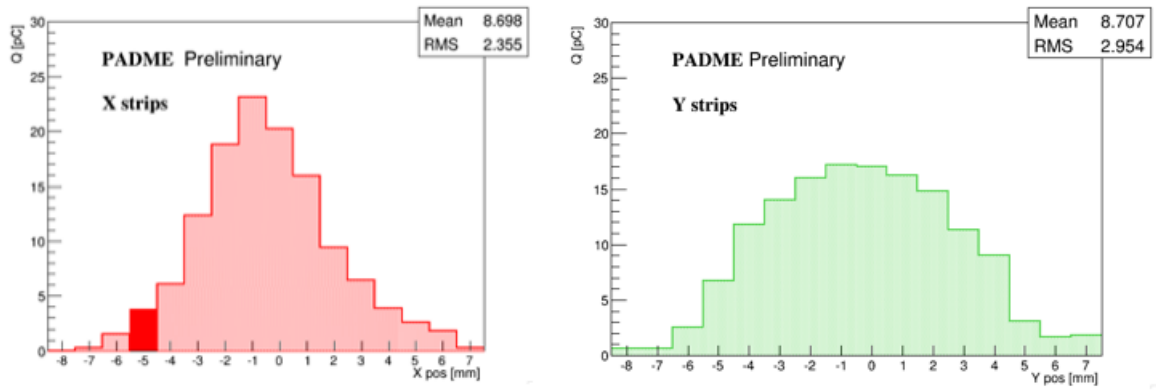

Figure 5.18: X (left) and Y (right) profiles of 100 events; the total charge collected in the X view was used to extract the fraction of charge loss due to the unconnected X strip.

This value can be contrasted the CCD of the 50 μm thick target prototype, built with CVD diamond from the same vendor and nominally of the same quality, measured to be 11 μm in a test beam held in November 2015[131]. The measured CCD value does not scale like the thickness of the CVD diamond film as one could naively expect, anyway a substantial increase is observed[147].

5.2.2 Spatial resolution

For each event the charge centroid for both views X and Y was stored. These quantities were obtained fitting the X and Y profiles with a Gauss function plus a constant background with initial parameters given by the average and the RMS of the profiles. The spatial resolution, measured as the width of the distribution of the charge centroid, is 0.0616 $\pm$0.0016 mm for the X view (Figure 5.19), well below the requirement dictated by the missing mass design resolution.

5.2.3 Beam position

The capability of the target to monitor the real position of the beam was studied by moving the target in the x direction thanks to the remotely controlled motor. The charge centroid in the X view, as a function of the real physics displacement, is shown in Figure 5.20. The position scan was done moving the active target direction in 10 steps of 1 mm each. The slope of the fit gives an estimate of the correlation between the X centroid and the X displacement is 0.9, which means that the response of the target is reasonably linear moving physically the detector and leaving the beam in the same position.

5.3 Performance with focused beam

With the beam of 2018-2019 data taking the absolute detector calibration was performed and the main detector properties measured. These are: dead strip maps, charge collection distance, noise, spatial resolution and beam profile reconstructions. The focused beam of the 2020 data taking allowed to understand the effect on the charge response of the presence of the inter-strip gap, to quantify the spatial uniformity of the detector response, and to study the behaviour of the detector at the border.

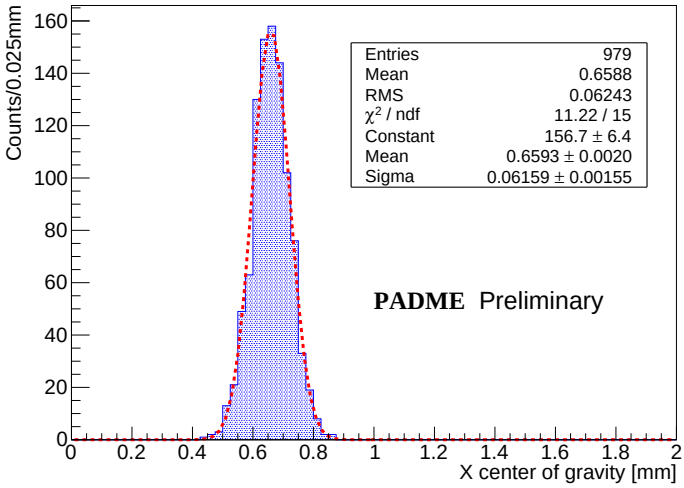

Figure 5.19: Distribution of the charge X centroid. The spatial resolution can be obtained from the width of the fit. The detector bias voltage is -250 V and the positron bunch multiplicity is about 20000 with an energy of 545 MeV.

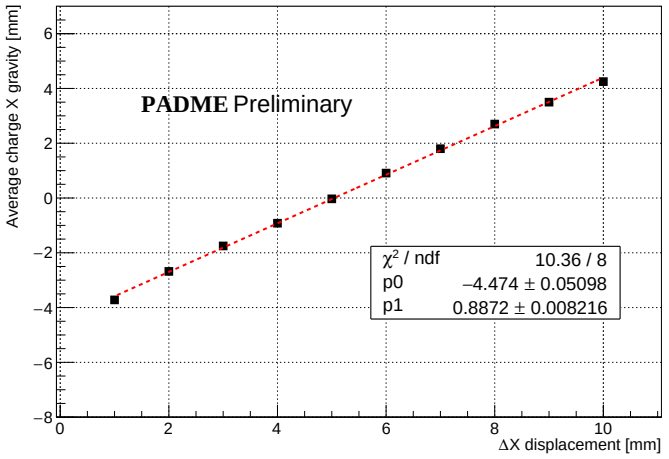

Figure 5.20: The X charge centroid as a function of detector horizontal displacement.

5.3.1 Charge sharing region

The presence of the inter-strip gap can be a source of charge collection inefficiency which should be quantified. The study was carried out in special runs collected in July 2020, featuring a beam spot diameter of about $\sim$ 1 mm and a beam multiplicity of about 7500 positrons per bunch, a condition that in PADME is as close as possible to the ideal setting for such study, i.e. small beam spot and low beam intensity to contain saturation effects. A scan of the target in the X position was performed in steps of 50 μm, spanning a total distance of 1 mm, which is equal to the strip pitch. The scan started with the beam centroid well centred on one strip and finished when the beam centroid reached the center of the next strip. In this way the inter-strip gap between the two strips was finely probed by the beam. Figure 5.21 (left) shows the central and the two extreme positions in the scan. In Figure 5.21 (right) the charges collected by the

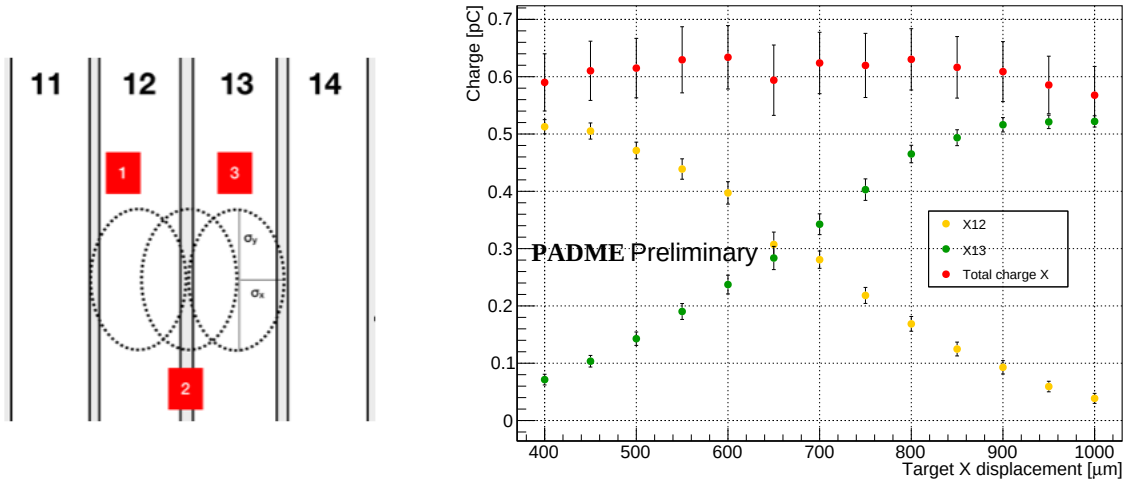

Figure 5.21: On the left a drawing of the beam spot in the estreme (1 and 3) and in the central (2) configurations of a position scan in steps of 50 μm meant to study the charge sharing effects. On the right the charge collected by the X view and for strips X12 and X13 for different target X displacement in steps of 50 μm. For the X displacement equals to 650 μm the beam is focused between strip X12 and X13. The errors are obtained from the width of the Gaussian fit of the charge distributions.

two vertical strips involved in the measurement, X12 and X13, are shown, together with the total charge collected by the X view as a function of the target absolute position measured with respect to an arbitrary origin. When the absolute position is 650 μm the beam centroid is in the gap as indicated by the charge equally shared between the two strips. The amount of charge loss due to the presence of the inter-gap can be inferred comparing the charge collected in the x plane when the beam centroid is at the center of the inter-gap and the charge recorded when the beam spot is contained on one strip. However, Figure 5.21 shows that for a displacement higher than 150 μm from the center of the inter-strip gap, the front-end channel of the strips start to saturate, since the apparent collected charge exceeds 0.5 pC. Therefore, the total charge collected when the beam is fully contained in one strip must be estimated with an extrapolation of the trend of the charge observed on that strip in conditions of even charge sharing between two strips. An extrapolation of the linear trend leads to an estimate of the relative variation of the charge above 15%, i.e. above the geometrical ratio between the strip pitch and the width of the gap. However, the linear approximation is clearly naive and overestimates the effect, since it assumes a flat profile of the beam spot. However, these considerations seem to confirm the assumption, used for the estimate of the CCD in section 5.2.1, that the inter-strip gap is a region of total inefficiency.

5.3.2 Detector border effects

The focused beam can measure the spatial uniformity of the detector response by scanning the detector in the x direction up to the border where the beam hits also the carrier board. In PADME the target can only be moved from its nominal (central) position towards its parking position on one side. The stop, used to avoid clashes with the MIMOSA pixel detector in case of positioning mistakes, does not allow to move the target beyond the central position.
For this reason the position scan can only be done for one half of the detector, from X9 to

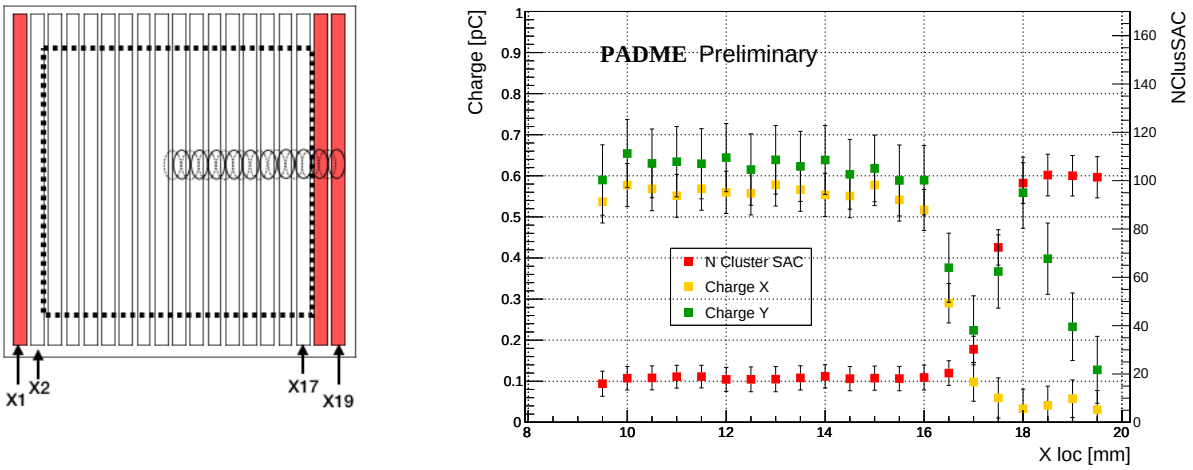

Figure 5.22: On the left, a schematic drawing of the varying beam spot position on the target during the position scan meant to study the target uniformity. The white strips are connected to the front-end and powered. The red strips are only powered. The dotted lines represent the carrier board edge. On the right the average charge collected by the X and Y strip planes and number of clusters on SAC during a position scan of the target in steps of 500 μm, starting from a position in the middle of strip 9 and 10. The errors are the width of the Gaussian fit of the charge distributions.

X19. For this spatial uniformity test the detector was moved in steps of 500 μm, with an initial position where two X strips were equally hit by the beam (see the drawing on the left in Figure 5.22). The graphs on the right in Figure 5.22 show the charge collected by the X and Y views as a function of the beam position in the x local reference frame. The total charge collected by X and Y views are quite constant far away from the detector border, with small but systematic jumps most likely due to the interplay between saturation and beam containment in the active area of the strip collecting most of the beam spot. In the same plot the red dots show the number of clusters observed in the SAC; it increases rapidly when the beam reaches strip 17 and 18, i.e. when the beam starts crossing the material of the diamond carrier board in addition to the diamond. The behaviour of the different curves can be explained considering the geometry of the detector (sketched in Figure 5.22 left) and the beam position changing in x but stable in y. Taking in mind that all Y and X strips, up to X19, are connected to the HV, one can understand that the Y plane collects a charge decreasing substantially only when the center of the beam is on strip 19, i.e. at the end of the region where the electric field guarantees charge collection. The hole at X17 can be explained by the absence of drift field in that region assuming the HV connection of this strip is damaged. On the other hand, the X plane reads the charge only up to strip X17, since X18 and 19 are not readout, and this, combined to the inefficiency of strip X17 to collect charge, explains the sharp drop at strip X17 of the charge measured on the X view. Unfortunately, during the assembly of the target detector it was not possible to verify the electrical connection of strips, like X17, overlapping with the carrier board, therefore the hypothesis of a damaged electrical connection for strip X17 does not clashes with any previous measurement.

Chapter 6

The Bremsstrahlung process in PADME

The challenge of identifying the dark photon signal in PADME relies mainly on the capability of the experiment to reject the background from Standard Model processes or from instrumental and beam related effects. The main source of physics background in the experiment is the Bremsstrahlung process that can produce a single photon in the final state in ECAL, mimicking the photon of a signal event. The target, consisting of a low Z material, helps to contain the Bremsstrahlung rate ($\sigma_{Bremm} \propto Z^2$). However, a specific background suppression strategy is necessary to accomplish the dark photon analysis. A positron slowed down in the interaction with the target by an amount of energy equal to the energy of the emitted photon, is bent by the PADME magnetic field and can hit the veto detector inside the dipole (PVeto) or the high energy positron veto (HEPVeto), next to the beam dump. Since the target is very thin, the total amount of energy in the final state is equal to the beam energy. A photon in time coincidence with a signal in the veto detectors, consistent with a positron having radiated that photon, can be rejected as a candidate Bremsstrahlung photon. Given the relevance of this background for the PADME sensitivity, it is crucial to identify in the data a clear signal of Bremsstrahlung interactions and to compare the total yield and the main features of this background with the expectations to ensure that it is well modelled by the simulation and, overall, well understood. In order to achieve such a goal several auxiliary studies are needed: the cross calibration in time of the PADME detectors, the tuning with data of the response in simulation of the veto detectors for charged particles, the calibration of the spectrometer for positrons, and, finally, the definition of a selection for Bremsstrahlung processes and the strategies for the subtraction of the beam induced background. Two different approaches to the identification of Bremsstrahlung interactions will be discussed. One of them relies only on the interpretation of the distribution of hits in the PVeto, the other exploits the coincidence of signals in the PVeto and in the Small Angle Calorimeter (SAC), where most of the Bremsstrahlung photons are detected. Therefore, the modelling in simulation of the SAC is also scrutinized. As a step preliminary to the discussion of these topics, section 6.1 will present the main features of the PADME simulation and reconstruction software. Section 6.2 and 6.3 collects the studies concerning the PVeto and SAC performance and simulation. Finally, in section 6.4 the strategies for the identification of the Bremsstrahulung signal will be applied to the PADME data of July 2019, corresponding to 9.3×10^9 positrons on target collected in a few hours of run with a primary positron beam of energy equal to 490 MeV and more than 20000 particles per bunch, evenly distributed in a 150 ns long pulse. The results will be compared with the predictions derived from simulation and from a theoretical estimate.

6.1 The PADME software

The full suite of the PADME software, available on GitHub[148], includes several sub-components. The PadmeDAQ package contains the on-line software responsible for the data acquisition, PadmeMC is the package implementing a GEANT4[149] based simulation of the PADME experimental apparatus, and PadmeReco contains the infrastructure and the algorithms for the data reconstruction running both on the real PADME data and on simulated data produced by PadmeMC. An important service package is PadmeRoot hosting all the classes describing hits and clusters for the various detectors in a format shared by data and MC. Finally, PadmeAnalysis is a package implementing the generic framework for event selection and analysis. The reconstruction and analysis software, but also the simulation, are in continuous evolution from the beginning of the experiment, with the aim of improving the performance and of matching the simulation to the real beam and detector conditions. In this section, the PADME simulation and reconstruction software will be briefly presented to help the discussion of the analysis of the Bremsstrahlung process. I've developed several components of the PADME software in the area of reconstruction and simulation, from general services, like the geometry and calibration services, to algorithm development and tuning for the reconstruction of the data of the active target and of the veto detectors. The target specific software is the natural complement of the work on the detector described in chapter 3. The veto reconstruction and the tuning to data of the simulation for this detector was a preliminary and necessary step for the study of the Bremsstrahlung signal in the PADME data that will be discussed in Section 6.2.

6.1.1 Simulation

When the experiment was only a project, a first PadmeMC release was used to assess the physics potential of the experiment and to optimize the layout of the detector within the constraints of the experimental site. Today, the simulation is based on a pretty detailed description of all detectors and passive materials, including the main elements of the beam-line, which is fed as geometry description to GEANT4.

Physics generators

Since the main physics processes occurring in PADME are common electromagnetic interactions of a high intensity positron beam with the material of a target, the emulation of the main physics backgrounds is also based on GEANT4. The GEANT4 physics list adopted, i.e. the list of physics processes emulated when particles travel inside the materials, is the commonly used QGS_BERT which does not make any specific treatment of the electromagnetic interactions. Hence, the annihilation in two photons, Bremsstrahlung emission, multiple Coulomb scattering, synchrotron radiation emission, and optionally optical photons tracking are treated in PadmeMC with the default GEANT4 setting. In particular, Bremsstrahlung is implemented according to the Seltzer-Berger model [150] based on extensive compilations of tables of theoretical cross sections differential in the photon energy both for the interaction of the beam particle with the nucleus and with the atomic electrons. The accuracy is expected to be below 5% in a wide range of the kinetic energy of the incoming electron or positron. The angular distribution of the emitted photon is described according to the approximation of the Tsai formula[151, 152] whose accuracy is not expected to exceed a few percent. The annihilation in flight of a positron with an electron of the material, leading to the production of two photons, is described by the differential cross section formula of Heitler[153] in the approximation of electron at rest and ignoring the suppressed contributions of three or more photons in the final state. The SM annihilation in three photons $e^+e^- \to \gamma\gamma\gamma$ is simulated with the CalcHEP [154] generator, outside Geant4. A

dedicated generator of the process $e^+e^- \to \gamma A'$ is implemented in PadmeMC to simulate the dark photon production. Finally, a single particle generator can be used to produce dedicated samples meant to perform software optimization or detector calibration studies.

Beam simulation

PadmeMC includes a simulation of the beam-line with all the junctions and pipes starting from the Be window of thickness 250 μm which divides the vacuum of the LINAC from the one of PADME. The last bending dipole before the PADME target is an essential component of the beam-line that is also simulated. The set-up of the BTF line in use up to July 2019 is therefore reproduced with a good level of details. A realistic simulation of the beam including energy spread, bunching, energy, intensity and beam spot is essential for PADME. The values of all these features can be chosen through data cards. In addition, it is possible to choose the starting point of the beam in the line, in order to allow the production of simulations useful to understand the detector behaviour. For example, samples with the beam originating just before the target allow to study the response of the veto system using single positron beam and also the behaviour of the calorimeters, producing photon probes. The upgrade of the beam-line occurred from September 2019 is not yet implemented in the simulation.

Magnetic field

The simulation of the magnetic field of the PADME magnet is implemented in a specific class. The Magnetic Measurements Laboratory of the INFN National Laboratory in Frascati provided a detailed map of the magnetic field produced by the dipole at nominal conditions inside the magnet yoke and extending also outside the physical size of the magnet. This map was included in the simulation using the electromagnetic field package provided by GEANT4. The effect of the fringe field, i.e. the magnetic field outside the dipole yoke, is also taken into account.

Detector simulation

The positioning, together with the dimensions of the components of each detector are adjustable parameters of the simulation. Their values are set according to design technical drawings and to on-site surveys. The main passive materials of the experiment are also simulated, in particular the vacuum vessel and all the detector supports, like the target carrier board, the veto Aluminum guides, the ECAL entry flange. A specific sub-package for each detector is responsible for implementing the collections of simulated hits, based on the interactions of the particles traversing the active volume of the detector with the material, managed by GEANT4. Every hit holds a position, the energy released to the material and the time of the interaction with no smearing and resolution effects other than those due to the physics processes relevant in particle propagation through matter, i.e. multiple scattering, stochastic fluctuations in the energy loss, etc. In a subsequent step, the simulated hits are re-organized into collections of digits, which appear as real data, i.e. they hold the identifier of the detector channel where the energy was deposited, in addition to a energy and a time that arise from the original hit properties modified by the emulation of the detector specific time and energy resolution. In some cases a digit is produced for each hit produced by GEANT4 in a given detector channel, in other cases hits close in time are merged into one digit.

The simulation flow

The MC flow is shown in Figure 6.1. The event generator produces the final state particles that are propagated inside the apparatus by GEANT4. In this process, simulated GEANT4 hits are

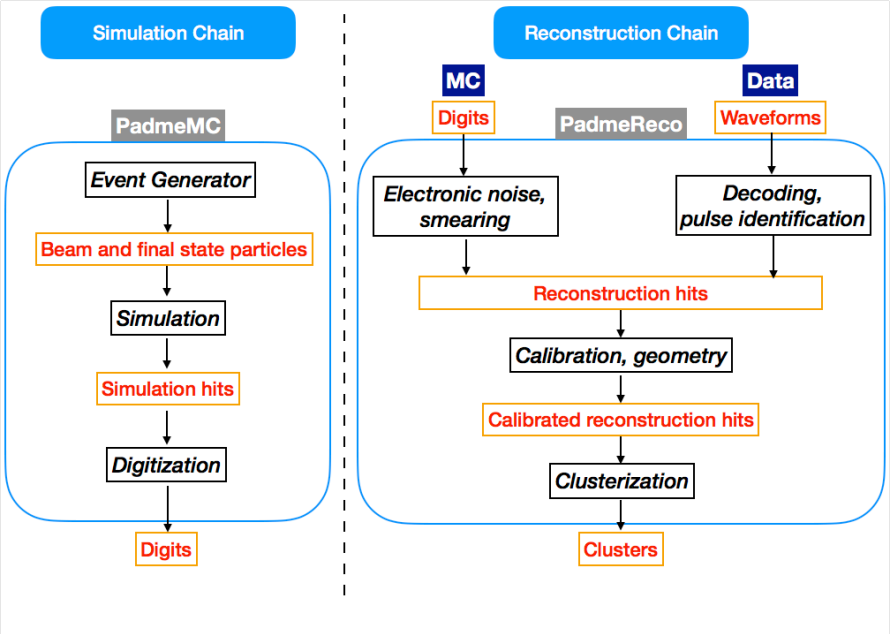

Figure 6.1: Block diagrams of the PADME software for the simulation chain, on the left, and the reconstruction chain, on the right.

generated according to the physical interaction of the particle with the material of the detector. Later, the GEANT4 hits has to be converted into digits. In this phase it is possibile to choose the digitisation time window. If two or more GEANT4 hits occurred in the same detector element with a distance in time one from the other smaller than the digitization time interval, they are merged into a single digit. This feature is useful to emulate the pile up due to the front-end response. The tuning of this feature for the veto detectors in particular will be discussed in detail in chapter 6.2.4. The output of the MC simulations consists of digit collections for all detectors. From this point the reconstruction software is able to run on both the MC output and data.

6.1.2 Reconstruction

The PADME reconstruction software is written in C++; both data and MC can be reconstructed using the same package, in order to have physical objects of the same format in output. The data flow is different for MC simulated events only in the first step (see Figure 6.1). When simulated data are input to the reconstruction, a dedicated method in the reconstruction class allows the conversion of digits into reconstruction-hits, instead when data are processed, a dedicated class analyses each waveform, extracting one or more reconstruction-hits. A calibration service processes the hits by applying calibration constants to adjust time and energy. A geometry service provides a conversion of the channel identifier into a position in space for the hit, according to the global PADME reference frame. Once the reconstruction-hits are produced, the same clusterization algorithm for MC and data builds the objects used by the analysis: clusters of energy in the calorimeters are candidate photons, and clusters of hits in the veto detectors are positron or electron candidates. Their position and time are the energy weighted average of the position and times of the constituent hits, while the cluster energy is the sum of the energies. The clusterization process starts from a seeding hit passing a threshold in energy and associates satellite hits next in space and time according to criteria that are optimized in simulation. In the special case of the target, the clusterization step is replaced by the reconstruction of the beam

profiles, i.e. the centroid and width in x and y, and the estimate of the number of positrons hitting the target in the event.
From the reconstruction output format is then possible to run the analysis.

6.1.3 MC and data samples

The different periods of PADME data taking runs were presented in Chapter 4.
During the last week of July 2019 one run was recorded in particular (referred to as the *July 2019 Golden Run*), which was taken as reference for the analysis study. In order to understand the SM background processes and the beam background, a run with the same beam conditions but with target off beam was recorded soon after the *Golden run*.
The two runs were used to perform the Bremsstrahlung analysis presented in this thesis work. In Tab. 6.1 the features of the two runs are summarized.
The DAQ setup of these runs included three trigger types: BTF, cosmic rays and a delayed trigger. The events recorded with these two last triggers were the $\sim 6\%$ of total events (CR) and only $\sim 2\%$ for the delayed one. A MC was produced with the same characteristics of the

Data sample	N events	BTF trg ev.	NPOT	Period
Target in	476288	440202 ($\sim$92.4%)	9.31×10^9	Jul.2019
Target out	429200	396719 ($\sim$92.4%)	8.4×10^9(ext)	Jul.2019

Table 6.1: Features of the Run 1 runs used to perform the Bremsstrahlung analysis presented in this thesis work.

reference run, 23000 positrons per bunch distributed in 150 ns.

6.2 Data processing and simulation of the Veto detectors

Similarly to what happens to all PADME detectors, the signals from the PVeto, HEPVeto and EVeto detectors are recorded as waveforms digitized by CAEN V1742, then processed by a hit reconstruction algorithm, and, finally, processed by a clusterization algorithm that groups hits produced by the same charged particle hitting one or more neighbouring scintillating bars. The position of the cluster can then be related to the initial kinetic energy of an electron or positron originated in the target. In this way the veto system, thanks to the PADME magnetic field acts as a spectrometer for charged particles.

6.2.1 Geometry and conventions

Before presenting data from the PADME veto and SAC detectors, it is useful to define the general PADME convention on geometry and detector identification that allow the description of the absolute and relative positions of the various detector elements. All of these conventions are shared by MC and data. The global reference frame adopted has its origin in the center of the PADME magnet, the z axis runs longitudinally in the direction of the incoming beam, the y axis is vertical and points upwards, and, as a consequence, the x axis, in the horizontal plane, is perpendicular to the beam and pointing towards the PVeto detector. In Figure 6.2 the reference frame is superimposed to a schematic view of the PADME detector, for illustration purposes. In the plot the conventional numbering of the scintillating bars in each of the veto detectors is shown. Hits obtained from the processing of signals readout by the ADC connected to a given bar, will be given in the software a label (channel identifier, sometimes shortened with Ch.ID, defined according to the numbering shown in the plot) that will be used to compute the position

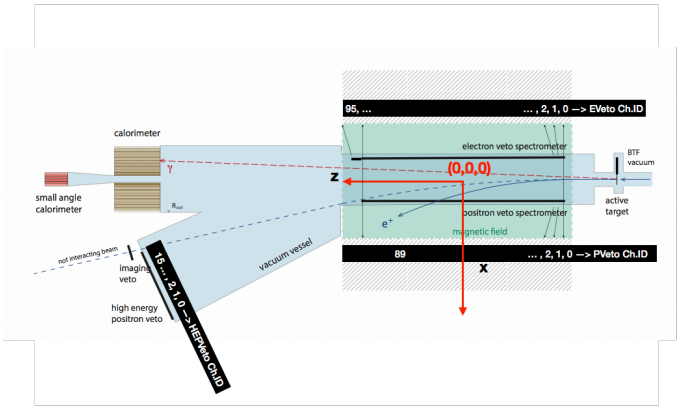

Figure 6.2: A schematic view of the PADME detector with the PADME reference frame and the convention on the numbering of the scintillating bars assembled in the PVeto, HEPVeto and EVeto detectors.

of the hit. The mapping of ADC boards and channel to channel identifiers of detector elements is loaded from configuration files in the initialization step of the reconstruction software and used in the data decoding, before any reconstruction algorithm is executed. In the case of a hit in a scintillating bar of the PVeto, for example, the geometry service, will assign a location to the hit in the global PADME reference frame with:

$$x = 192.5 \text{ mm}, \quad y = 0 \text{ mm}, \quad z = -446.55 \text{ mm} + \text{ChId} * 11 \text{ mm}$$

where 11 mm is the pitch of a scintillating bar in the array. From the sketch in Figure 6.2 one can see that the beam of particles of nominal energy, i.e. the positrons that do not undergo relevant interactions in the target (or elsewhere in their path to PADME), reach the beam dump location, where Timepix is hosted, passing just outside the acceptance of the PVeto. Positrons of energy close but below the nominal beam energy cross the latest bars of the PVeto impinging with a large incidence angle with respect to the PVeto array, so that often they traverse more than one bar. Eventually, these tracks reach the HEPVeto detector hitting the plane of the detector almost normally. The same convention is also used for the MC reconstruction.

6.2.2 Hit reconstruction

A typical veto waveform is digitized at a rate of 2.5 GS/s, hence 1000 samples span 400 ns. Figure 6.3 shows several pulses overlapping in the recording time window of the signal. The scintillating bar where this signal is produced, channel 72, is close to the exit of the PADME magnet where the rate of positrons releasing a small amount of energy in the interaction with the target is high. In addition, any particle in the low energy tail of the energy distribution of the beam may give additional contributions to the occupancy in that region of the positron veto detector. However, the fast response of the scintillators and of the SiPM used for the readout allows to pursue the strategy of a multi-hit reconstruction, aiming at resolving the multiplicity of hits occurring in a single channel at each burst of the beam. The first step of the waveform processing, preliminary to the hit reconstruction, is the pedestal determination and subtraction. The approach of deriving, with high statistical precision, stable values of the pedestals for each channel to be loaded and used in each event was studied and contrasted with the strategy of computing event by event and channel by channel the pedestal using the first 200 samples of

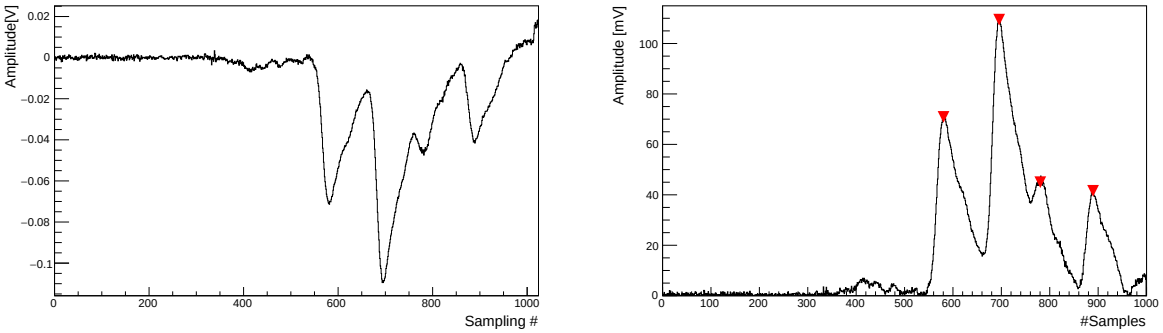

Figure 6.3: On the left a typical signal from channel 72 of the PVeto detector from a run with a primary positron beam. On the right, the same signal, changed in sign and marks indicating the peaks identified by TSpectrum.

the waveform that are free from signal pulses due to the trigger delay. The latter was found to be more robust against instabilities of the baseline of the digtizers and precise enough for the purpose of identifying candidate signals from ionizing particles.
A multi-hit reconstruction was performed using the TSpectrum algorithm, a one-dimensional peak search function of the ROOT[145] library. The position and height of each peak identified by the algorithm provide physical informations relevant for the analysis, representing the time and amplitude of the hit. The waveform of the veto is typically negative. For the peak search the absolute value of the samples is taken, in order to recognize positive peaks. A waveform is processed with TSpectrum if at least one sample is above 20 mV. The parameters of the TSpectrum are set in such a way that peaks must have an height exceeding 10 mV and a width of at least 6 samples. The validity of the method and the choice of the parameters is proven by the Landau-like shape of the pulse height distribution of the hits in the veto detectors. Examples are shown in Figure 6.4.

6.2.3 Energy and time calibration

Before any kind of analysis, it is important to obtain a gain equalization and a time alignment across all veto channels. Channel dependent calibration constants derived with special procedures are loaded from a database and applied as scale factors to the hit energy and as offsets to the hit time. As a consequence, the resulting distributions of energy and time becomes consistent for all channels, having corrected off-line any mismatch in the readout hardware of the different detector elements. The energy calibration impacts mainly on the result of the clusterization procedure. The time calibration affects not only the clusterization, but also any analysis involving time coincidence criteria among two or more detectors.

Gain equalization

The relative calibration constants for PVeto, HEPVeto and EVeto were obtained evaluating the distribution of the hit energy for each electronic channel of the vetoes, after setting a very low threshold for the hit reconstruction. A Gaussian fit in the region of the peak of the distributions allowed to estimate the most probable value of the pulse height distribution (see Figure 6.4) and the relative calibration constant for channel i, CC(i), was computed by rescaling the most probable pulse height to 50 mV, as follows:

$$\mathrm{CC\,(i)} \;=\; 50\ \mathrm{mV} / \,\mathrm{GM\ (i)}\,, \tag{6.1}$$

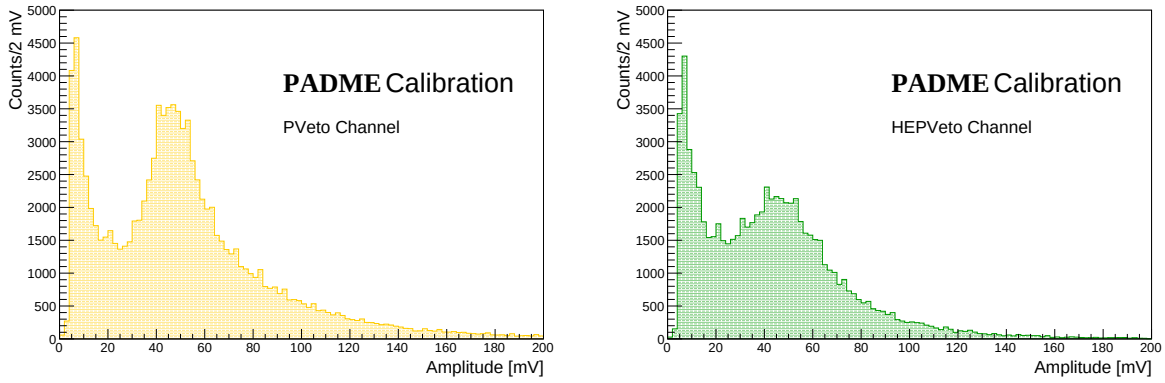

Figure 6.4: Pulse height distributions for hits in two veto channels, one from the PVeto (left) and one from the HEPVeto (right). The position of the peak is used to perform the gain equalization.

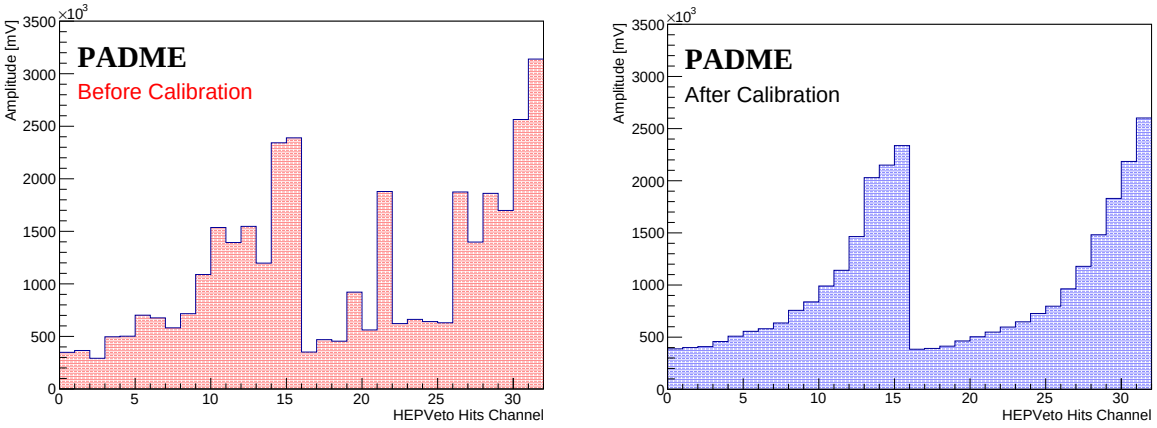

Figure 6.5: HEPVeto hit profile weighted with the pulse height, before (left) and after (right) the gain equalization. All the HEP Veto channels are shown, corresponding to the readout of two SiPMs per scrintillator, as already explained in Section 2.2.3.

where GM(i) is the mean of the Gaussian fit to the peak of the pulse height distribution for channel i.
These energy calibration constants are managed by the calibration service and applied only to data. In Figures 6.5 and 6.6 the HEP Veto and PVeto hit profiles weighted with the pulse height are shown, respectively, before and after the gain equalization.

Time alignment

A good global time alignment is crucial for the PADME experiment, due to the measurement strategy and the pulsed beam structure. The forward calorimeter (SAC) was taken as reference as it is the detector with the best time resolution in PADME. The time alignment was performed based on the conventional choice that hits produced by a Bremsstrahlung interaction have the same time stamp; hence the hit from an electron of any kinetic energy (i.e. in any scintillator of the positron veto, including the HEPVeto) produced along with a forward photon and the hit in the central crystal of the SAC from this photon share the same time stamp. It's worth noticing that this common time stamp is not the physical time when the hits are generated, but

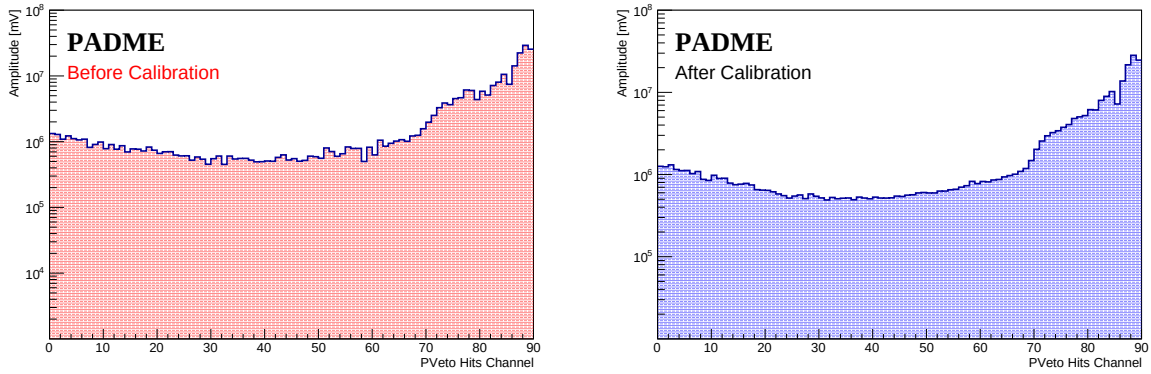

Figure 6.6: PVeto hit profile weighted with the pulse height, before (left) and after (right) the gain equalization.

it is a useful conventional choice to allow for easy coincidence logic at the event analysis level. In addition, based on this convention, hits in different, and far away, scintillating bars of the veto system produced by simultaneous interactions in the target share the same time stamp. Distributions of the difference in time between any pair of hits, one in a bar of the positron veto and the other in the central crystal of the SAC (ChID =22), were produced for each scintillating bar. The time correlation induced by Bremsstrahlung interactions is the key ingredient enabling the time alignment procedure, since they are responsible for a narrow peak in the distributions emerging over a combinatorial background. Figure 6.7 shows two examples of such distributions. The triangular shape of the background is indicative of the flat distribution of the hit time in each channel. A Gaussian fit of the peak is used to extract the original time shift providing the calibration constants to be applied at reconstruction level. The Bremsstrahlung process cannot help to define a time calibration for the EVeto unless special data taking conditions are established. For example, after inverting the sign of the current in the PADME magnet, Bremsstrahlung positrons are deviated towards the EVeto and the same procedure used for PVeto and HEPVeto might be applied. This study has not been performed yet. At the moment, the beam induced background provides the only way to achieve the global alignment of the EVeto with the other detectors. On the other hand, the internal time alignment can be obtained by requiring that the average time difference between hits in neighbouring scintillating bars is zero, profiting from tacks crossing more than one bar and from correlations induced by delta-rays. The same procedure was used both for data and MC and the time offset correction was applied by the calibration service both in the reconstruction of data and MC. The alignment in time between PVeto hits and hits in crystal 22 of the SAC as a function of the PVeto hit channel for data corresponding to the entire statistics of the *July 2019 Golden Run*, is reported in Figure 6.8. The plots for the MC simulation were produced emulating data conditions, described in Section 6.1.3. A global time offset between the PVeto and all ECAL channels (assuming no relevant time offsets are present between different BGO crystals) was corrected by centering to zero the peak in the distribution of the differences between the hits in the PVeto scintillating bar at the position z=0 mm (ChId 41) and the ECAL hits in any crystal.
The time alignment for ECAL is implemented based on the convention that photons produced at the same time (in the same interaction of a positron beam with the target) gives hits in the calorimeter that have the same time, irrespectively of the crystal position. After calibration, the scatter plots of the difference in time between the ECAL and PVeto hits as a function of the channel identifier shows that both for data and MC the time difference is well centred at zero (see Figures 6.10 and 6.11).

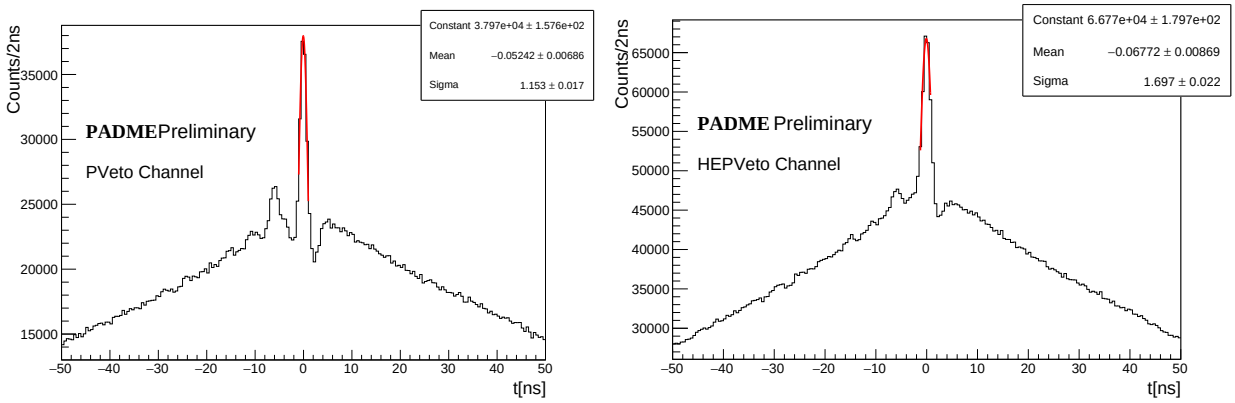

Figure 6.7: Distributions of the difference in time between a hit of PVeto (left) or HEPVeto (right) and a hit on the SAC central crystal. The mean of the Gaussian fit allows to obtain the offset to be applied in the calibration procedure.

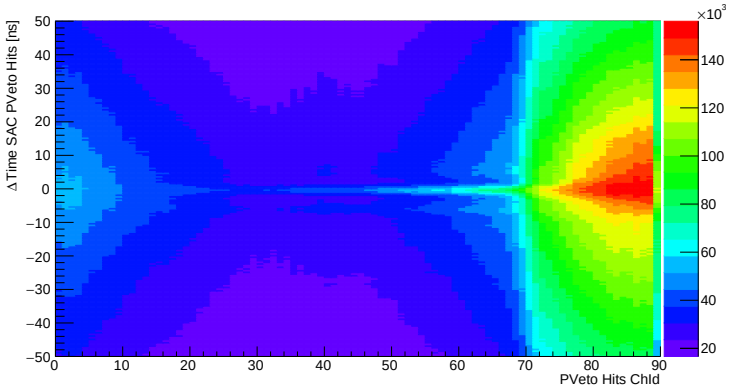

Figure 6.8: Time difference between SAC and PVeto hits as a function of the PVeto hit channel in the *July 2019 Golden Run*.

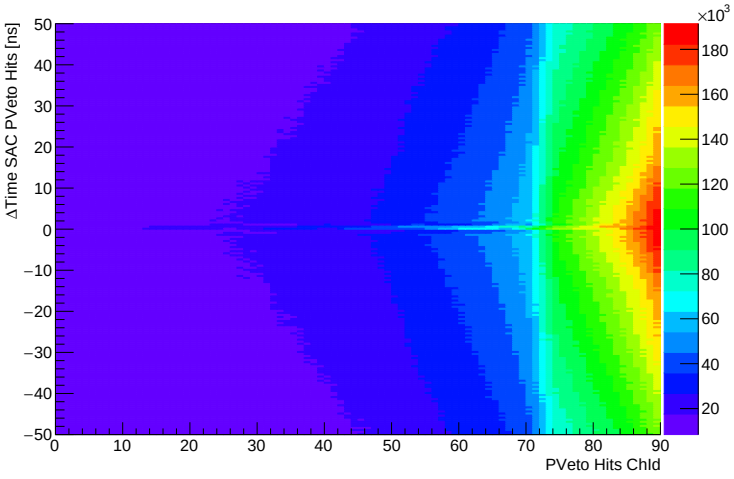

Figure 6.9: Time difference between SAC and PVeto hits as a function of the PVeto hit channel in MC.

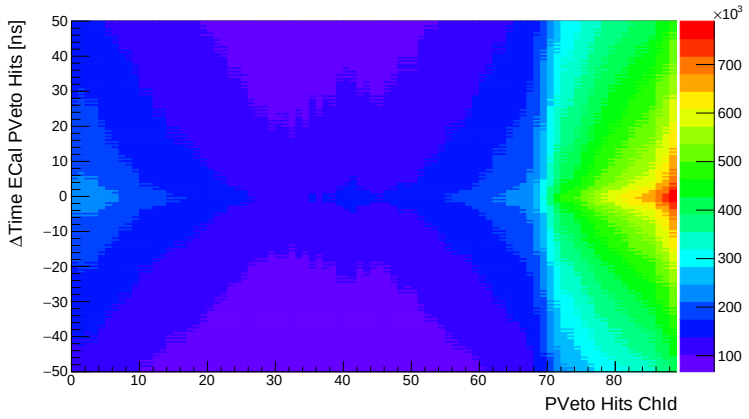

Figure 6.10: Time difference between ECAL and PVeto hits as a function of the PVeto hit channel in the *July 2019 Golden Run*.

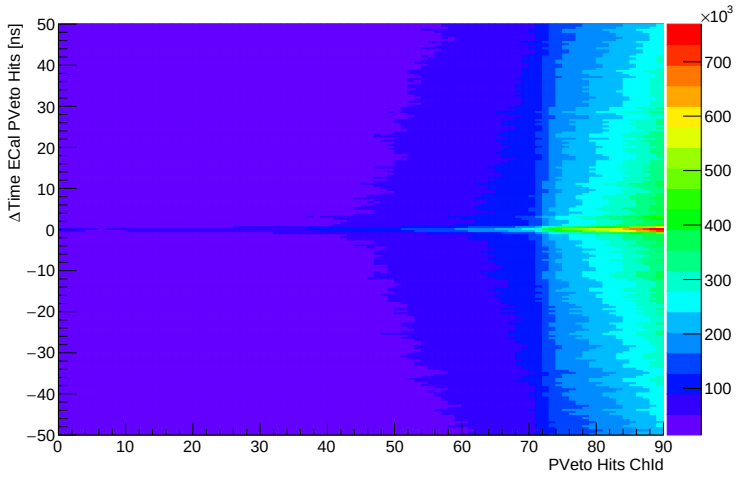

Figure 6.11: Time difference between ECAL and PVeto hits as a function of the PVeto hit channel in MC.

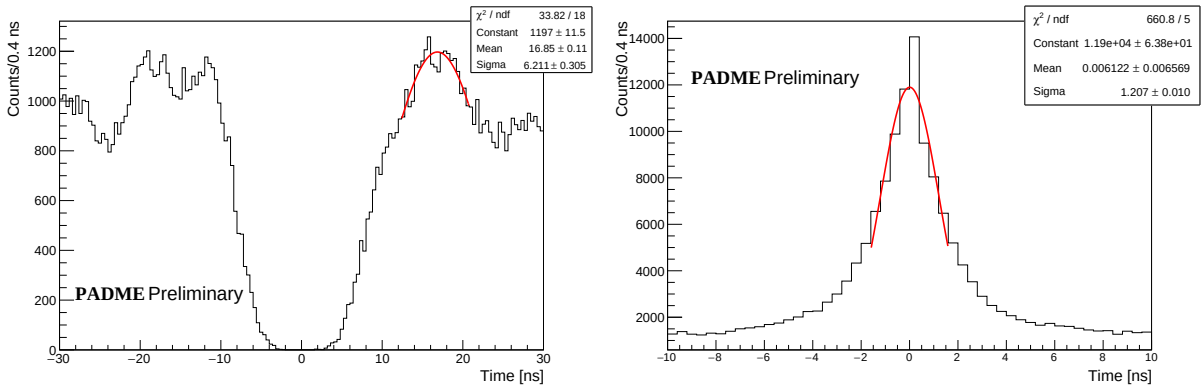

Figure 6.12: Difference in time between pairs of hits in the same scintillator bar and in two adjacent scintillators (right).

6.2.4 Tuning of simulation with data and reconstruction optimization

The response of a Silicon Photomultiplier (SiPM) to optical signals depends on many factors including photon-detection efficiency, recovery time, gain, optical crosstalk, dark count and also detector dead time. In addition, many of these parameters can vary with voltage and temperature. Also, the response of the SiPM to the incident light is usually non-linear. The impact of these effects on the detection of a single particle are limited, however, when combined with the presence of electronic noise, event overlapping due to pile-up or dead-times; their accurate simulation becomes essential to have a good description of the global response of the Veto detectors. The integration time of the veto front-end and also the finite capability of the reconstruction to distinguish two hits close in time are additional sources of inefficiencies, worsening the confusion arising from the pile-up. A handle in the simulation that can be used to tune the behaviour of the MC and adjust the PVeto response to that observed in data is the size of the digitization time window, i.e. the minimum time distance between simulated hits in the same detector element that are merged into the same digit. The minimum distance in time needed to resolve two hits in the same channel of the Veto detectors was estimated by considering the distribution of the time difference between any pair of hits in the same channel in data sample. The distribution is shown in Figure 6.12. The maximum of the distribution, occurring at a time distance of 17 ns, tells that this value is the effective double hit resolution in data, resulting from all the effects both hardware and software limiting the capability of distinguishing hits next to each other in time. Therefore this value has been applied as digitization time window.

In real data, the detector energy resolution, noise and threshold sensitivity are all effects that lead to an energy measurement not really matching the real energy released in the active material. The use of a conventional energy scale and reconstruction effects introduce additional reasons for a mismatch between measured and expected energy. A key step of the simulation tuning is, therefore, the matching of the energy response of the PVeto scintillators to data. To emulate the electronic noise, a random Gaussian noise centred in zero with fixed sigma was applied before the conversion of the digits into hits. Several tests allowed to choose the value of 0.4 MeV for the width of the noise distribution leading to a good agreement between MC and data. In the Veto reconstruction with the TSpectrum, the peak search applied to data (already described in Section 6.2.2) was set a threshold of 6 mV and the information associated to each hit in data was the pulse height, proportional to the energy released. The peak amplitude was set lower than the default one to perform energy cuts only at the analysis level. Hence, a conversion

factor between pulse height and energy was required to match the scale of data and simulation. This factor was derived looking at the MPV of the pulse height distribution in data, which exhibits a Landau-like shape, and the MPV of the Landau energy distribution of the energy of simulated hits in MC. The conversion factor equal to 29.52 mV/MeV factor was applied to data during the calibration process.
The resulting distributions of hit energy in the PVeto and HEPVeto for data and MC are shown in Figures 6.13 (left) and 6.14 (left). All the energy distributions shown refer to the *July 2019 Golden Run* and MC simulation with 23000 positrons per bunch, with a bunch length of 150 ns, similar to the one during data taking. The distributions are normalized to the number of positrons on target of the data sample (nPOT=9.3×10^9).

6.2.5 Clusterization: the candidate charged particle signal

Subsequent to hit identification and calibration, the clusterization leads to the reconstruction of candidate particle signals. For the veto detectors the clusterization merges in the same cluster adjacent hits that are far from the seed no more than two bars, where the seed is the most energetic hit.. The minimum distance in time allowed is set to 4 ns. The choice of this parameter is based on the study of the typical separation in time between hits in neighbouring scintillators. Figure 6.12 right shows the distribution observed in data, which has a width of about 1.2 ns. As a consequence, the clusterization time window is chosen to be about 3.3 times the time resolution. A very low energy threshold (0.1 MeV) was applied both to the cluster seed and to any other hit contributing to the cluster. The parameters of the reconstruction of the veto detectors are collected in table 6.2. The comparison between the cluster energy spectra

Parameters for Veto clusterization	
Threshold seed	0.1 MeV
Threshold hit	0.1 MeV
Δt clusterization	4 ns
Δcell	2 bars

Table 6.2: Parameters chosen for clusterization of the veto detector in MC and data.

in MC and data, for PVeto and HEPVeto are shown in Figures 6.13 (right) and 6.14 (right). Figure 6.15 shows the cluster size distribution in data and MC both for PVeto and HEPVeto. These studies and the resulting optimisation of reconstruction and simulation proved to be mandatory for the study of the Bremsstrahlung signal in the PADME data.

6.2.6 Positron momentum calibration

In PADME a charged particle emerging from the target enters in a region with a uniform magnetic field and it is deflected: most of the beam particles, that did not lose an appreciable amount of energy in the target, follow a trajectory that ends on the TimePix detector, while a slowed down positron hits the positron veto in a z position related to the component of its momentum in the direction perpendicular to the magnetic field. For this reason it is possible to measure the charged particle momentum directly from the z position of the veto cluster. A schematic drawing of the spectrometer capability of the veto system is shown in Figure 6.16; the positron passing through a uniform field follows a trajectory that is an arc of circumference. The momentum measured in GeV can be written as p = 0.3 BR, where B is the magnetic field measured in Tesla and R, measured in meters, is the radius of the particle trajectory inside the

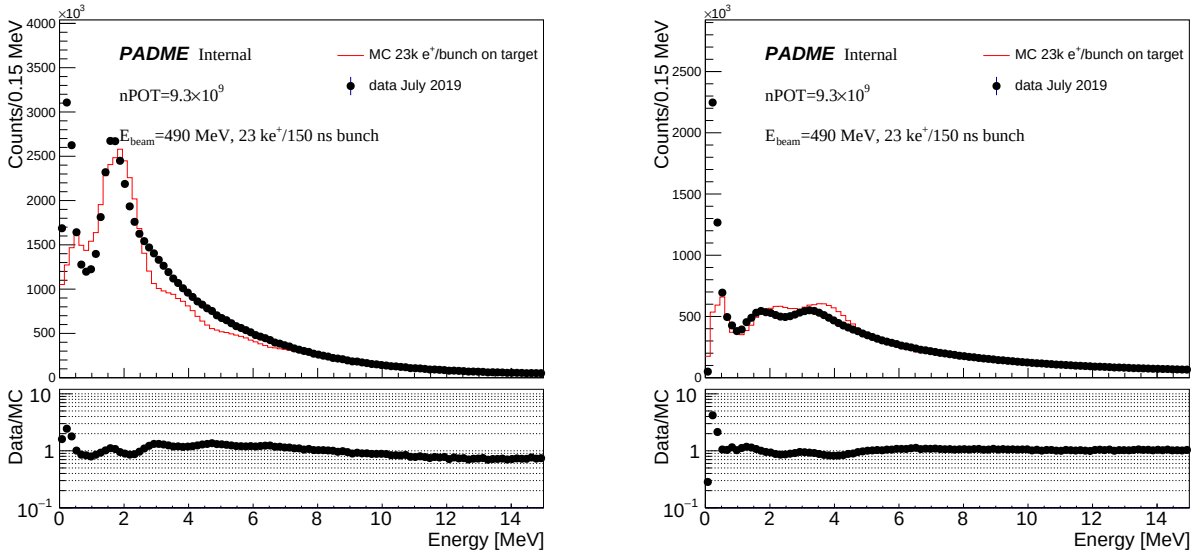

Figure 6.13: PVeto hits (on the left) and cluster energy (on the right) distributions for data and MC after tuning with data. The distributions are normalized to number of positrons on target recorded in data.

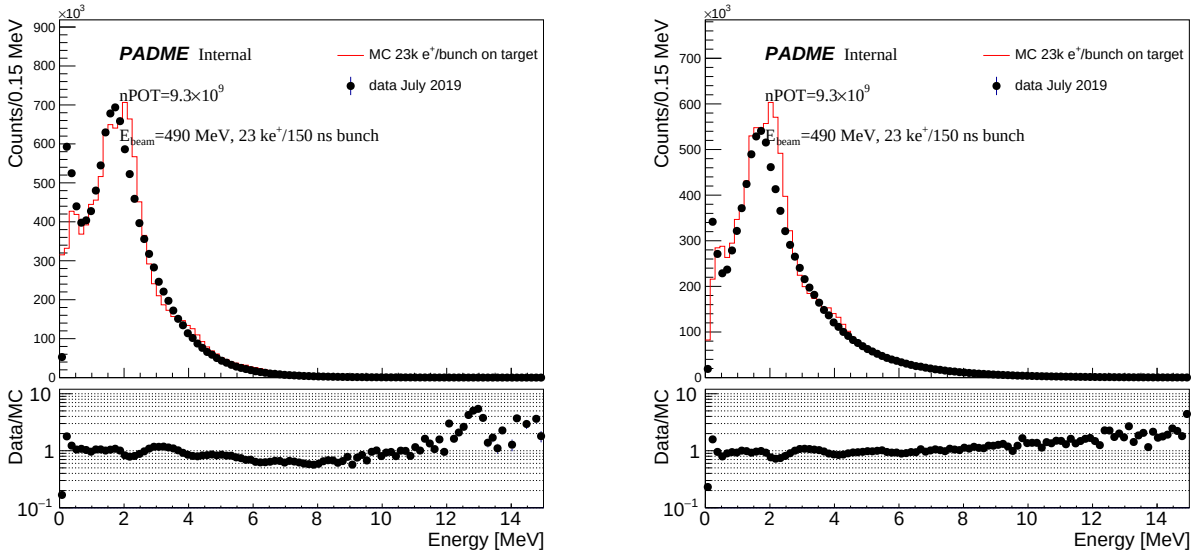

Figure 6.14: HEPVeto hits (on the left) and cluster energy (on the right) distributions for data and MC after tuning with data. The distribution are normalized for the number of positrons on target recorded in data.

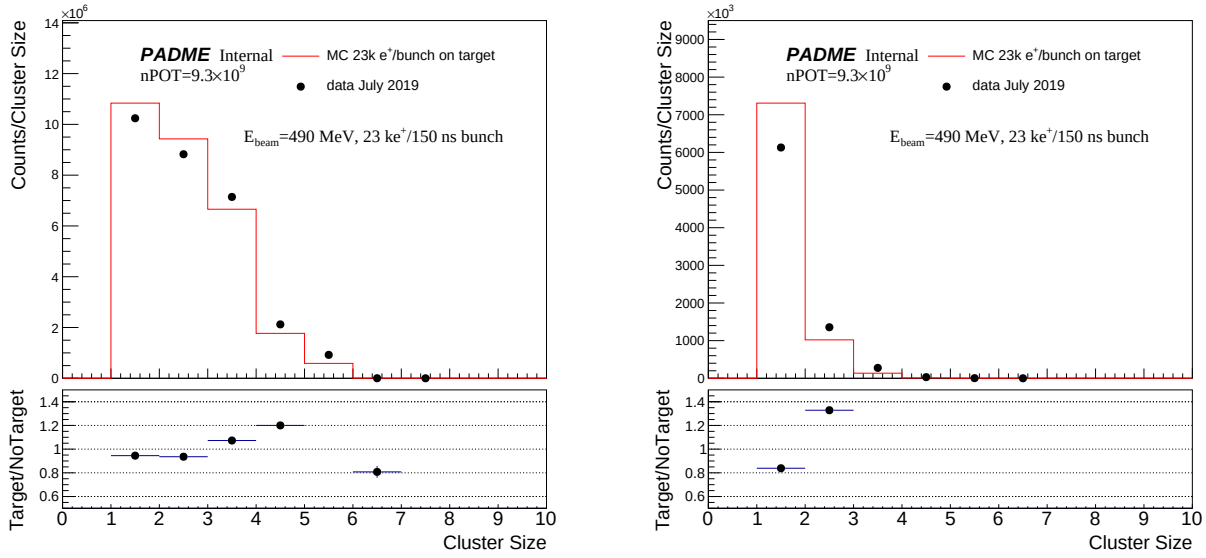

Figure 6.15: Cluster size in PVeto (left) and HEP Veto (right) after the tuning. The clusters considered have an energy >1 MeV.

PADME magnet. In the PADME reference frame this relation is specialized as follows:

$$p\,(z) = \frac{0.3\ B[(z - z_C)^2 + x^2]}{2x}, \tag{6.2}$$

where z_C is the z coordinate of the circular trajectory center and it is also the location where the magnetic field sets on. The x position is fixed for all the PVeto bars and set to 192.5 mm, which is the distance between the trajectory of the incoming beam, before deflection in the magnet, and the center of each bar.
This treatment does not account for the fringe field, i.e. the gradual decrease from the nominal value to zero of the beam intensity at the entrance of the dipole magnet.
A MC single positron simulation was used to extract the z position of the positron hitting the PVeto as a function of its energy assuming normal incidence at the center of the diamond target. In the simulation the magnetic field was described in details, including the map of the fringe field and the weak dependence on x of the intensity. The magnetic field in the nominal MC was rescaled to the beam energy of the July 2019 data taking (490 MeV) and set to a value of 0.408 T. The positron energy was varied from a minimum of 10 MeV to 490 MeV. In the MC the simulation of the chamber was disabled. Indeed the emulation of the internal vacuum chamber causes the first scintillating bars to be shielded by the low energy positrons that, bent by the magnetic field on a high curvature trajectory, would, otherwise, reach them. The correlation between z coordinate of the cluster in the PVeto and the kinetic energy of the positron predicted by this ad-hoc simulations is shown in Figure 6.17. This relationship can be considered a calibration in transverse (to the magnetic field) momentum of Bremsstrahlung photons of the PVeto detector. Indeed, the positrons that can be detected are ultra-relativistic and their momentum is well approximated by the energy; moreover in Bremsstrahlung processes the opening angle of photon and electron is with high probability very small, therefore, the projection of the positron momentum on the field direction is negligible. The trend is fitted well by the analytic expression of eq. 6.2 but, as expected, the best fit values of the parameters, B and $z_0 = -z_C$, do not match the naive interpretation of nominal field intensity and sharp edge in z of the field region. However, provided they are considered as *effective parameters*, Eq. 6.2

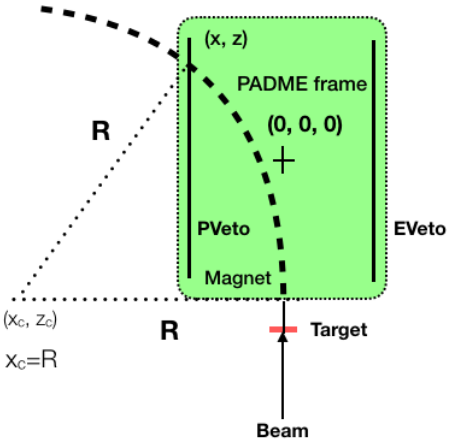

Figure 6.16: Trajectory of a positron slowed down after hitting the target. An analytic function that correlates the momentum of the positron with the z position of the PVeto cluster is extracted.

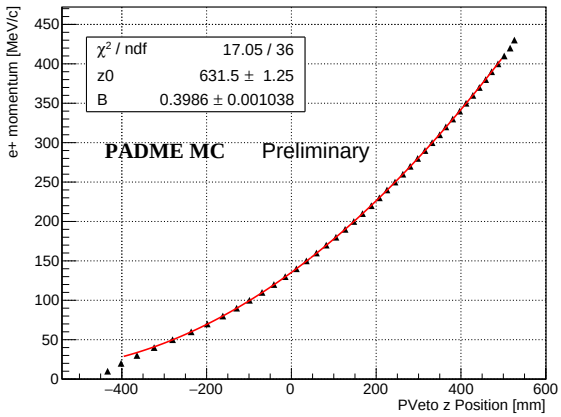

Figure 6.17: The momentum of the positron as a function of the z position of the PVeto scintillating bar.

appears to be a suitable parameterization of the relation between kinetic energy and impact point on the PVeto for a positron. The calibration of the PVeto in terms of positron energy obtained through the simulation can be used for data if a preliminary agreement of the geometry description in data and MC and a good simulation of the magnetic field are established. The same MC based procedure applied to the HEP veto allowed to obtain the linear calibration curve shown in Figure 6.18. This plot shows that, with the magnetic field simulated, the HEPVeto is reached by positrons with energy ranging from 340 to 410 MeV. Both for the PVeto and the HEPVeto, these momentum calibration curves are valid for positrons originating from the center of the target with momentum parallel to the z axis.

Validation with data

During an ECAL calibration run using a single positron beam of energy equal to 490 MeV, the magnetic field was changed twice allowing the beam to hit the positron veto for a few events. These data allow to perform a consistency check of the analytic function obtained from the MC

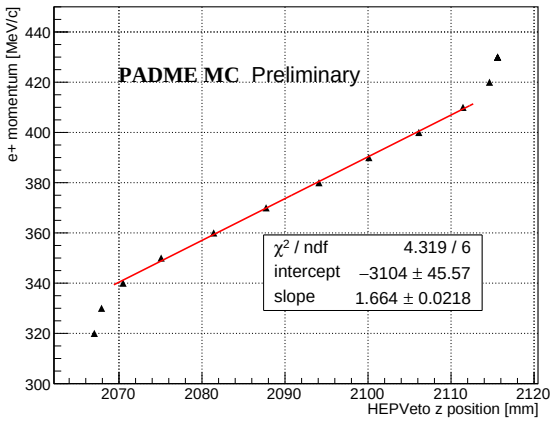

Figure 6.18: MC Single Positron Calibration of the HEP Veto

in data. The magnetic field can be calculated starting from the two current values, from the calibration of the PADME magnet in Section 2.2.2. The z position of the clusters for these two different magnetic values is estimated with a Gaussian fit to the distribution of the PVeto cluster z position. In table 6.3 the values of the current, the resulting nominal magnetic field and the observed z position of the PVeto cluster are reported. After that, by exploiting the linear scaling of the positron energy estimated from a given z impact point in the PVeto and the magnetic field, the relationship in Figure 6.17 has been used to give an estimate of the beam energy. This calculation took into account the value of the nominal magnetic field used in the MC, 0.408 T. The energy obtained is in agreement within 3% with the beam energy of 490 MeV

I [A]	B [T]	z [mm]	E [MeV]	E_{scaled} [MeV]
311.8	0.605	366.25	321	476
381.8	0.746	263.58	260	475

Table 6.3: Positron beam energy estimated from the calibration in momentum of the PVeto spectrometer obtained from MC single positron calibration samples.

measured though the calibration of the bending dipole DHSTB001. The difference contributes to the systematic uncertainty on the knowledge of the positron momentum scale. A consistent value of the beam energy is also determined by studies of the ECAL energy response for the same run. In summary this test provides a successful validation of the momentum calibration based on the simulation and gives an handle to assess an important systematic uncertainty.

6.2.7 Understanding the main features of PVeto occupancy with MC

Figure 6.6 on the right shows the PVeto hit profile, i.e. the distribution of hits across the array of scintillating bars, observed in a run with a positron beam of energy 490 MeV, with pulses of 23000 particles per bunch and a bunch length of 150 ns. The distribution exhibits several features that are not of obvious interpretation. The higher rate of hits in high-z PVeto channels at increasing Pveto channel can be understood in terms of the higher probabilty of emission of low energy photons in the Bremsstrahlung process, assuming that this process is the dominant contribution. However, this assumption does not allow to explain the apparent saturation in the latest scintillator bars at the end of the PVeto and the high rate in the first scintillator bars.

Moreover, the complex geometry of the PVeto, with the stack of scintillators slightly rotated around their axis and the bending of the positron tracks that entails an incidence angle strongly dependent on the positron momentum makes difficult to figure out how all of these effects impact on the PVeto profile. The pile-up of signals from simultaneous interactions and also from beam related background are additional sources of confusion. Achieving a realistic simulation of the effect of pile-up is clearly a non trivial task, since it requires a good emulation of the distribution in time of the particles in the beam pulse, and an excellent tuning of the response of the detector to the passage of particles, taking into account not only the effects arising from the physics of the electromagnetic interactions but also the resolution induced by the readout device (SiPM and ADC), the overall linearity and the time response. The most tricky task for a full simulation of the PVeto data, however, is most likely the simulation of the beam induced background. This requires a detailed simulation of the beam-line in all components, from the optics of the beam to the inert materials that induce the production of secondary particles or of positrons out of the nominal beam orbit that can contribute to the background in the positron veto as well as in the other PADME detectors. In Section 6.2.4 a dedicated study helped to tune the MC simulation, to address the problem of achieving a realistic emulation of the PVeto response. In addition, the analysis of special data sets will be used to infer the contribution of beam related background. Here, some preliminary MC studies based on special test configurations of the beam and of the PADME set-up will be presented to clarify the intrinsic response of the PVeto to positrons from the target under well controlled conditions. The first step was to understand a single positron simulation. A special single positron MC sample with 100000 events was produced to understand hit and cluster energy spectra and to study the dependence of the cluster size on the positron momentum, and hence on the z coordinate of the impact point on the PVeto. Each event in the sample contains one single positron, born in front of the diamond target, of energy randomly assigned according to a uniform probability distribution with boundaries 0 and 500 MeV, to ensure that all relevant kinematic configurations are simulated and each scintillator is traversed. In PadmeMC, in the process of producing digits out of the GEANT4 hits, the digitization time was set to 1 ns. As explained in section 6.1.1, this means that energy deposits in the same bar closer than 1 ns in time were merged into a single digit with energy equal to the sum of the hits. In the reconstruction, all simulated digits were converted into reconstruction-hits, without any additional processing and they were given as input to the clusterization. The thresholds for the cluster seed and for hits selected to contribute to clusters were both set to 0.1 MeV, with a clusterization time of 1 ns. The same number of events were simulated with and without the vacuum chamber, to understand its impact. The effect of the vacuum chamber can be observed in the hit profile of the PVeto, shown in Figure 6.19, where the first ten scintillating bars (ChId$<$ 10) are not reached by the positrons. The plot on the left in Figure 6.20 shows that the cluster size increases with the z position; this is a consequence of the the trajectory of the particles, that impinges on the PVeto with an incident angle that increases with the z coordinate (drawing in Figure 6.20 right). Eventually, the positrons cross more than a bar, given also to the geometrical arrangement of the bars inside the chamber. The most probable value of the energy released in a scintillator depends on the track length. For normal incidence, when the cluster size is one, the track length is about one cm and in this case the simulation predicts a most probable value of the energy lost in the bar is 2.3 MeV. This is observed for example for 50 MeV positrons that produce just one cluster (as shown in Figure 6.21 left), in the scintillating bar number 15, releasing an amount of energy which is distributed as shown in Figure 6.21 right. The effect of the Beryllium window and of the beam-line on the veto profile can be appreciated with a dedicated MC study. For this purpose a sample with a bunch multiplicity equal to 23000, evenly distributed in 250 ns, matching the features of a typical PADME run, was produced both with Be window and beam-line and in the simplified configuration where the

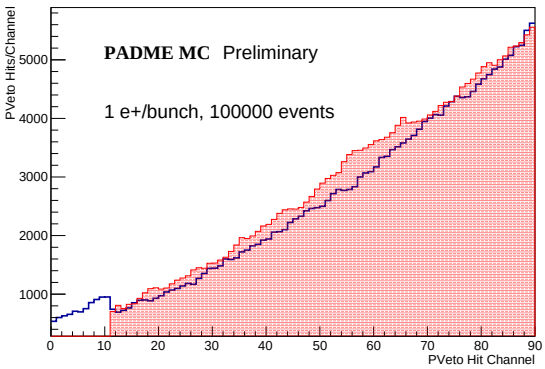

Figure 6.19: PVeto hit profile with (red histogram) and without (blue histogram) the simulation of the vacuum vessel.

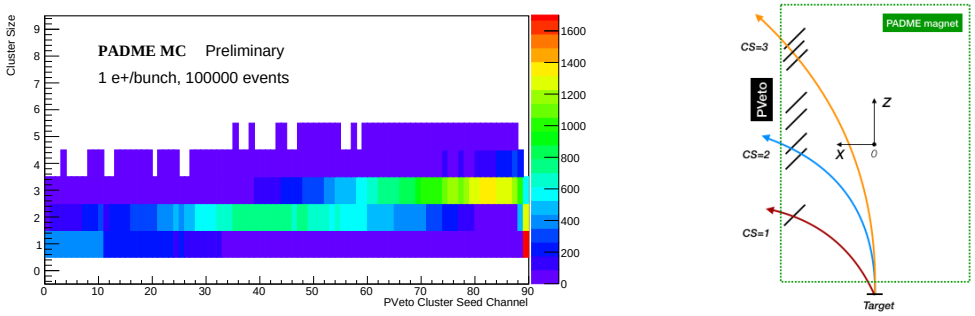

Figure 6.20: On the left, the cluster size is shown as a function of the seed channel of the cluster for MC with vacuum chamber. On the right a sketch showing the geometrical increase of the cluster size with the z position of the cluster.

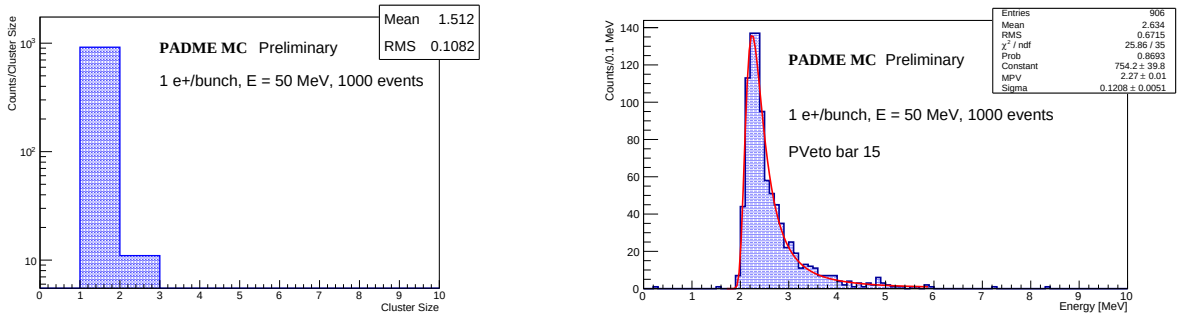

Figure 6.21: The cluster size (left) and the hit energy (right) distributions of a positron of 50 MeV energy.

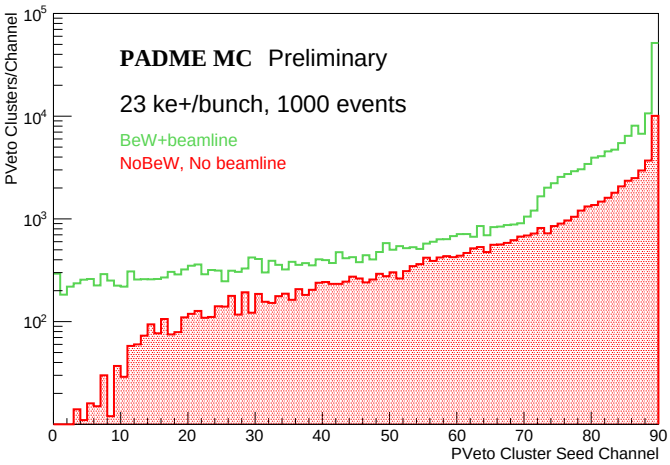

Figure 6.22: PVeto cluster profile with (in green) and without (in red) the beam-line and Be window. The digitization time was 1 ns, to emulate an ideal response of the detector, and the clusterization time 1 ns.

positrons are generated just in front of the target.
The digitization time window was set to 1 ns for both samples, together with a clusterization time of 1 ns. The energy threshold for seed and hit was set to 0.1 MeV. In Figure 6.22 the PVeto profiles obtained in the two simulations are superimposed. The comparison allows to establish that the particle rate on the veto is dominated in all the fingers by background caused by the interactions of positrons of the beam with the elements of the beam-line and due also to the presence of the Be window. The shape of the distribution appears modified and particularly affected at the two edges of the PVeto array.

6.3 Data processing and simulation of the SAC detector

6.3.1 Hit and cluster reconstruction

The signals of the SAC are digitized by CAEN V1742, with the same sampling frequency of the Veto, 2.5 GHz, thanks to the fast time response of the detector. Each waveform is reconstructed with a multi-hit algorithm similar to the one implemented for the veto. The pedestals are computed on-line by the average of the fist 80 samples. The minimum pulse height with respect to the baseline, after sign inversion, is requested to be above 10 mV. The SAC signals are very narrows, conversely to the one of the veto. To detect with high efficiency the position of the peak the derivative of the waveform is determined. The charge released in SAC was calculated by the integral in a small time window of a few bins, centred around each peak. The conversion between charge and energy was obtained considering the nominal gain of the PMT for the working voltage from the data-sheet of Hamamatsu[83] and the light yield of $\sim$2 photo-electrons per MeV measured during a beam test[84]. The energy calibration constants, applied by the calibration service, were obtained by the SAC experts, studying the response of the detector in single positron runs and compared with those obtained with the cosmic ray triggers. A 2D-clusterization merges into a single cluster all the hits that are close in time to the seed, the most energetic hit. The default clusterization parameters are: threshold of 2 MeV for the energy of the hit and 3 MeV for the seed; hits must be close in time within 1 ns and they must be at a distance of no more than two crystals from the seed in both direction.

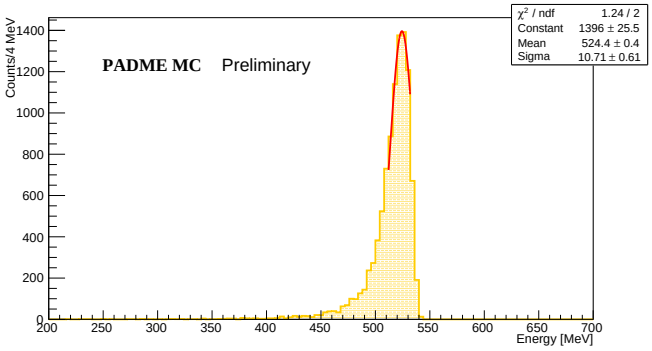

Figure 6.23: SAC cluster energy spectrum obtained firing 10000 photons on SAC.

6.3.2 Tuning of SAC simulation with data

In order to study the response of SAC in MC, a simulation of 10000 photons of known energy (545 MeV, the same energy of the single positron calibration of the SAC done with data) was performed. As shown in Figure 6.23 the energy distribution peaks at a value slightly lower than the nominal value of the beam energy, therefore a scale factor of 1.04 was applied to the energy reconstructed in the SAC. The linearity of the SAC response in MC was also verified by firing photons of different energies in a wide range, from 50 MeV to 500 MeV. The scaling factor obtained at 545 MeV was shown to be adequate at all energies and therefore it was applied in all SAC simulations used in the studies presented here. As discussed before, adjusting the digitisation time in the conversion of simulated hits into digits is a step necessary to achieve a good match between data and simulation. The same procedure followed for the veto has been applied to the SAC in data.
After this study the digitization time in MC was set to 4 ns. Figure 6.24 shows the distribution of the hit energy in data compared with a MC sample produced with the original digitization time of 1 ns on the left and with the digitization time of 4 ns on the right. Also, Figure 6.25 shows the PVeto profile in time coincidence, within 1 ns, with SAC clusters in data compared with MC samples obtained with a digitization time of 1 ns (left) and 4 ns (right). The plots clearly show that the tuned digitization time improves the general agreement between data and simulation.

6.4 Identification and measurement of the Bremsstrahlung process in PADME

In this section the search for a clear Bremsstrahlung signal in the PADME data collected in July 2019 will be discussed. Two methods will be presented: the first exploits the analysis of the PVeto profile alone, that, in the case of null background, can be mapped into a distribution of energy for the positrons reaching the detector after loosing energy for the emission of a photon in the electric field of nuclei or atomic electrons in the target. However, as already anticipated, in these data the PVeto profile is dominated by beam related background. Therefore a dedicated strategy has to be envisaged to get rid of the component unrelated to interactions in the target. This study, exploiting a background run collected with the PADME beam and detectors in order to overcome the difficulty of simulating the beam related background, is presented in section 6.4.1. An estimate of the integrated Bremsstrahlung yield, inclusive over the angular distribution of the photon, will be derived and compared with simulation and with an analytical prediction.

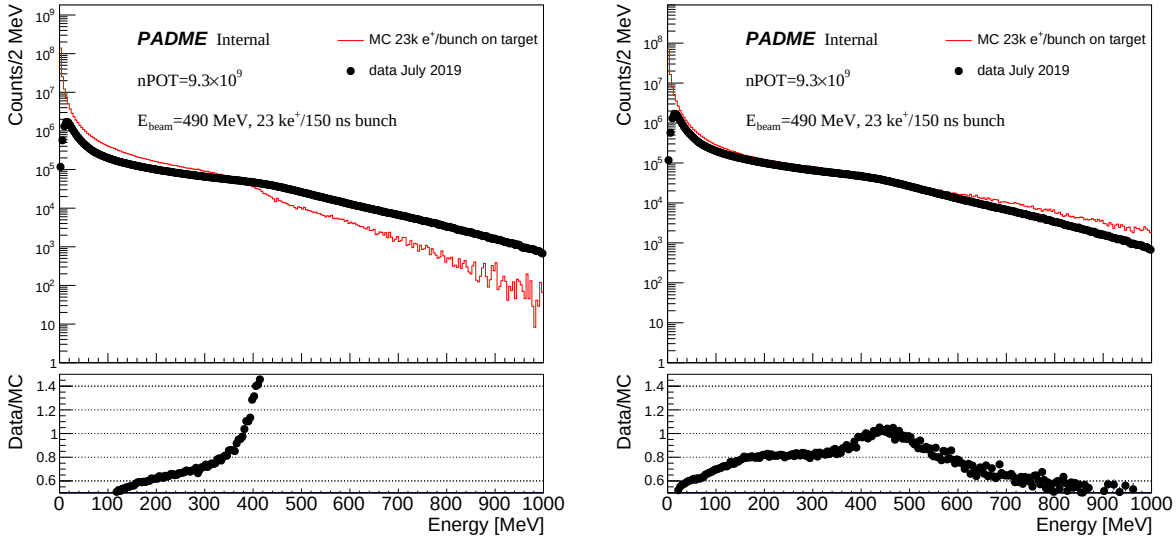

Figure 6.24: Comparison data/MC of the SAC hit energy for MC digitization time window of 1 ns (left) and MC digitization time window of 4 ns (on the right).

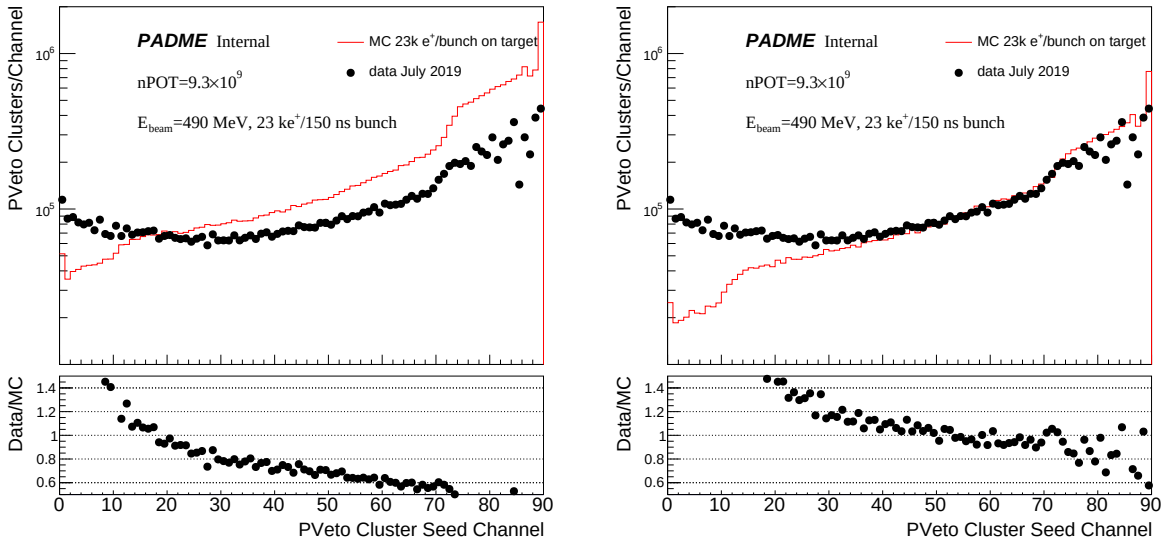

Figure 6.25: PVeto cluster profile in time coincidence with the SAC central crystal. The MC digitization time is set to 1 ns (on the left) and 4 ns (on the right).

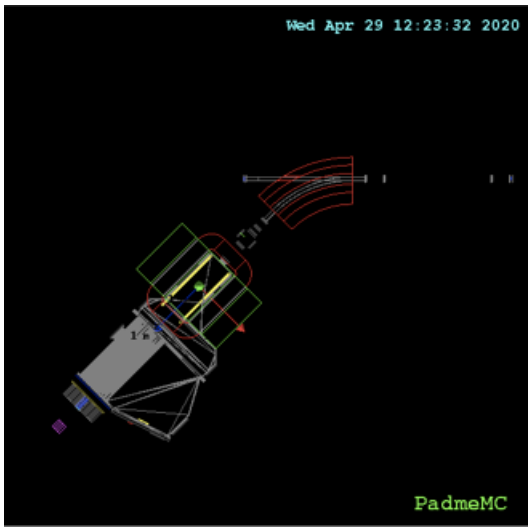

Figure 6.26: PADME geometry in MC with target out of beam.

The second method requires the explicit identification of the signature of a Bremsstrahlung interaction, i.e. a positron of energy lower than the beam energy, observed in the positron Veto, and a photon of energy matching the energy lost by the positron. The application of this second strategy to the data, and a comparison with the simulation, is described in section 6.4.5 with focus on photons identified in the SAC.
These studies use the data of July 2019 and a MC simulation (see 6.1.3) of the PADME beam-line set-up and beam parameters corresponding to those data taking conditions. Finally, this explicit selection strategy will be applied to a small sample of PADME data collected in July 2020 with the most recent configuration of the beam-line. Section 6.4.6 will show the benefit arising from the reduced background resulting in a much cleaner signal even before any optimisation of the data reconstruction and calibration.

6.4.1 Inclusive Bremsstrahlung yield in the positron veto detectors

A good understanding of the Bremsstrahlung process can be achieved with a comparison of the PVeto cluster spatial profile observed in data collected with the target in the nominal position in the beam-line and in a special run recorded with the target out of the beam-line and approximately with the same statistics. Thanks to a remote control of the positioning motor, the target can be moved in the parking position where it does not interact with the beam. Therefore, the run without target is representative of the background seen by the PADME detectors due to primary and secondary beam interactions with the materials of the beam-line and of the detectors with the exclusion of active and passive material target.
Two special MC samples were also prepared to simulate the beam background run:

- removing completely the target from the beam;
- removing only the diamond sensor and leaving the diamond carrier board in the beam.

A sketch of the MC geometry in the sample produced with the target and the carrier board out of beam, is shown in Figure 6.26. The MC samples were processed by applying all tunings and optimizations discussed in Section 6.2.4, both in the case of the nominal and beam background data samples.

6.4.2 Results in PVeto

The PVeto profiles for data in comparison with MC simulations are shown in Figure 6.27 for all clusters of energy above 1 MeV. All the distributions are normalized to the number of positrons on target in the data run with the target in the beam. The normalization of the run without target in real data is obtained by imposing the same occupancy of the first ten bins where there is no contribution of interactions in the target. Indeed, from Figure 6.27, where the data of a nominal run are compared to data of a beam background run, shows that the profile in the scintillators with channel below 10 has the same shape and similar rate, with target in or out of the beam, which means that the source of background does not depend on interactions in the target. Similar shapes are also visible at high z scintillator bars of the PVeto, for channel identifiers above ∼75. In this very high rate region the PVeto is not able to provide precise information on interactions occurring in the target, because, due to the very high pile-up probability, multiple hits occurring on the same finger can not be separated in time with high efficiency. Such a high background comes from the primary positrons in the low energy tails of the beam which are bent at a larger angle, with respect to the beam core, hitting the high z scintillators of the PVeto. The low energy tail is due to the intrinsic energy spread of the beam from the LINAC and to the energy degradation of a small fraction of positrons undergoing Bremsstrahlung interactions in the Berillium window separating the BTF and the PADME vacuum. Concerning the simulations, the comparison among the sample with diamond out of beam and target out of beam shows that the carrier board represents a not negligible source of hits from channel 10 to 70.
The PVeto cluster profile is described quite well for scintillating bars above number 50. The MC is also able to describe quite well the behaviour of the last 20 scintillator bars of the array, i.e. in the regime of very high rate. This makes more solid the interpretation of the profile shape in that region in terms of the low energy tails of the beam due to soft Bremsstrahlung and in the Berillium window and the saturation of the PVeto response. Also the difference between the profile with and without the target in the region between ChId = 10 and ChId = 70, which increases in size with the channel number, is reproduced by the simulation at a qualitative level by the two flavours of MC. This gap appears to be the likely contribution of hard Bremsstrahlung interactions in the target. On the other hand, the shape of the distribution at low channel numbers is very different in data and simulations. The data indicate the presence of a large background which does not arise from beam interactions in the target, since it is seen, apparently with the same rate, both with the target in and out of the beam. The high background on the first PVeto bars is still an open question. In any case, the difference between the profile with the target and without it in data is representative of the interactions of the beam with the target and possibly with the materials around it. Therefore, it can be interpreted as a Bremsstrahlung signal inclusive over the angular distribution of a radiated photon of energy ranging between the kinematic boundaries corresponding to the interval of kinetic energy of the positron contributing to the PVeto hit distribution. Comparing the subtracted spectra in data and in simulation allows to validate the interpretation. Figure 6.28 shows the PVeto profile subtracted of the contribution from the beam background run in data and in simulation. On the left plot, the simulation corresponds to the nominal configuration subtracted of the profile obtained with the diamond target removed from its location, while the carrier board is still simulated in its nominal position. On the right plot the MC prediction is obtained as the difference between the nominal simulation and the simulation with the entire target (diamond and carrier board) displaced from the nominal position, so that no material related to the target is met by the beam.
The distributions in data and MC nicely matches in shape in the region between channel number 20 and 70, with a mismatch in the normalization that is below 10% in the left plot and about 25% in the right plot. One should notice that the MC prediction with a geometry coherent

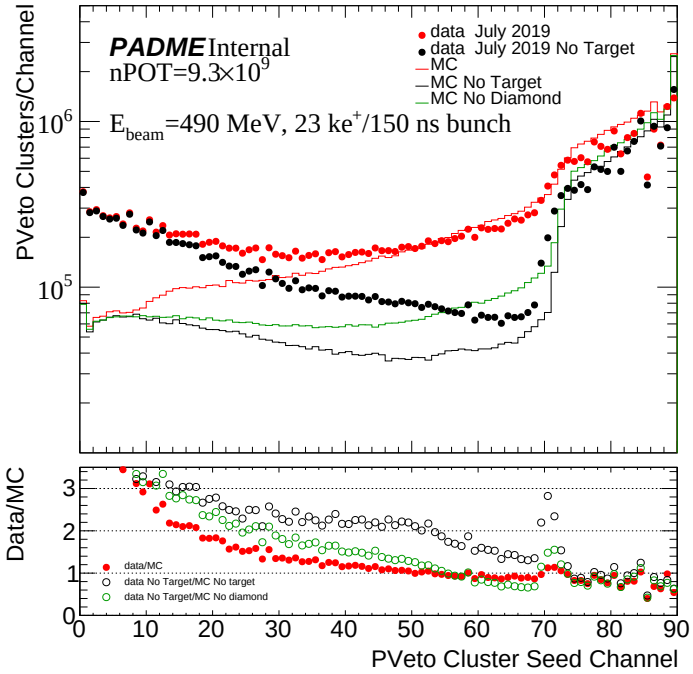

Figure 6.27: PVeto cluster profile observed in data with the target in and out of the beam line. Overlayed the MC predictions for the target in the beam line, for the diamond removed from its location, and for the target (diamond and carrier board) out of the beam line. The ratio data/MC is shown in the bottom pad.

with data is the one in the right plot, where the difference in the global normalization is higher. However, the contribution of the carrier board of the target to the Bremsstrahlung rate might be overestimated in MC if the tails of the beam were more extended in simulation than in real data; this might well be possible taking into account that the focusing effect of the quadrupoles on the beam is not emulated in simulation, as well as the inert materials of the quadrupoles and of some collimators.

6.4.3 A look at HEPVeto and EVeto

The same study performed for the PVeto can be repeated for the HEPVeto, in order to gain further insight. The HEPVeto profiles for data and MC simulations, are shown in Figure 6.29. Also in this case all the distributions are normalized to the number of positrons on target from data.
From this plot there is a good agreement between MC and data for the no target profiles at least at low scintillator bars. The corresponding Bremsstrahlung spectrum in data and MC, after the subtraction of the background contribution, is shown in Figure 6.30. While in the first case an overall agreement in rate is observed, the comparison with the MC on the right gives a good agreement in shape, but a 25% deficit of rate in data.
Finally, a comparison of the EVeto cluster profile with and without the target in the beam has been done with the goal of checking how good is the MC in predicting the background. Figure 6.31 shows the distributions in data and in the MC. In the plot the EVeto channels in MC are more than in data because in July 2019 the readout of the last 16 EVeto bars was turned off. The amount of beam related background appears to be higher in data than in MC but the

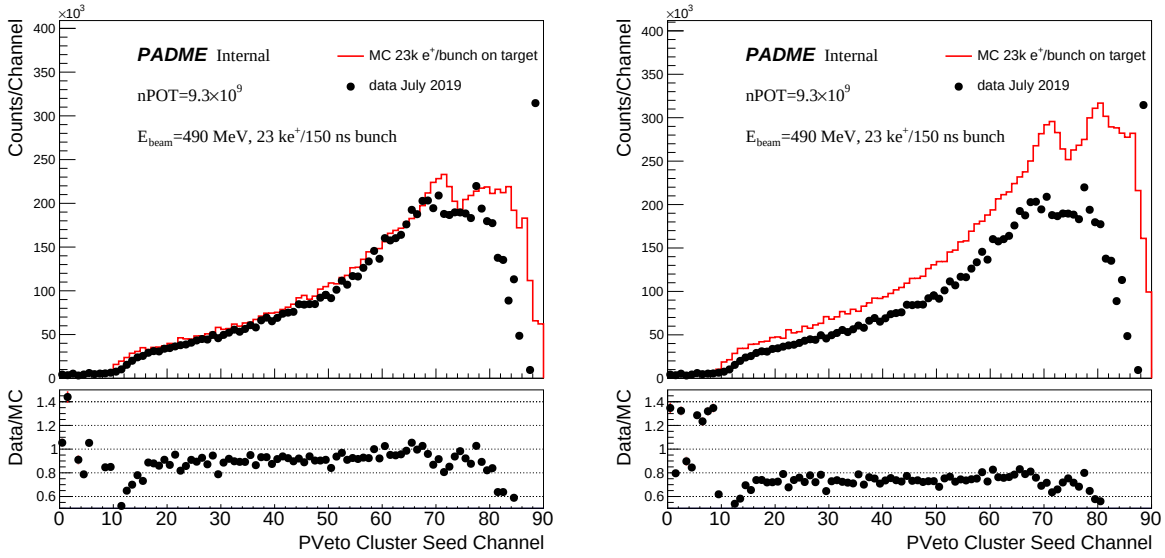

Figure 6.28: Bremsstrahlung yield in the PVeto as a function of the PVeto channel number, obtained after the subtraction of the beam background estimated from the beam background run for MC and data. In the left (right) plot the MC prediction is given by the difference between nominal MC and the MC without the diamond (target).

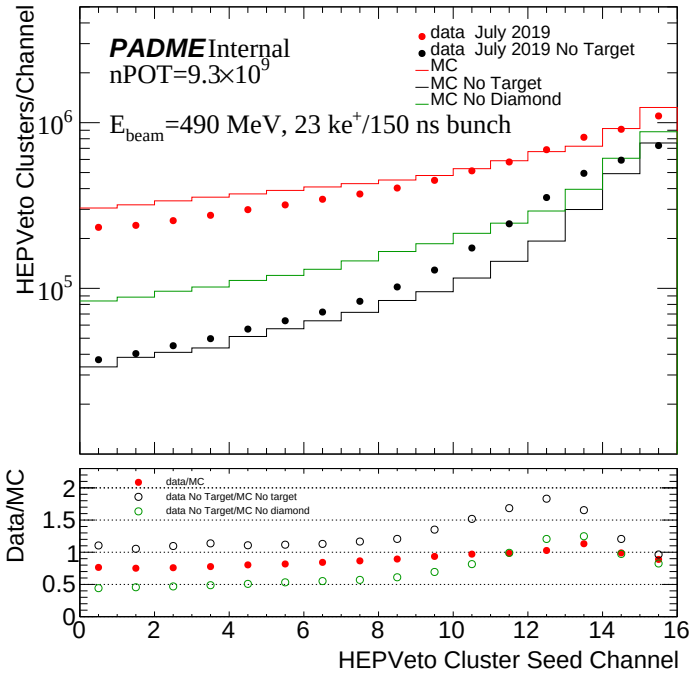

Figure 6.29: HEPVeto cluster profile observed in data with the target in and out of the beam line. Overlayed the MC predictions for the target in the beam line, for the diamond removed from its location, and for the target (diamond and carrier board) out of the beam line. The ratio data/MC is shown in the bottom pad.

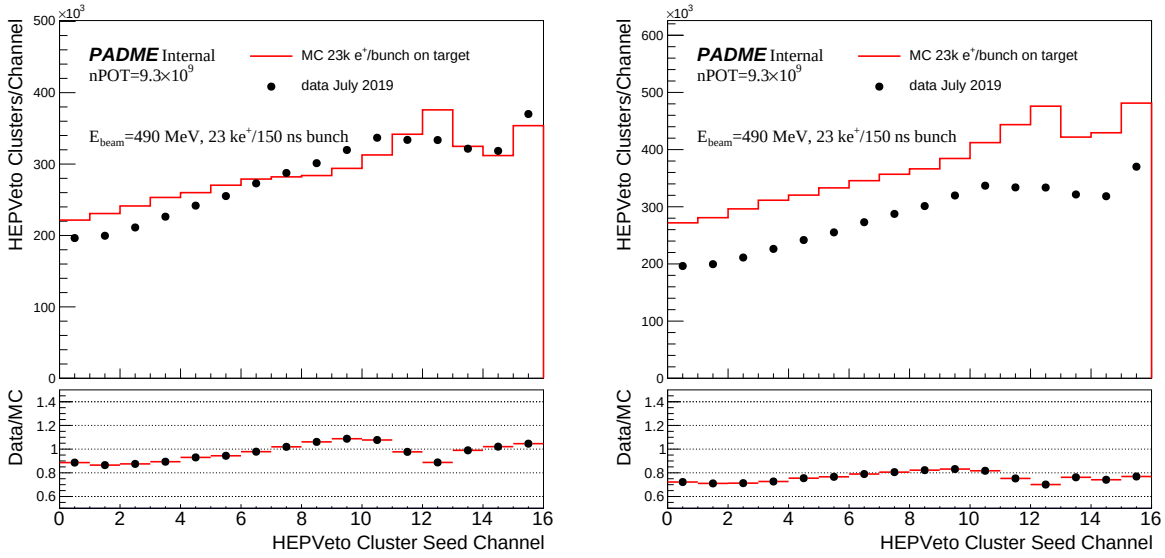

Figure 6.30: Bremsstrahlung yield in the HEPVeto as a function of the scintillator channel number, obtained after the subtraction of the background estimated from the background run for MC and data. In the left (right) plot the MC prediction is given by the difference between nominal MC and the MC without the diamond (target).

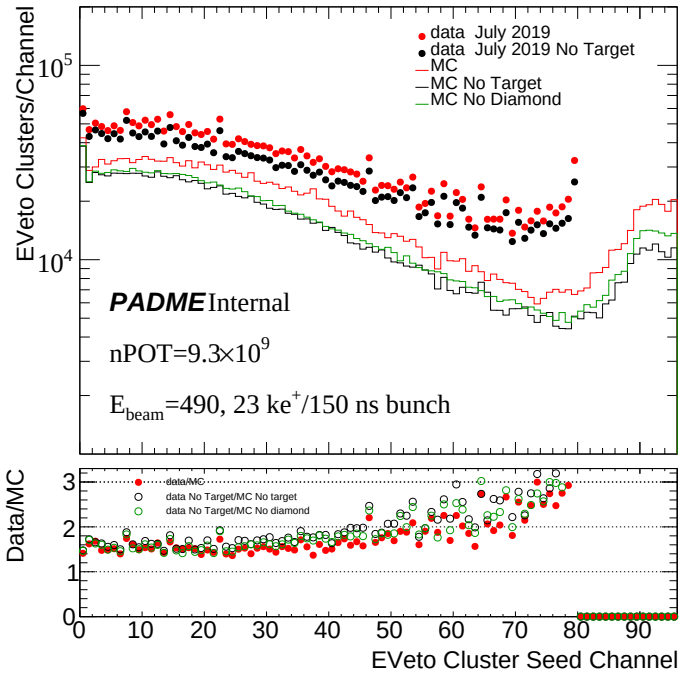

Figure 6.31: EVeto cluster profile observed in data with the target in and out of the beam line. Overlayed the MC predictions for the target in the beam line, for the diamond removed from its location, and for the target (diamond and carrier board) out of the beam line. The ratio data/MC is shown in the bottom pad.

shape is well reproduced at least up to about finger number 70. In addition, the rate of hits induced by interactions in the target is quite uniform and well reproduced in MC. The EVeto cluster profile in MC is not to much different with diamond out of the beam or with diamond and carrier board out of the beam. This seems to indicate that in MC the source of electrons are mainly from interactions in the diamond and not from the carrier board.

6.4.4 Comparison with predictions

An expression for the rate of Bremsstrahlung interactions leading to the emission of a photon with energy in the range $[k_{min}, k_{max}]$ gives the estimate of the number of photons emitted by an electron passing through a detector of a thickness d, in the approximation $d << X_0$ where X_0 is the radiation length of the material, is reported in the review of the Particle data Group[155]. The formula, valid in the "complete screening case", reads as follows:

$$N_\gamma = \frac{d}{X_0}\left[\frac{4}{3}ln\left(\frac{k_{max}}{k_{min}}\right) - \frac{4(k_{max}-k_{min})}{3E} + \frac{k_{max}^2 - k_{min}^2}{2E^2}\right] \tag{6.3}$$

In the case of PADME, d is the thickness of the diamond target, 100 μm, X_0 is the radiation length (42.7 g/cm^2) for a density ρ of the diamond of 3.5 g/cm^3, E is the energy of the incident positron, k_{max} and k_{min} are respectively the maximum and the minimum energy of the emitted photon. The total Bremsstrahlung interactions, equal to the number of photons ($N_{\gamma TOT}$) emitted during a run, can be calculated as:

$$\mathrm{N_{\gamma TOT}} = \mathrm{N_{POT}} \times \mathrm{N_\gamma} \tag{6.4}$$

where N_{POT} is the number of the total positrons collected in the run and N_γ is computed with the Eq. 6.3. From the number of photons emitted, it is possible to obtain the cross section observed in PADME, using the formula:

$$\sigma = \frac{\mathrm{N_\gamma}}{\mathrm{N_{POT}}}\frac{\mathrm{A}}{\rho \mathrm{N_A d}} \tag{6.5}$$

where N_A is the Avogradro's number. In such a way, for a beam energy of 490 MeV, setting numerically $k_{min} = 1$ MeV and $k_{max} = 490$ MeV, the Bremsstrahlung cross section is roughly equal to 3.5 barn, in agreement with the estimate provided by the CalcHEP generator, reported in the PADME proposal[75] and shown in Figure 6.32. The distributions in Figure 6.28 can be compared with the analytical prediction. Each scintillator bar corresponds to a photon energy interval, and therefore to a corresponding range of energy of the slowed down positron. The number of Bremsstrahlung interactions predicted by Eq. 6.3 is superimposed to the yield observed in data and the corresponding simulation in Figure 6.33. The analytical calculation is in agreement with the prediction of the simulation corresponding to the set-up Target-No Diamond and with the data within 10-15%, while it is about 25% lower than the simulation for the set-up Target-no Target. It is worth reminding the systematic uncertainties affecting this comparison between data and prediction. The momentum scale was validated with data within 3% as described in section 6.2.6. In addition one has to notice that the golden July 2019 run was recorded with a value of the magnetic field of 0.415 T, about 2% higher than the magnetic field used in the simulation. The resulting total uncertainty on the momentum scale ($\sim 3.6\%$) was used to evaluate the corresponding systematic error on the yield predicted by the calculation or the MC to be compared with data. The procedure is based on Figure6.34 where the Bremsstrahlung prediction from Eq. 6.3 obtained with the nominal momentum calibration of the Veto is shown together with the prediction corresponding to a momentum scale shifted upward and downward by 3.6%. The relative change in the yield is used as systematic error

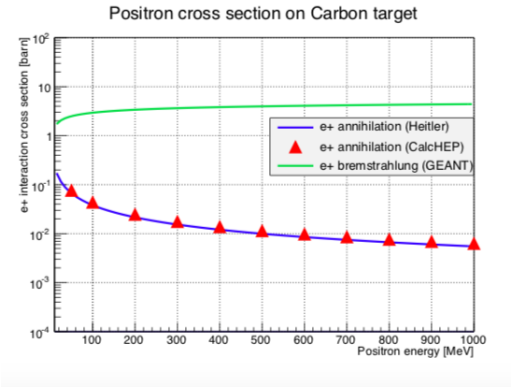

Figure 6.32: Cross sections of the two main PADME background processes as a function of the beam energy[75]. The Bremsstrahlung cross section refers to an energy of the photon higher than 1 MeV.

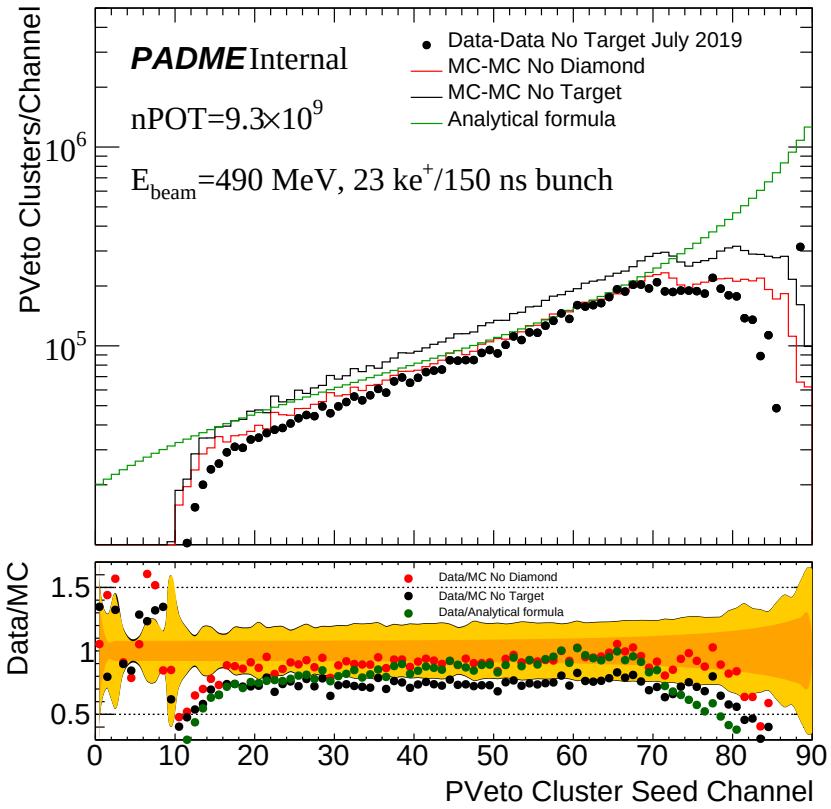

Figure 6.33: Bremsstrahlung yield in the PVeto as a function of the scintillator channel number for MC and data superimposed with the spectrum obtain from the analytical formula.

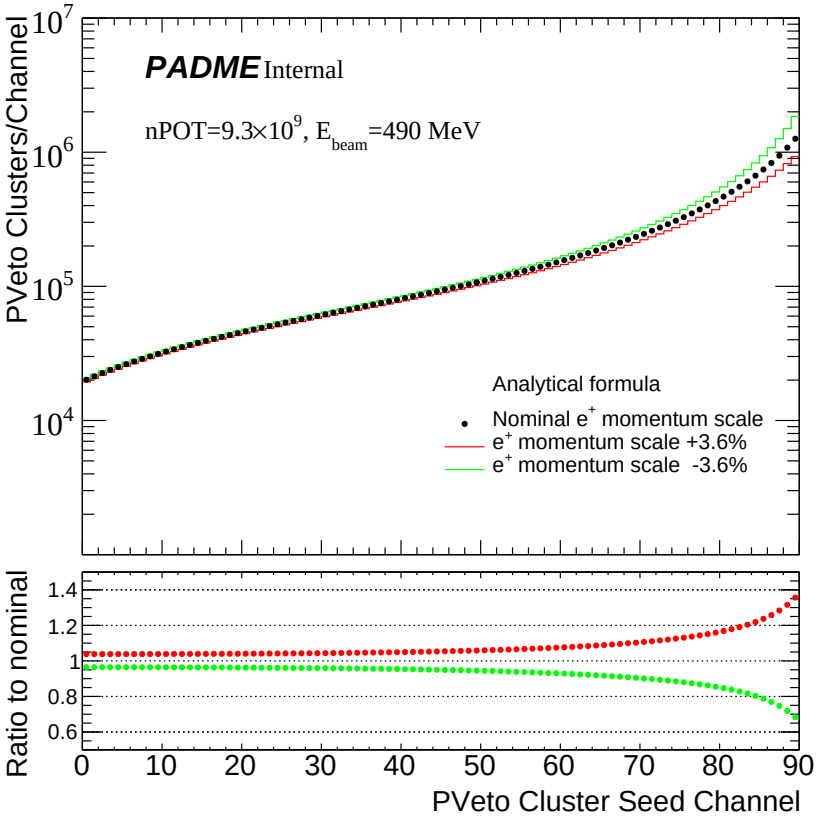

Figure 6.34: In black dots the Bremsstrahlung yield as predicted by the analytical formula with the nominal momentum scale is reported. The red and the green lines refer to a +3.6% and -3.6% momentum scale, respectively.

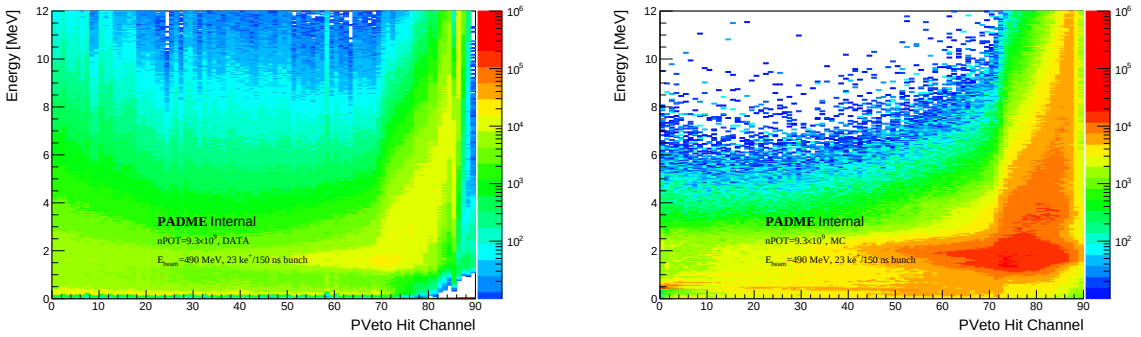

Figure 6.35: Hit energy of the positron veto as a function of the channel identification number for data (on the left) and MC (on the right).

related to the momentum scale uncertainty. In addition, a global uncertainty affects the overall normalization of the data, due to the systematic error on the number of positrons on target measured by the active target.
The cross calibration of the target with the BTF calorimeter allows to assume a total systematic uncertainty of about 5%. This must be combined with an additional 5% uncertainty affecting the BFT calorimeter response. The combined errors from the overall normalization and from the momentum scale are shown in the bottom pad of Figure 6.33 by the dark orange band around 1. In addition, the ratio between the two profiles obtained in MC varying the beam background sample (no Target and no Diamond) can be used to set an upper bound on the systematic uncertainty on the tails of the beam profile contributing the Bremsstrahlung spectrum through interactions outside the diamond target. When this error is combined with the systematic uncertainties previously discussed the light orange band in the same plot is obtained. Finally, the implementation of Bremsstrahlung in Geant4, as discussed in Section 6.1.1, is based on a parameterization known to be accurate at the level of 3- 5%, while the complete screening approximation in Eq. 6.3 is most likely less accurate. When considering an additional 5% error on the theory, the black boundary shown in Figure 6.33 is obtained as a representation of the total systematic uncertainty. Other systematic uncertainties that may affect the comparison are geometry mismatch and normalization of the no target run in data.
The low rate observed both in data and simulation in the scintillators above channel number 70 when compared to the prediction deserve some comments. This region is the most crowded of the detector and the reconstruction clearly suffers from effects of pile-up. An important confirmation of this picture comes from Figure 6.35 where the energy of PVeto hits is shown as a function of the channel identifier for data and for MC. The typical value of the energy released is about 1.8 MeV over all channels, but a consistent population of hits in PVeto channels above 70 exhibits a value of the energy that corresponds to the release of energy from two or more minimum ionizing particles. This is a clear sign of pile-up of particles concurrent in time, therefore above channel 70 the number of clusters cannot be considered an estimate of the number of positrons hitting those scintillators and the comparison with the analytical prediction is not meaningful in that region.

6.4.5 Bremsstrahlung identification with PVeto and SAC

The golden method to measure the Bremsstrahlung yield consists in identifying both the positron after the interaction and the photon. A preliminary study was developed and is summarised here; it is based on the use of the SAC for the detection of forward photons or of ECAL, with

a much lower statistics. The aim is to demonstrate the feasibility of the method with a careful calibration of the analysis and of the reconstruction chain. A fundamental requirement is a good time alignment, described in Section 6.2.3. In fact, the time coincidence allows to select only PVeto and calorimeter clusters coming from the same interaction. Bremsstrahlung candidates are requested to satisfy:

$$| t_{cl\,PVeto} - t_{cl\,CALO} | < 1\,ns\,,$$

with $t_{cl\,PVeto}$ and $t_{cl\,CALO}$ respectively the cluster time of the PVeto and the calorimeter.
The yield can be extracted in several conceptually equivalent ways including:

- for every scintillating bar, the photon energy appears as a peak centred at the difference between the beam energy and the positron energy over the combinatorial background around a value equal to the difference between the beam energy and the positron energy associated to that scintillator by the momentum calibration function;
- the distribution of the sum of photon energy and positron energy appears as a peak centred at the beam energy.

This analysis motivated the preliminary study also of the SAC reconstruction performance and tuning in the simulation, described in section 6.3.2, in addition to the study of the PVeto described in section 6.2.4. Moreover, a time alignment of SAC and veto detectors in MC was also necessary in order to cancel the time of flight offsets and allow tight time coincidence cuts to be applied. After MC tunings, the simulation can be used to validate the general concept behind all of these methods. The scatter plot of the SAC cluster energy as a function of the PVeto cluster seed in coincidence can be projected on slices corresponding to Bremsstrahlung events hitting a given veto bar. Such distribution exhibits a peak at a value of the SAC cluster energy, E_γ, obtained with a Gaussian fit, that allows to compute the associated positron energy as:

$$E_{e^+} = E_{beam} - E_\gamma. \tag{6.6}$$

This estimated positron energy should be the same of the momentum associated to the PVeto z coordinate, as obtained from the PVeto momentum calibration described in section 6.2.6. Figure 6.36 shows the positron energy as a function of the PVeto z positon as obtained from Eq. 6.6, before and after the SAC energy scale correction in MC, and to the momentum calibration function obtained with dedicated simulations of single positrons. The agreement within a few percent observed certifies the methodology to be applied to data and validate the energy and time calibration applied to MC.

Bremsstrahlung selection cuts for SAC

After the validation on MC of the method, thanks to the accurate time calibration achieved, it is possible to require a time coincidence of 1 ns between PVeto and SAC clusters in order to select Bremsstrahlung candidate $e^+\gamma$ pairs in data. The energy of the photon is obtained directly from the energy of the cluster reconstructed in the SAC, while the energy of the positron is extracted from the z position of the veto cluster, converted into positron energy using the calibration obtained from the single positron study, described in Section 6.2.6. Only PVeto clusters with an energy above 1 MeV are considered. For this selection, Figure 6.37 shows the energy of the SAC cluster as a function of the veto channel number in the range 40-70 for data and MC. It is possible to see that SAC clusters correlated to PVeto clusters have energy higher that 150 MeV. Therefore the selection criteria:

$$\mathrm{E_{SAC}} > 150\ \mathrm{MeV},\ 40 \leq \text{PVeto channel} \leq 70$$

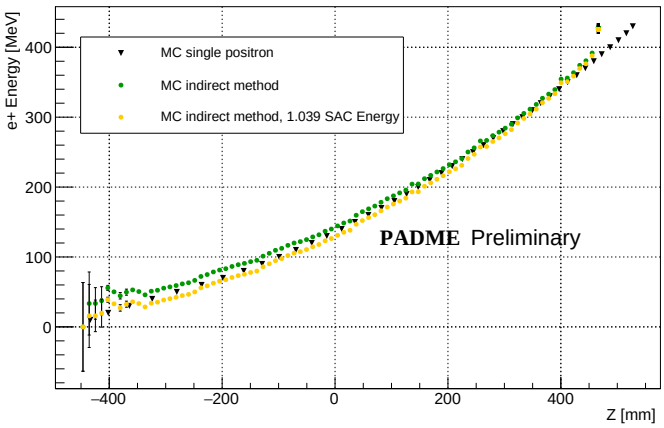

Figure 6.36: Study of the positron energy as a function of the z Pveto position, using different methods. In particular, it is important to underlined the agreement between the points obtained with single MC positron calibration and points obtained with the indirect method, requiring the time coincidence with SAC as explained in the section.

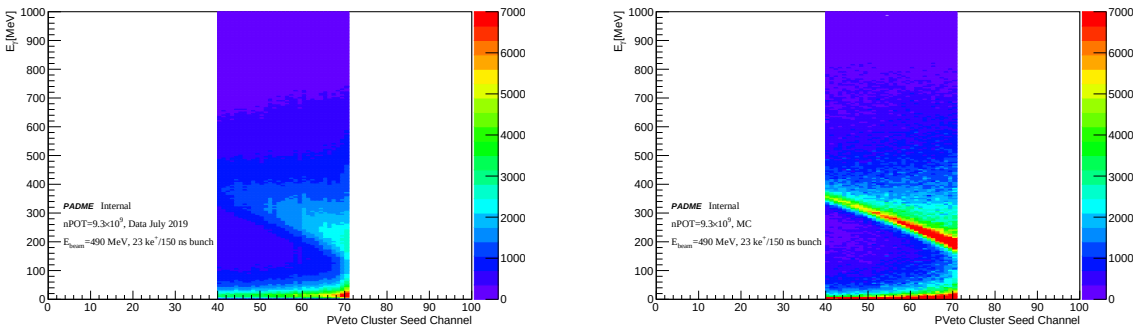

Figure 6.37: SAC cluster energy as a function of the PVeto channels where a cluster in time with the photon is found, both for data (left) and MC (right). Only the range 40≤PVeto channel≤ 70 is considered. Bremsstrahlung events can be selected inserting a cut on the SAC energy ($E_{SAC} > 150$ MeV).

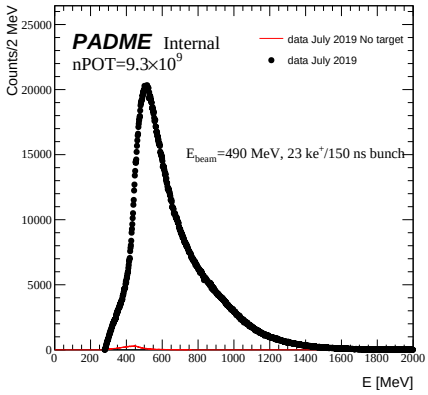

Figure 6.38: Sum of the energy of the forward photon detected in SAC ($E_{SAC} > 150$ MeV) and of the positron observed in a range of 40≤ChId≤ 70 of the PVeto. The black distribution refers to the nominal *July 2019 Golden Run*, the red histogram to the corresponding background run, with the target out of the beam-line.

gives a rather pure sample of Bremsstrahlung interactions. For these events, the distribution of the sum of the energy of the candidate photon and positron pair, shown in Figure 6.38 both for the usual *July 2019 Golden Run* and for the corresponding no target run, confirms that the background is negligible. In Figure 6.39 the distribution in data is compared to MC before and after the tuning of the SAC digitization time. The number of events selected in data, i.e. the integral of the distribution, is 3.4×10^6, 20% lower than the theoretical calculation in the same range ($\sim 4.2 \times 10^6$) and 15% lower than the estimate obtained from the analysis of the PVeto profile in the same range of channels ($\sim 4.01 \times 10^6$). Finally, Figure 6.40-6.43 show the distributions of the sum of the energies of photon and positron as a function of the PVeto or HEPVeto cluster seed cluster number for data and simulation with $E_{SAC} > 150$ MeV for PVeto and $E_{SAC} > 50$ MeV for HEPVeto.

6.4.6 Bremsstrahlung signal with reduced background in recent data

In July 2020 a a short data taking took place with the goal of commissioning beam and detectors for Run 2 after the beam-line intervention. The same analysis presented in this chapter was applied to extract qualitative results from a run with 10000 positrons on target, bunch length 150 ns and beam energy of 450 MeV. This beam intensity is low enough to avoid saturation effects in the target even with a well focused beam. The total number of positrons collected by the target was 2.7×10^9. By just requiring a time coincidence of 1 ns between PVeto and SAC clusters, without any cuts on the SAC energy, the distribution of the sum of the energies of the SAC cluster and the energy of the positron obtained from the Z position of the PVeto cluster is shown in Figure 6.44. The distribution exhibits a clean and narrow peak above a low background compatible with the beam energy, related to the Bremsstrahlung process. A new momentum calibration changing the magnetic field value to the different beam energy (450 MeV instead 490 MeV) was performed following the same procedure of Section 6.2.6. Thanks to the reduced beam background, these data, although analysed with a very preliminary determination of the calibration constants, allowed also for the first time to see the Bremsstrahlung signal through the correlation of PVeto clusters and ECAL clusters.
In Figure 6.45 the sum of the energy of the photon in ECAL and of the positron in the PVeto in a time coincidence of 2 ns is shown. Also in this case, the Bremsstrahlung signal clearly emerges

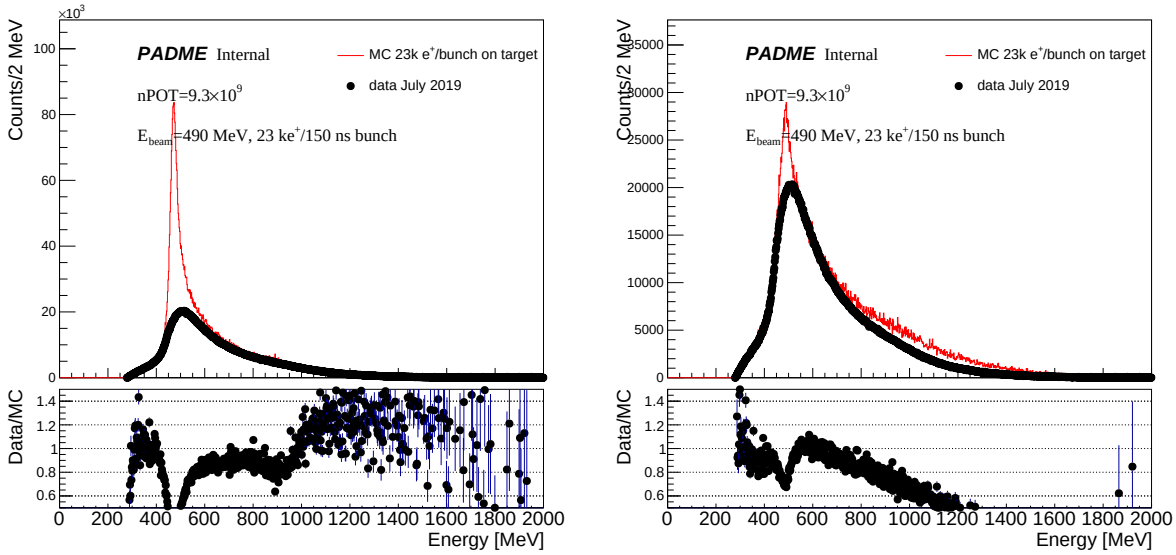

Figure 6.39: Sum of the energy of the forward photon detected in SAC ($E_{SAC} > 150$ MeV) and of the positron observed in a range of 40≤PVeto channel≤ 70 for data and MC. The MC was produced with a SAC digi time window of 1 ns (on the left) and 4 ns (on the right).

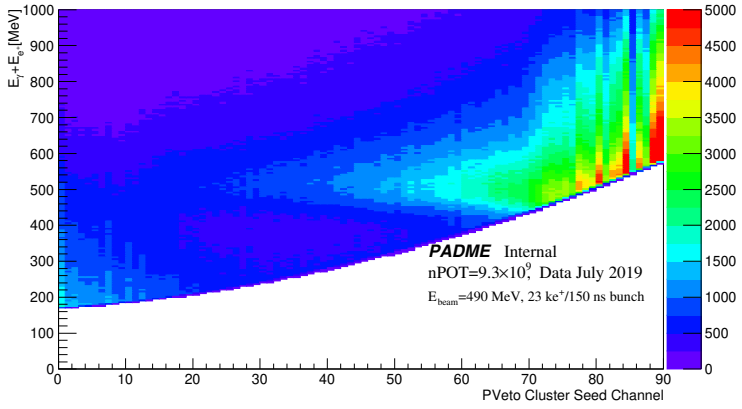

Figure 6.40: Sum of the energy of a photon detected in SAC ($E_{SAC} > 150$ MeV) and a positron in time detected in the PVeto as a function of the PVeto channel seed of the cluster. Data are from the *July 2019 Golden Run*.

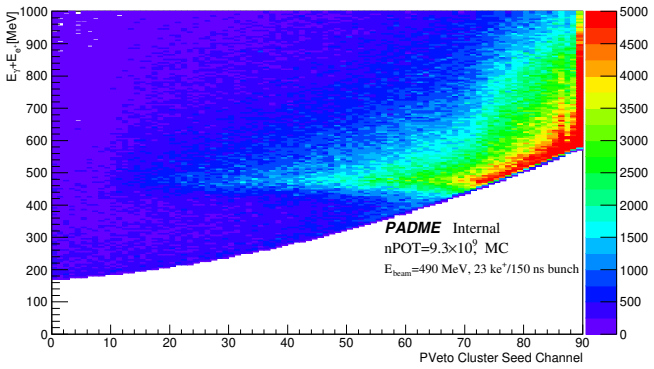

Figure 6.41: Sum of the energy of a photon detected in SAC ($E_{SAC} > 150$ MeV) and a positron in time detected in the PVeto as a function of the PVeto channel seed of the cluster in MC.

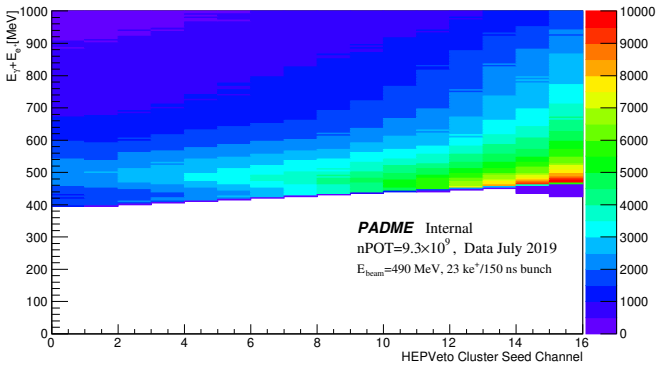

Figure 6.42: Sum of the energy of a photon detected in SAC ($E_{SAC} > 50$ MeV) and a positron in time detected in the HEPVeto as a function of the HEPVeto channel seed of the cluster. Data are from the *July 2019 Golden Run*.

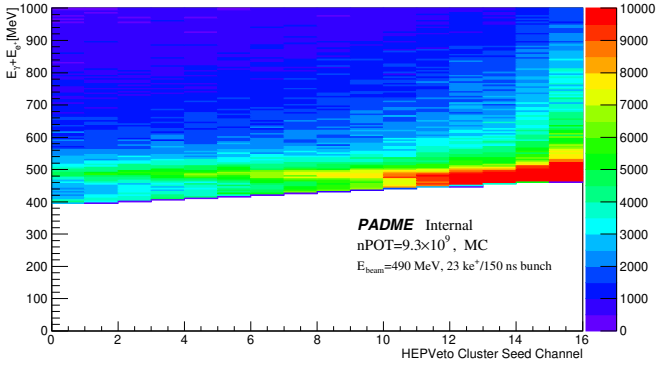

Figure 6.43: Sum of the energy of a photon detected in SAC ($E_{SAC} > 50$ MeV) and a positron in time detected in the HEPVeto as a function of the HEPVeto channel seed of the cluster in MC.

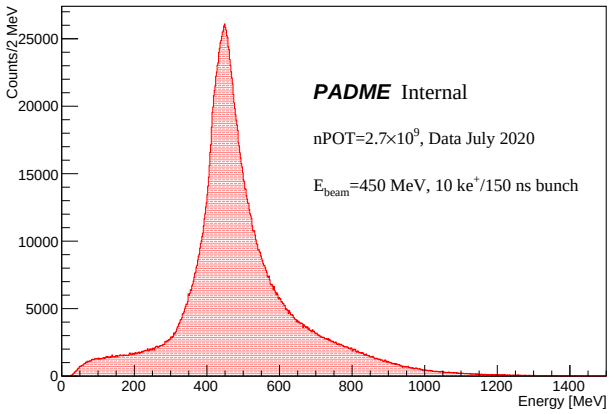

Figure 6.44: Sum of the energy of a photon detected in SAC and a positron in time detected in the PVeto, in a time coincidence of 1 ns.

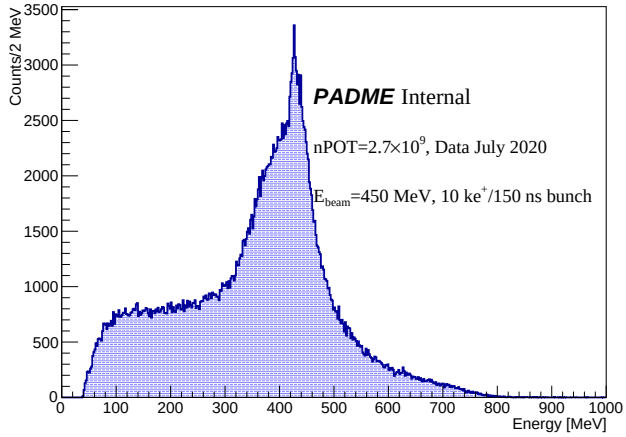

Figure 6.45: Sum of the energy of a photon detected in ECAL and a positron in time detected in the PVeto, in a time coincidence of 2 ns.

over the background. Both the spectra show a narrow peak compatible with the beam energy, related to the Bremsstrahlung process.

Conclusions

PADME is one of the experiments that the European Strategy for Particle Physics of 2020 suggested to support. It is a small size fixed target experiment located at the Beam Test Facility (BTF) of the Laboratori Nazionali di Frascati. It is mainly devoted to search for a hypothetical massive dark photon and it makes use of a positron beam hitting a thin diamond target implementing the missing mass technique.
In my PhD I had the opportunity to participate in the PADME experiment from the very beginning, designing and building the full carbon active diamond target and during all the data taking periods from September 2018 to December 2020, contributing to the development of the Detector Control System, on-line monitor and alarms, software reconstruction and physics analysis.
Thanks to the expertise I gained in my Bachelor and Laurea thesis I built, installed and maintained the active diamond target of PADME, which operated continuously and stably in vacuum since its installation in September 2018. This proves the validity of the mechanical and electrical interconnection I did between the double-sided graphitic strips of the sensor and the front-end electronics board. In addition, the diamond detector fulfils its design goals of providing the average transverse position of the beam with a precision much better than 1 mm and of measuring the integrated luminosity at few percent level after cross-calibration with an external electromagnetic calorimeter. This was possible thanks to the mitigation of the beam correlated noise observed during data taking. The diamond detector was also the best bunch-to-bunch beam monitor during the beam commissioning, optimization and during the data taking.
My thesis work was not limited to detector development and construction but I tackled the challenge of performing the first study of the Bremsstrahlung process, which is the most dangerous background in the dark photon search. First of all, this required the development and the implementation of software calibration and geometry services capable to handle calibration constants and geometry parameters in a uniform and general way for all sub-detectors. Consequently, I had to put in place a strategy to measure in-situ the time calibration constants and equalize the response of all charged particle veto channels, in order to detect the first Bremsstrahlung signal. In addition, due to the large charged veto's occupancy, I implemented a multi-hit algorithm based on a peak finder software tool named TSpectrum. This allowed to extract the pulse-height and arrival time of hits also in presence of overlapping signals due to different minimum ionizing particles crossing the same scintillating bar. A crucial step forward was to quantify the yield of the Bremsstrahlung signal in the positron veto detectors and to compare with the predictions of an analytical calculation and of the simulation. A fine tuning of the simulation to the data was required before the comparison. The Bremsstrahlung yield was measured in data from the positron profile in presence of the target subtracted by the same distribution observed when the target was removed from the beam. In this way the dominant contribution to the positron profile due to the beam background was removed and only the Bremsstrahlung signal left. With this analysis strategy the measured and expected yields were found to be comparable in a wide region of the positron veto. However, in the last tenth of scintillating bars the large

crossing angle of the positron tracks, involving several channels, and the high rate introduce an important inefficiency. This comparison permits to prove the high efficiency of the scintillating bars and of the multi-hit algorithm (with the above mentioned exception) and to validate the measurement of the number of positron on target made by the diamond detector. A detailed tuning of the simulated detector parameters, in order to reproduce the real response in data, was needed, and a good agreement of positron profiles in data and simulation was achieved also in the high rate region where the positron veto is inefficient. This means that also the beam background was reasonably reproduced in simulation. This is an important result because reproducing in simulation the beam background is the main step to envisage future strategies for its mitigation. The beam background observed in data and reproduced in simulation are mainly caused by two phenomena. First of all, positrons in the beam halo could touch the beam line or the magnet finite apertures and induce electromagnetic showers which can reach the experiment. These particle splashes leave in the PADME detectors lower energy charged particles and photons with large angular spread. Second, the beam positrons crossing the thin window separating the LINAC vacuum from the BTF vacuum could radiate a photon of several MeV of energy. These positrons are going to populate the beam low energy non-gaussian tail and after angular dispersion in the last bending dipole can touch the beam line, the target support, or the PADME vacuum vessel and increase the pile-up in the high z positron veto scintillating bars. To handle these backgrounds the development of an efficient multi-hits reconstruction algorithm is necessary along with an accurate time calibration for all detectors.
A preliminary study showed a good correlation between the Small Angle Calorimeter (SAC) and the positron veto, allowing to detect the Bremsstrahlung signal. A fine time alignment and a tuning of the simulation also for the SAC, allowed to show the Bremsstrahlung signal by exploiting the energy correlation between photon and positron.
The PADME data analysed in this thesis are crucial to underline the potential and the limitations of the experiment and of the beam, suggesting the way for possible improvements through further developments and upgrades. Despite the high background, the studies allowed to achieve a preliminary successful comparison between the data and the simulation. The results suggest that the rate of positrons in the region of the detector next to the beam dump is too high to allow an efficient ad safe use of the positron veto in order to tag Bremsstrahlung processes. This is due to the high density of positrons in the limited bunch length of the pulsed BTF beam and also to the non projective geometry of the positron veto, implying that positrons of energy close to the beam energy cross several scintillators. With the present detector set-up, a dilution in time of the particles impinging on the target would be essential to reduce the pileup and make the reconstruction of single particle clusters in the positron veto robust and efficient. Some improvement of the beam quality, with a bunch length almost doubled and an overall reduction of the beam related background, already took place in the Run 2 of PADME and repeating the Bremsstrahlung analysis with the new data will allow to understand the benefit they brought. In summary, this work paved the way to the dark photon search with the data collected in PADME, because it addresses many issues related to the ability to tag and veto the main background and than to establish the final sensitivity of the experiment.

Bibliography

[1] F. Zwicky. Die Rotverschiebung von extragalaktischen Nebeln. *Helv. Phys. Acta*, 6:110–127, 1933.

[2] H. Andernach and F. Zwicky. English and Spanish Translation of Zwicky's (1933) The Redshift of Extragalactic Nebulae, 2017.

[3] E. Hubble and M.L. Humason. *The Astrophysical Journal*, 74:43, 1931.

[4] Sidney van den Bergh. The early history of dark matter. *Publications of the Astronomical Society of the Pacific*, 111(760):657–660, Jun 1999.

[5] V. C. Rubin and W. K. Ford, Jr. Rotation of the Andromeda Nebula from a Spectroscopic Survey of Emission Regions. 159:379, February 1970.

[6] V. C. Rubin, Jr. Ford, W. K., and N. Thonnard. Rotational properties of 21 SC galaxies with a large range of luminosities and radii, from NGC 4605 (R=4 kpc) to UGC 2885 (R=122 kpc). *Astrophysical Journal*, 238:471–487, June 1980.

[7] K. G. Begeman, A. H. Broeils, and R. H. Sanders. Extended rotation curves of spiral galaxies: dark haloes and modified dynamics. *Monthly Notices of the Royal Astronomical Society*, 249(3):523–537, Apr 1991.

[8] M. S. Mirakhor. Properties of the inctracluster medium assuming an einasto dark matter profile. *The Astrophysical Journal*, 866(2):148, Oct 2018.

[9] A. Vikhlinin, A. Kravtsov, W. Forman, C. Jones, M. Markevitch, S. S. Murray, and L. Van Speybroeck. Chandrasample of nearby relaxed galaxy clusters: Mass, gas fraction, and mass-temperature relation. *The Astrophysical Journal*, 640(2):691–709, Apr 2006.

[10] H. Böhringer and N. Werner. X-ray spectroscopy of galaxy clusters: studying astrophysical processes in the largest celestial laboratories. *The Astronomy and Astrophysics Review*, 18(1):127–196, 2010.

[11] R. Massey, T. Kitching, and J. Richard. The dark matter of gravitational lensing. *Rept. Prog. Phys.*, 73:086901, 2010.

[12] D. Clowe et al. A direct empirical proof of the existence of dark matter. *The Astrophysical Journal*, 648(2):L109–L113, Aug 2006.

[13] Esa. `https://www.esa.int`.

[14] M. Markevitch. Chandra observation of the most interesting cluster in the universe. *ESA Spec. Publ.*, 604:723, 2006.

[15] M. Bauer and T. Plehn. Yet Another Introduction to Dark Matter: The Particle Physics Approach. *Lecture Notes in Physics*, 959, 2018.

[16] G. et al. Hinshaw. Nine-Year Wilkinson Microwave Anisotropy Probe (WMAP) Observations: Cosmological Parameter Results. *Astrophys. J. Suppl.*, 208:19, 2013.

[17] N. et al. Aghanim. Planck 2018 results. *Astronomy and Astrophysics*, 641:A6, Sep 2020.

[18] A. Del Popolo. Dark matter, density perturbations and structure formation. Sep 2002.

[19] A. Doroshkevich, D. Tucker, S. Allam, and M. Way. Large scale structure in the SDSS galaxy survey. *Astronomy and Astrophysics*, 418, Jul 2003.

[20] M. Milgrom. Mond theory. *Canadian Journal of Physics*, 93(2):107–118, Feb 2015.

[21] O. et al. Adriani. An anomalous positron abundance in cosmic rays with energies 1.5–100GeV. *Nature*, 458(7238):607–609, Apr 2009.

[22] M. et. al. Aguilar. First result from the alpha magnetic spectrometer on the international space station: Precision measurement of the positron fraction in primary cosmic rays of 0.5-350 GeV. *Phys. Rev. Lett.*, 110:141102, Apr 2013.

[23] M. et al. Ackermann. Measurement of Separate Cosmic-Ray Electron and Positron Spectra with the Fermi Large Area Telescope. *Phys. Rev. Lett.*, 108:011103, Jan 2012.

[24] A. V. Belikov, J.F. Gunion, D. Hooper, and T. M. P. Tait. CoGeNT, DAMA, and light neutralino dark matter. *Physics Letters B*, 705(1):82 – 86, 2011.

[25] D. Hooper, J. I. Collar, J. Hall, D. McKinsey, and C. M. Kelso. Consistent dark matter interpretation for CoGeNT and DAMA/LIBRA. *Physical Review D*, 82(12), Dec 2010.

[26] B. W. Lee and S. Weinberg. Cosmological lower bound on heavy-neutrino masses. *Phys. Rev. Lett.*, 39:165–168, Jul 1977.

[27] E. Aprile et al. Dark Matter Search Results from a One Ton-Year Exposure of XENON1T. *Phys. Rev. Lett.*, 121:111302, Sep 2018.

[28] J. Alexander et al. Dark sectors 2016 workshop: Community report, 2016.

[29] Bob Holdom. Searching for ϵ charges and a new U(1). *Physics Letters B*, 178(1):65 – 70, 1986.

[30] H. Ruegg and M. Ruiz-Altaba. The Stueckelberg field. *Int. J. Mod. Phys. A*, 19:3265–3348, 2004.

[31] F. Curciarello. Review on Dark Photon. *EPJ Web Conf.*, 118:01008, 2016.

[32] M. Fabbrichesi, E. Gabrielli, and G. Lanfranchi. The Dark Photon. May 2020.

[33] M. Gasperini. *Lezioni di Cosmologia Teorica*. UNITEXT. Springer Milan, Milano, 2012.

[34] M. Pospelov, A. Ritz, and M. Voloshin. Secluded wimp dark matter. *Physics Letters B*, 662(1):53–61, Apr 2008.

[35] J. Beacham et al. Physics beyond colliders at CERN: beyond the Standard Model working group report. *Journal of Physics G: Nuclear and Particle Physics*, 47(1):010501, Dec 2019.

[36] Eder Izaguirre, Gordan Krnjaic, Philip Schuster, and Natalia Toro. Analyzing the discovery potential for light dark matter. *Phys. Rev. Lett.*, 115:251301, Dec 2015.

[37] D. Banerjee, V.E. Burtsev, A.G. Chumakov, D. Cooke, P. Crivelli, E. Depero, A.V. Dermenev, S.V. Donskov, R.R. Dusaev, T. Enik, and et al. Dark matter search in missing energy events with na64. *Physical Review Letters*, 123(12), Sep 2019.

[38] L. J. Hall, K. Jedamzik, J. March-R., and S. M. West. Freeze-in production of FIMP dark matter. *Journal of High Energy Physics*, 2010(3), Mar 2010.

[39] A. E. Nelson and J. Scholtz. Dark Light, Dark Matter and the Misalignment Mechanism. *Phys. Rev. D*, 84:103501, 2011.

[40] M. Kamionkowski. *WIMP and axion dark matter*. Jun 1997.

[41] P. W. Graham, J. Mardon, and S. Rajendran. Vector Dark Matter from Inflationary Fluctuations. *Phys. Rev. D*, 93(10):103520, 2016.

[42] K. Enqvist, R. J. Hardwick, T. Tenkanen, V. Vennin, and D. Wands. A novel way to determine the scale of inflation. *Journal of Cosmology and Astroparticle Physics*, 2018(02):006–006, Feb 2018.

[43] Y. Nakai, R. Namba, and Z. Wang. Light dark photon dark matter from inflation. *Journal of High Energy Physics*, 2020(12), Dec 2020.

[44] G.W. Bennett et al. Final Report of the Muon E821 Anomalous Magnetic Moment Measurement at BNL. *Phys. Rev. D*, 73:072003, 2006.

[45] J. H. Chang, R. Essig, and S. D. McDermott. Revisiting Supernova 1987A constraints on dark photons. *Journal of High Energy Physics*, 2017(1), Jan 2017.

[46] E.M. et al. Riordan. A Search for Short Lived Axions in an Electron Beam Dump Experiment. *Phys. Rev. Lett.*, 59:755, 1987.

[47] B. Batell, R. Essig, and Z. Surujon. Strong Constraints on Sub-GeV Dark Sectors from SLAC Beam Dump E137. *Phys. Rev. Lett.*, 113(17):171802, 2014.

[48] A. Bross, M. Crisler, S. Pordes, J. Volk, S. Errede, and J. Wrbanek. Search for short-lived particles produced in an electron beam dump. *Phys. Rev. Lett.*, 67:2942–2945, Nov 1991.

[49] S. Andreas, C. Niebuhr, and A. Ringwald. New limits on hidden photons from past electron beam dumps. *Phys. Rev. D*, 86:095019, Nov 2012.

[50] H. Merkel, P. Achenbach, C. Ayerbe Gayoso, J. C. Bernauer, R. Böhm, D. Bosnar, L. Debenjak, A. Denig, M. O. Distler, A. Esser, and et al. Search for light gauge bosons of the dark sector at the mainz microtron. *Physical Review Letters*, 106(25), Jun 2011.

[51] Evgueni Goudzovski. Search for the dark photon in π^0 decays by the NA48/2 experiment at CERN. *EPJ Web Conf.*, 96:01017, 2015.

[52] S. Abrahamyan et. al. Search for a New Gauge Boson in Electron-Nucleus Fixed-Target Scattering by the APEX Experiment. *Phys. Rev. Lett.*, 107:191804, Nov 2011.

[53] Omar M. The heavy photon search experiment at Jefferson Lab, 2013.

[54] J. et. al Balewski. The DarkLight Experiment: A Precision Search for New Physics at Low Energies. Dec 2014.

[55] L. Doria, P. Achenbach, M. Christmann, A. Denig, and H. Merkel. Dark matter at the intensity frontier: the new mesa electron accelerator facility, 2019.

[56] J. P. Lees et al. Search for a Dark Photon in e^+e^- Collisions at BaBar. *Phys. Rev. Lett.*, 113:201801, Nov 2014.

[57] F. Archilli, D. Babusci, D. Badoni, I. Balwierz, G. Bencivenni, C. Bini, C. Bloise, V. Bocci, F. Bossi, P. Branchini, and et al. Search for a vector gauge boson in ϕ meson decays with the KLOE detector. *Physics Letters B*, 706(4-5):251–255, Jan 2012.

[58] D. et al. Babusci. Limit on the production of a light vector gauge boson in phi meson decays with the KLOE detector. *Physics Letters B*, 720:111–115, 2013.

[59] R. Aaij et al. Search for $A \to \mu^+\mu^-$ decays. *Physical Review Letters*, 124(4), Jan 2020.

[60] E. et al. Kou. The Belle II Physics Book. *Progress of Theoretical and Experimental Physics*, 2019(12), Dec 2019.

[61] LHCb collaboration. Physics case for an LHCb Upgrade II - opportunities in flavour physics, and beyond, in the HL-LHC era, 2018.

[62] S. et. al. Adler. Further evidence for the decay $K^+ \to \pi^+\nu\bar{\nu}$. *Physical Review Letters*, 88(4):041803, Jan 2002.

[63] J. P. et al. Lees. Search for Invisible Decays of a Dark Photon Produced in e^+e^- Collisions at BaBar. *Phys. Rev. Lett.*, 119:131804, Sep 2017.

[64] The BaBar Collaboration and B. Aubert. Search for Invisible Decays of a Light Scalar in Radiative Transitions $\Upsilon_{3S} \to \gamma$ A0. In *34th International Conference on High Energy Physics*, Jul 2008.

[65] Jim Alexander. MMAPS: Missing-Mass A-Prime Search. *EPJ Web Conf.*, 142:01001, 2017.

[66] B. Wojtsekhowski, D. Nikolenko, and I. Rachek. Searching for a new force at VEPP-3, 2012.

[67] The European Strategy Group. Deliberation document on the 2020 Update of the European Strategy for Particle Physics. Technical Report CERN-ESU-014, Geneva, 2020.

[68] I. Rachek, Dmitri Nikolenko, and Bogdan Wojtsekhowski. Status of the experiment for the search of a dark photon at VEPP–3. *EPJ Web of Conferences*, 142:01025, Jan 2017.

[69] Torsten Åkesson et. al. Light Dark Matter eXperiment (LDMX), 2018.

[70] P. deNiverville, M. Pospelov, and A. Ritz. Observing a light dark matter beam with neutrino experiments. *Physical Review D*, 84(7), Oct 2011.

[71] A. A. Aguilar-Arevalo et al. Dark matter search in nucleon, pion, and electron channels from a proton beam dump with MiniBooNE. *Physical Review D*, 98(11), Dec 2018.

[72] M. Battaglieri et.al. Dark matter search in a Beam-Dump eXperiment (BDX) at Jefferson Lab: an update on PR12-16-001, 2018.

[73] M. Raggi, V. Kozhuharov, and P. Valente. The PADME experiment at LNF, 2015.

[74] Paolo Valente, Bruno Buonomo, and Giovanni Mazzitelli. Diagnostics and upgrade of the DAFNE Beam Test Facility (BTF). *Nucl. Phys. Proc. Suppl.*, 150:362–365, Jan 2006.

[75] M. Raggi and V. Kozhuharov. Proposal to search for a dark photon in positron on target collisions at daϕne linac. *Advances in High Energy Physics*, 2014:1–14, 2014.

[76] A. Ghigo, G. Mazzitelli, F. Sannibale, P. Valente, and G. Vignola. Commissioning of the DAFNE beam test facility. *Nucl. Instrum. Meth. A*, 515:524–542, 2003.

[77] F. Ferrarotto et.al. Performance of the Prototype of the Charged-Particle Veto System of the PADME Experiment. *IEEE Transactions on Nuclear Science*, 65(8):2029–2035, 2018.

[78] B. Adeva et al. The Construction of the L3 Experiment. *Nucl. Instrum. Meth. A*, 289:35–102, 1990.

[79] HZCphotonics. `http://www.hzcphotonics.com`.

[80] Ej500. `http://www.ggg-tech.co.jp/maker/eljen/ej-500.html`.

[81] Ej510. `http://www.ggg-tech.co.jp/maker/eljen/ej-510.html`.

[82] P. Albicocco et.al. Characterisation and performance of the padme electromagnetic calorimeter, 2020.

[83] Hamamatsu photomultiplier tubes. `http://www.hamamatsu.com/resources/pdf/etd/R13478_R13449_R13408_R13089_TPMH1363E.pdf`.

[84] A. et al. Frankenthal. Characterization and performance of PADME's Cherenkov-based small-angle calorimeter. *Nuclear Instruments and Methods in Physics Research Section A: Accelerators, Spectrometers, Detectors and Associated Equipment*, 919:89–97, Mar 2019.

[85] A. et. al. Besson. From vertex detectors to inner trackers with CMOS pixel sensors. *Nucl. Instrum. Meth. A*, 845:33–37, 2017.

[86] Caen. `https://www.caen.it`.

[87] The PADME collaboration. *The PADME experiment Technical Proposal* . Sep 2015.

[88] M. Raggi on behalf the PADME collaboration. The PADME experiment. *Frascati Physics Series*, 66, 2018.

[89] V. Kozhuharov. Searching for dark sector with missing mass technique in fixed target experiments. *EPJ Web Conf.*, 212:06001, 2019.

[90] L. Marsicano. Searching for dark photon with positrons at Jefferson Lab. *AIP Conference Proceedings*, 1970(1):020008, 2018.

[91] F. Giacchino. A light dark matter portal: The axion-like particle. *Frascati Phys. Ser.*, 69:206–211, 2019.

[92] M. Raggi and V. Kozhuharov. Results and perspectives in dark photon physics. *Riv. Nuovo Cim.*, 38(10):449–505, 2015.

[93] Search for invisible Higgs boson decays with vector boson fusion signatures with the ATLAS detector using an integrated luminosity of 139 fb^{-1}. Apr 2020.

[94] A. M. Sirunyan and The CMS collaboration. Search for dark photons in decays of Higgs bosons produced in association with Z bosons in proton-proton collisions at $\sqrt{s} = 13$ TeV. *Journal of High Energy Physics*, 2019(10):139, 2019.

[95] J. Gulyás, T.J. Ketel, A.J. Krasznahorkay, M. Csatlós, L. Csige, Z. Gácsi, M. Hunyadi, A. Krasznahorkay, A. Vitéz, and T.G. Tornyi. A pair spectrometer for measuring multipolarities of energetic nuclear transitions. *Nucl. Instrum. Meth. A*, 808:21–28, 2016.

[96] A.J. Krasznahorkay, M. Csatlós, L. Csige, Z. Gácsi, J. Gulyás, M. Hunyadi, I. Kuti, B.M. Nyakó, L. Stuhl, J. Timár, and et al. Observation of Anomalous Internal Pair Creation in ^{8}Be: A Possible Indication of a Light, Neutral Boson. *Physical Review Letters*, 116(4), Jan 2016.

[97] A J Krasznahorkay, M Csatlós, L Csige, Z Gácsi, J Gulyás, Á Nagy, N Sas, J Timár, T G Tornyi, I Vajda, and A J Krasznahorkay. New results on the 8be anomaly. *Journal of Physics: Conference Series*, 1056:012028, Jul 2018.

[98] A. J. et al Krasznahorkay. New evidence supporting the existence of the hypothetic X17 particle. Oct 2019.

[99] J. L. et al. Feng. Particle physics models for the 17 MeV anomaly in beryllium nuclear decays. *Phys. Rev. D*, 95:035017, Feb 2017.

[100] L. Delle Rose, S. Khalil, S. J. D. King, and S. Moretti. New Physics Suggested by Atomki Anomaly. *Frontiers in Physics*, 7:73, 2019.

[101] A. Konaka et al. Search for Neutral Particles in Electron Beam Dump Experiment. *Phys. Rev. Lett.*, 57:659, 1986.

[102] M. Davier and H. Nguyen Ngoc. An unambiguous search for a light higgs boson. *Physics Letters B*, 229(1):150 – 155, 1989.

[103] J. D. Bjorken, S. Ecklund, W. R. Nelson, A. Abashian, C. Church, B. Lu, L. W. Mo, T. A. Nunamaker, and P. Rassmann. Search for neutral metastable penetrating particles produced in the SLAC beam dump. *Phys. Rev. D*, 38:3375–3386, Dec 1988.

[104] A. J. Krasznahorkay, M. Csatlos, L. Csige, J. Gulyas, M. Koszta, B. Szihalmi, J. Timar, D. S. Firak, A. Nagy, N. J. Sas, and A. Krasznahorkay. New evidence supporting the existence of the hypothetic x17 particle, 2019.

[105] E. Nardi, C. D.R. Carvajal, A. Ghoshal, D. Meloni, and M. Raggi. Resonant production of dark photons in positron beam dump experiments. *Physical Review D*, 97(9), May 2018.

[106] C. J. H. Wort and R. S. Balmer. Diamond as an electronic material. *Materials Today*, 11(1):22 – 28, 2008.

[107] J. J. Gracio, Q. H. Fan, and J. C. Madaleno. Diamond growth by chemical vapour deposition. *Journal of Physics D: Applied Physics*, 43(37):374017, Sep 2010.

[108] J. E. Field. The mechanical and strength properties of diamond. *Reports on Progress in Physics*, 75(12):126505, Nov 2012.

[109] R. L. Aggarwal and A. K. Ramdas. *Physical Properties of Diamond and Sapphire*. CRC Press, 2019.

[110] T. Stachel and J. W. Harris. Formation of diamond in the Earth's mantle. *J Phys Condens. Matter*, 36:21, 2009.

[111] F. Bundy, H. Hall, H. Strong, and R. Wentorf. Man-made diamonds. *Nature*, 176:51–55, Jul 1955.

[112] R. S. Balmer et. al. Chemical vapour deposition synthetic diamond: materials, technology and applications. *Journal of Physics: Condensed Matter*, 21(36):364221, Aug 2009.

[113] M. Schwander and K. Partes. A review of diamond synthesis by CVD processes. *Diamond and Related Materials*, 20(9):1287 – 1301, 2011.

[114] M. Mikuz et al. Diamond Sensors in HEP. *PoS*, ICHEP2012:524, 2013.

[115] W. Shockley. Currents to Conductors Induced by a Moving Point Charge. *Journal of Applied Physics*, 9(10):635–636, Oct 1938.

[116] S. Ramo. Currents induced by electron motion. *Proceedings of the IRE*, 27(9):584–585, 1939.

[117] K. E. Spear and J. P. Dismukes. *Synthetic Diamond-Emerging CVD Science and Technology*. 1994.

[118] P. R. Chalker. *Wide band-gap semiconductor: how good is diamond?* Nov 1993.

[119] R. J. Tapper. Diamond detectors in particle physics. *Reports on Progress in Physics*, 63(8):1273–1316, Jul 2000.

[120] L. Bäni et. al. Diamond detectors for high energy physics experiments. *Journal of Instrumentation*, 13(01):C01029–C01029, Jan 2018.

[121] M. ˇCerv. The ATLAS Diamond Beam Monitor. *JINST*, 9:C02026, 2014.

[122] F. Bachmair. Diamond sensors for future high energy experiments. *Nuclear Instruments and Methods in Physics Research Section A: Accelerators, Spectrometers, Detectors and Associated Equipment*, 831:370 – 377, 2016.

[123] A. J. Edwards, B. Brau, M. Bruinsma, P. Burchat, H. Kagan, R. Kass, D. Kirkby, B. A. Petersen, and M. Zoeller. Radiation monitoring with diamond sensors in BaBar. *IEEE Transactions on Nuclear Science*, 51(4):1808–1811, 2004.

[124] P. Dong, R. Eusebi, C. Schrupp, A. Sfyrla, R. Tesarek, and R. Wallny. Beam Condition Monitoring with Diamonds at CDF. *Nuclear Science, IEEE Transactions on*, 55:328 – 332, Mar 2008.

[125] Applied diamond. `http://usapplieddiamond.com`.

[126] H.A. Hoff, G.L. Waytena, C.L. Vold, J.S. Suehle, I.P. Isaacson, M.L. Rebbert, D.I. Ma, and K. Harris. Ohmic contacts to semiconducting diamond using a ti/pt/au trilayer metallization scheme. *Diamond and Related Materials*, 5(12):1450 – 1456, 1996.

[127] V.I. Konov. Laser in micro and nanoprocessing of diamond materials. *Laser & Photonics Reviews*, 6(6):739–766, 2012.

[128] E. Alemanno et. al. Laser induced nano-graphite electrical contacts on synthetic polycrystalline CVD diamond for nuclear radiation detection. *Diamond and Related Materials*, 38:32 – 35, 2013.

[129] M. De Feudis et al. Diamond graphitization by laser-writing for all-carbon detector applications. *Diamond and Related Materials*, 75:25 – 33, 2017.

[130] M. De Feudis et al. Characterization of surface graphitic electrodes made by excimer laser on cvd diamond. *Diamond and Related Materials*, 65:137 – 143, 2016.

[131] R. Assiro et al. Performance of the diamond active target prototype for the PADME experiment at the DAΦNE BTF. *NIM A*, 898:105–110, 2018.

[132] Epoxy. `http://epoxy-produkte.de`.

[133] G. G. Harman. *Wire Bonding in Microelectronics*. McGraw Hill, New York, NY, 2010.

[134] Yong Ding, Jang-Kyo Kim, and Pin Tong. Numerical analysis of ultrasonic wire bonding: Effects of bonding parameters on contact pressure and frictional energy. *Mechanics of Materials - MECH MATER*, 38:11–24, Feb 2006.

[135] M. Schuettler and T. Stieglitz. *4 - Microassembly and micropackaging of implantable systems*. Woodhead Publishing Series in Biomaterials. Woodhead Publishing, 2013.

[136] Delvotec. `http://www.fkdelvotec.com`.

[137] W. Caiyuan and S. Ronglu. The quality test of wire bonding. *Modern Applied Science*, 3, Nov 2009.

[138] S. Schmitz, J. Kripfgans, M. Schneider-Ramelow, W. H. Müller, and K. . Lang. *Investigating wire bonding pull testing and its calculation basics*. 2014.

[139] Keithley. `https://www.tek.com/keithley`.

[140] Ideas. `https://ideas.no`.

[141] Gefran. `https://www.gefran.com`.

[142] M. Iskander. Chapter 3 - Geotechnical Underground Sensing and Monitoring. In Sibel Pamukcu and Liang Cheng, editors, *Underground Sensing*, pages 141 – 202. Academic Press, 2018.

[143] Agilent. `https://www.agilent.com`.

[144] M. Raggi. PADME status report. *60th meeting of the LNF Scientific Committee*, 17th Nov 2020.

[145] Root data analysis framework. `https://root.cern.ch`.

[146] F. Oliva. Operation and performance of the active target of padme. *Nuclear Instruments and Methods in Physics Research Section A: Accelerators, Spectrometers, Detectors and Associated Equipment*, 958:162354, 2020.

[147] Report on Element Six Samples, No. 1/2005. Apr 2005.

[148] PADME software package. `https://github.com/PADME-Experiment/padme-fw/`.

[149] Geant4 a simulation toolkit. `https://geant4.web.cern.ch/`.

[150] S. M. Seltzer and M. J. Berger. Bremsstrahlung spectra from electron interactions with screened atomic nuclei and orbital electrons. *Nuclear Instruments and Methods in Physics Research Section B: Beam Interactions with Materials and Atoms*, 12(1):95 – 134, 1985.

[151] Yung-Su Tsai. Pair Production and Bremsstrahlung of Charged Leptons. *Rev. Mod. Phys.*, 46:815, 1974. [Erratum: Rev.Mod.Phys. 49, 421–423 (1977)].

[152] Yung-Su Tsai. Erratum: Pair production and Bremsstrahlung of charged leptons. *Rev. Mod. Phys.*, 49:421–423, Apr 1977.

[153] W. Heitler. *The quantum theory of radiation*, volume 5 of *International Series of Monographs on Physics*. Oxford University Press, Oxford, 1936.

[154] A. Belyaev, N. D. Christensen, and A. Pukhov. Calchep 3.4 for collider physics within and beyond the standard model. *Computer Physics Communications*, 184(7):1729–1769, 2013.

[155] M. Tanabashi et al. Review of particle physics. *Phys. Rev. D*, 98:030001, Aug 2018.

Acknowledgements

This PhD has come to an end. I haven't realised it yet.
I think that sometimes words are not enough.
I am very grateful to my supervisors G.Chiodini and S.Spagnolo, who have always believed in me, encouraging me to do my best.

For me, PADME is not just an experiment.

PADME means a lot. It is my second family, a human and academic experience that I would do another thousand times. I've done everything I could over these years for the growth of the experiment, giving my all, hoping to be enough. But I've been rewarded for the effort.
Not only has PADME allowed me to increase my skills, from hardware to software and analysis, but I have also had the opportunity to meet wonderful people.
Thanks to the PADME people and the BTFers, who have contributed to my professional and personal growth during this journey.
I will miss the PADME atmosphere during each shift operation.
I hope to collaborate with them all in the future.
A special thank you to the young people of PADME: they are not only colleagues but first of all friends to me.

As always, thanks to my essential roots: my family and my friends, who have always supported me.

Thanks to music and poetry.

Emily Dickinson wrote:
"A word is dead
When it is said,
Some say.
I say it just
Begins to live
That day".

This word, addressed to you all is: Grazie.

"Well, big wheels roll through fields where sunlight streams
Meet me in a land of hope and dreams."

B.Springsteen